UiT The Arctic University of Norway

Faculty of Health Sciences, Department of Pharmacy

Molecular Pharmacology and Toxicology Research Group

Molecular modeling of the monoamine transporters and their interactions with psychostimulants and other substances

Ejona Gashi

Thesis for the degree Master of Pharmacy, May 2023

Acknowledgements

This master's thesis is dedicated to and in honor of every single person who carries a psychiatric- or neurological condition, ranging from clinical depression to multiple sclerosis.

The master project was performed at the Molecular Pharmacology and Toxicology Research Group, at the Department of Medical Biology, UiT – The Arctic University of Norway, in the period August 2022 – May 2023. I am beyond grateful for having this opportunity, and for being included in the research group.

First, I would like to express my gratitude towards my supervisors, Associate Professor Kurt Kristiansen and Professor Ingebrigt Sylte. Thank you for making this thesis possible for me, the valuable guidance, and learning experience throughout this year. To Hanna-Kirsti Schrøder Leiros, Professor in structural biology at the Department of Chemistry - thank you for inspiring me, and for giving me a deep introduction to the field of structural chemistry and biology. Further, I would also like to thank the educational team of Schrödinger, LLC., for the scientific and technical support.

Finally, my dearest family, you are and have always been my driving force. To my beloved father and mother, Enver Gashi and Fatime Vitija Gashi, thank you for the tremendous support, encouragement, and for always having faith in me. To my cherished siblings, Elizabeth Edona, Engjëll, and Emira, thank you for the motivational speeches, laughter, and for always being there for me. My family, you have taught me to seek beyond the sparkling stars to the very end of the universe - the infinite. My gratitude for you is indescribable – you are the ones who keep every systole and diastole going: from aorta, through the arteries and veins, to vena cava.

Familja ime e dashur, faleminderit për mbështetjen, dashurinë, dhe forcën që më jepni per çdo ditë. Ju dua pa fundëshisht (albanian language).

Tromsø, May 2023

Table of Contents

List of abbreviations

2D	*Two-dimensional*
3D	*Three-dimensional*
5-HT	*5-hydroxytryptamine, Serotonin*
5-HT receptor	*5-hydroxytryptamine receptor*
Ach	*Acetylcholine*
ADHD	*Attention deficit hyperactivity disorder*
BBB	*Blood-brain barrier*
BLAST	*Basic Local Alignment Search tool*
CNS	*Central nervous system*
CPK representation	*Corey-Pauling-Koltun representation*
CPU	*Central processing units*
Cryo-EM	*Cryogenic electron microscopy*
C-terminus	*COOH, carboxyl terminus*
DA	*Dopamine*
DAT	*Dopamine transporter*
dDAT	*Drosophila melanogaster dopamine transporter*
EL	*Extracellular loop*
FDA	*Food and Drug Administration*
GABA	*Gamma aminobutyric acid*
GPCR	*G-protein-coupled receptor*
H-bond	*Hydrogen bond*
hDAT	*Human dopamine transporter*
hNET	*Human norepinephrine transporter*
hSERT	*Human serotonin transporter*
IC50	*Half maximal inhibitory concentration*
IFD	*Induced fit docking*
IL	*Intracellular loop*
JHW007	*N-(n-butyl)-3α-[bis(4'-fluorophenyl) methoxy]-tropane*
K_b	*Affinity, binding constant*
K_i	*Inhibition constant*
K_v channel	*Voltage-gated potassium channel*
LC	*Locus coeruleus*
MAT	*Monoamine transporter*

MD simulation	*Molecular dynamics simulation*
MDMA	*3,4-methylenedioxymethamphetamine*
MDPV	*3,4- Methylenedioxypyrovalerone*
MMAI	*5-Methoxy-6-methyl-2-aminoindane*
MSV	*Multiple sequence viewer*
N- terminus	*NH_2, amino terminus*
Na_v channel	*Voltage-gated sodium channel*
NE	*Norepinephrine*
NET	*Norepinephrine transporter*
NMR	*Nuclear magnetic resonance*
NPS	*New psychoactive substances*
NS	*Nervous system*
OPLS 4	*Optimized Potentials for Liquid Simulations 4*
OPM	*Orientations of Proteins in Membranes*
PDB	*Protein Data Bank*
PDSP	*Psychoactive Drug Screening Program*
PE	*Potential energy*
PMMA	*Paramethoxy-methamphetamine*
PNS	*Peripheral nervous system*
POPC	*1-palmitoyl-2-oleoylphosphatidylcholine*
RMSD	*Root mean square deviation*
RMSF	*Root mean square fluctuation*
SAR	*Structure-activity relationship*
SERT	*Serotonin transporter*
SLC1 transporter family	*Solute carrier 1 transporter family*
SLC6 transporter family	*Solute carrier 6 transporter family*
SMILES	*Simplified Molecular Input Line Entry Systems*
SNc	*Substantia nigra pars compact*
sNRI	*Selective norepinephrine reuptake inhibitor*
SPC water model	*Simple point charge water model*
SSRI	*Selective serotonin reuptake inhibitor*
TCA	*Tricyclic antidepressants*
TMH	*Transmembrane helix*
tnH	*Tertiary amine in tropane rings*

ts3-construct	*3 Thermostabilizing constructs (Ile291Ala, Thr439Ser, and Tyr110Ala in the serotonin transporter)*
UniProtKB	*Universal Protein Resource Knowledge base*
VTA	*Ventral tegmental area*
WHO	*World Health Organization*
α-PVP	*Alpha-pyrrolidinovalerophenone*
β-CFT	*2β-carbomethoxy-3β-(4-fluorophenyl) tropane*
ΔG	*Change in Gibbs free energy*

Abstract

The monoamines (i.e., dopamine (DA), serotonin (5-HT), and norepinephrine (NE)) are vital to the ontogeny, function, and plasticity of the nervous system. These neurotransmitters affect each other, impact, and regulate, amongst others, attention, motor function, aggression, cognitive state, motivation, and stress reactions. The neurotransmission is mainly terminated by reuptake in monoamine transporters (MATs), i.e., the dopamine (DAT)-, serotonin (SERT)-, and norepinephrine (NET) transporter.

Imbalance in the monoamine systems in the central nervous system (CNS) is associated with neurological disorders, such as attention-deficit hyperactivity disorder (ADHD), multiple sclerosis, and Parkinson's disease. These conditions are substantially linked to psychiatric disorders like clinical depression and anxiety. Consequently, the MATs are targets for several drugs used to treat these conditions, including therapeutic psychostimulants, non-stimulants, and antidepressants. Most of these drugs bind the outward-facing conformation of the MATs, and their effects depend highly on the selectivity for a single MAT. On the other hand, the increased use of illicit stimulants, predominantly acting on DAT, has risen alarms due to their unpredictable effects and high abuse potential. Regarding the additive phenomena of stimulants, some research standards, suggested to bind the inward-facing conformation of the MATs, have shown anti-additive properties.

Hence, the overall aim of this study was to identify determinants for selective binding to each MAT, which is an important contribution to development of drugs with high selectivity and potency for a specific MAT in the treatment of CNS disorders and stimulant addiction.

In this study, homology models of the outward-facing human DAT (hDAT)- and NET (hNET) were constructed, whose three-dimensional (3D) structures were unknown. Models of the outward-and inward hSERT were likewise generated - 3D structures of SERT were known at the study start. Based on the models of the human MATs, conserved and divergent residues in the highly conserved S1-site could be mapped. The models were also validated. 23 ligands (distinct psychostimulants, a non-stimulant, antidepressants, atypical inhibitors, and some research standards) with different intrinsic properties and selectivity-preferences were docket to each model by induced fit docking (IFD). The generated poses were ranked by a scoring function according to binding energies. Ligands that exhibited high preference for specific MATs were further investigated for differences and similarities in their binding mode

and the creation of intermolecular interactions in each MAT. Lastly, molecular dynamics (MD) simulations were applied to further examine the stability of the IFD-poses and interactions in each complex. Both ligands that bind the inward-and outward-facing MATs were assessed.

The results indicate that non-conserved, divergent, residues in the S1-site play a key role in MAT-selectivity. These residues shape the polarity and steric environment in the orthosteric (S1) pocket, thus affecting the stabilization of both substrates and inhibitors, interactions, and orientation of ligands in each MAT. Structural features in the ligands appeared to also play a role in the selectivity for a MAT, concerning the binding mode and formation of interactions. There was, however, no correlation between selectivity for a MAT and the IFD-scores. In the inward-facing hSERT-model, the MD simulations revealed that the movement of four residues (i.e., Phe335, Phe341, Phe347, and Ala441) closer into the S1-site, compared to the position in the outward-facing conformation, was important for the creation of a hydrophobic pocket, where aromatic moieties of atypical inhibitors could stabilize and interact.

1. Introduction

1.1 The Nervous System

The nervous system (NS) is a complex network, consisting of vast neural associations, which enables interactions between an organism and its surroundings, as well as many mechanisms inside the body are controlled by this network. Signaling and communication between the interconnected neuron circuits facilitate feelings, thinking, learning, memory, sensation, and body function (e.g., the ability to digestion, breathing, and heart beating). All in all, the nervous system is a way to interpret and respond to everything that is experienced – both with and without our conscious control (1, 2).

The central- and peripheral nervous systems (CNS and PNS, respectively) are the two parts of the nervous system. Comprehensive of the CNS is the nerves in the brain and spinal cord, while all the other nerves in the body constitute the PNS (1, 2).

The brain of the CNS can further be divided into three different subgroups; the brainstem (consisting of the medulla, the pons, and the midbrain), the forebrain (consisting of the diencephalon and cerebral hemispheres), and the cerebellum (3). The spinal cord function as an intermediary between the CNS and PNS (4). More of the CNS will be discussed in the later chapters.

In short, the PNS is divided into two main divisions: the somatic- and the autonomic nervous system (5). The somatic NS is associated with the voluntary control and movement of the body, meaning the actions we are aware of and can consciously influence. That is by voluntary movement of the skeletal muscles, and transmission of sensory signals from organs such as the eyes, ears, nose, skin, and joints to the CNS (5, 6). The autonomic NS is, on the other hand, responsible for involuntary processes, including the heart rate, blood pressure, respiration, digestive organs, excretory - and reproductive systems. Both the enteric-, sympathetic- and parasympathetic nervous systems constitute the autonomic NS, which, respectively, drives the gastrointestinal behavior, “fight or flight” – and “rest and digest” conditions by visceral sensory neurons (7, 8).

In total, both afferent and efferent neurons connect the CNS and PNS, through the spinal cord. Where the afferent nerves comprise the sensory nerves and carry information to the

CNS, while the efferent nerves comprise motor nerves and carry information from the CNS to the effector cells (e.g., smooth muscles and glandular tissue). Together, these systems participate to keep us in touch with our environment – both external and internal – through communication, regulation, and control mechanisms in the body. Figure 1 shows a simplified schematic illustration of the nervous system (2, 9).

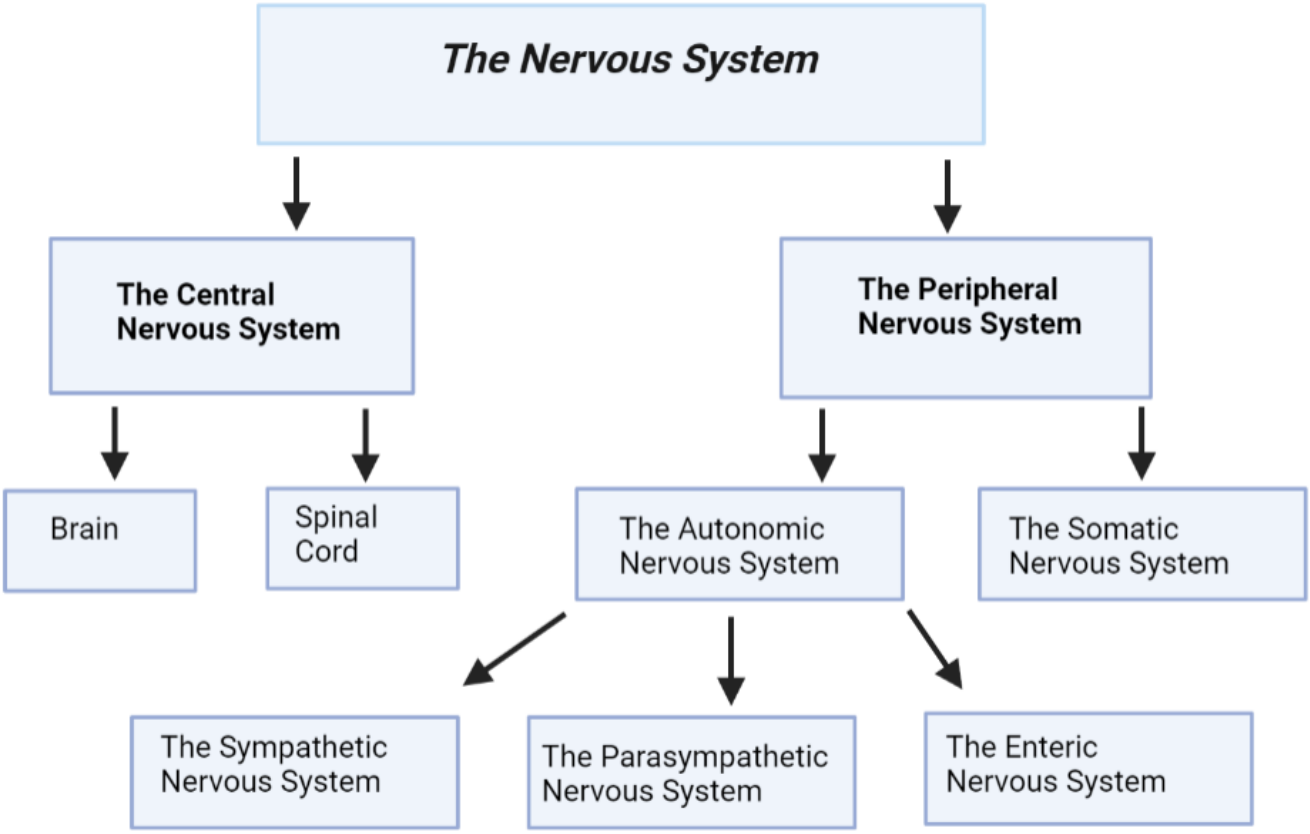

Figure 1: *Simplified schematic overview of the main components of the NS. Created with BioRender.com.*

In this thesis, the focus will be on the central nervous system.

1.2 The Central Nervous System

The central nervous system (CNS) is constituted by the brain and the spinal cord. Above all, the brain is a vital aspect of the CNS, comprising nervous tissue that is responsible for the ability to sensation, movement, emotions, communication, thought processing, and memory. The spinal cord connects the PNS, the rest of the body, to the CNS - through descending- and ascending pathways. Indeed, there is a vast network of neurons that can relay information via afferent first-, second-, and third-order neurons from sensory organs to specific locations in the brain (i.e., ascending pathway), or send commands from the brain to the effector organs through efferent motor neurons (i.e., descending pathway) or efferent postganglionic neurons (3, 10).

The nervous system (NS) is built up of nerve cells (i.e., neurons) and glial cells. Characteristic for the neurons is the ability to rapid communication over long distances, through fast conductions of an electrical discharge, nerve impulse, as a response to a stimulus. This kind of communication happens for every action in the NS, and neurons are therefore a vital part of this network. The function of the non-neuronal glial cells in the NS is, however, not completely known. It is, on the other hand, established that glial cells are crucial for supporting and isolating neural processes, controlling the neural environment, as well the repairing process of neurons (11).

All in all, the structures and function of the CNS are highly immune privileged, and therefore it is necessary with a stable environment. This is maintained by the blood-brain barrier (BBB), as one of two systems. The BBB is a dynamic interface between the cerebral capillary blood and the interstitial fluid of the brain. Structurally, the BBB is composed of capillary endothelial cells, a non-cellular vascular basement membrane (comprised of fibronectin, lamin, and collagen), a neuroglial membrane, and glial podocytes (i.e., projections of astrocytes). By this composition, the BBB ensures the homeostatic environment in the CNS (12, 13).

Tight junctions between the endothelial cells lining the capillaries, make the transport over the BBB highly specific. Only some selected types of substances can passage over the semipermeable barrier through passive transport mechanisms, such as small lipophilic substances (e.g., oxygen and carbon dioxide). Also, small hydrophilic substances (e.g., water molecules, glucose, and cations) can cross the barrier by passive carrier-mediated transport.

Large solutes and vital substances (e.g., proteins and peptides) are dependent on active receptor-mediated- or endocytic transport mechanisms (12, 14). The barrier also prevents foreign substances and toxins to enter the CNS via, amongst others, efflux pumps. The latter property is a significant roadblock for oral drug delivery to the brain (12, 14).

Figure 2 shows the blood brain barrier in a simplified illustration.

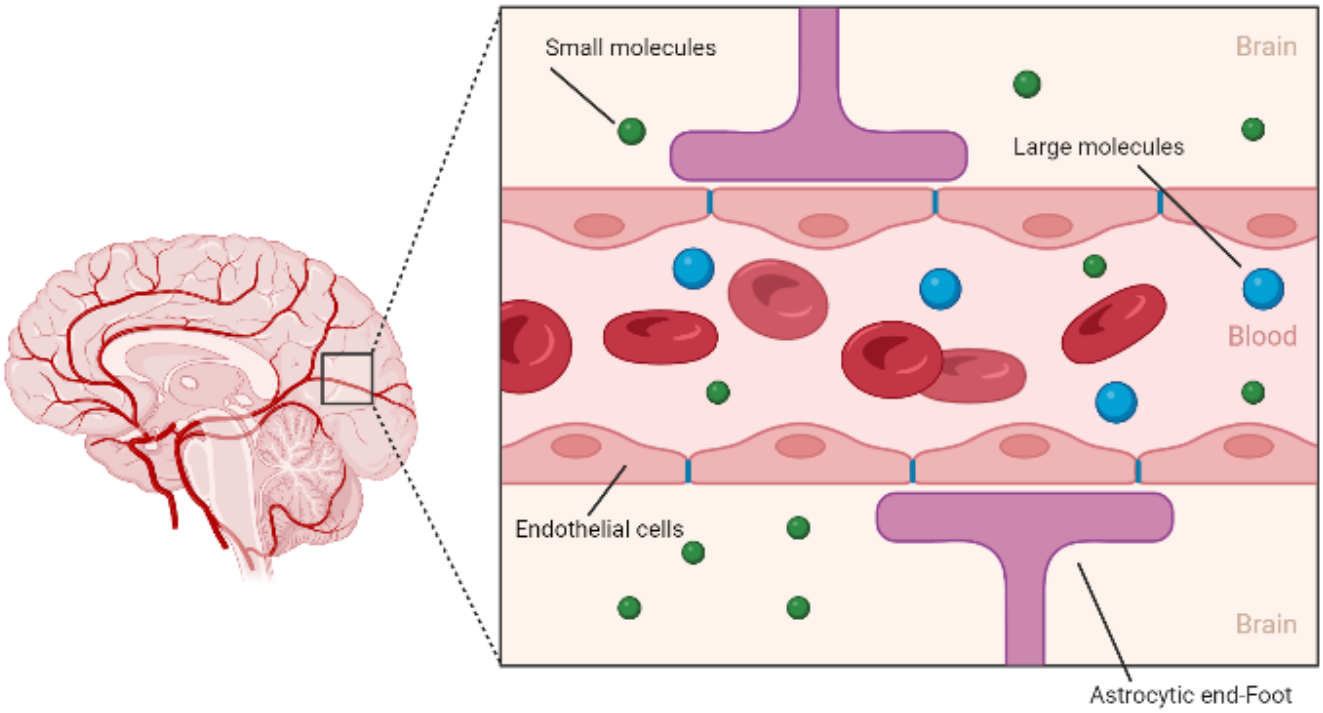

Figure 2: *Simplified illustration of the BBB created with BioRender.com. Tight junctions (illustrated as blue gaps between the endothelial cells) make the transport over the semipermeable membrane of the BBB highly specific. Small molecules can cross the barrier through passive transport mechanisms, while large molecules are dependent on active transport mechanisms. Unfamiliar substances, such as drugs, are usually recognized and prevented from the CNS (12, 13, 14).*

1.3 Neurotransmission

Neurons are composed of a cell body (the soma), from which multiple dendrites and a single axon branch off. The dendrites are the receiving surface of the neuron, while the axon is responsible for conducting nerve impulses to muscle cells or other neurons. Both the dendrites and axons can branch to, respectively, dendritic "trees" and axon collaterals. Hence, the neurons are interconnected and form vast neural networks, where a single neuron influences many target cells (also termed divergence), as well as each neuron receives synaptic contacts from many other neurons (also termed convergence) (11).

Several axons in the CNS are insulted with a myelin sheath, which is mainly made up of proteins and lipids, that isolate the axon and increase the speed of impulse transmission (11, 15). The cytoskeleton in the neuron, comprising various neurofibrils, plays a role in pursuing the neuronal processes and transport of substances from the soma to the nerve terminals, and vice versa (11).

Communication between neurons occurs across microscopic gaps known as synaptic clefts. Endogenous signaling substances, i.e., neurotransmitters, are released from the presynaptic terminals (i.e., in the presynaptic neuron) and received by the dendrites on postsynaptic neurons. Only a few types of neurotransmitters are produced and released by each neuron, but they can carry receptors (i.e., Ligand-Gated Channel Receptors and G-protein-coupled receptors (GPCRs)) that can respond to several neurotransmitters. Some of the neurotransmitters will stimulate excitatory effects, while others will induce inhibitory effects – depending on which receptor and neurotransmitter that is involved. Whereas the total input is excitatory or inhibitory depends on the summation of the total inputs. This communication among neurons is called synaptic transmission (16, 17).

It is established that at least 100 substances can act as neurotransmitters. However, the amino acids glutamate and aspartate contribute to the major of excitatory effects, while gamma-aminobutyric acid (GABA) is the major inhibitory neurotransmitter in the CNS (17). Moreover, the monoamine neurotransmitters (i.e., dopamine (DA), serotonin (5-hydroxytryptamine, 5-HT), and norepinephrine (NE)) have multiple functions in the CNS, including regulation of emotions, learning, memory, and controlling of physiological processes in the body (17, 18). Acetylcholine (ACh) is, on the other hand, a major neurotransmitter of the motor neurons, autonomic preganglionic- and postganglionic

cholinergic (parasympathetic) nerve fibers (i.e., axons). The ACh is both important in the CNS and the PNS. Lastly, most of the neurotransmitters are stored in vesicles at the nerve terminal, and trigger reactions in another neuron or effector cells (e.g., muscle cells, gland, most exocrine and endocrine cells) (17).

The neurotransmission is mainly terminated by removing neurotransmitters from the extracellular fluid by reuptake into the glial cells or neurons. The reuptake mechanism is carried by integrated transporter proteins, which are driven by ion-concentration gradients over the cell membrane. Thus, there are two families of transmitter transporters: one is driven by concentration gradients of sodium and chloride (i.e., the solute carrier 6 (SLC6) transporter family), and the second family (i.e., the SLC1 transporter family) comprises five different glutamate transporters driven by concentration gradients of sodium and potassium. The SLC6 family includes transporters that mediate the reuptake of, amongst others, GABA, DA, 5-HT, and NE. Some neurotransmitters are, however, removed by diffusion and enzymatic degradation (e.g., Ach) (19).

Transporters do not remove all the neurotransmitters from the extracellular fluid. The task is to modulate the concentration of neurotransmitters up or down to a certain baseline. Thus, even a slight alteration of the transporter activity can change the transmission caused by transmitter-receptor activation. In such manner, the transmitter transporters contribute to the control of neural excitability and synaptic transmission (19). The general synaptic transmission is summarized and displayed in figure 3.

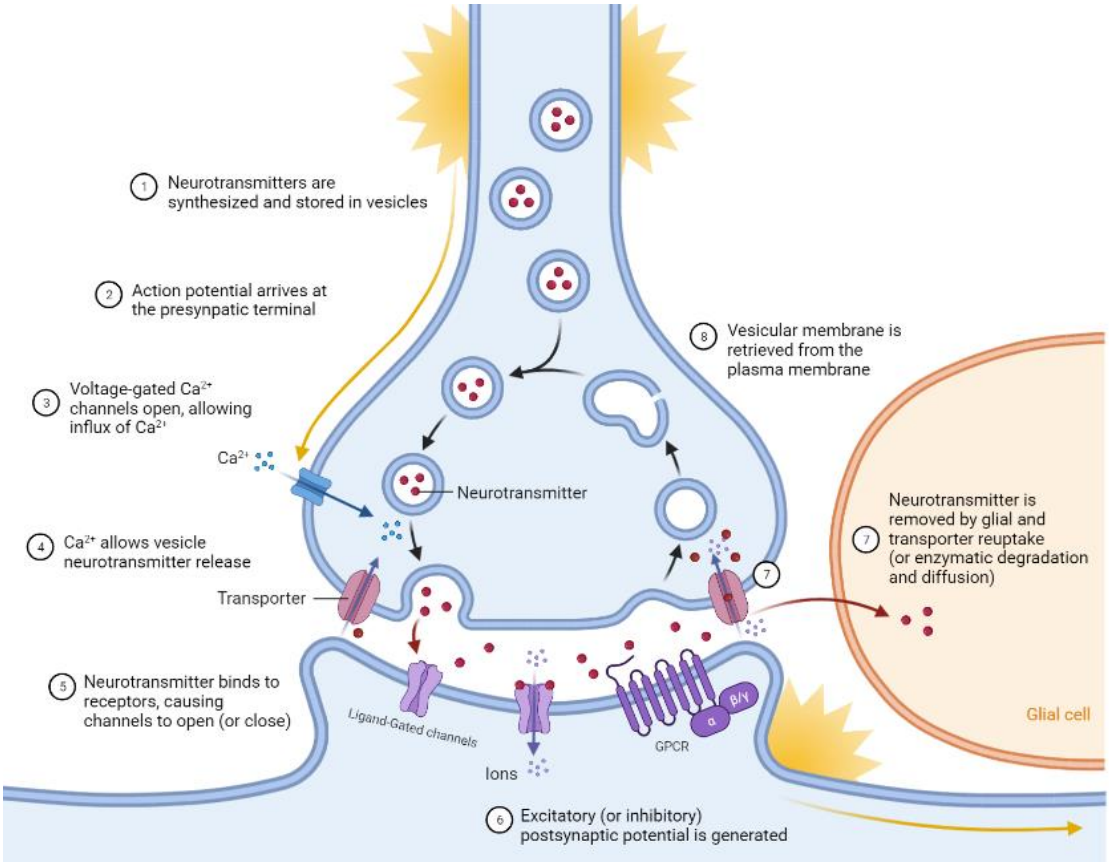

Figure 3: *Step-by-step illustration of the synaptic transmission. Figure created based on templates from BioRender.com.*

The mechanism underlying signal transmission among neurons is based on membrane potentials (i.e., voltage differences) between the inside and outside of the neuron. The potential is created due to an uneven distribution of ions across the membrane, mainly driven by sodium- (Na^+), potassium- (K^+), calcium- (Ca^{2+}), and chloride (Cl^-) ions (16).

Most of the time the neurons have a negative concentration gradient, meaning that there are more positively charged ions outside the neuron compared to the inside. Hence, there are normally more Na^+ ions extracellularly than K^+ ions intracellularly. The neuron mainly maintains the negative concentration gradient by using sodium-potassium pumps to pump potassium back into the cell and sodium out of the cell in a 2:3 ratio, respectively.

As a result, the overall potential is usually at a negative voltage (between -40 to -90 millivolts). This state is called the resting membrane potential. However, these ions are constantly moving in and out through the membrane, trying to equalize their concentration, implying that the concentration gradient is not static (20).

Synaptic transmission begins when the action potential reaches the axonal terminal of the presynaptic neuron. This triggers the opening of voltage-gated Ca^{2+}- channels. Thus, Ca^{2+} enters the presynaptic neuron and triggers the release of neurotransmitters from synaptic vesicles to the synaptic cleft through fusion pores (21). Henceforth, the transmitters can bind receptors on dendrites and influence the postsynaptic neuron - by either causing a depolarization or hyperpolarization. The neuronal action potential has three main steps: depolarization, repolarization, and hyperpolarization (21, 22).

The binding of excitatory neurotransmitters to the postsynaptic receptors activates voltage-gated sodium channels (Na_v channels). The opening of the Na_v channels lets positively charged sodium to influx the axon, causing a depolarization. During the depolarization, the membrane potential in the surrounding axon increases as the Na_v channels along the axon are activated one by one - as falling dominos (20, 22). The repolarization begins as voltage-gated potassium channels (K_v channels) are activated; this happens approximately one millisecond after the depolarization, due to the slower kinetics of the K_v channels. The activation of the K_v channels is coincident with the inactivation of the Na_v channels. Moreover, the efflux of K^+ out of the neuron results in a decrease in the membrane potential - towards the resting potential (22).

As the action potential passes through the axon, the K_v channels remain open slightly longer than needed to return to the resting potential, owing to the slower kinetics. With this, the cell is temporarily hyperpolarized, meaning that the membrane potential is more negative than the resting state. When the K_v channels close, the sodium-potassium pump works to regenerate the resting membrane potential (20, 22).

On the other hand, the binding of inhibitory neurotransmitters to dendrites inhibits transmission. Typically, channels that are selectively permeable to chloride ions (Cl^-) are activated. As negatively charged chloride ions enter the cell, the membrane potential gets lower than the action potential threshold. Thus, the neuron is hyperpolarized and inhibited for further transmission (23).

Figure 4 displays an action potential diagram, where changes in the membrane potential during depolarization, repolarization, and hyperpolarization are included.

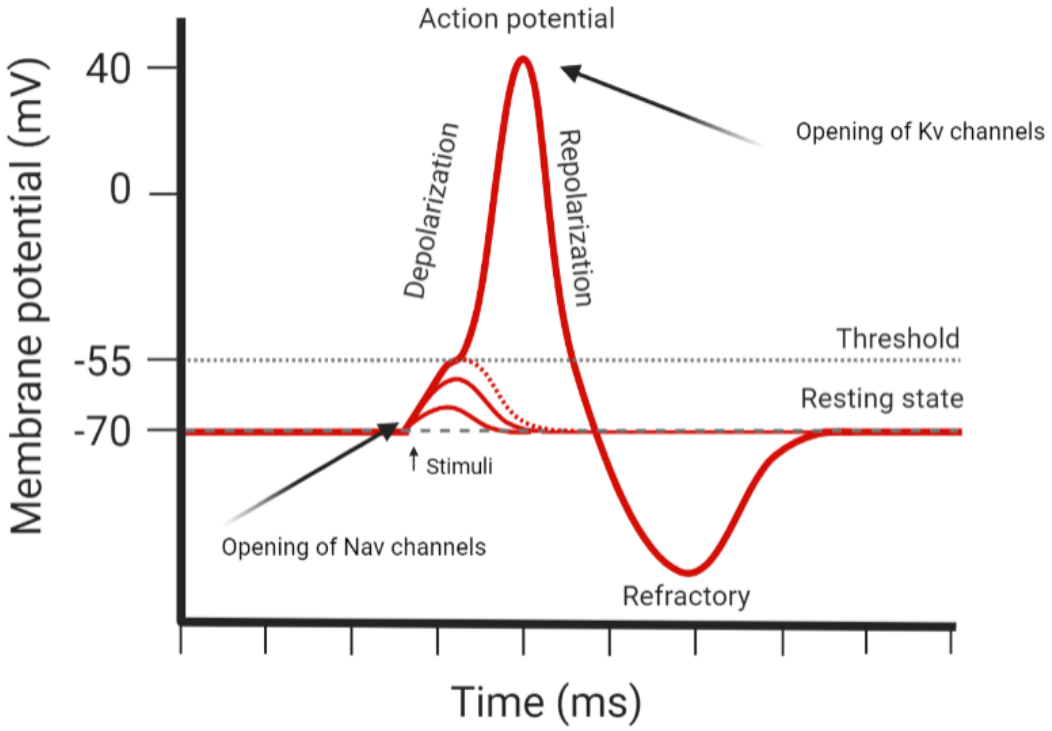

Figure 4: *A general action potential diagram. Figure created based on templates from BioRender.com. An excitatory stimulus trigger opening of Na_v channels, which allows an influx of Na^+ ions into the negatively charged axon. Overall, this leads to an increased membrane potential from the resting state. When the threshold (between -50 to 55 mV) is reached, an action potential will be generated. Approximately one millisecond after the depolarization, the repolarization begins by activation of K_v channels. The K_v channels allow efflux of K^+, which decreases the membrane potential. Opening of K_v channels is coincident with the inactivation of Na_v channels. A short refractory period (i.e., the membrane potential is under the resting state) will occur, due to the slightly longer kinetics of the K_v channels. When these channels close, the Na^+/K^+- pump works to regenerate the resting membrane potential (20, 22).*

1.4 The monoamines: Dopamine, Serotonin and Norepinephrine

In this project it is of interest to create an understanding of the monoamines, i.e., DA, 5-HT, and NE, and the monoaminergic transporters, to later investigate determinants for selective binding to these transporters by using computational modeling techniques. Different substances that act on the monoamine transporters (MATs) will be examined to reach this goal.

The monoamines have been an integrated part of the nervous system throughout the evolution and are vital to the ontogeny, function, and plasticity of the NS. The monoaminergic neurons are structured in symmetrical clusters and are found in the executive (prefrontal cortex)-, limbic- and sensory association areas in the brain. Thus, the monoamines impact the regulation of, amongst others, consciousness, mood, emotions, attention, motor function, and cognitive state (24). Disruption in the monoamine levels play, henceforth, a role in a significant number of CNS conditions (such as major clinical depression, anxiety, Parkinson's disease, and schizophrenia). A metaphor is that the CNS operates as a "processer", while the monoamines (in addition to other neurotransmitters and hormones) modulate the processing (24, 25).

Figure 5 implies the reach of monoaminergic projections from the brainstem to the different regions of the brain.

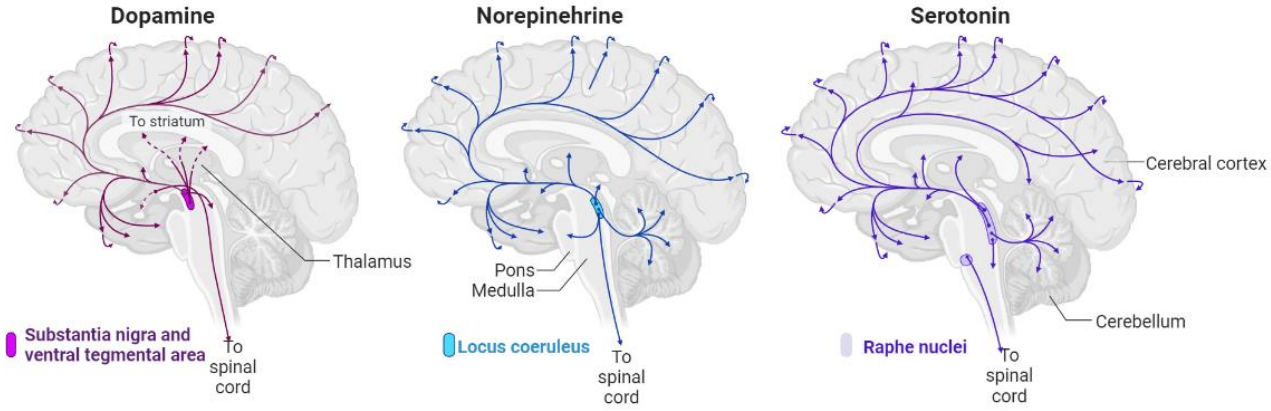

Figure 5: *Simplified overview of the reach of the monoamines in, respectively, the dopaminergic, noradrenergic-, and serotonergic brain pathways and their main origin. Figure created with templates from Biorender.com.*

Dopamine (DA) is crucial in the regulation of extrapyramidal movement and cognitive functions. This neurotransmitter is mainly produced and found in dopaminergic neurons in the ventral tegmental area (VTA), the substantia nigra pars compact (SNc), and the hypothalamus, where they project to different brain areas through four major pathways: the mesocortical -, mesolimbic, nigrostriatal, and tuberoinfundibular pathway (26).

Equally both the mesolimbic- and mesocortical pathways originate in VTA. In the mesolimbic pathway, VTA is connected to, amongst others, nucleus accumbens (NAc), amygdala, hippocampus, and prefrontal cortex through ascending dopaminergic neurons. While the mesocortical pathway, in contrast, projects to the prefrontal cortex. These two pathways are highly associated and therefore often referred to as the mesocorticolimbic system. Thus, the mesocorticolimbic system is the pathway contributing to associations such as reward associations, emotion, motivation, and habit learning (27, 28). Consumption of, for instance, psychostimulants enhancing the concentration of DA in the synaptic cleft, mainly by acting on DAT (i.e., as substrates or inhibitors), can lead to temporary pleasant psychoactive effects – the feeling of relief – but the backside of the medal is often adverse side effects, tolerance development, and addiction (24, 25).

However, the *feeling* of "hedonic pleasure" (meaning the process of *liking*, e.g., cognitive, social, moral, and aesthetic), "incentive salience" (the motivation process of *wanting*), and learning (e.g., considering behaviors and actions accordingly), is interwoven by more complex factors and endogenous substances than DA alone. This is important to consider, despite only DA will be discussed in this thesis, with respect to the mentioned properties (26, 28).

Moreover, the nigrostriatal pathway is important for controlling voluntary movements through the motor loops in the basal ganglia circuitry. This pathway links the SNc in the midbrain with the dorsal striatum in the forebrain (27). The tuberoinfundibular pathway from the hypothalamus to the pituitary gland is mainly responsible for the regulation of prolactin secretion, where binding of DA to D_2- receptors in the pituitary gland inhibits prolactin synthesis and secretion (29).

Above all, DA act on dopaminergic GPCRs which are classified in two groups: D1-like receptors (D_1- and D_5) and D_2-like receptors (D_2- , D_3-, and D_4). Briefly, the action of DA on these receptors is also crucial for the regulation of sleep, attention, reproductive behavior,

food intake, and making decisions – including the previously mentioned functions of DA (30).

Serotonin (5-HT) modulates behavioral processes such as mood, reward, aggression, appetite, anxiety, attention, and libido. Other effects of 5-HT in the CNS are the regulation of sleep, respiratory drive, body temperature, and motor control. However, 5-HT is also vital in functions in the PNS, including vasoconstriction- and dilation, intestinal peristalsis, and respiratory drive through pulmonary vasculature. Lastly, this neurotransmitter is mainly originated and produced by neurons in the raphe nuclei, situated in the midline of the brainstem (31).

The effects of 5-HT come from the act on 5-hydroxytryptamine (5-HT) receptors. These receptors are classified into seven groups, 5-HT_1 to 5-HT_7. Moreover, the 5-HT receptors are distributed both peripheral and in the brain. Most of these receptors are located postsynaptic – and give the direct effects of 5-HT, while 5-HT_{1A} and 5-HT_{1B} are mainly found presynaptic and modulate the release of 5-HT. Nevertheless, the function of the receptors differs depending on their location. Lastly, the 5-HT receptors are GPCRs, with the only exception in 5-HT_3 which is an excitatory ligand-gated ion channel receptor (32).

Furthermore, NE is essential in the general function of arousal, stress reactions, and cognitive functions in the CNS. NE exerts its effects by acting on alpha (α)- and beta (β)- adrenergic receptors. The α_1- and α_2- adrenergic receptors have been found to affect working memory, attention, fear, and spatial learning (i.e., cognitive function). Functions such as auditory fear, fear memory, and retrieval of memory are influenced by the β_1- and β_2- adrenergic receptors. In general, the α_1- and β-adrenergic receptors enhance neurotransmission, while α_2 adrenergic receptors have inhibitory effects in the CNS. These receptors are both found in the CNS and PNS (33).

The major source of NE is the nucleus locus coeruleus (LC) in the brainstem. From this location, the NE neurons project throughout almost all the brain regions, including the thalamus, amygdala, and hippocampus (with remarkable exceptions in the basal ganglia and hypothalamus). The projection from the LC is the source of NE to the cerebral-, cerebellar-, and hippocampal cortices (34).

Norepinephrine (NE) is also important in the PNS. Activation of the “fight or flight” responses in the sympathetic nervous system is mainly regulated by NE; meaning the

response to, for instance, stress or anxiety with e.g., dilation of the bronchioles, increasing of the heart rate, vasoconstriction of blood vessels, increasing renin secretion from the kidneys, and inhibiting peristalsis in the gut (33).

In figure 6 the two-dimensional (2D) structure of the three monoamines is displayed.

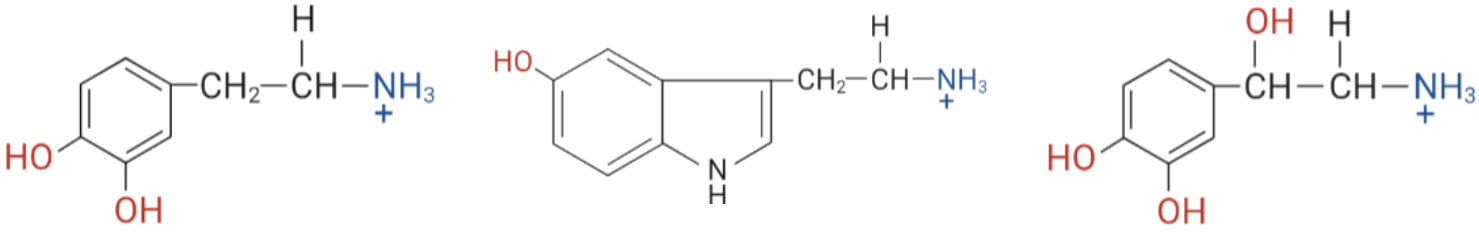

Figure 6: *From left to right, the 2D structure of DA, 5-HT, and NE, respectively. The characteristics of the structures are the aromatic ring attached to a two-carbon chain and an amino group (25). The figure is created with templates from BioRender.com.*

Disruption and imbalance of the monoamines can attribute to diseases in NS. In, for instance, Parkinson's disease, dopaminergic neurons in the substantia nigra progressively degenerate, leading to a lowered amount of DA available for neurotransmission in the corpus striatum. The lowered DA levels in the nigrostriatal pathway will induce clinical symptoms like tremor, rigidity, and bradykinesia (35). More on neurological disorders will be portrayed in chapter 1.6.

1.4.1 Relationship between the monoamines

The monoamines do not perform and act independently. Each of the neurotransmitters is linked, acts together, and affects each other to retain the chemical balance in the body.

Studies have implied that 5-HT modulates the DA levels in the brain, by acting through several 5-HT receptor subtypes. More specifically the 5-HT_{1A}, 5-HT_{1B}, 5-HT_{2A}, 5-HT_3, and 5-HT_4 receptors facilitate the release of DA, while the 5-HT_{2C} acts inhibitory on the DA release. As a result, the clinical effect of, amongst other, psychotherapeutic drugs that act on the serotonergic system, may be due to their indirect action on the dopaminergic system. For instance, 5-HT_3 receptors appear to play an inducing role in the effects of dopamine (DA) agonists (36, 37).

Impulsive aggression (i.e., the inability to control affect and aggressive impulses) and comorbid conditions such as depression, substance abuse, and suicidal behavior are suggested to arise due to an underlying mechanism with dysfunctional interplay between the 5-HT- and DA systems in the prefrontal cortex. A hypofunction of 5-HT predisposes to impulsivity, aggressive behaviors, and depression, with a co-occurring hyperfunction of DA that reinforces these effects by increasing impulsive aggression. Thus, the balance between DA- and 5-HT activity is believed to determine the approach and withdrawal-related behaviors (38).

The NE system is connected both anatomically and functionally to the mesolimbic dopamine (DA) system. From locus coeruleus (LC) noradrenergic neurons project to VTA, where the neural firing of dopaminergic neurons is influenced. If the LC is stimulated, the activity of the DA neurons increases. This effect is blocked by α_1- adrenoreceptor antagonists (37).

Moreover, the noradrenergic neurons in the LC project to serotonergic neurons in the dorsal raphe – and vice versa. NE acts stimulating on the 5-HT system, while 5-HT exerts inhibitory effects on the noradrenergic neurons. However, it appears that although the excitatory NE input on the raphe serotonergic neurons occurs under some conditions, the continuous activity of the LC noradrenergic neurons is not required to provide the firing activity of the 5-HT neurons (39, 40).

Overall, the interplay between the monoamines implies how complex the monoaminergic system is alone. If one transmitter system is the target of a specific drug therapy, it is highly likely that projecting neural systems are affected too.

1.5 The monoamine transporters: structure and activation

The three MATs belong to the group of Na^+/Cl^- - dependent transporters in the SLC6 transporter family. These transporters contain 12 integrated alpha-helical transmembrane domains, including flexible intra (IL)- and extracellular (EL) loops, and are found in neural terminals. The TMH 1-5 and TMH 6-10 (refers to transmembrane helix 1-5 and 6-10, respectively) contribute to a pseudo-two-fold axis arrangement in the transporters, where both the N- (NH_2, amino) and C- (COOH, carboxyl) terminus are located intracellularly. In general, the primary substrate binding pocket (also termed the S1-site) is positioned between TMH1 and TMH6. A simplified 2D illustration of the monoamine SLC6 transporter family is displayed in figure 7 (41).

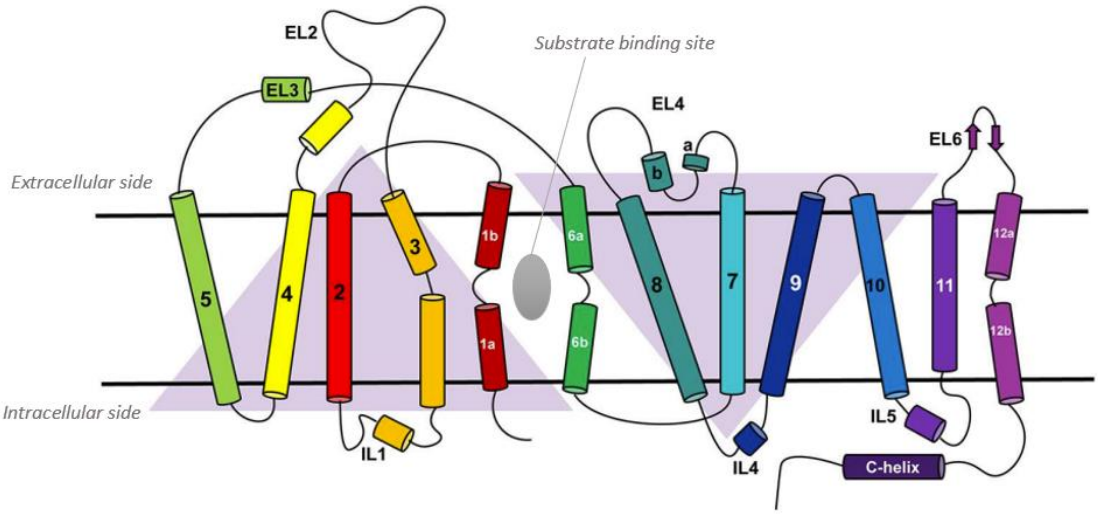

Figure 7: *A simplified 2D-illustration (topology) of the monoamine SLC6 transporter family structure, from (42). The color patterns for each helix are the same throughout the thesis.*

The S1-site of the MATs is assumed to consist of three subpockets: pocket A, B, and C. Subpocket A (constituted of TMH1b, TMH6, and TMH8) comprises highly conserved residues, and is particularly important for the formation of a salt-bridge between the amine moiety of a ligand and the conserved aspartate in TMH1 (human SERT (hSERT): Asp98, human DAT (hDAT): Asp79, human NET (hNET): Asp75). On the other hand, subpocket B (TMH3 and TMH8) consists of hydrophobic residues that provide π-π- and hydrophobic interactions with aromatic moieties. Lastly, subpocket C (TMH3, TMH6A, and TMH10)

creates the shape of the binding site itself and is also constituted by conserved aromatic residues (41, 43).

The MATs can change the conformation in a manner that "locks" the entrance to the S1-pocket in an inward- or outward-facing alternating conformation. By that, the translocation of substrates by the transporters follows a three-state mechanism. The conformational changes are initiated by the binding of a Na^+-ion to the extracellular side, which enables substrate binding to the S1-site in an outward-facing transporter conformation. "Closing" of the extracellular gate (created by specific amino acid residues) forms an occluded state, where ions and the substrate are "sealed" in a channel – protected both from the extra-and intracellular side by the gating networks. Lastly, the intracellular gate opens and establishes an inward-facing conformation of the transporter; the substrate and ions are then released into the cytoplasm by diffusion (41). A simplified illustration of the three-step transporter cycle is shown in figure 8.

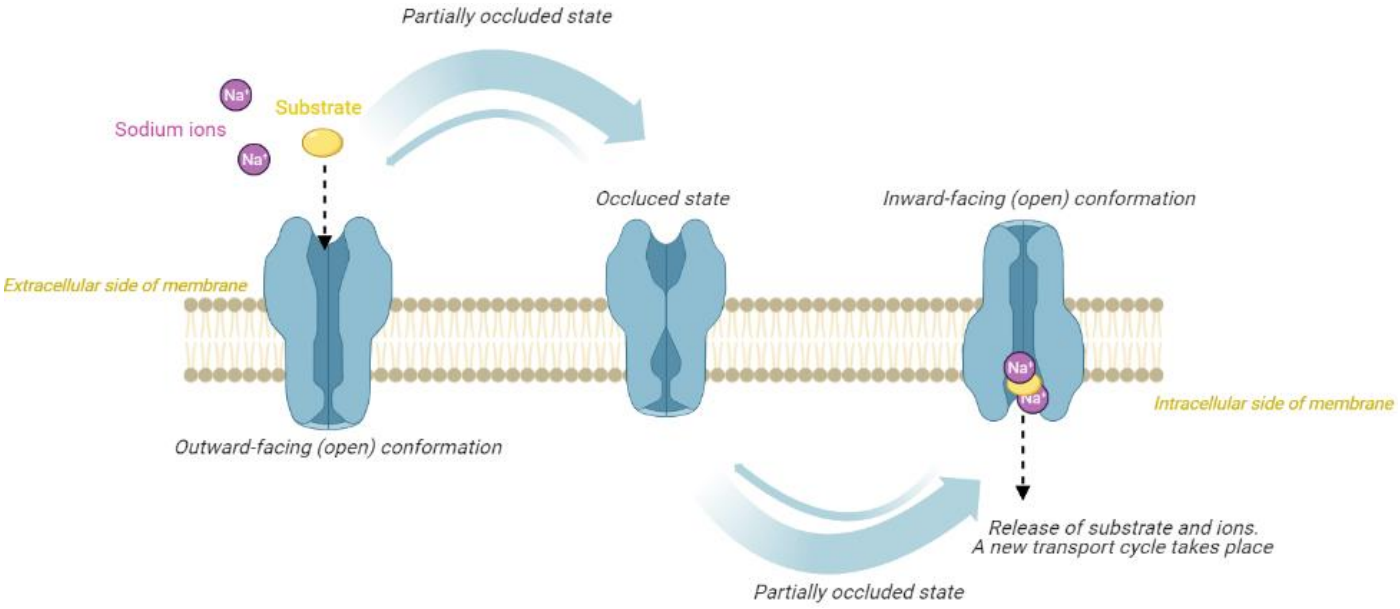

Figure 8: *Simplified overview of the three-step mechanism for translocation of substrates and ions in MATs, modified from (41). The illustration is created with Biorender.com.*

The translocation of substrates is driven by the concentration gradient created by Na^+/K^+ ATPase. In DAT, DA is believed to be co-transported along with two Na^+ and one Cl^-, while SERT moves substrates along with one Na^+ and one Cl^- in one direction. K^+ is also counter-

transported in SERT. No three-dimensional (3D) structures of NET have been obtained yet; however, it is suggested that the translocation of substrates through NET is along with one Cl^-, and one or two Na^+ in one direction. Nonetheless, two sodium (Na1- and Na2) - and one chloride- binding site are found in each MAT. The binding site of K^+ is still unidentified. Although only one sodium is expected to be transported with substrates in SERT, it is yet believed that binding of sodium to both the Na1- and Na2 sites is important for the total function of the transporter. Hence, MATs are also termed Na^+/Cl^- - symporters (41, 42, 44).

Moreover, the MATs are believed to additionally have another low-affinity binding site (also referred to as the S2-site), located in the extracellular vestibule. The structural and molecular determinants linked to the binding selectivity of the S2-site are, however, still not completely understood. Mapped 3D structures of hSERT support the suggestion that the secondary pocket may have a functional role, especially in SERT and NET; this includes a function in alternating conformational changes for substrate translocation. In fact, the extracellular loops EL4 and EL6 contribute partially to the shape and plasticity of the S2-site, by their ability to adopt distinct conformations. Nevertheless, the main emphasis in this thesis will not lie in the effects and determinants for binding to the S2-site or other allosteric sites (41, 43).

In total, the three biogenic MATs (i.e., DAT, SERT, and NET) have a structurally similar core. This leads to overlapping substrate specificity. For instance, it is reported that SERT can transport DA at low affinity – and vice versa. The affinity, velocity, and amount of sodium and chloride needed for the transport can, however, differ between the MATs for each substrate. On the other hand, the extracellular loops, N- and C- terminuses vary significantly between the MATs both in length and the amino acid sequence. This may be important for differences in post-translational modifications, protein-protein interactions, localization, stability, the activity of each transporter, and may also play a role in the three-state mechanism and selectivity (41, 43).

1.5.1 The dopamine transporter

The main function of DAT is to regulate dopaminergic neurotransmission. Dysfunction of this transporter and alterations in DA transmission are related to several CNS disorders, such as depression, Parkinson's disease, ADHD, epilepsy, and autism [for more reviews, see reference: (45, 46, 47, 48)]. Therapeutic drugs used to treat these disorders, perform their action by modulation of the structure and function of DAT through different mechanisms. For psychostimulants, such as cocaine- and amphetamine-like substances, it is commonly understood that their ability to enhance dopaminergic neurotransmission plays a key role in their effects – both the behavioral and reinforcing effects (49).

Substrates (e.g., amphetamine) are transported through hDAT and trigger the release of intracellular DA. The binding of substrates to the S1-site, in the outward-facing transporter conformation, leads to a closure of two extracellular gates (hDAT: Arg85 (TMH1)-Asp476 (TMH10) and Tyr156 (TMH3)-Phe320 (TMH6)). Further, the TMH1b and TMH6a are tilted inward to the center of the extracellular vestibule (10-15° and 2-10°, respectively). This results in an inward substrate-bound outward-facing closed conformation. In this state, the S1-site is minimally hydrated, and hydrophobic interactions from each side of the binding site occur. Some amino acids coordinating the binding of substrates, thus contributing to this state is: Phe76 and the crucial Asp79 (TMH1); Ser149, Val152, Gly153, Tyr156 (TMH3); Phe320, Ser321, Phe326, and Val328 (TMH6); Ser422 and Gly426 (TMH10). Lastly, the substrate will be released intracellularly – when the transporter alters to an inward-facing conformation (49).

Typical inhibitors (e.g., cocaine), however, block hDAT in an outward-facing conformation and are not transportable. That is mainly due to their bulky size that prevents the closure of the extracellular gating pairs, hence hindering the inward tilting of the TMHs exposed to the extracellular side. Finally, the conserved Asp79 (TMH1) in the S1-site is also stabilizing and crucial for interaction with protonated amino groups in inhibitors (49).

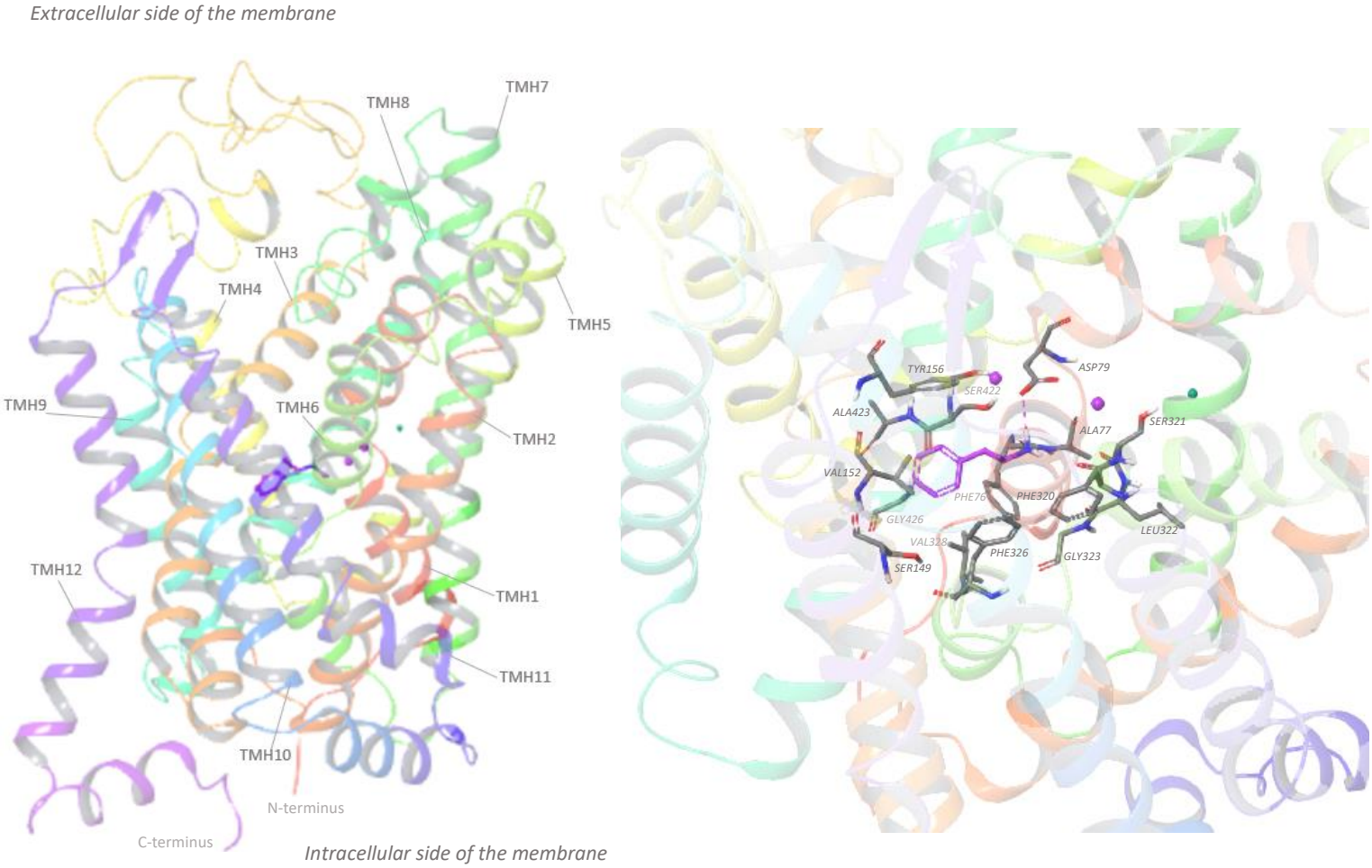

Figure 9: *3D representation of a homology model of hDAT bound to methamphetamine (purple ligand) in the S1-site. The twelve transmembrane helices (TMH1-TMH12) are labeled with gray front. The ionic interaction with Asp79 (TMH1) is marked with a purple dashed line. For each helix, the color pattern is the same throughout this thesis. The sodium ions are represented as purple spheres, while the chloride is sea green.*

The homology model was constructed using the X-ray structure of Drosophila Melanogaster DAT bound to methamphetamine from the Protein Data Bank as a template (code: 4XP6) (50). This will be discussed later in the thesis. The 3D visualization is created in Maestro (Schrödinger, release 2022-3).

1.5.2 The serotonin transporter

SERT plays an important role in the regulation of serotonergic transmission. Similar to DAT, typical inhibitors (e.g., the selective serotonin reuptake inhibitors (SSRIs)) tend to arrest the transporter in an outward-facing conformation, while substrates (e.g., 3,4-methylenedioxy-methamphetamine, MDMA) are transported into the neurons and trigger the release of intracellular 5-HT (51, 52).

The S1-site of hSERT has a Y-shape. This shape, in an outward-occluded-conformation, is contributed by partly unwound TMH1 (Ala96- Asp98) and TMH6 (Leu337- Gly342), as well TMH2 (Tyr175) and TMH8 (Ser438). Typical SERT inhibitors (e.g., the SSRI citalopram) are large distinct substances that each bind the transporter in a different conformation. Hence, the distance between the residues Tyr176 (TMH2) and Phe335 (TMH6) is most likely increased compared to the initial outward- facing SERT, to accommodate their size. Characteristic for most of the typical inhibitors is their ionic interaction with Asp98 (TMH1), the formation of aromatic interactions with the residues in the extracellular gate (Tyr176 and Phe335) via their aromatic moiety, and the creation of hydrophobic or aromatic interactions in the locality of Ala169, Ile172, Ala173, and Val343 (51).

Additionally, SERT is reported to have a vestibular S2-site, located around 13 Å above the S1-site, where some typical inhibitors also can bind. The vestibular site has been shown to have allosteric effects on the S1-site – and vice versa. For instance, the binding of citalopram (SSRI) to the S2-site is proposed to delay the dissociation of S-citalopram at the orthosteric S1-site by steric hindrance, while binding to the S1-site enhances binding to the S2-site. In this project, however, the binding in the S1-site of hSERT will be examined (53, 54).

Substrates (e.g., MDMA) drive hSERT from an outward- to inward-facing conformation, and trigger the release of intracellular 5-HT. In the S1-site, the charged amine in substrates tends to establish a salt bridge with Asp98 (TMH1) in subsite A, while the aryl moiety is oriented in subsite B (via hydrogen bonds). Interactions in the subsite C do not in general occur. Thus, this type of orientation in the binding pocket is argued as important for transport through SERT. Finally, the substrates often have no or small alkyl substituents at the amine moiety, while the inhibitors mostly do not (52).

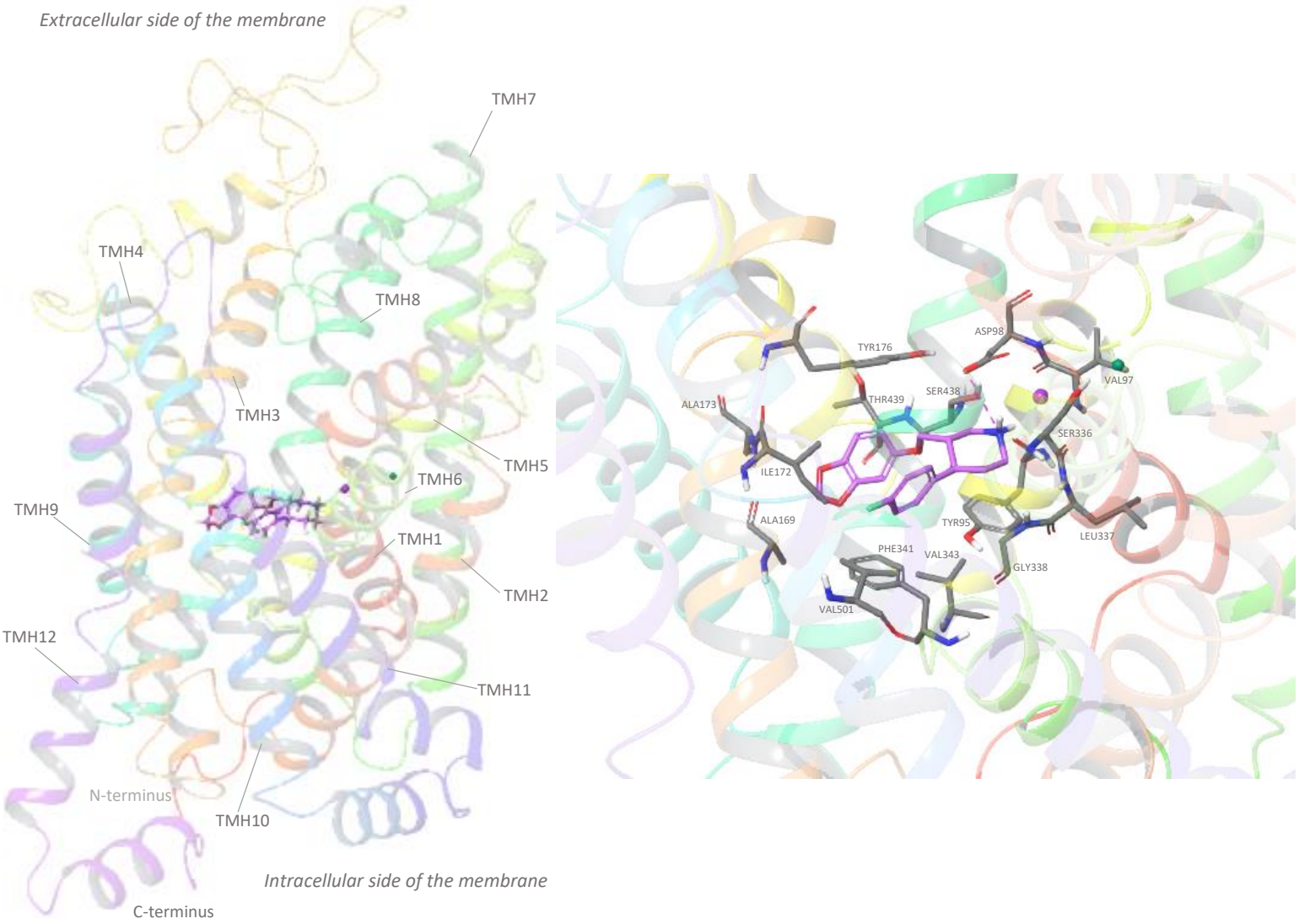

Figure 10: *3D representation of a model of hSERT bound to paroxetine (purple ligand) in the S1-site. The twelve transmembrane helices (TMH1-TMH12) are labeled with gray front. The ionic interaction with Asp98 (TMH1) is marked with a purple dashed line. For each helix, the color pattern is the same throughout this thesis. The sodium ion is represented as a purple sphere, while the chloride is sea green.*

The model was constructed using the X-ray structure of the mutated hSERT bound to paroxetine, with only one sodium- and one chloride ion, from the Protein Data Bank as a template (code: 5I6X) (55). This will be discussed later in the thesis. The 3D visualization is created in Maestro (Schrödinger, release 2022-3).

1.5.3 The norepinephrine transporter

The norepinephrine transporter (NET) is to a high extent found in noradrenergic neurons (and glial cells) and stands for almost 70-90 % of the reuptake of released NE in synaptic clefts. This transporter is the target for, amongst others, the non-stimulant atomoxetine - which is defined as a "highly specific" NET inhibitor – and antidepressants like the tricyclic antidepressants (TCAs) (44, 56).

The available structural information for NET is based on templates from homologous proteins. In this section the hNET-structure is provided from homology models constructed based on two Drosophila melanogaster DATs (dDATs) (Protein Data Bank (PDB) codes: 4m47 and 4xpg) by Góral et.al (44). In addition to homology models of hNET built based on one hSERT (PDB-code: 5I6X) and two dDATs (PDB-codes: 4m48 and 4XPA) by Jha et.al (57) where used to obtain structural information. Homology modeling was also used in this study and will be described more in later chapters.

The S1-binding pocket of hNET is built of two regions: one hydrophobic- and one hydrophilic region. It is, however, believed that both regions constitute the general binding mode to NET for both substrates and inhibitors. Hence, the hydrophobic region is responsible for establishing interactions - and orientation of aromatic moieties. This region includes: Ala145, Val148 Gly149, Tyr151 and Tyr152 (TMH3); Ser419, Ser420, Gly423, MET424 (TMH8); Gly320, and Phe323 (TMH6). Further, the hydrophilic region includes Phe72, Asp75 TMH1); as well as Phe317 and Ser318 (TMH6). These are some of the residues that contribute to interactions with ligands. The Asp75 residue is crucial in forming a salt bridge with positively charged moieties (44).

Moreover, typical inhibitors tend to bind and block NET in an outward-facing conformation, while the substrates similar to DAT and SERT trigger a conformational change from an outward-to inward-facing NET – thus promoting the release of intracellular NE (44, 57). The three-step mechanism for translocation in NET also involves TMH1b and TMH6a with EL4, which provide structural flexibility for the transport of substrates. This flexibility is important due to the small size of the primary binding pocket in NET. Finally, the translocation of substrates to the cytosol is contributed by an outward movement of TMH1a and an inward movement of EL4 (44, 57).

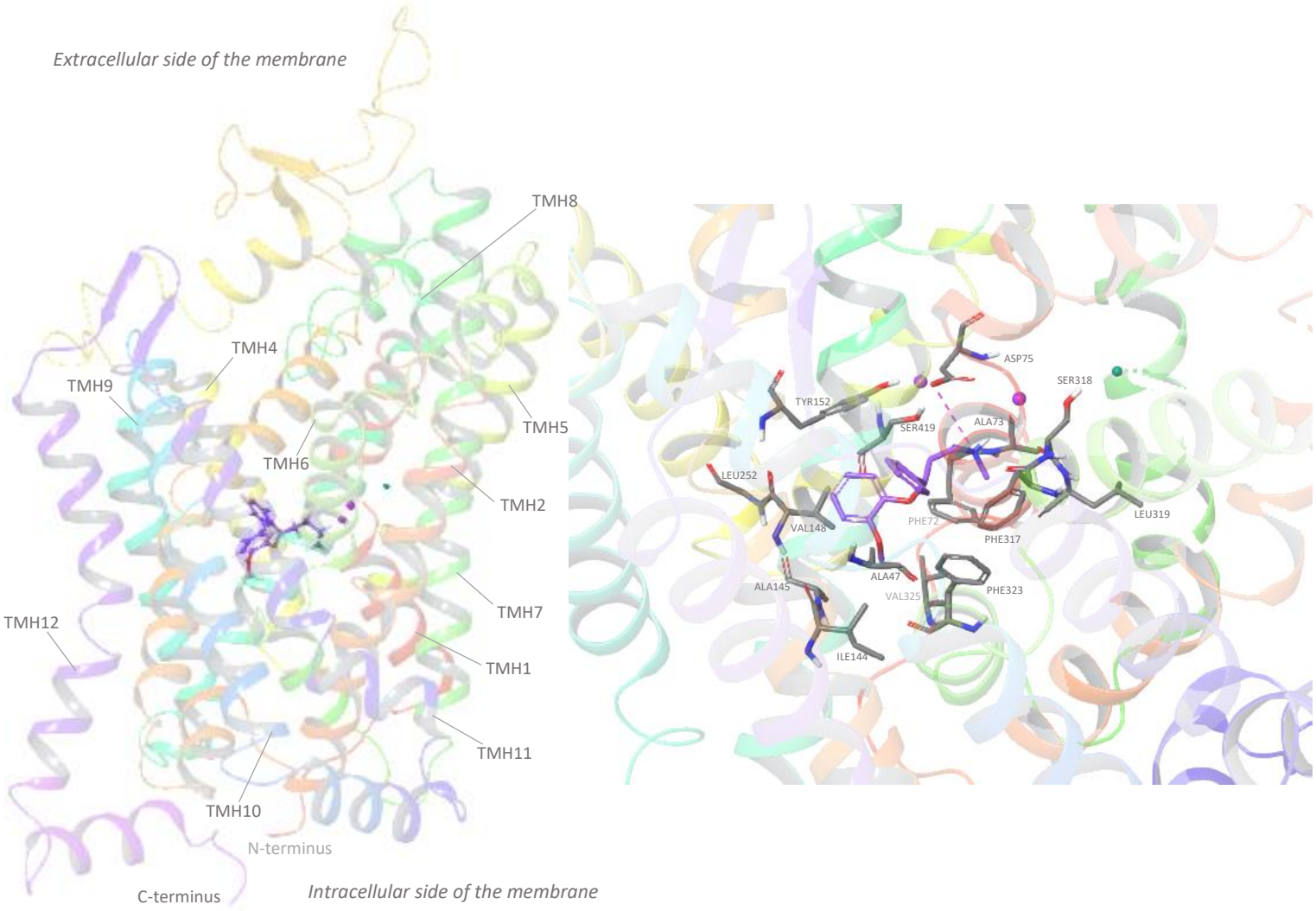

Figure 11: *3D representation of a homology model of hNET bound to nisoxetine (purple ligand) in the S1-site. The twelve transmembrane helices (TMH1-TMH12) are labeled with gray front. The ionic interaction with Asp75 (TMH1) is marked with a purple dashed line. For each helix, the color pattern is the same throughout this thesis. The sodium ions are represented as purple spheres, while the chloride is sea green.*

The homology model was constructed using the the X-ray structure of the Drosophila DAT bound to nisoxetine from the Protein Data Bank as a template (code: 4XNU) (58). This will be discussed later in the thesis. The 3D visualization is created in Maestro (Schrödinger, release 2022-3).

1.6 Central nervous system disorders: In terms of clinical imbalance in the monoamine levels

The monoamines are crucial for interneuronal communication, growth, and differentiation of neurons, along with the development of neuronal circuitry through neurotransmission. To terminate transmission, control duration, and maintain normal levels of monoamines in the synaptic clefts, the MATs, i.e., SERT, DAT, and NET play a key role. This will be discussed in more detail in later chapters (59).

Disturbances in the homeostasis of the neurotransmitters are often associated with neurological and neurodegenerative disorders. This includes variation in the biological levels, production, and metabolism, as well as imbalances due to impairment of neural receptors and transporters, exocytosis of vesicles, degeneration of neurons in the synaptic cleft, and intracellular signaling (60). Other underlying causes for the development of neurological disorders are infections, malnutrition, environmental health, genetic disorders, brain- or nerve injury, and lifestyle (61).

Neurological disorders are defined as "conditions of the central- and peripheral nervous systems" by the World Health Organization (WHO) (62). This embrace amongst other epilepsy, headache disorders (e.g., migraine), neurodegenerative disorders (e.g., Parkinson's disease), neuroimmunological disorders (e.g., multiple sclerosis), cancer, and neurodevelopmental disorders (e.g., attention deficit hyperactivity disorder (ADHD)) (62). Symptoms, due to altered levels of the monoamines, are followed by the nature and severity of the neurological disorder. Hence, the symptoms can appear in several forms, ranging from delusions, hallucinations, impulsivity, hyperactivity, spontaneity, tremors, rigidity, bradykinesia, throbbing headache, reduced concentration, sleep disorders, pessimistic thoughts, confusion, and numbness (61). The neurological disorders are highly associated with psychiatric disorders, such as major clinical depression and anxiety (63).

Overall, the neural network functions as an enormous telephone system. Poor coverage and weakening of the telephone connection will result in diminished communication and sound, which in turn leads to misinterpretation of important and correct information. For us, humans, a weakened neural network will cause unpleasant symptoms in terms of CNS disorders.

These types of conditions are more complex than explained by the monoamine changes alone; genetics and neuroplasticity are equally important factors.

1.7 Psychostimulants and other ligands that interact with the monoamine transporters

In this project, it was of interest to study drugs that interact with the MATs and explore determinants for binding preferences and selectivity. With regard to this, both new psychoactive substances (NPS), illicit traditional stimulants, and therapeutic stimulants will be analyzed. For the sake of simplicity, however, the sack term central nervous system stimulants, *psychostimulants*, will be used as a collective term for these substances throughout the thesis. Psychostimulants are generally drugs that enhance the activity of the CNS, meaning that both cognitive and affective behaviors are impacted (64). Besides, a selection of some antidepressants, atypical inhibitors, substances used as research standards, and a non-stimulant that interacts with the MATs, are included for comparison with the stimulants (the included ligands are described more in chapter 3.4.1).

Therapeutic psychostimulants, such as methylphenidate, constitute an established part of the therapy of ADHD. However, these drugs also play a role in the improvement of patients with treatment-resistant depression, as well as some evidence point out that therapeutic stimulants may be effective in the treatment of narcolepsy and chronic fatigue (65, 66).

Short-term effects of the stimulants are often described as euphoric – the feeling of powerful excitement, which is associated with the increased dopaminergic transmission in the mesolimbic pathway. The pleasurable boosts may involve the flourishing of passionate happiness and joy, increased libido, easier sociability, strengthened self-esteem and self-belief, suppressed appetite, and enhanced attention (67). Unfortunately, the short-term effects of the stimulants may be the basis for abuse ("incentive salience"); the desire to escape from reality – feel good or don't feel bad, perform better in school or work, the wish of fitting in, or just be able to "live for the night", as well as certain stimulants may be easily, but illegal, accessible in certain environments.

New psychoactive substances (NPS) are specified as psychotropic substances of abuse that are not controlled by the United Nation Drug Conventions. These drugs can appear in pure forms or preparations and are considered as health threats. Thus, they are often referred to as

legal highs, *bath salts*, or *research chemicals* in everyday speech and marketing (68, 69). Amongst the NPS, the synthetic stimulants, such as 3,4- methylenedioxypyrovalerone (MDPV) and mephedrone, are the largest group that is monitored by the EMCDDA (European Monitoring Centre for Drugs and Drug Addiction) and UNODC (United Nations Office on Drugs and Crime). Synthetic stimulants are often designed to mimic the effects of the traditional illicit simulants, like cocaine, amphetamine, and MDMA (70).

The effects of psychostimulants are, in general, a result of the act on monoaminergic transporters, followed by an increased level of monoamines in CNS. However, the characteristic *stimulating, dopaminergic, effects* mainly come from the act on DAT in the mesolimbic dopaminergic pathway. This will be examined more in later chapters. Nonetheless, stimulants act as substrates that stimulate neurotransmitter vesicle release (e.g., amphetamine), or inhibitors that block the transporters (e.g., cocaine). Substrates will both compete for the reuptake transporter in the plasma membrane and interfere with the intracellular vesicular monoamine transporter 2 (VMAT2), thus causing exocytosis of the neurotransmitters. Even if the structures of the MATs are related, the sensitivity to the stimulants may differ and distinct substances also have different selectivity for the MATs (71).

In this project, it was additionally of interest to study "*other ligands that act on the MATs*", meaning that they also cause a rise in the monoamine levels. Therefore, some FDA (Food and Drug Administration) approved antidepressants that act as inhibitors on the biogenic MATs were included as well. The following classes of antidepressants will be discussed: the SSRIs and the nonselective TCAs. Antidepressants are mainly used for the treatment of depressive disorders (e.g., major unipolar depression, persistent depressive disorder, and depression as a side effect of another medical condition), but they are also approved for the treatment of several other medical disorders by FDA. That applies to, for instance, the treatment of social phobia, panic disorder, generalized anxiety, and post-traumatic stress disorder (72).

SSRIs are considered as the first-line pharmacotherapy for the treatment of depression. This is mostly due to the major support of its safety, tolerability, and efficacy. This drug class acts by selective inhibition of the presynaptic SERT in the axon terminal, resulting in that an increased amount of 5-HT remains in the synaptic cleft. The 5-HT receptors can thus be stimulated for an extended period, and the activity is increased. Examples of SSRIs are citalopram and paroxetine (73).

The TCAs (e.g., clomipramine) exert their effect by blocking the presynaptic SERT and NET, which increases these neurotransmitters' concentration in the synaptic cleft. However, TCAs also act as competitive antagonists on postsynaptic cholinergic muscarine receptors, α_1- and α_2 adrenergic receptors, additionally H_1 histaminergic receptors. The last actions will not be discussed in this thesis, but are important in terms of the several side effects of the TCAs compared to the other antidepressants, and this is mainly the reason why they are not used as much in therapy today (74).

Antidepressants will in psychiatric disorders, such as major clinical depression, harmonize with the monoamine hypothesis of depression (i.e., depression is associated with a prolonged deficiency in monoamine transmission). However, the monoamine hypothesis unsuccess in the explanation of the latency of their effects. The latency is rather supported according to the neuroplasticity – and neurogenesis hypothesis in, for instance, depression. Consequently, many psychiatric conditions are more complex than the need for an immediate rise in the monoamine levels. Finally, important for antidepressants is their ability to enhance the mood positively without exposing stimulant effects on the CNS, as they do not directly and significantly enhance mesolimbic dopaminergic neurotransmission by acting on DAT like the psychostimulants do (66, 75, 76, 77).

Today, there are still inconsistencies between studies with the respect to the comparable efficacy and safety of psychostimulants and antidepressants in the treatment of depression. Most studies have established that there is limited evidence for treatment with psychostimulants in depression, which substantiates why they are not practiced in today's guidelines (66, 78, 79). Other downsides are the risk of abuse, addiction, and unfavorable long-term effects of the psychostimulants. However, some therapeutic stimulants (e.g., methylphenidate) are indicated as "add-on" therapy in late-life patients with treatment-resistant, or inadequate responses, to monotherapy with antidepressants. For the rest of the adult population, stimulants may be indicated in patients who lack, e.g., energy, motivation, and pleasure. The additional effects of stimulants are suggested to be due to their enhancing effects on dopaminergic activity (66, 78, 79). On the other hand, antidepressants are not as effective in the treatment of ADHD, but there is evidence for small effects on attention and impulse control, along with hyperactivity and aggressiveness. A positive advantage of antidepressants is their low potential for abuse and addiction (80).

The selective norepinephrine inhibitors (sNRI) are not classified as antidepressants but act similarly by inhibiting NET, hence increasing the NE activity. An example is the non-stimulant atomoxetine, which is FDA-approved in the treatment of ADHD (66, 81, 82).

All in all, it is of particular interest to precisely study how these substances cooperate with the monoaminergic transporters. By including some selected substances that *act on* the MATs and different psychostimulants, it may be possible to increase the knowledge and get closer to the goal. Some of the substances included in this study, e.g., mazindol, are not used in clinical practice today but are rather investigated for their effect on the treatment of CNS disorders (81). The research standards are therefore important in creating a better understanding of MATs. Lastly, some atypical inhibitors (e.g., ibogaine) which are proposed to bind the inward-facing conformation of the transporters – in contrast to the mentioned typical inhibitors that bind the MATs in an outward-facing conformation - are also included for comparison to the typical inhibitors and substrates. The atypical inhibitors are suggested to be beneficial in the treatment of stimulant-addiction, but are not currently in clinical use either (83). All these substances will be reviewed in more detail in later chapters, in terms of their preferences for DAT, NET, and SERT – as well as their effects regarding the selectivity for the MATs (i.e., if the effects lean to a serotonergic-, noradrenergic-, or dopaminergic pharmacology).

1.7.1 Side effects of psychostimulants and drugs that interact with the monoamine transporters

Adverse side effects of psychostimulants and, in general, substances that interact with the MATs are often influenced by the type of substance, dosage, tolerance, the user's weight, food intake, the administration route of the drug, comorbidities, and the user's health in the first place. Consequently, several of the side effects are linked to the systemic circulation of the substance. That includes symptoms such as decreased appetite followed by weight loss, sweating, chest pain, shortness of breath, hypertension, tachycardia, heart arrhythmias, electrocardiogram (EKG) abnormalities (e.g., prolonged QT), palpitations, and jitteriness. Other side effects linked to the CNS are anxiety, insomnia, headaches, paranoia, and seizures (84).

The most common prevalent side effects of antidepressants (e.g., citalopram and paroxetine) are, amongst others, headache, dry mouth, gastrointestinal disturbances, nausea, dizziness,

and decreased libido. Again, the TCAs (e.g., clomipramine) cause more adverse effects due to interactions with off-target adrenergic-, histaminergic-, and muscarinic- receptors. This includes anticholinergic effects such as: urinary retention, blurred vision, constipation, orthostatic hypotension, sedation, weight gain and confusion (85). However, antidepressants are unfortunately associated with increased risk for suicidal thoughts during the first months of treatment in children and adolescents. Therefore, the treatment should be followed up and the user should be warned about being patient with the delayed effect of these drugs (86).

Moreover, long-term use of high doses, suddenly elevated doses, or combinations of drugs that each increase the concentration of the monoamines in the synaptic cleft, can lead to toxicity and adverse side effects. Psychostimulants acting on the dopaminergic system (e.g., MDPV) are, for instance, associated with stimulant-induced psychosis. In a simplified view, increased DA concentration in the mesolimbic pathway can cause "positive symptoms" such as hallucinations and delusions. The mesocortical pathway is, however, associated with "negative symptoms" like the lack of motivation, inexpressive emotions, and absence of interest – as a consequence of lowered DA levels (87).

Serotonin toxicity (often called serotonin syndrome) is an example of a drug-induced condition where the amount of 5-HT is too high in the synapsis, leading to symptoms such as restlessness, confusion, delirium, agitation, hallucinations, tachypnea (increased breath rate), and tachycardia (increased heart rate). Abuse and overdosage of psychostimulants with a preference for SERT, such as the NPS paramethoxy-methamphetamine (PMMA) with a high preference for SERT, can also cause serotonin toxicity (88). Clinical data on the side effects concerning the toxicity of elevated levels of NE (e.g., an overdose of the NET-inhibitor atomoxetine) in CNS is restricted, however, mild tachycardia, hypertension, tremor, drowsiness, insomnia, and agitation have been reported (89).

1.7.1.1 Neuroplasticity and addiction

Several studies (90, 91, 92) indicate that repeated exposure of, in particular, psychostimulants and antidepressants induce morphological (structural) - and biochemical (synaptic) changes in the brain. Structural plasticity involves changes in axons, dendrites and dendritic spines, neurogenesis, and suppression or genesis of synapses. Synaptic plasticity, however, refers to changes in synaptic activity. Overall, this phenomenon is called neuroplasticity.

Neuroplasticity allows changes in behavior, motivation, and emotions based on neurobiological adaptions (90, 91, 92).

The delayed effect before response and remission when using antidepressants, which act on the monoaminergic transporters, can partly be explained by the theory of neuroplasticity. One hypothesis is that increased levels of monoamines are suggested to downregulate monoaminergic receptors. Suppression in the inhibitory presynaptic- and facilitatory postsynaptic receptors will, respectively, increase the activity of presynaptic neurons and decrease the activity of postsynaptic neurons. Consequently, it may take a few weeks for neural activity to be restored. However, the pathology of CNS disorders such as depression is more complex than a chemical imbalance and includes, amongst others, dysfunctional changes in the histology of the prefrontal cortex, hippocampus, and amygdala. Antidepressants are also suggested to act by reversing these changes. In total, the onset action of antidepressants may be delayed. Nonetheless, abrupt discontinuation of antidepressants can cause withdrawal and rebound effects – but antidepressants are not considered addictive (90, 93).

Psychostimulants are, however, known to be addictive and bear the risk of being abused. The alteration in the plasticity of especially the *dopaminergic* mesolimbic circuits of the brain, is suggested to contribute to the addictive phenomena. This includes, for instance, synaptic changes such as up-and downregulation of dopaminergic D_1-, D_2-, and D_3 receptors. Moreover, addiction is also partly explained to be due to sensitized or hyper-reactive dopaminergic systems (i.e., the mesolimbic pathway) that amplify the feeling of "wanting", meaning an excessive incentive salience (28, 92).

The rewards from normally stimulating activities (such as food and good deeds) and psychostimulants are like whispers compared to loud shouts to the brain, respectively. The difference can, according to National Institute on Drug Abuse (94), be up to 2-10 times higher for abused stimulants. Thus, regular intake of stimulants may cause a chemical imbalance, where the production and transmission of the monoamines alters. Consequently, the lower amounts of neurotransmitters in the reward circuits (i.e., dopaminergic neurotransmission in particular) by previous stimulating activities may not be "enough", and cause the user to require stimulants to experience *normal* levels of rewards – "just whispering". Higher and higher doses are often needed over time, in other words, tolerance can be developed as well (94, 95).

Earlier, it was amongst others thought that all drugs affecting DAT would provoke effects highly similar to those of inhibitors like, for instance, cocaine. Interestingly, “atypical” MAT inhibitors, such as vanoxerine (atypical DAT inhibitor), have been shown to exert milder psychomotor effects and anti-addiction actions. These kinds of behavioral effects evoked by the atypical inhibitors are associated with a binding mode to an inward-facing conformation of the MATs (i.e., atypical binding mode) (83, 96, 97). This binding mode will, however, be investigated more in later chapters.

1.8 Computational molecular modeling

Computational methods, also called molecular modeling, have become an integrated part of contemporary molecular research (98). These terms include several computational techniques used to generate and collect molecular information, counting; geometry (torsion angles, bond lengths, and bond angles), energy (e.g., enthalpy and activation energy), electronic- (affinity and charges), bulk- (e.g., volume, viscosity, and diffusion), and spectroscopic properties (e.g., vibration and intensity). The background for such characterizations of 3D structures lies in advanced mathematical equations (99). Hence, molecular modeling is applied for the description and understanding of the dynamic- and mechanistic behavior of biomolecular systems at an atomistic level (99, 100).

In this thesis, three main methods; modeling of the human MATs based on the principle of homology modeling, induced fit docking (IFD), and molecular dynamics (MD) simulation, will be utilized to examine interactions between models of the human MATs and, respectively, different psychostimulants and other substances that interact with the MATs. Additionally, to assess determinants for selective binding to the MATs.

1.8.1 Homology modeling

Primary amino acid sequences can provide useful information about the chemical- and physical properties of a protein. These physicochemical properties form an assumption of how the protein acts, but the context of the biological function in living cells remains unknown. To gain a greater insight into the biochemical activity, binding specificities, protein folding, and biological purpose, a 3D structure of the protein is required (101, 102).

It is assumed that proteins with homologous primary amino acid sequences have similar 3D folding – and therefore function, even though the proteins are found in different organisms (102). Seen in the light of evolution, amino acid sequences are less conserved than protein structures. Meaning that change, over time, happens slower in the protein folding. The binding site residues - the most important part for activity - are significantly even higher conserved compared to the non-binding residues of a protein. Therefore, homologous primary sequences fold into similar 3D structures (103, 104, 105).

Considering that the binding sites of proteins are targets for several drugs, the 3D structure is valuable in gaining information about the pharmacodynamics between a protein and its ligands. This includes an increased understanding of the effects and side effects of drugs, as well as providing information (e.g., interactions and affinity) for new drug development (106).

Both nuclear magnetic resonance (NMR) spectroscopy and X-ray crystallography are widely known methods used to discover 3D structures of proteins. In recent years, cryogenic electron microscopy (Cryo-EM) has also been commonly used, due to the so-called "resolution revolution" in the Cryo-EM field. However, a disadvantage of the last method is still the insufficient ability to identify non-protein densities, such as bound ions vital for functional roles. Further, common downsides for all three experimental methods are still the time consumption and lack of success in the determination of membrane proteins (101, 107).

In a deficiency of experimental data of a 3D protein structure with a known amino acid sequence, homology modeling can be used to build a model protein, *homologous protein*, based on a known protein structure (101). Homology modeling is an *in silico* method, which predicts a 3D representation of a target sequence (with an unknown protein structure), based on an alignment to one or more template sequences (with a known protein structure) (108). The model includes imitation of the environmental residues, and their corresponding topological positions, to the template sequences (101).

There are five main steps in homology modeling; finding a suitable template, alignment of the target and template, building the model, refinement of the model, and validation of the product (106).

1.8.1.1 Identification of the template

To construct the protein of interest, the target sequence must first be matched and compared with the sequence of an experimentally (e.g., NMR, X-ray crystallography, or Cryo-EM) known protein structure (101).

A commonly used server for searching similarities between a target- and template sequence, is BLAST (*Basic Local Alignment Search Tool*). BLAST searches for optimal local alignments and calculates the statistical significance between the matches - based on the target sequence and known 3D structures (106, 109). Mapped and known 3D structures are

stored in databases, whereas PDB is the most used one (101). Generally, two sequences are homologous if the sequence identity is more than 30 % over the entire lengths. However, the desired percentage identity also depends on the purpose of a study (e.g., models built based on more than 50 % in sequence similarities are accurate enough for use in drug discovery) (101, 110). Overall, this process is called template identification (106).

When choosing a template, it is also important to take the conformation of the experimentally determined protein into account. Ligands have different intrinsic properties and bind the protein in a structure- and stereospecific way. Affinity to the protein depends on both the functional groups and spatial orientation. For the MATs, inhibitors and substrates will, respectively, bind the protein in different- and certain conformations (106).

Moreover, it is also desirable to have template structures with high resolutions. Membrane proteins contain both hydrophobic- and hydrophilic surfaces that, respectively, interact with the nonpolar alkyl chains of phospholipids, as well as the extra- and intracellular aqueous medium. This amphiphilic nature makes it hard to prepare a stable and homogeneous protein. An example is the formation of contacts between hydrophobic- and hydrophilic surfaces during crystallization (X-ray crystallography), which prevents the protein from being in its natural environment. Hence, the crystallized protein conformation may not represent the complete realistic conformation. Low resolutions will introduce more uncertainty in the model, while high resolutions provide models with å higher degree of detail (106).

Generally, a template structure with high sequence identity and resolution, including a suitable protein conformation by type of ligand (i.e., typical inhibitor, substrate, or atypical inhibitor), will be the best template to choose (106).

1.8.1.2 Target- template alignment

When the most suitable templates are chosen, the next step in homology modeling is to perform an alignment of the target- and template sequences. Corrections will also be prepared if necessary. The process of alignment is sensitive in detecting corresponding positions in the sequences, hence detecting evolutionary associations among proteins. To strengthen the final input alignments, secondary structure predictions of the start- and end points of transmembrane helices (TMHs) may be important (101, 105, 106).

However, the alignment can be challenging, due to cases with low homology between the target- and template sequence. An error in the alignment of one residue will cause a shifting of an α-carbon, while a residue gap in an α-helix section may entail rotation of the subsequent residues in the helix. Therefore, correction and checkups during the alignment will contribute to building 3D protein structures with enhanced quality – with the highest similarity to the experimental protein structure. Also, multiple sequence alignments are beneficial, since they increase the probability that corresponding amino acids are correctly aligned concerning the sequence position, as well as evolutionary relationships are emphasized (101, 105, 106).

1.8.1.3 Building the model

Building a protein model of the target sequence involves the construction of the core areas and loops, based on the template structure. There are three steps in the construction of the model: 1) modeling of the core, which implies modeling of the transmembrane domains; 2) modeling of the loops, meaning the ILs- and ELs in transporters; and 3) side chain (and backbone) optimizations (101, 105, 106). In this study, the building process was done in Prime (Schrödinger release 2022-3). Prime (Schrödinger release 2022-3) performs all the mentioned steps by default, including the closing of deletions and building of insertions in the alignment, as well as minimization of target residues (111).

1.8.1.4 Refinement of the model

Building of protein models often involves substitutions of amino acid residues, insertions, and deletions, which can lead to errors. Therefore, further refinement of the model is usually required. The purpose of the refinement is to fix and adjust possible inaccuracies from the construction, by using energy minimizations, Monte Carlo simulations, or molecular dynamics calculations. As a thumb rule, the refinement depends on the accuracy of the homology between the template and target during the alignment: low homology can lead to errors that can be hard to eliminate. The refinement often starts by improving the most uncertain parts of the model (101, 106).

1.8.1.5 Validation of the model

Due to the several sources of error, model validation is an important last-step procedure, before applying the model in a study. The validations contribute to create the best possible

model for the understanding of proteins (e.g., transporters) and their ligands. A common method is to analyze the stereochemical quality of the model, by for instance using Ramachandran plots where energetically allowed regions, and distribution of the torsional, dihedral, angles of the protein-backbone are visualized (i.e., a 2D plot of the phi (φ) - and psi (ψ) angles of the backbone amino acids). Other methods include testing if the results from the modeling "match" experimental tests, or redocking of experimentally known structures to the theoretically constructed model. Lastly, MD simulations may also be used to validate the energetic stability of the model (106, 112). This will be discussed more in later chapters.

1.8.2 Induced fit docking and scoring

Rational drug design based on the known 3D structure and geometry of a biological target is defined as structure-based design. Structure-based design can be used to construct completely new ligands or optimize the properties of already known ligands. Consequently, the complementarities, mainly intermolecular interactions, between a ligand and a target form the basis for molecular recognition. This, as well as the preferred orientation of the ligand in the binding pocket can be observed through docking. The goal of docking ligands to the corresponding target is to recreate a ligand-protein complex, which imitates a native biological complex (113).

In standard docking studies, freely movable ligands are usually docked into the binding site of a target that is held rigid. Yet, this type of method is somewhat deviating from reality and can contribute to misleading results. The biological systems are in constant movement, and both lipids and proteins in the membrane bilayer are mobile. Lipids can undergo flip-flops, transverse movements, and rotations (114, 115, 116). While membrane proteins, such as transporter proteins, are mobile through lateral diffusion. Transporter proteins will also undergo conformational changes upon ligand binding, embracing sidechain- or backbone movements. The latter dynamic conformational change allows a transporter protein to alter its binding pocket for a more favorable – and specific binding mode for a ligand. In other words, these movements occur to make the ligand fit the binding pocket better. This is referred to as *induced fit* (115, 116, 117).

In this study, IFD was applied to generate all the possible conformations of the docked ligand-transporter complexes (also termed *poses*). Hence, the most favorable structural

conformation of the MATs and binding mode of the psychostimulants and other substances that interact with the MATs could be observed (116).

After an IFD the binding energy of a ligand and its target can be calculated. This is also referred to as scoring (113).

1.8.2.1 Docking score

Alongside creating poses near the native binding between a ligand and transporter, it is also important to know if the binding is energetically favorable, as well as distinguish between active ligands and inactive, random molecules (113).

In a spontaneous biological process, binding of a ligand to a protein only occurs when the changes in the free energy of the system are negative. These changes in free energy are also called Gibbs free energy (ΔG), where the total binding energy, respectively, depends on the ΔG for both the solvent, conformation of the target and ligand, and the electrostatic interactions between the ligand and binding-site residues. Additionally, the motions of the ligand-protein complex are considered. The latter term includes variations in vibrational free energy, changes in the rotational- and translational free energies upon ligand-binding, and freezing of the ligand- and protein rotation (113).

The total ΔG (kcal/mol) of a system can be summarized in equation 1.

$$\Delta G_{binding} = \Delta G_{solvent} + \Delta G_{conformational\ changes} + \Delta G_{interactions} + \Delta G_{motion} \quad [1]$$

Since the extent of the ligand-protein association depends on the magnitude of the negative ΔG, it can be assumed that ΔG contributes to the stability of a ligand-protein complex (113, 118).

Further, the association between ΔG and binding affinity (termed as K_b) can be described by equation 2. In this equation, R is the universal gas constant (1.987 $cal*K^{-1}*mol^{-1}$), T is the temperature in Kelvin (298 K at standard conditions), while K_b corresponds to the ratio between the kinetic rate constants k_{on} ($M^{-1}*S^{-1}$) and k_{off} (S^{-1}) (118, 119).

$$\Delta G° = -RT * lnK_b \quad [2]$$

The formula implies that greater negative ΔG- scores result in greater K_b-values, thus, indicating a higher binding affinity between a ligand and its target. This also applies outside

the standard conditions (i.e., temperature at 298 K, one atmosphere pressure, and reactant concentrations of one molar) (119, 120).

Overall, the docking score for each pose after running IFD is based on calculations of theoretical changes in free energies, ΔG. Docking scores are therefore used to evaluate the most energetically favorable binding modes (118).

1.8.3 Molecular dynamics (MD) simulation

3D structures of ligand-protein complexes, from IFD studies, are helpful in getting insight into the protein function, intermolecular interactions, and binding sites in a protein. However, this is just a static snapshot of the entire "truth". The atoms building up a biological system are in constant movement; the creation of intermolecular interactions, conformational changes upon binding, protein folding, and the deeper understanding of protein function are more complex than a still image. Nature is dynamic. Therefore, it is of interest to study the actual action of a protein and its ligands, to gain a clearer conception at an atomistic level (121).

Molecular dynamics (MD) simulations were in this project used to predict how molecular systems, the selected MAT-ligand complexes, move over time. The dynamic response of the monoaminergic transporters upon binding to different ligands could then be observed and more understood, e.g., conformational flexibility and stability, as well as ligand binding to the orthosteric (S1-) site (other studies may also study allosteric sites), and response to different ligands. Membrane transport and dynamic behavior of salt ions which are important for protein function and binding to the MATs will not, however, be examined in this project (121).

An MD simulation creates a trajectory based on the positions of the atoms in the biomolecular system, e.g., protein-ligand complexes in a lipid bilayer, and the force applied on each atom from other atoms. Simplified, Newton's laws of motion are used to calculate the position and velocity of each atom for a selected timeframe. The molecular calculations of the forces are done by the use of molecular mechanical force fields, as well as energy minimizations and geometry calculations are done in order to "relax the system" and generate low energy conformations (121, 122).

1.8.4 Force fields and energy minimalization

A protein-ligand complex is thermodynamically stable when the energy is as low as possibly achievable. That is at the global energy minimum. In molecular modeling, energy minimalization is applied to find the spatial conformation of both the ligand and protein, which is close to the 3D structure with the lowest energy strain (i.e., the native structure). Thus, steric hindrance, clashes, unfavorable bond lengths- and angles, among other things, are adjusted during the energy minimalizations (123, 124, 125, 126).

To define the energies between interacting atoms and the geometry of a biological system, molecular mechanical force fields are used. Force fields, in molecular modeling, calculate the total potential energy of the system by applying explicit energy functions. Contributing to these calculations are bond length, bond stretch, angle bending, dihedral torsion rotation, bond valence angles (i.e., intramolecular, bonded, interactions), electrostatic forces including the polarization energy (i.e., intermolecular, nonbonded, interactions), and Van der Waals (vdW) interactions.

Equation 3 and 4 summarizes the variables influencing the total potential energy (termed PE) in force field calculations, respectively (127, 128, 129, 130):

$$PE_{Bond} = PE_{stretch} + PE_{length} + PE_{angle\ bending} + PE_{torsion} + PE_{vdW} + PE_{valence\ angles} \quad [3]$$

$$PE_{Nonbond} = PE_{electrostatic} + PE_{vdW} \quad [4]$$

The total potential energy is, hence, given by the sum of both the bonded- and nonbonded potential energies in the ligand-protein complex – together with the solvation-free energy ($PE_{solvent}$). This is shown in equation 5 (128, 129, 130).

$$PE_{Total} = PE_{Bonded\ interactions} + PE_{Nonbonded\ interactions} + PE_{Solvent} \quad [5]$$

Energy minimalizations and force fields were both used in the preparation of the ligands and proteins – as well as during the IFD and MD simulations.

2 Aim

CNS disorders are a major and increasing global health challenge. Regarding this, WHO (62) has set a vision to value the brain health for 2022-2031, comprising a reduced impact, stigma, and burden of these conditions. Several CNS disorders are correlated to disruption of monoaminergic transmission: FDA has approved both simulant (e.g., methylphenidate) and non-stimulant (e.g., atomoxetine) medication for the treatment of, for instance, ADHD, while clinical depression is treated with antidepressants. Nonetheless, the vision board of 2022-2031 draws the attention towards development of new effective prevention and strengthening disease-modifying treatments. On the contrary, a rising concern is the use and availability of illicit stimulants (i.e., traditional stimulants and NPSs) at an alarming rate. EMCDDA (131) estimated that among adults from 15-64, the use of cocaine and MDMA was, respectively, 3.5 million and 2.6 million in 2022. Concerning the risk of addiction and abuse when using stimulants acting on DAT, research on substances binding the inward-facing conformation of the MATs (e.g., vanoxerine) has profiled anti-addictive behavior of these drugs.

A greater comprehensive understanding of these substances' selectivity, act, and preferred conformation for binding the MATs is a useful aid for future design of drugs with high selectivity and better potency for a specific MAT – intended to be used in the treatment of CNS disorders and stimulant addiction.

The aim of this study is therefore to construct and validate models of the human MATs. Homology models of the outward-facing hDAT and hNET were built, due to the lack of known 3D structures. Models of the outward-and inward-facing hSERT, based on experimentally determined hSERT-structures, were also generated. Further, the study aims to identify determinants for selective binding to each MAT, and to get a deeper understanding of the putative structural mechanism of stimulants, and other substances (i.e., antidepressants, non-simulants, atypical inhibitors, and some research standards). The selectivity for each MAT is investigated regarding; interactions with ligands having different MAT-selectivity and intrinsic properties, binding mode with respect to conserved and divergent residues in the S1-site, binding energy in terms of IFD-score, and structural features in the ligands. Additionally, the aim included achieving more insight and training in computational methods, in particular homology modeling, IFD, and MD simulations.

3 Methods

3.1 Software packages

3.1.1 Schrödinger Maestro (release 2022-3)

Schrödinger Maestro is a graphical user interface containing tools for building, displaying, and manipulating chemical structures. The software is, among other things, applied for visualizing and evaluating structures, interpreting molecular interactions, and editing molecules in both one-, two (2D) -, and three (3D) -dimensional conformations, including the building and assessing of biological models. The software consists of almost all of Schrödinger's computational programs (132, 133).

Maestro (Schrödinger release 2022-3) was, in this project, utilized to create a 3D visualization of the biogenic MATs and the ligands included in the project. Moreover, the embedded programs were used for the preparation of the proteins (*Protein Preparation Wizard*) and ligands (*LigPrep).* Alignment of the protein template- and target sequences, and building of the models of the MATs, was done by using the *Multiple Sequence Viewer* in *Prime* (Schrödinger, release 2022-3). The software was also used to dock (*Induced Fit Docking* in *Prime and Glide*) the prepared ligands to the MAT-models and run MD-simulations in *Desmond* (Schrödinger release 2022-3) – to further assess interactions and determinants for selective binding to the MATs (132, 133).

3.1.2 Basic Local Alignment Search Tool (BLAST)

Basic Local Alignment Search Tool (BLAST) is a collection of programs applied to analyze and compare biological sequences. BLAST is a part of the National Center for Biotechnology Information (NCBI) and is available from: https://blast.ncbi.nlm.nih.gov/Blast.cgi. This approach detects and defines weak but biologically significant regions of local similarity between sequences (134).

In this project, BLAST was used to find proteins from databases (i.e., PDB), with solved 3D structures (template proteins), which had a sequence significant homologous to the target sequences (proteins with unknown 3D structures) of interest.

3.2 Databases

3.2.1 Protein Data Bank (PDB)

The Protein Data Bank (PDB) is a library containing experimentally determined 3D-structures of biological macromolecules, e.g., proteins and nucleic acids. These structures are mainly mapped by X-ray crystallography, NMR, or Cryo-EM. Included in the database are the experimental data, and related metadata used to derive the structures (135). In this project, the structures of the template proteins were accessible and downloaded from PDB. PDB is available from: https://www.rcsb.org.

The data files from PDB used in the project were: **4XP1** (136) – the structure of dDAT bound to the substrate dopamine (DA), **4XP4** (137) – the structure of dDAT in complex with the inhibitor cocaine, **4XP6** (50) – the structure of dDAT bound to the substrate methamphetamine, **4XP9** (138)– the structure of dDAT bound to the substrate D-amphetamine, **5I73** (139) – the structure of the ts3-construct (three-thermostabilizing constructs, see section 3.3) of hSERT in complex with the inhibitor S-citalopram, at the central (S1)- and allosteric (S2) site, **5I6X** (55) – the structure of the ts3-construct of hSERT in complex with the inhibitor paroxetine in the central site, and **4XNU** (58) – the structure of the dDAT in complex with the selective NET-inhibitor nisoxetine. All these outward-facing transporter structures were solved by X-ray diffraction, and the resolutions were, respectively, 2.89 Å (4XP1), 2.80 Å (4XP4), 3.10 Å (4XP6), 2.80 Å (4XP9), 3.24 Å (5I73), 3.14 Å (5I6X) and 2.98 Å (4XNU).

The structure of the inward conformation of the wild-type hSERT in complex with ibogaine, **6DZZ** (140), was also included in the project. This structure was solved by Cryo-EM, and the resolution was 3.60 Å.

3.2.2 Universal Protein Resource Knowledgebase (UniProtKB) (Release 2022-03)

The target sequences, corresponding to the human MATs, were obtained from the Universal Protein Resource Knowledgebase (UniProtKB), release 2022-03. UniProtKB is a source containing protein sequences and their corresponding function information. Additionally, the genome, type of gene, the number of amino acids, and the organism of origin are stated for each sequence. The following entry codes were retrieved from UniProtKB in this study: **Q01959** (entry name: *SC6A3_HUMAN*), **P31645** (entry name: *SC6A4_HUMAN*), and **P23975** (entry name: *SC6A2_HUMAN*), which, in that order, are the sequences for DAT, SERT, and NET in humans (141). UniProtKB is available from: https://www.uniprot.org.

3.2.3 Orientations of Proteins in Membranes (OPM)

The exact arrangement of the experimentally determined proteins from PDB is not entirely precise with the respect to the lipid bilayer. However, the position in the membrane plays a key role in the biological function, intermolecular interactions, folding, and stability of membrane proteins. For that reason, the Orientation of Proteins in Membranes (OPM) is a useful database in studies of these types of proteins, thus, including the MATs (142).

The OPM is a database that provides spatial positions of a collection of membrane proteins (e.g., transmembrane-, monotopic-, and peripheral proteins), concerning the hydrocarbon core of the lipid bilayer. This type of positioning in the membrane is calculated theoretically and compared to experimental data. Moreover, the database also provides, amongst others, structural classification of proteins in four levels (i.e., type, class, superfamily, and family), species, number of transmembrane subunits, and secondary structures (142, 143). The OPM database is available from: https://opm.phar.umich.edu/.

In this project the OPM database was utilized to predict the spatial arrangement of selected IFD-complexes in membrane lipids that was used as starting complexes for the MD-simulations. More of this will be described in section 3.5. The following OPM-files were retrieved in this thesis: *4m48* ("dopamine transporter, outward-facing conformation"), *6dzz*

("serotonin transporter, inward-facing conformation"), and *5i6x* ("serotonin transporter, outward-facing conformation").

3.2.4 Psychoactive Drug Screening Program (PDSP)

The Psychoactive Drug Screening Program (PDSP) is a useful tool in supplying information about the functional activity of psychoactive compounds at targets derived from different species, such as cloned human MATs. Comprehensive of the PDSP is the Inhibition constant (K_i) Database, which implies the ability of a substance to interact with its target by providing published affinity values (K_i) for the substance and target of interest (144).

In this study, the PDSP K_i Database was used to obtain the potencies of the included substances to each MATs, except for the psychostimulants where the potency was defined by the half maximal inhibitory concentration (IC_{50}).

3.3 Construction of the monoamine transporter models

During this project, the solved 3D structures of the biogenic hNET and hDAT were not available from the PDB. Therefore, it was necessary to build homology models derived from corresponding outward-facing dDAT-structures. Structures of the outward-facing hSERTs were, however, accessible in the PDB. These structures included, amongst others, three thermostabilizing mutations (i.e., Ile291Ala, Thr439Ser, and Tyr110Ala) in order to stabilize the 3D structure for crystallization. Hence, the outward-facing SERTs from PDB were so-called ts3 constructs (i.e., three thermostabilizing constructs), and not directly the wild-type hSERT (145). Two other mutations were also found in the sequences (Cys554Ala, and Cys580Ala). Moreover, a human wild-type, inward-facing conformation, of SERT was available in the PDB, but this transporter had as well a modification in form of truncated N- and C- terminuses (146). For that reason, models of hSERT were built based on alignments to the hSERT-sequence from UniProtKB. Due to that the models of hSERT were built on hSERT-templates with only a few mutations, these models are not considered as *homology* models. In this thesis, however, the homology modeling procedure was used to build all the MAT-models.

3.3.1 Template identification

The first step in the modeling of the human MATs was to identify if any structures of them already had been solved and studied. From the database UniProtKB (available from: https://www.uniprot.org), a FASTA file, containing the unique primary amino acid sequence for each human MAT, was downloaded.

The FASTA files were further uploaded to the Protein BLAST (available from: https://blast.ncib.nlm.nih.gov/Blast.gci), where a search against PDB was performed. With this, experimentally determined proteins with significant homology to the human MAT-sequences could be found. Several matches were proposed by the Protein BLAST.

In this study, experimentally determined 3D structures bound to ligands with different intrinsic properties (i.e., various inhibitors and substrates) were of interest to choose for further analysis. That was to observe how distinct inhibitors and substrates induce conformational changes into the MATs upon binding, examine the type of intermolecular interactions that occurred in the S1-site, as well as docking scores for ligands to each MAT

could be calculated. Additionally, the docking studies and MD simulations, done after the MAT-models were built, contributed to gaining greater insight into these phenomena, as well as determinants for selective binding to the MATs could be inspected more deeply.

Mainly, it was desirable with templates that had solved 3D structures with both high resolution and sequence identity (101, 110). *Table 1* shows an overview of the codes from UniProtKB and the chosen PDB-structures, derived from the BLAST search. The query identity comprises the percentage of the query sequence (i.e., length of the target sequences) that is included in the alignment by BLAST. Further, the Expect (E)-value represents how well the target sequence matches the sequences from the database (i.e., templates from PDB), and how significant the match is. The lower E-values, the better the match is (taking both the number of matching residues, and the total length of the alignment into account). Thus, it is less likely that the sequence was found by random chance. In general, the higher percentage query coverage, the lower E-value (147).

Table 1: *Overview of the output from the Protein BLAST search: both the templates chosen from PDB, and the human sequence entry name (and code) from UniProtKB (targets) for each MAT are represented in the table. The percent-identity refers to the identity between the sequences. In addition, the query identity (%) represents the percentage of the target (query) sequence's lengths that are included in the alignment by BLAST, while the E-value represents how significant the match is (147).*

UniProtKB Entry name (UniProtKB code)	**Percent-Identity**	**Query-Identity (and E-value)**	**PDB Code**	**PDB Name (and organism of origin)**	**Resolution**
SC6A3_HUMAN (DAT) (Q01959)	54,68 %	87 % (0.0)	4XP1	Outward-facing DAT bound to DA (Drosophila melanogaster)	2.89 Å
	54,74 %	88 % (0.0)	4XP9	Outward-facing DAT bound to D-amphetamine (Drosophila melanogaster)	2.80 Å
	54,63 %	88 % (0.0)	4XP4	DAT bound to cocaine (Drosophila melanogaster)	2.80 Å
SC6A4_HUMAN (SERT) (P31645)	100.00 %	85 % (0.0)	6DZZ	Wild-type inward-facing SERT bound to ibogaine (Homo Sapiens)	3.60 Å
	98,72 %	86 % (0.0)	5I6X	Outward-facing ts3- constructed SERT bound to paroxetine at the central site (Homo sapiens)	3.14 Å

SC6A2_HUMAN (NET) (P23975)	58,38 %	87 % (0.0)	4XNU	Outward-facing DAT bound to nisoxetine (Drosophila melanogaster)	2.98 Å

In addition, 4XP6 (resolution: 3.10 Å, outward-facing dDAT bound to methamphetamine) and 5I73 (resolution: 3.24 Å, outward-facing ts3-construct of hSERT bound to S-citalopram in the central-and allosteric site) were also chosen for building a homology model of hDAT and model of hSERT, respectively. These PDB- structures were not proposed by the Protein BLAST, by the time this project was performed, but were directly retrieved from PDB. However, the PDB-structure 4XP6 was solved by the same researchers, Wang et. al. (148), as for the four other dDATs – and these dDATs are classified as related structures in PDB, hence it is expected that the percentage identity, query identity, and E-value will be around the same for 4XP6 as for the other four dDATs from PDB. The same also applies to the PDB-structure 5I73, which was solved by the same researchers as for 5I6X, Coleman et.al (145).

3.3.2 Protein preparation

Protein structures retrieved from PDB are not immediately appropriate as templates for building protein models, and performing molecular modeling calculations. The structures only consist of heavy atoms, as well as water molecules, metal ions, cofactors, and cocrystallized ligands often are included. Due to the limited resolution of the electron density maps for the determination of the experimentally structures, there might also be challenging to distinguish between NH-groups and oxygen atoms in the structure (149).

The *Protein Preparation Wizard* (Schrödinger release 2022-3) (150) was therefore, according to the Protein Preparation Guide (149), used to prepare the PDB templates for further use. Overall, the tool will generate a reliable all-atom structure, with low strain, by correcting and locating common structural problems. That, amongst others, includes; fixing incomplete side chains, loops, flipped residues, and ambiguous protonation states – as well as adjusting missing hydrogen atoms, connectivity, and bond orders (149, 151). This process was, in this study, run with 12 central processors (CPUs) using default settings. The cap-termini (not a default setting)- option was also selected: this option adds N-acetyl and N-methyl amide groups to uncapped N-and C terminuses, besides to breaks in the chain far from the binding site (region of interest), to avoid misplacing charges (152).

In all the PDB-structures unnecessary molecules, such as cholesterol, cholesterol hemisuccinate, acetylglucosamine, ethylene glycol, tetradecane, and dodecyl maltoside, were removed from the structure in the workspace. For the inward structure of the modified wild-type hSERT (PDB code: 6DZZ), the 15B8 antibody heavy chain was also removed. In total, only the ligand, water molecules near the MAT, and ions (i.e., sodium and chloride) crucial for the cotransport were retained.

3.3.2.1 Special case: Ligands not identified by the Protein Preparation Wizard (Schrödinger release 2022-3)

The ligands in the PDB-structures 4XP6 (50) and 4XP9 (138), respectively, methamphetamine and D-amphetamine, were not identified as ligands by the Protein Preparation Wizard (Schrödinger release 2022-3) (150). Therefore, these ligands had to manually be moved from the classification as het groups in the "substructure"- to the "include as a ligand"- option in the wizard before running the protein preparations (149, 150).

3.3.3 Target-template alignment

Based on information from the previous sections, alignments of the template- and target sequences could further be done. This was performed by using the application Multiple Sequence Viewer (MSV) in Prime (Schrödinger, release 2022-3). The applied annotations during the sequence alignments included a visualization of disulfide bonds, secondary structure assignments (i.e., helices, β-sheets, and loops), and displaying of S1-binding site residues within 5 Å distances from the cocrystallized ligand.

The MSV (Schrödinger, release 2022-3) uses both the target-and template sequence to perform the superposition, hence corresponding amino acids are aligned. To make the template sequence imitate the target sequence, mutations of single amino acid residues in the template are exerted by the MSV (153). However, gaps in the transmembrane helices (TMHs) and beta-sheets were corrected by manually moving amino acid residues, along the sequence, to these regions. That was to ensure that the secondary structures were in the correct positions and preserved. A simplified illustration of the alignments (including the percentage identity) used to build the homology models of hDAT and hNET, and models of hSERT, is provided in the supplementary material, figure S1-S3. The percentage identity is also profiled for the template structures with PDB-codes 4XP6 and 5I73, showing a

percentage identity equal to 56 % and 97 % to the hDAT- and hSERT- sequences, respectively.

3.3.3.1 Special case: alignment of the hDAT-sequence (entry code: SC6A3_human) to 4XP6 and 4XP9

The ligands in the PDB-structures 4XP6 (50) and 4XP9 (138), respectively, methamphetamine and D-amphetamine, were not either recognized as actual ligands by the MSV (Schrödinger, release 2022-3). These ligands were rather classified as "other het groups" named *residue "CA"* by Prime, and were included in the alignment.

To help the software recognize these ligands, the project files with the prepared protein structures were first converted into pdb- text files. In the text files, the name of the ligands was changed to a unique one, which differed from both the other het groups and amino acid residues. In this way, incorrect interpretation of these ligands and the residues (as well as the other het groups) was avoided. The alignment was done after the ligands were made recognizable by Prime (Schrödinger release 2022-3), by using the pdb- text file as the starting point. An overview of the text files is attached in the supplementary material (figure S4 and S5).

3.3.4 Building the models

Eight human MAT-models were generated based on alignments to the PDB- structures in the Multiple Sequence Viewer (MSV) panel (Schrödinger release 2022-3). The sequences that were aligned, and the corresponding models (including the ligands) are shown in table 2.

Table 2: *Models made of the human MATs based on alignments between template structures from PDB and primary target sequences from UniProtKB. The conformation of the MATs is shown in parentheses. The ligands in the PDB-structures are also included in the table.*

Monoamine transporter model	**UniProtKB** (Entry name)	**PDB-code**	**Ligand**
Human dopamine transporter models (hDAT)			
	hDAT sequence		
hDAT based on 4XP1 (outward-facing conformation)	SC6A3_human	4XP1	Dopamine
hDAT based on 4XP4 (outward-facing conformation)	SC6A3_human	4XP4	Cocaine
hDAT based on 4XP6 (outward-facing conformation)	SC6A3_human	4XP6	Methamphetamine
hDAT based on 4XP9 (outward-facing conformation)	SC6A3_human	4XP9	D-amphetamine
Human serotonin transporter models (hSERT)			
	hSERT sequence		
hSERT based on 5I6X (outward-facing conformation)	SC6A4_human	5I6X	Paroxetine
hSERT based on 5I73 (outward-facing conformation)	SC6A4_human	5I73	S-Citalopram
hSERT based on 6DZZ (inward-facing conformation)	SC6A4 human	6DZZ	Ibogaine
Human norepinephrine transporter model (hNET)			
	hNET sequence		
hNET based on 4XNU (outward-facing conformation)	SC6A2 _human	4XNU	Nisoxetine

The models were built on a knowledge-based setting by default. During the construction, both the ligands and ions (sodium ions and chloride) from the PDB-structures were included, to retain the same conformations of the protein, as well the same orientation of the ligand, as in the crystal structures. A total of 12 CPUs were used in the building process.

3.3.4.1 Special case: Ligand bound to both the orthosteric- and allosteric site of 5I73

In this project, it was of interest to look at ligands bound to the orthosteric, S1, site of the human MATs. The PDB-structure of 5I73 (139) has S-citalopram bound both in an allosteric- and the orthosteric site. For that reason, only the ligand bound to the S1-site (as well as sodium- and chlorine ions) were included in the model building of hSERT based on 5I73, while S-citalopram in the allosteric site was manually removed from the workspace before running the building-process. The orthosteric- and allosteric site were identified and distinguished according to the following article by Coleman, Green, and Gouaux: (145).

3.3.5 Validation and refinement of the models

Two methods were, in this study, used to assess the quality of each model: generation of Ramachandran plots, and analysis of the "overlap" between ligands in each model, after the induced fit docking (see section 3.4), and the corresponding ligands in the PDB-templates.

Ramachandran plots feature a graphical visualization of the phi (φ)- and psi (ψ) dihedral torsion angles of the protein backbone, where the residues are classified into "allowed" (favored and expected values)- and "disallowed" (unfavored) regions. Regarding this, the Ramachandran plot is one of the most used tools to validate the geometry of protein structures. This particularly applies since the phi- and psi angles are not usually restrained in the refinement. Hence, these plots were used as a method to indicate if there were any critical local problems in the structures. The plots were created via the server "PROCHECK" (available from: https://bio.tools/procheck) (154, 155).

PROCHECK was also applied to interpret the Ramachandran plots, and to provide a detailed inspection of the stereochemical quality of the dihedral torsion angles. Relevant to this thesis, were the statistics of the percentage of residues in, respectively, the favored-, allowed-, generously allowed-, and disallowed regions. This will be examined more in later chapters (156).

Moreover, it was also desired to examine the predictability of the transporter models, which in this study was the most essential method to validate the binding site of the MAT-models. This was done by performing a superposition of the ligands in each model to the corresponding ligands from the PDB-templates, after the ligands were docket into the human

MAT-models by induced fitting (see section 3.4). In other words, the ligand (i.e., DA) in, for instance, the hDAT-model, was superimposed to DA in the template (PDB-code: 4XP1) to observe differences in the orientation and overlap in the binding pocket. Thus, it was possible to access if the ligands from the templates, could be redocked into the models of the human MATs. The superposition was performed by using the *Superposition Panel* in Maestro (Schrödinger, release 2022-3) (157).

However, to be able to execute the superposition, the SMARTS-option in the Superposition Panel (Schrödinger, release 2022-3) had to be used. In short, this option made it possible to superimpose the ligands based on corresponding atom pairs – defined by the selection in the workspace, even though the numbering system of the atoms in the template and the human MAT- models created in MSV (Schrödinger, release 2022-3) were different. In each case, the ligand in the template was selected as the reference structure (158).

The output of the superimposing was a measurement of the root mean square deviation (RMSD) between the ligands in the MAT-models and templates from PDB. The RMSD is a quantitative value that describes the similarity between two structures that are superimposed, based on atomic coordinates (159). On a general basis, an RMSD value ≤ 2 Å between an experimental- and redocked pose is considered reasonably good (160). In Maestro (Schrödinger, release 2022-3) it was selected that the RMSD value should be calculated based on the selected atom-pairs, without changing the structures in the workspace.

Lastly, refinement of generated protein models is a built-in step in the building wizard of the MSV in Prime (Schrödinger, release 2022-3), in terms of several minimization and optimization steps. Additionally, proteins retrieved from PDB are also refined during the preparation in the Protein Preparation Wizard (Schrödinger, release 2022-3). No further manually refinements were done in this project.

.

3.4 Induced Fit Docking

3.4.1 Ligand preparation

Before running the IFD, the ligands had to be prepared. The three-dimensional (3D) structures of the substances included in this study were first made available in Maestro by using the SMILES-code (*Simplified molecular- input line- entry systems*) of each ligand. Hence, the following NPSs were created: **Mephedrone,** Paramethoxy-methamphetamine (**PMMA**), 3,4- Methylenedioxypyrovalerone (**MDPV**), and Alpha-pyrrolidinovalerophenone (**α-PVP**). Including the following traditional illicit stimulants: **Amphetamine**, **Methamphetamine**, **Cocaine,** and 3,4-methylenedioxymethamphetamine (**MDMA**). Followed by the creation of one therapeutic psychostimulant, **Methylphenidate**, and one therapeutic non-stimulant, **Atomoxetine.** Further, the following antidepressants were also created: **Citalopram** (an SSRI), **Paroxetine** (an SSRI), and **Clomipramine** (a TCA).

For comparison, three atypical inhibitors: **Ibogaine**, N-(n-butyl)-3α-[bis(4'-fluorophenyl) methoxy]-tropane (**JHW 007**), and **Vanoxerine** were also produced in Maestro. Along with some selected research standards: **Mazindol**, 5-Methoxy-6-methyl-2-aminoindane (**MMAI**), **Nisoxetine**, including the cocaine-derivate 2*β*-carbomethoxy-3*β*-(4-fluorophenyl) tropane (**β-CFT**). The biogenic neurotransmitters **NE**, **5-HT**, and **DA** were also incorporated.

The 2D structures of the totally 23 ligands are shown in figure 12.

Moreover, the ligands were prepared by using the *LigPrep command* (Schrödinger, release 2022-3) in Maestro. LigPrep optimizes structures by generating low-energy 3D conformations, as well as the ionization state and configurations (e.g., cis-trans stereochemistry and chiral centers), among other things, can be controlled (161, 162).

When running the ligand preparation, the settings were set by default with physiological pH at 7.0 $\pm$ 2.0 and OPLS 4 (*Optimized Potentials for Liquid Simulations*) as the selected force field. The protonated ligands were chosen for further use, as the protonated amino group was critical for the characteristic ionic interaction with aspartic acid in TMH1 (hSERT: Asp98, hDAT: Asp79, hNET: Asp75) in the active site of each MAT (41). A total of 12 CPUs were used to run the preparations.

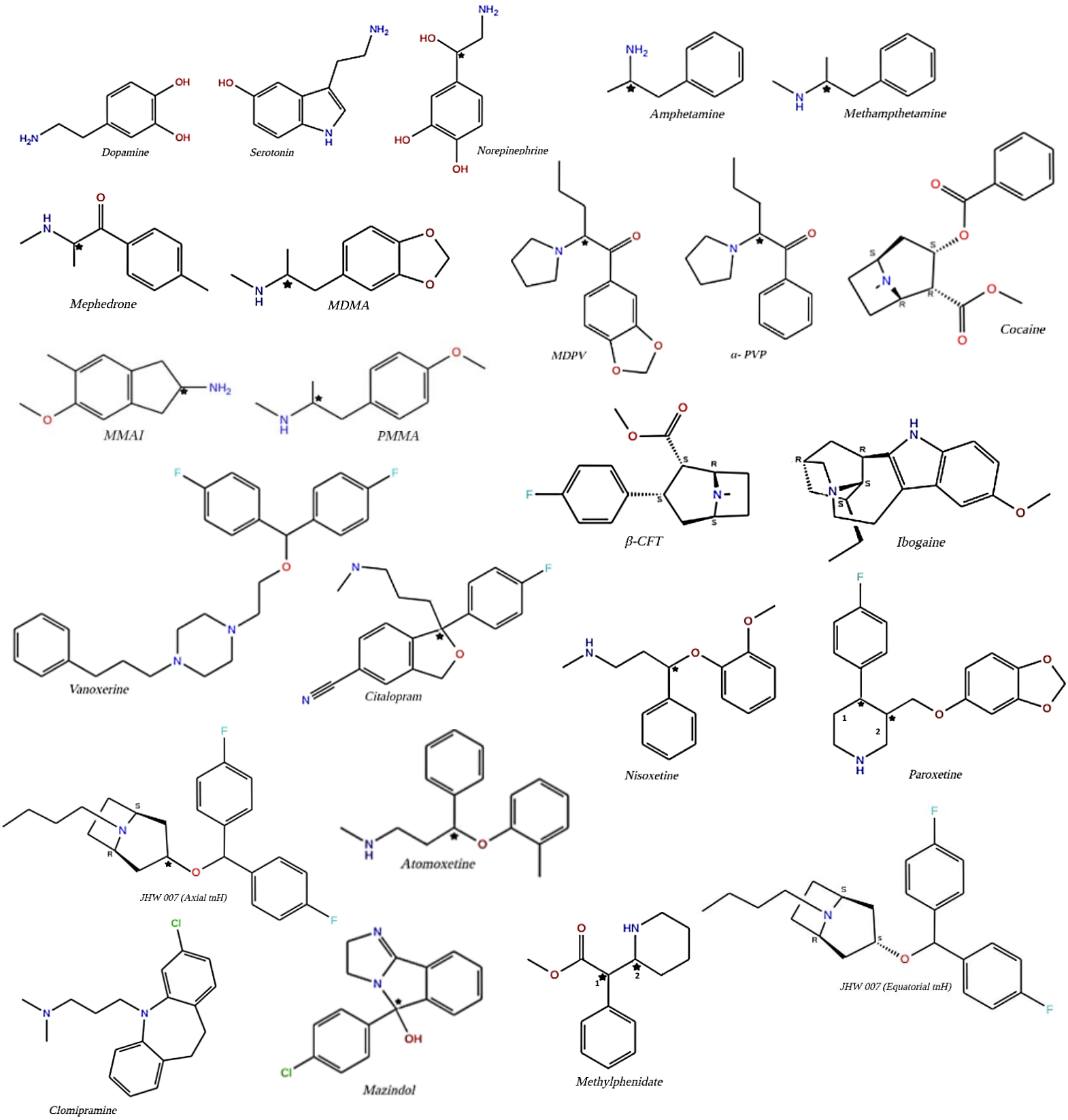

Figure 12: *2D structures of the 23 ligands included in this study. The stars indicate the chiral centers in the ligands where the configuration was not predetermined (see section 3.4.1.1). Ligands with several chiral centers are numbered. The figures are created with the 2D-sketcher in Maestro (Schrödinger, release 2022-3) and Biorender.com. A clearer 3D view of the JHW007 axial- and equatorial configurations is shown in the supplementary material (figure S6).*

3.4.1.1 Special cases: ligand preparation and stereochemistry

For some of the ligands, it was, however, desired to retain a particular stereochemistry during- and after the preparation of the ligands.

Cocaine has four chiral centers, which would have provided many generated configurational suggestions from LigPrep (Schrödinger, release 2022-3). Thus, this ligand was specified and determined to retain the same stereochemistry in each chiral center as cocaine in the PDB-structure of cocaine in complex with dDAT (PDB-code: 4XP4), before running the ligand preparation, in the LigPrep-command (Schrödinger, release 2022-3). We anticipated that this cocaine molecule was in a favorable stereochemistry for creating interactions with the MATs. The final absolute configuration for cocaine is illustrated in figure 12.

It was also desired to keep ibogaine in the same cyclic conformation as in the PDB- structure (PDB-code: 6DZZ), where the wild-type of hSERT is in an inward conformation. In addition, ibogaine also has four chiral centers, thus it was desired to limit the number of generated configurations proposed by Ligprep (Schrödinger, release 2022-3). To achieve this, only ibogaine was copied from the PDB-structure and downloaded to a new workspace window in Maestro (Schrödinger, release 2022-3), where it was determined to maintain the same stereochemistry under- and after the preparation. The final conformation and configuration of ibogaine are shown in figure 12.

Beta-CFT was similarly copied from the X-ray structure of the Drosophila DAT bound to β-CFT in the PDB file 4XPG (163), and downloaded to a new workspace window in Maestro (Schrödinger, release 2022-3). In the PDB-structure, β-CFT has an axial configuration, meaning the axial configuration of the hydrogen attached to the tertiary amine in the tropane ring (*tNH*) (164). The stereochemistry of the ligand was specified and retained as shown in figure 12.

There were no mapped crystal structures of JHW007 bound to the MATs available in PDB. To create the 3D structure of JHW007 in the workspace, the 2D-sketcher tool and 3D-builder in Maestro (Schrödinger, release 2022-3) were used to draw the structure. The 2D sketch of β-CFT in its axial configuration (from PDB-structure 4XPG), was used as a starting point to further draw the 2D structure of JHW007. The drawing corresponded to JHW007 in the following article: (164), by Abramyan and Stolzenberg et al. Both the axial- and equatorial

conformation were kept, meaning the axial-and equatorial configuration of tNH (164). The final structures are illustrated in figure 12 as 2D representations, while figure S6 in the supplementary material shows the 3D representation – for a clearer view of the differences.

3.4.2 Induced Fit Docking calculations

When the ligands were fully prepared and protonated by the LigPrep command (Schrödinger, release 2022-3), they were further docket to each of the MAT-models by the *Induced Fit Docking* (IFD) facility in Maestro (Schrödinger, release 2022-3). The docking was done conforming to the Induced Fit Docking protocol (116).

To identify the S1 binding pocket in each of the transporter models, the ligands from the PDB- structures were kept in the orthosteric, S1-, site. Thus, a grid was generated to specify these ligands as the centroid of the workspace before running the IFD, i.e., the center box where the psychostimulants and the other included substances that interact with the MATs were docket by induced fitting. The total box size where the ligands could be docket was 20 Å in each direction (20 $Å^3$). The process was run by default settings and 12 CPUs was used.

Lastly, the poses with the best predicted binding modes and energetically favored conformations were mainly chosen based on the docking score, and the orientation of the ligand in the binding pocket according to the required interaction with Asp (TMH1) in the active site of each model of the human MATs.

3.5 Molecular dynamics simulations

MD simulations were in this study utilized to understand and analyze the physical motions of the MATs upon binding. Including, the investigation of interactions important to stabilize the inward- and outward-facing conformations, at an atomistic and molecular level. During the MD simulations a trajectory of velocities, energies, and coordinates of each particle in the model system is analyzed, meaning that this computational method provides a deeper understanding of the dynamical behaviors of a biological system – in this thesis, the focus is on the MATs.

3.5.1 Constructing the model systems

The five following molecular systems were created as a platform to understand the dynamics upon binding to each MAT: "vanoxerine (atypical inhibitor) in complex with the outward-facing hSERT (based on PDB-structure 5I6X)", "vanoxerine in complex with the inward-facing hSERT (based on PDB- structure 6DZZ)", "MDMA (substrate) in complex with the outward-facing hSERT (based on PDB- structure 5I6X)", "nisoxetine (typical inhibitor) in complex with the outward-facing hNET (based on PDB-structure 4XNU)", and "methylphenidate (typical inhibitor) in complex with the outward-facing hDAT (based on PDB-structure 4XP4)". The construction of the model systems was achieved according to the Desmond protocol (165).

Performing MD simulations in aqueous biological systems initially requires preparation of the proteins and ligands. Therefore, it was first desired to choose the ligand-MAT complexes with the best IFD-scores from the IFD, involving the abovementioned ligands. Hence, these poses were the most stable ones – including that both the ligands and transporter proteins had been prepared (in the Ligprep command and Protein preparation Wizard (Schrödinger, release 2022-3), respectively), as described in previous sections.

To imitate the transporter proteins' natural biological environment, each of the five systems was further orientated with respect to the membrane bilayer. Hereafter, three PDB files from the OPM database were downloaded to the workspace in Maestro (Schrödinger, release 2022-3) which, respectively, provided the spatial and structural arrangement of outward-facing dDAT (OPM-file: 4m48), outward-facing hSERT (OPM-file: 5i6x), and the inward-facing

hSERT (OPM-file: 6dzz) in the lipid bilayer. As aforementioned, dDAT could be used as a template for the homology models of hDAT and hNET, due to that similar amino acid sequences correspond to similar membrane- and folding related characteristics (166).

The five chosen poses were, in each turn, further superimposed on the "belonging" protein-structure from the OPM database. Meaning that "vanoxerine in outward-facing hSERT" and "MDMA in outward-facing hSERT" was superimposed to the 5i6x-structure, "methylphenidate in outward-facing hDAT" and "nisoxetine in outward-facing hNET" was each superimposed to the 4m48-structure, as well as "vanoxerine in inward facing hSERT" was superimposed to the 6dzz-structure from the OPM database.

The superposition was performed by the *Superposition panel* in Maestro (Schrödinger, release 2022-3) based on the SMARTS tab, due to different residue numbering in the OPM-structures and IFD-poses. The SMARTS pattern allowed to create SMARTS expressions of the protein structures in the workspace, where corresponding atoms were defined by the alpha-carbons. However, while the first simulations were running, another method for superposition of two protein structures was discovered. Therefore, the complexes of "methylphenidate in hDAT" and "vanoxerine in outward-facing hSERT" were superimposed to the OPM-proteins by the *Protein Structure Alignment Panel* (Schrödinger, release 2022-3). Ideally, the latter method would have been used for all the systems, owing that this panel facilitates the superposition by attempting to align secondary structure elements with, amongst others, low structural similarity and different sequence numbering. On the other hand, both methods worked well to obtain the desired orientations of the five systems concerning the lipid bilayer, in this study. The structure from the OPM database was, nevertheless, selected as the reference in both methods. After the superimposing was done, the protein from OPM was removed from the workspace (158, 167).

Moreover, the next steps of constructing the systems were done in the *System builder* tool in Desmond (Schrödinger, release 2022-3). First, all the systems were each merged with a 1-palmitoyl-2-oleoylphosphatidylcholine (POPC) membrane bilayer at 300 K. The lipid bilayer was placed according to the structural position of the membrane protein from the OPM database, owing the performed superposition.

Additionally, the systems were solvated by adding a Simple Point Charge (SPC) water model. In the SPC water model, the molecules are represented as rigid triangles (3-point

model),with a geometry based on the tetrahedral structure of water molecules (168). The solvent was placed in a repeating orthorhombic box shape. Likewise, a 0.15 M NaCl solution was added to each of the five systems, to imitate the physiological salt concentration. The salt ions were randomly distributed in the solvent, contributing to an electrically neutral system for the simulations. Lastly, the rest of the options were set by default settings and the selected force field was OPLS4, before running the construction with 12 CPUs (165). Figure 13 displays the "methylphenidate-hDAT" complex as an illustration.

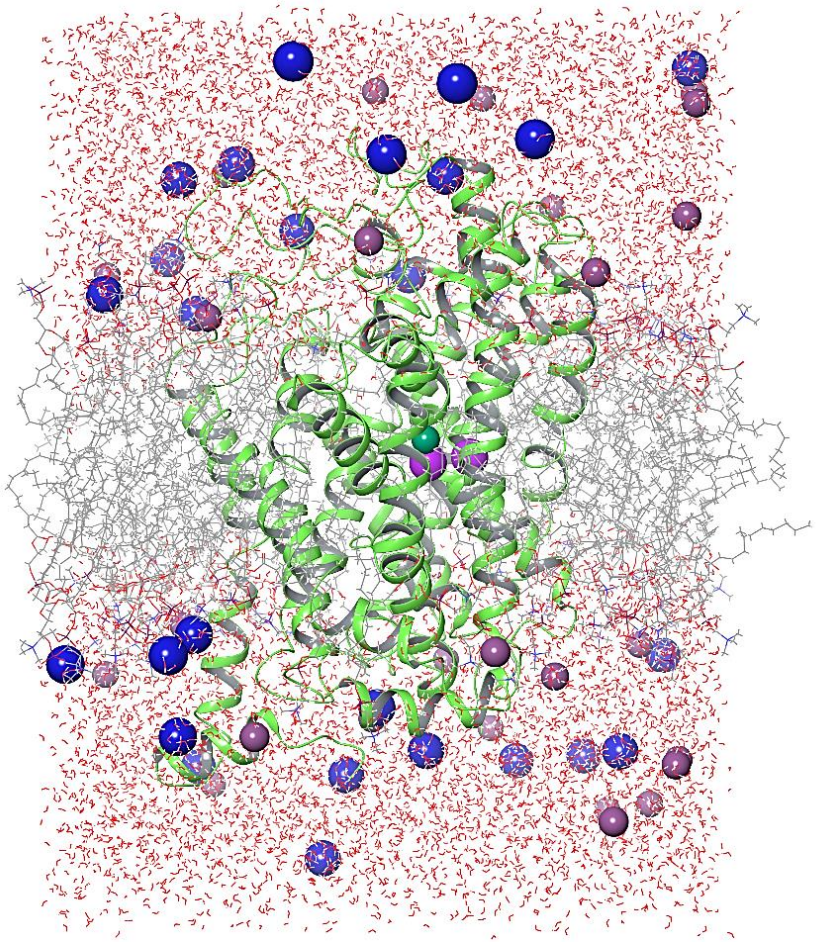

Figure 13: *Illustration of the "methylphenidate-hDAT" complex (based on PDB-structure 4XP4) orientated concerning the POPC-lipid bilayer (in grey). TMHs are colored in green. The crucial ions for the transporter function, sodium ions (purple) and chloride ion (sea-green), are shown in a Corey-Pauling-Koltun (CPK) representation. The ions in the 0.15 M NaCl solution are represented as spheres, where sodium ions are colored in violet and chloride ions in dark blue. SPC-water molecules are shown as red triangles.*

When the preparation and creation of the systems were done, MD simulations were performed in the *Molecular Dynamics* panel in Desmond (Schrödinger, release 2022-3) on a single graphics processor (GPU). The simulation time was set to 100 ns, with the NPT

ensemble (i.e., isothermal-isobaric ensemble) at a temperature of 300 K and pressure of 1.01325 bar. With this, the temperature and pressure of the systems were controlled during the simulations. The default time step size was two femtoseconds. Finally, the default protocols of MD simulations also followed a relaxation of the model systems by, amongst others, running a series of minimizations (165).

4 Results

The main purpose of this study is to identify determinants for selective binding of the psychostimulants (i.e., the traditional illicit stimulants, therapeutic stimulants, and NPSs) to each MAT, as well for a selection of other substances that act on the MATs (i.e., antidepressants, atypical inhibitors, a non-stimulant, and some research standards). Hence, a selection of various inhibitors and substrates were therefore examined; both considering the formation of intermolecular interactions and binding mode in each MAT. An overview of the results is shown in this section.

4.1 Construction of the monoamine transporter models

A 3D interpretation of the eight MAT-models, without a bound ligand, which were created in this study is shown in the figure 14. Each of the twelve TMHs is colored and labeled in the figures, as well as other secondary structures (i.e., turns and beta-sheets), that also are found in the MATs, are displayed. In addition, the crucial ions for the function of this SLC6 transporter family are shown in a CPK- representation, to make it easier to distinguish these ions from the protein itself and each other. The sodium ions are colored purple, while the chloride ions are colored in a sea green color.

The models of the hDATs were, respectively, based on the dDAT PDB-structures named 4XP1, 4XP4, 4XP6, and 4XP9. Thus, the high resolution of the X-ray crystallization of these templates made it possible to observe the two sodium ions and one chloride ion which is important for the function of DAT. This also applies to the model of hNET based on the dDAT template 4XNU (148, 169). On the other hand, the authors, Coleman et. al., of the associated abstract (145) to the X-ray structures of the outward conformation of the SERT-templates (PDB code: 5I6X and 5I73) notifies that the density of the Na2-site in the paroxetine-bound SERT (PDB: 5I6X) was weak (overall resolution: 3.14 Å), while for the (S)-citalopram-bound SERT (PDB: 5I73) the density of the chloride site was weak (overall resolution: 3.24 Å). Therefore, it is not possible to see these ions in the figures below. Lastly, the inward-facing template of SERT (PDB: 6DZZ) was solved by Cryo-EM, which either did not give a high enough resolution (overall resolution 3.60 Å for 6DZZ) to resolve any of the ions in the complex (146). Additionally, this applies to the β-turn between TMH11 and

TMH12 in the hSERT-models based on 5I6X and 6DZZ, leading to that this secondary structure nor are observed in the models based on these templates.

Outlined next to the human MAT-models are the belonging Ramachandran plots. The x-and y- axis show, respectively, the degree of the phi (φ) - and psi (ψ) torsion angles. The color schemes illustrate the allowed and most favorable region (in red), the allowed region (in yellow), the generously allowed region (in pale yellow), as well as the unfavorable and disallowed region (in white). All the residues are marked as black dots, except for glycine residues which are represented as triangles. Due to that glycine has no sidechain on the beta-carbon, it contributes minimally to the steric hindrance in proteins in general. By that, glycine residues that end up in the disallowed area are not counted by PROCHECK. As a thumb rule, it is preferred to have most of the amino acid residues placed in the favorable core (red area) to avoid as much steric hindrance as achievable, and to have a better stereochemical quality in the model. Also, it is desired to have as few residues as possible in the unfavorable (white) area. In the figures, the residues that fall outside the permitted areas are colored in red. According to PROCHECK, a good model would have over 90 % of the residues in the most favorable region (156).

Homology model of outward- facing hDAT based on the PDB-structure 4XP1:

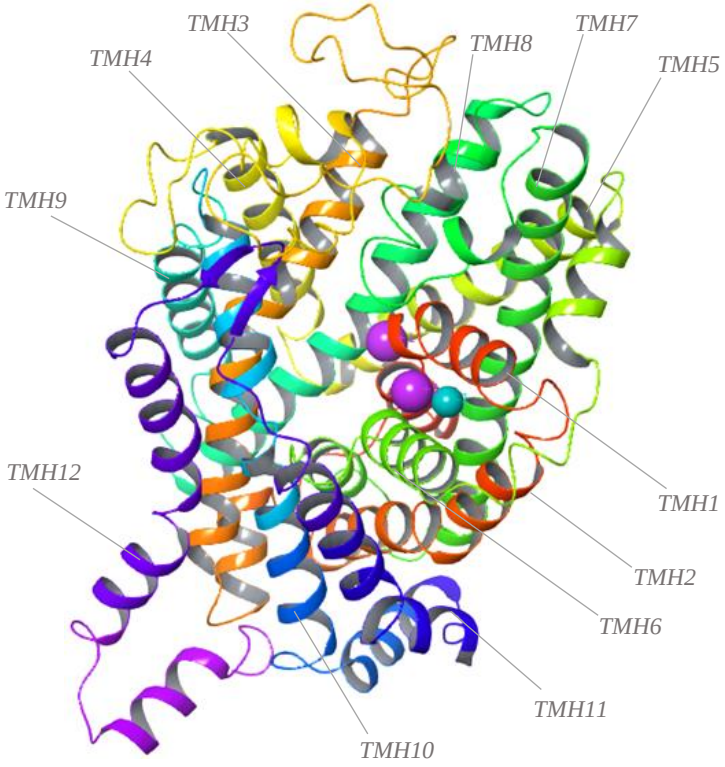

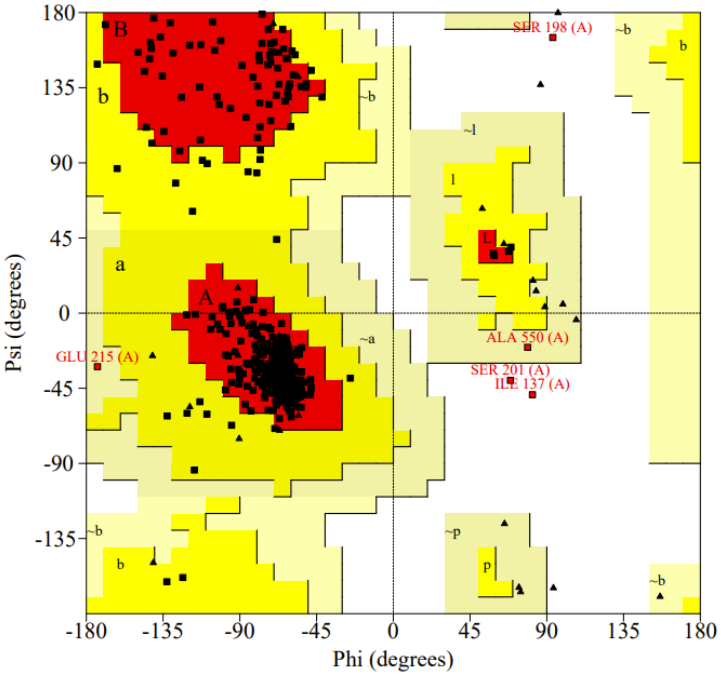

Homology model of outward- facing hDAT based on the PDB-structure 4XP4:

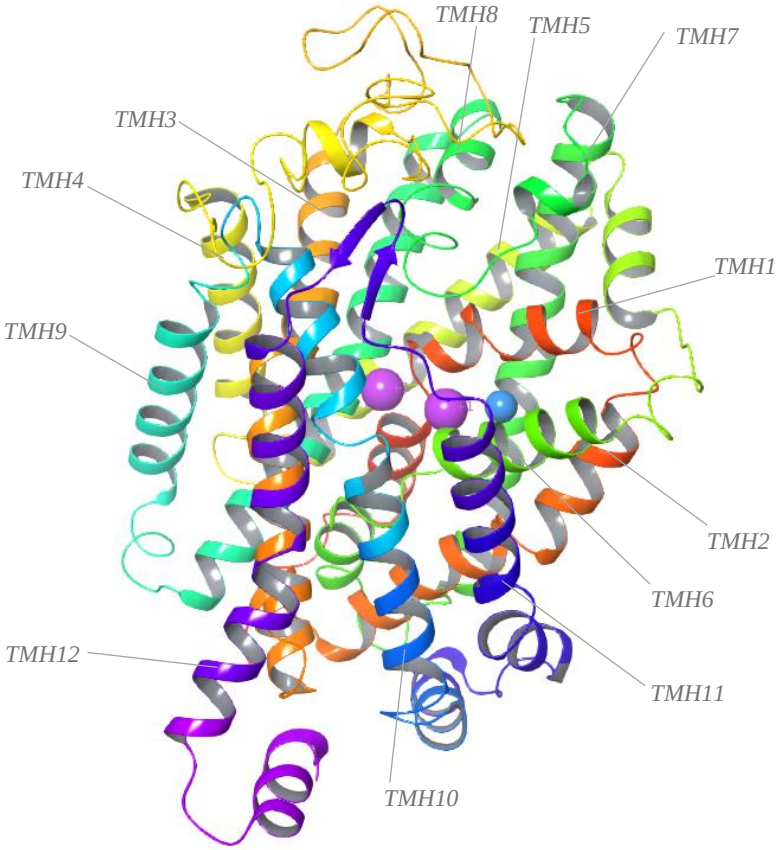

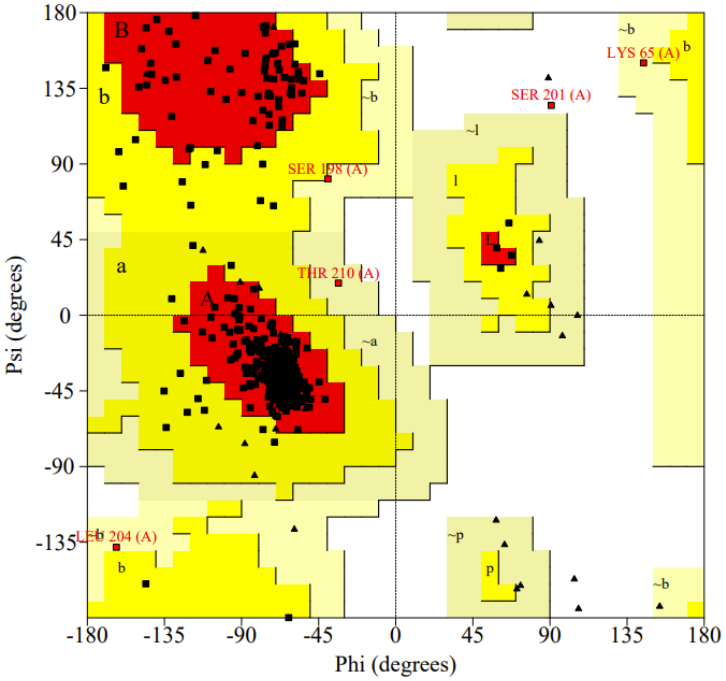

Homology model of outward-facing hDAT based on the PDB-structure 4XP6:

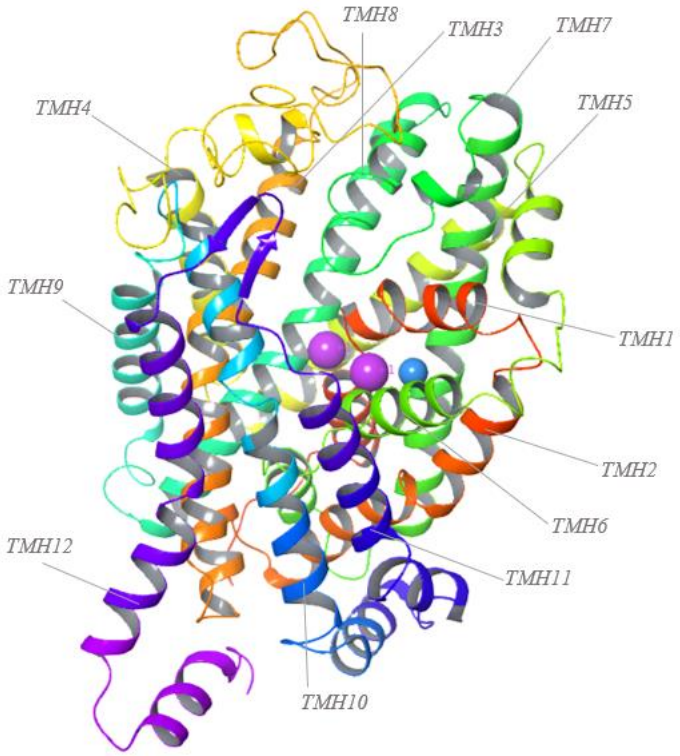

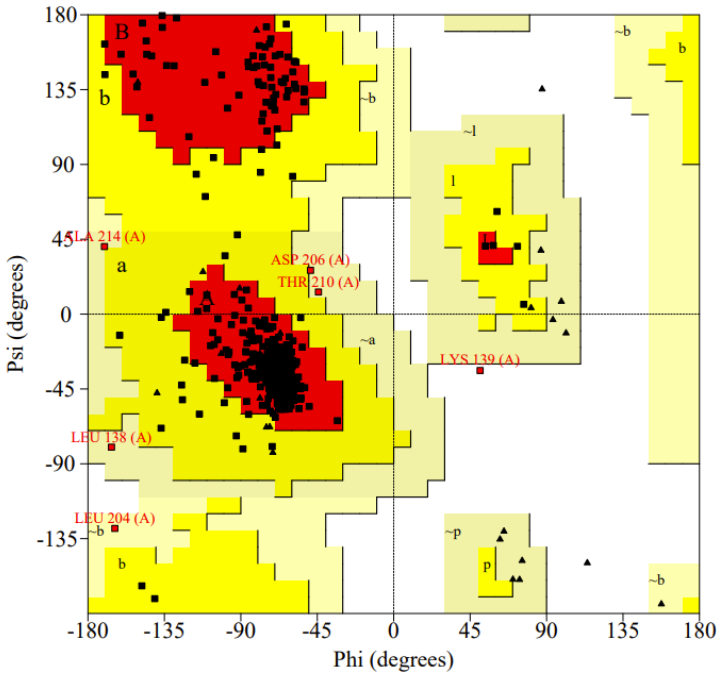

Homology model of outward- facing hDAT based on the PDB- structure 4XP9:

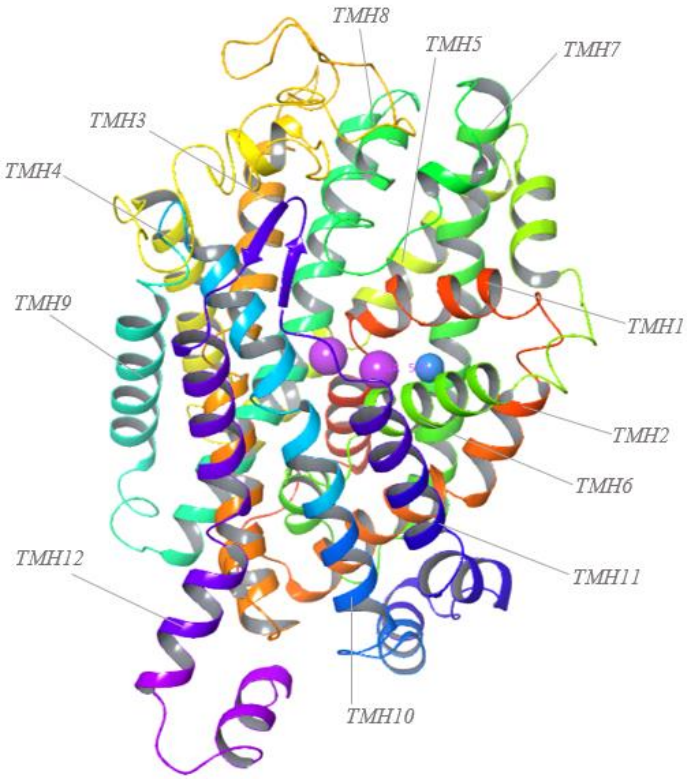

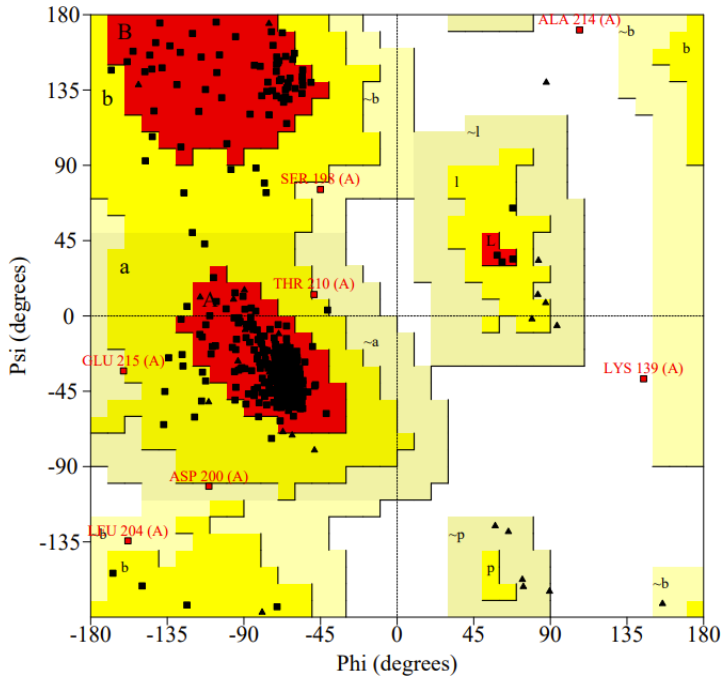

Homology model of outward-facing human NET based on the PDB structure of 4XNU:

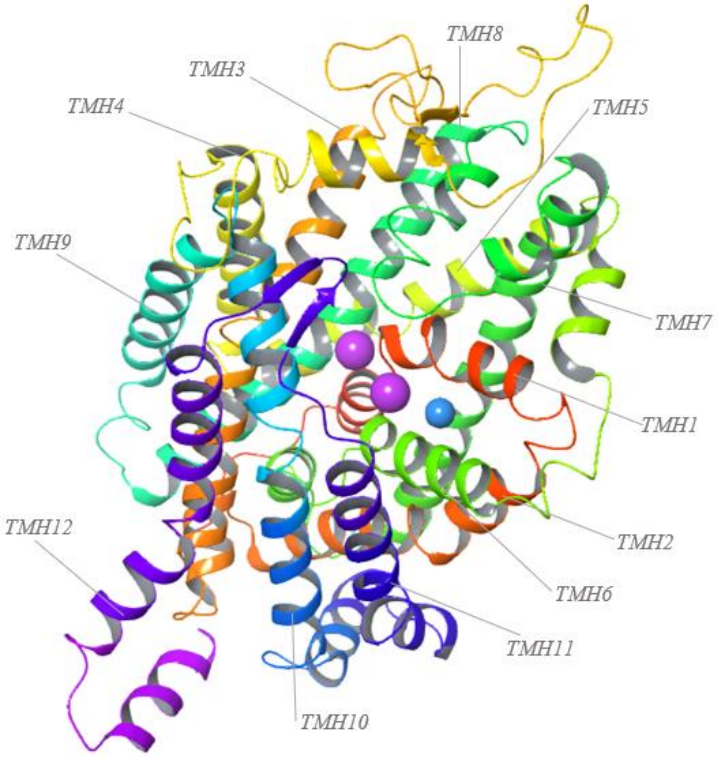

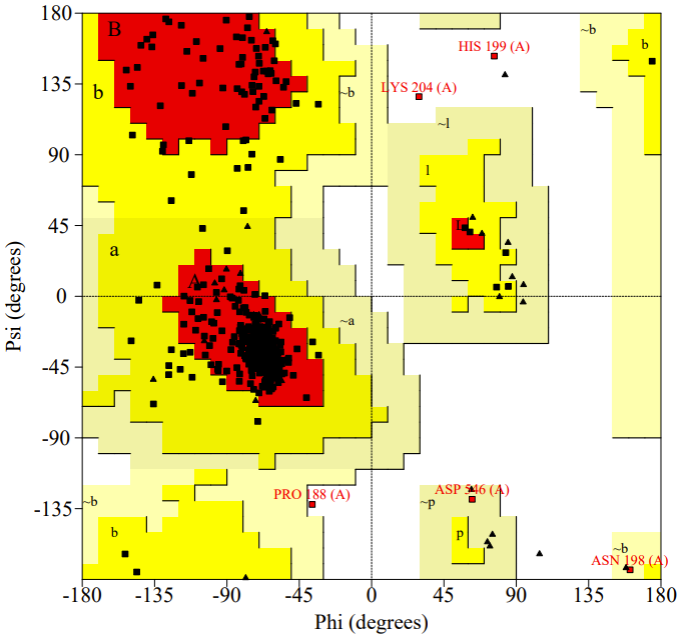

Model of outward- facing hSERT based on the PDB- structure 5I6X:

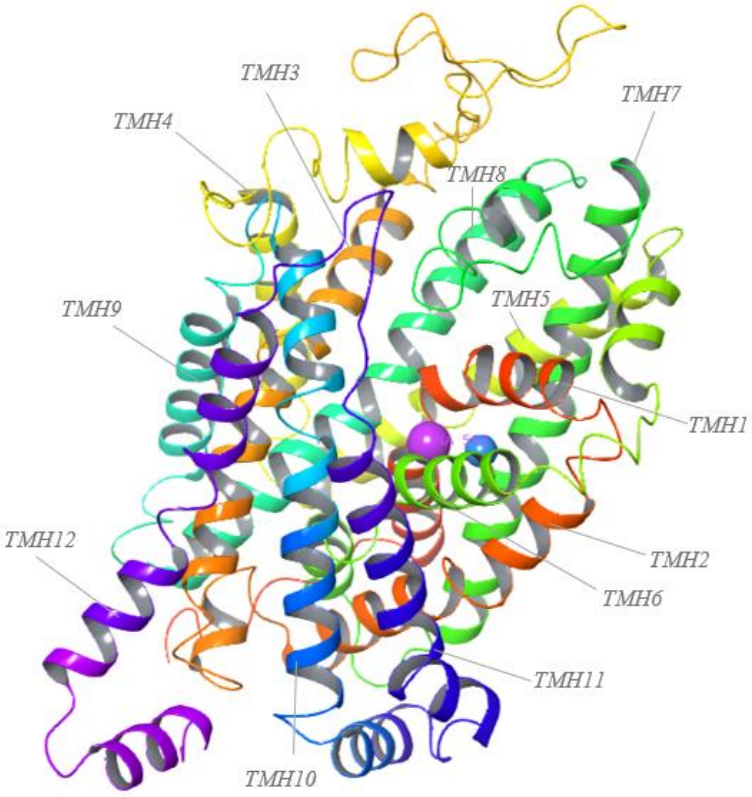

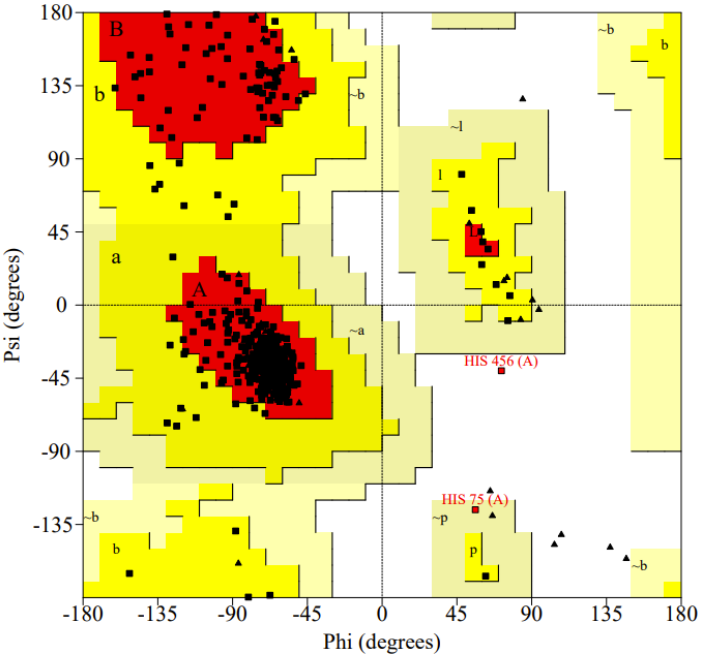

Model of outward- facing hSERT based on the PDB-structure 5I73:

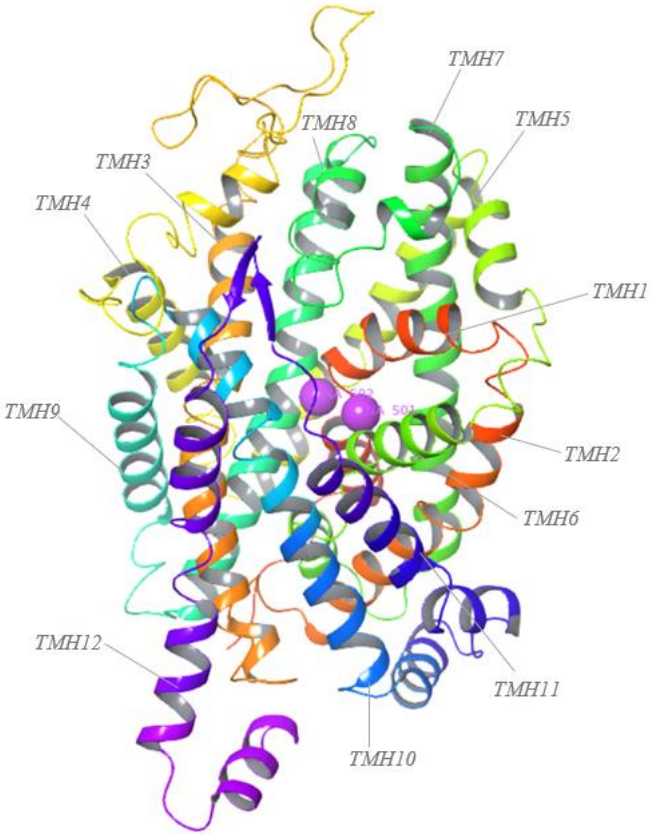

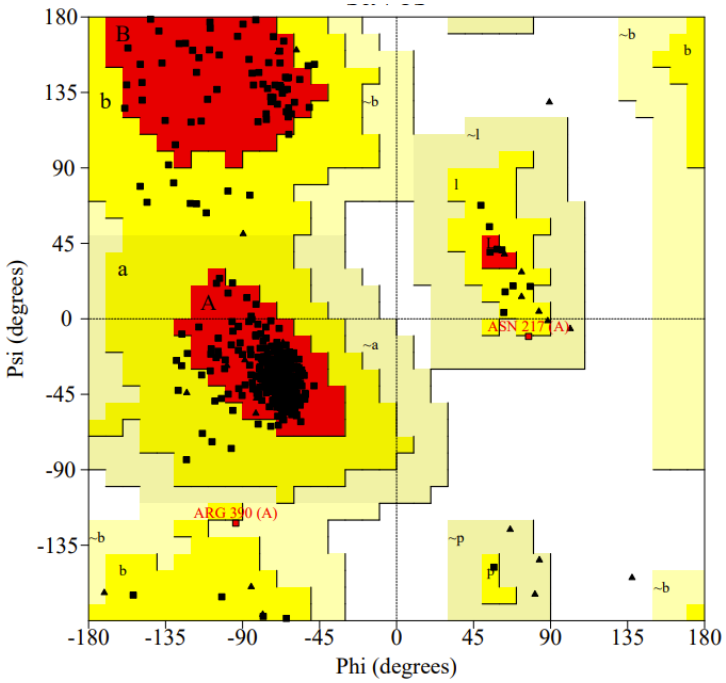

Model of inward- facing hSERT based on the PDB- structure 6DZZ:

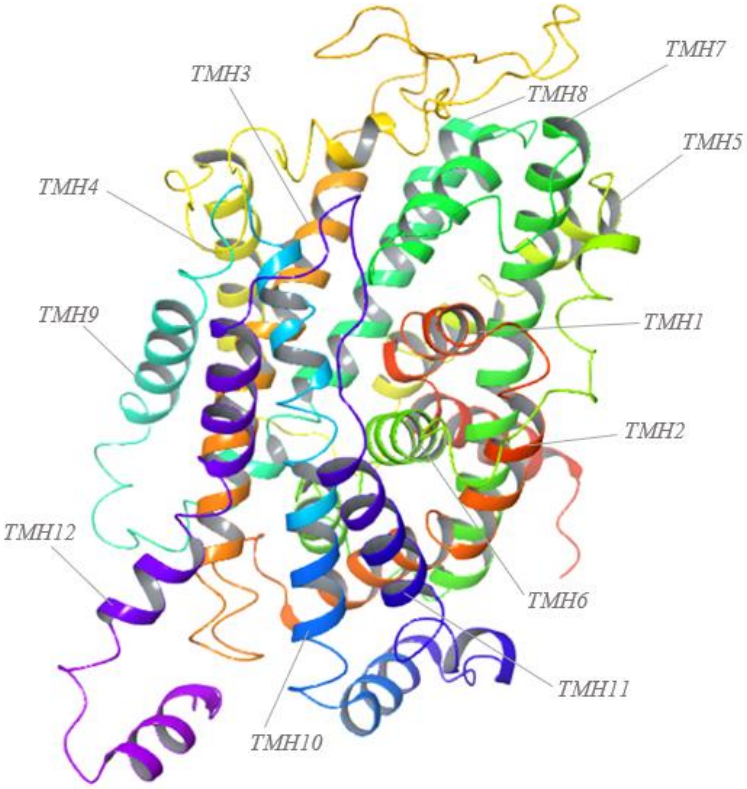

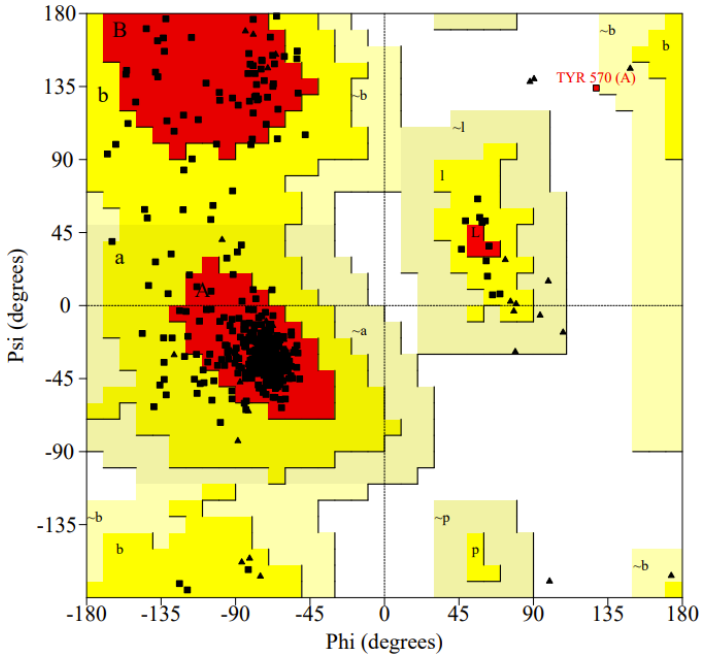

Figure 14: *3D representation of the eight MAT-models generated in this study. The twelve TMHs (TMH1-TMH12) are labeled with a gray front in italics. For each helix, the color pattern is the same in all the models. At the top of the figures is the extracellular area, while the intracellular area is at the bottom. Sodium ions are colored purple, while chloride ions are colored sea green.*

Beside the MAT-models are the belonging Ramachandran plots, where the most favorable region is colored in red, the allowed region in yellow, the generously allowed region in pale yellow, and the unfavorable region is colored in white. The dots represent all the residues in each protein model: black dots represent amino acids in the permitted areas, while red dots represent residues that are in the disallowed region. Glycine is, on the other hand, displayed as black triangles.

The output from the PROCHECK server, after performing the Ramachandran plots, is displayed in table 3. The residues that are found in the disallowed regions are listed in this table, along with the angle degree of the phi- and psi dihedral torsion angles – these degrees were, however, obtained from the *Ramachandran Plot Panel* in Maestro (Schrödinger, release 2022-3). The glycine residues are not included in the table.

Table 3: *Overview of the output from the Ramachandran plots derived from PROCHECK. There were no residues in the disallowed area in the hSERT-model based on the PDB-template 5I73 (marked with hyphen).*

Homology model	**Residues in most favored area**	**Residues in allowed area**	**Residues in the generously allowed area**	**Residues in disallowed area**	**Residues in the disallowed area: phi- and psi angles**
hDAT based on 4XP1	94, 3 %	4,7 %	0,4 %	0,6 %	Ser198: φ = 93.4 & ψ = 165.0 Ser201: φ= 68.7 & ψ = -40.3 Ile137: φ = 81.5 & ψ = -48.9
hDAT based on 4XP4	93,2 %	5,7 %	0,9 %	0,2 %	Ser201: φ = 90.8 & ψ = 124.9
hDAT based on 4XP6	91,7 %	7,0 %	1,1 %	0,2 %	Lys139: φ = 50.8 & ψ = -33.9
hDAT based on 4XP9	92,4 %	6,1 %	1,1 %	0,4 %	Ala214: φ= 107.2 & ψ = 170.8 Lys139: φ = 144.7 & ψ= 37.6
hNET based on 4XNU	91.2 %	8.0 %	0,4 %	0,4 %	Lys204: φ= 29.4 & ψ = 126.9 His199: φ = 76.3 & ψ = 152.7
hSERT based on 5I6X	93,1 %	6,5 %	0,2 %	0,2 %	His456: φ= 71.8 & ψ = -40.4
hSERT based on 5I73	92,2 %	7,4 %	0,4 %	0,0 %	-
hSERT based on 6DZZ	87,8 %	12,0 %	0 %	0,2 %	Tyr570: φ = 128.0 & ψ= 134.0

To further examine if the MAT-models were of the desired quality, the predictability of each model was also assessed. Thus, it was of interest to investigate if the IFD-procedure could redock the cocrystallized ligands in the models in approximately the same orientation as the ligands from the corresponding PDB-templates. This was done by superimposing the ligands from each MAT-model to the corresponding ligands in the PDB-templates. Additionally, RMSD-values were calculated to have a quantitative basis for the qualitative visualization.

The results from the superimposing are presented in the figures below (figure 15-22), along with the RMSD-value between the ligands in the MAT-models and PDB-templates. To get a better imagining of the orientation in the binding pocket, residues in a circumference of 4 Å from the cocrystallized ligands are also displayed. However, the RMSD-value for the secondary structures of the MAT-models and templates was not calculated, but the figures show that they "overlap" well. In each illustration, the crucial salt bridge formed with Asp (hSERT: Asp98; hDAT: Asp79; hNET: Asp75) in TMH1 is marked with purple dashed lines. Moreover, the models of hDAT are colored in green, hNET is colored in orange, the outward-facing hSERT models are colored in yellow, and the inward-facing hSERT is colored in purple. In some of the illustrations the loops of the extracellular side are "cropped" to make the visualization of the transmembrane parts clearer.

Overall, the human MAT-models showed great overlap to the templates from PDB. The alignment (figure S1 in the supplementary material) of the hDAT-sequence to each dDAT-template from PDB (PDB-codes: 4XP1, 4XP4, 4XP6, and 4XP9) demonstrated that there were some variations in single amino acid residues between humans and drosophila melanogaster. However, the alignment from MSV (Schrödinger release 2022-3) also showed that all dDAT-templates had more than 50 % sequence identity to the hDAT-sequence. Furthermore, the hNET-sequence was aligned to a dDAT-template (PDB-code: 4XNU) to be able to build hNET. Some differences in single amino acid residues were also observed between these two sequences (see figure S3 in the supplementary material), nonetheless, the overall sequence identity was over 50 %. Lastly, the outward-facing hSERT-models were built based on ts3-constructs of the hSERT-templates (PDB-codes 5I6X and 5I73) with the following thermostabilizing mutations Ile291Ala; Thr439Ser; and Tyr110Ala, including two point-mutations: Cys554Ala and Cys580Ala. The inward-facing hSERT was built based on a N-and C- terminus truncated outward-facing hSERT- template (PDB-code: 6DZZ), without any mutations in the sequence (the alignment is provided in figure S2 in the supplementary

material). All in all, the hSERT-models therefore had high sequence identity (over 95 % and 100 %, respectively).

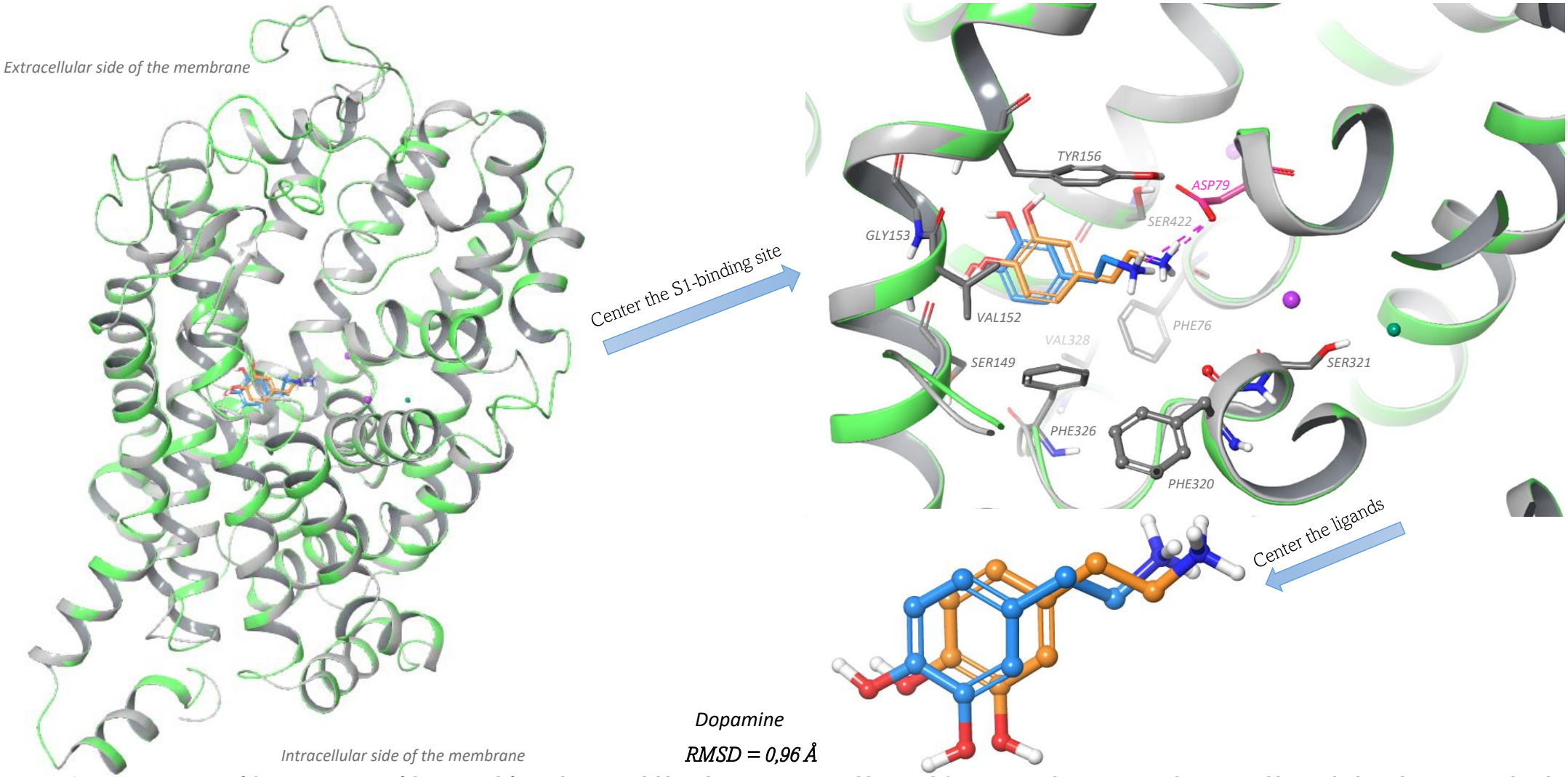

Figure 15: *Overview of the superposition of the outward-facing hDAT-model based on 4XP1 (green ribbon) and the corresponding 4XP1-template (grey ribbon). The ligands (DA) are colored orange and blue, respectively, with an RMSD equal to 0,96 Å. Only some binding site residues, 4Å from the cocrystallized ligand, are viewed (labeled in cursive) for simplicity. The ions are illustrated as spheres, where sodium is purple and chloride is sea green. In the illustration, the salt bridge between Asp79 and the protonated amine (in DA) is marked with pink dashed lines.*

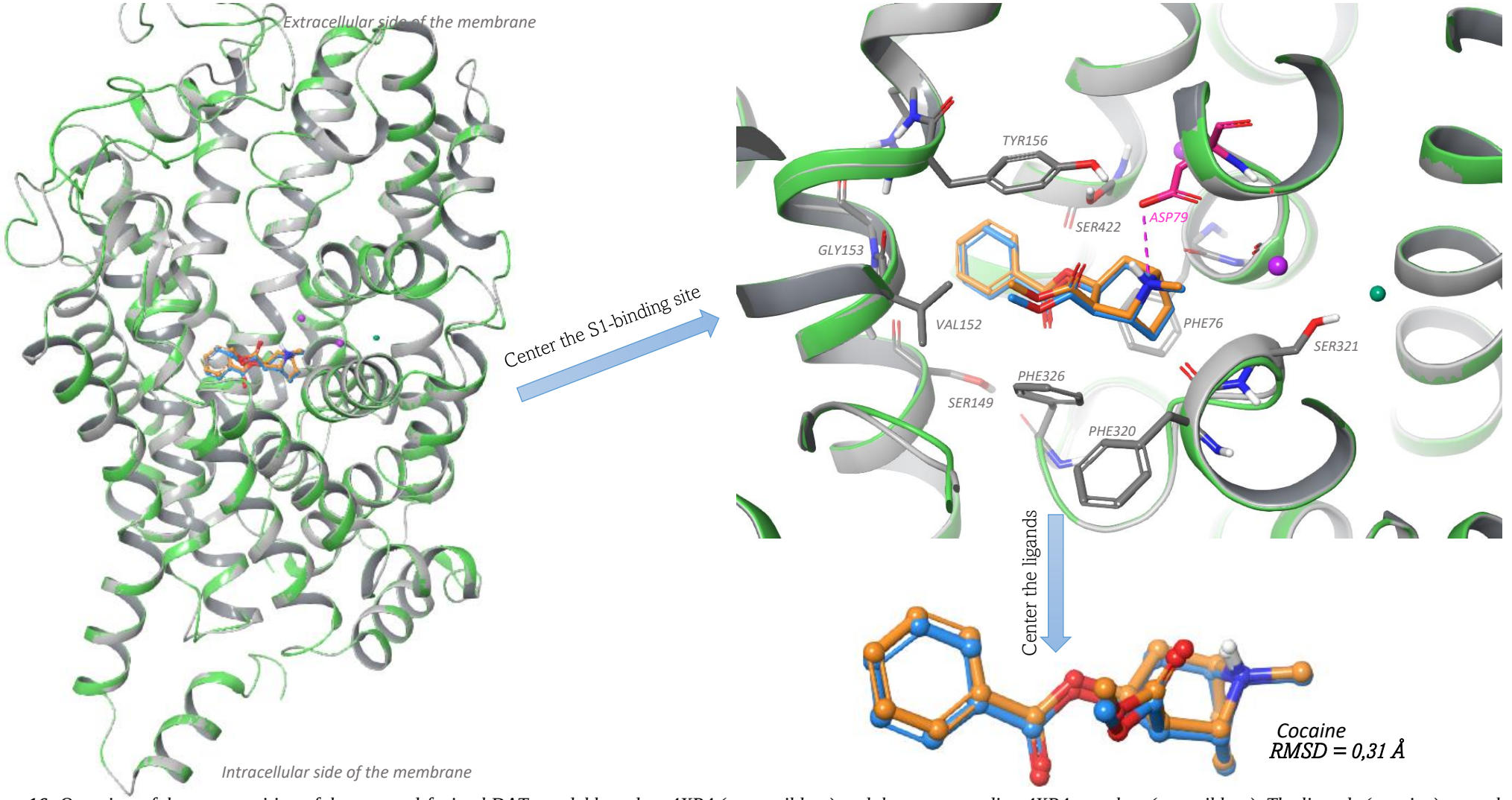

Figure 16: *Overview of the superposition of the outward-facing hDAT- model based on 4XP4 (green ribbon) and the corresponding 4XP4-template (grey ribbon). The ligands (cocaine) are colored orange and blue, respectively, with an RMSD equal to 0,31 Å. Only some binding site residues, 4Å from the cocrystallized ligand, are viewed (labeled in cursive) for simplicity. The ions are illustrated as spheres, where sodium is purple and chloride is sea green. In the illustration, the salt bridge between Asp79 and the protonated amine (in cocaine) is marked with pink dashed lines.*

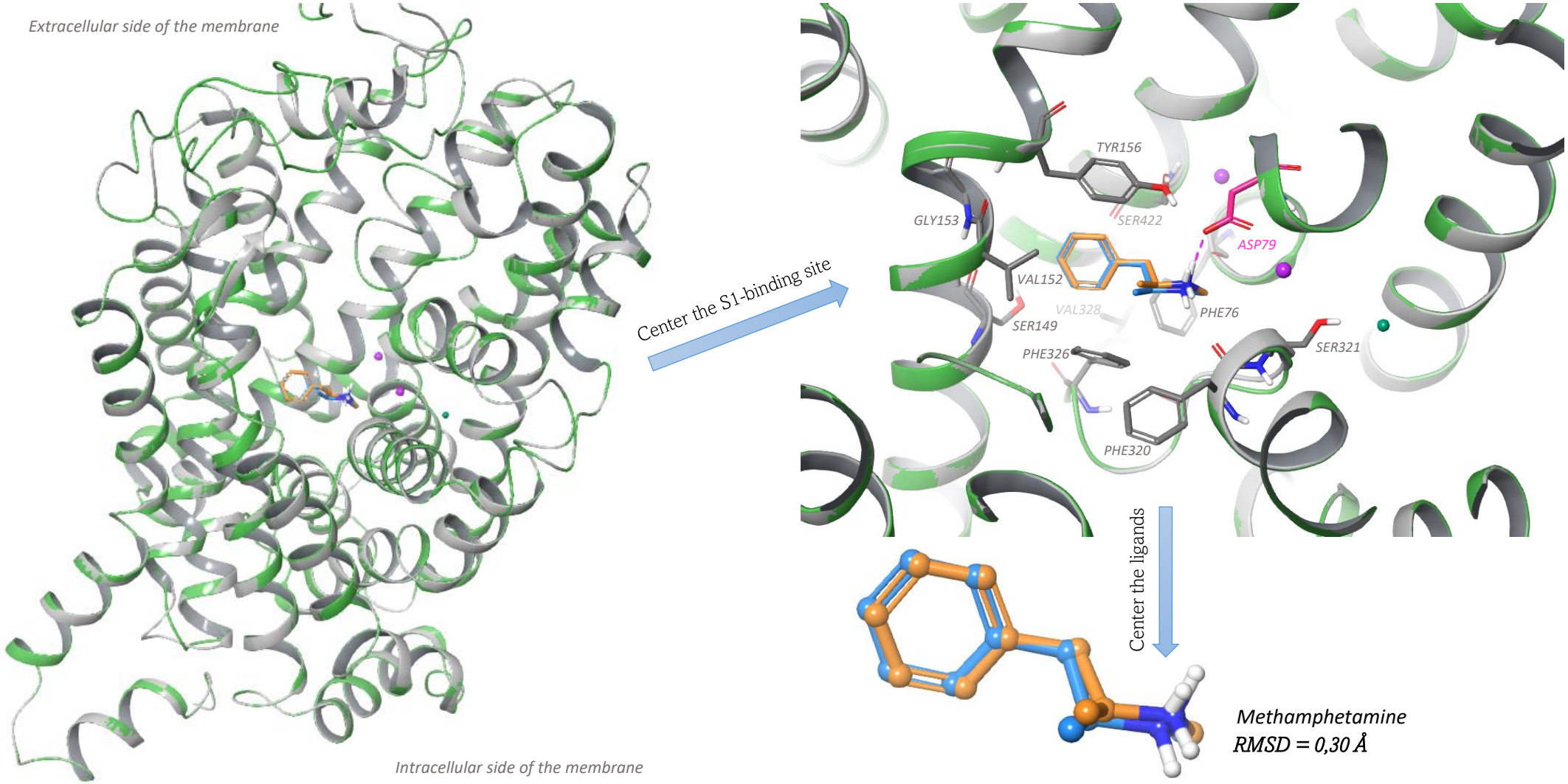

Figure 17: *Overview of the superposition of the outward-facing hDAT-model based on 4XP6 (green ribbon) and the corresponding 4XP6-template (grey ribbon). The ligands (methamphetamine) are colored orange and blue, respectively, with an RMSD equal to 0,30 Å. Only some binding site residues, 4Å from the cocrystallized ligand, are viewed (labeled in cursive) for simplicity. The ions are illustrated as spheres, where sodium is purple and chloride is sea green. In the illustration, the salt bridge between Asp79 and the protonated amine (in methamphetamine) is marked with dashed lines.*

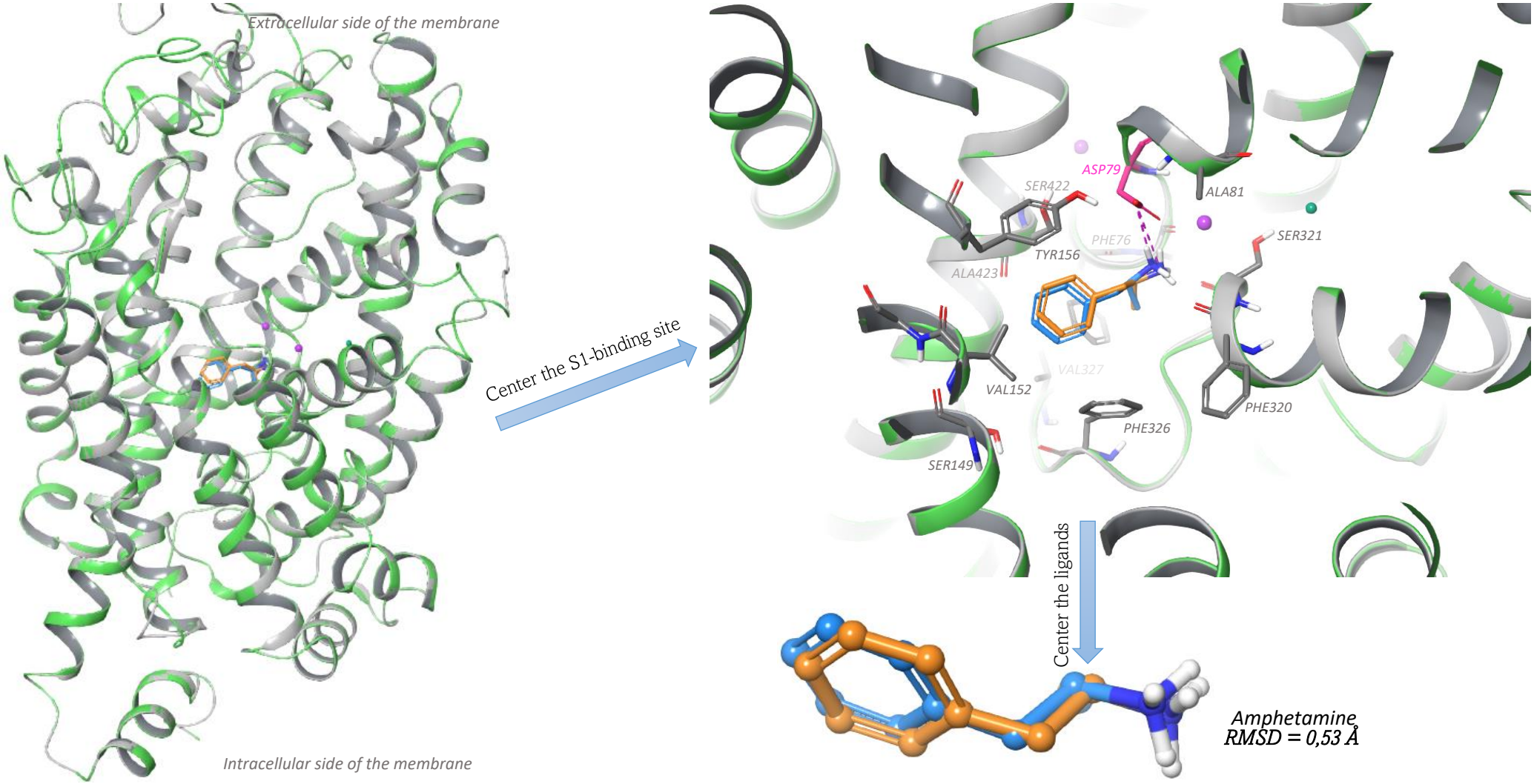

Figure 18: *Overview of the superposition of the outward-facing hDAT-model based on 4XP9 (green ribbon) and the corresponding 4XP9-template (grey ribbon). The ligands (amphetamine) are colored orange and blue, respectively, with an RMSD equal to 0,53 Å. Only some binding site residues, 4Å from the cocrystallized ligand, are viewed (labeled in cursive) for simplicity. The ions are illustrated as spheres, where sodium is purple and chloride is sea green. In the illustration, the salt bridge between Asp79 and the protonated amine (in amphetamine) is marked with pink dashed lines.*

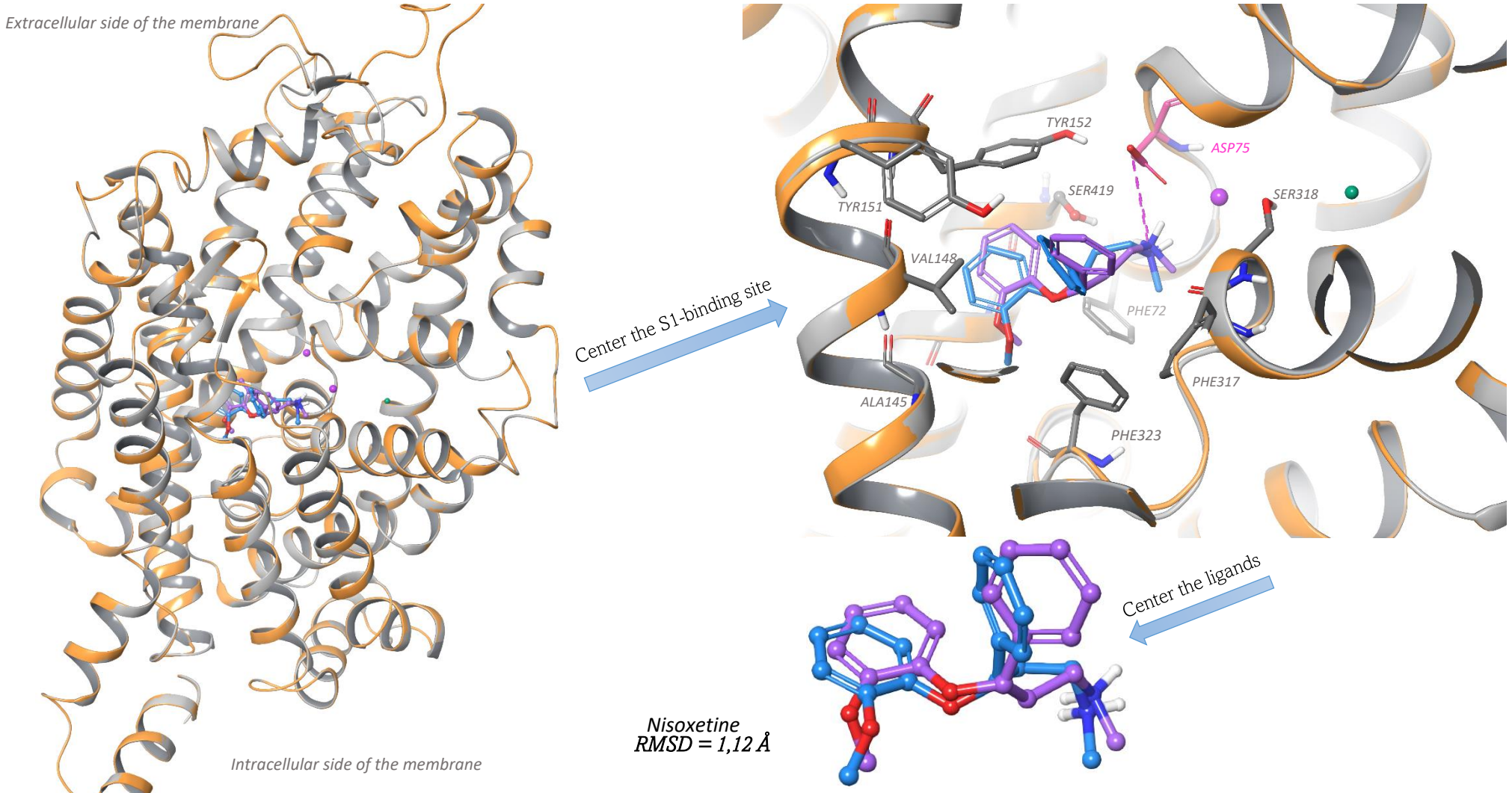

Figure 19: *Overview of the superposition of the outward-facing hNET- model based on 4XNU (orange ribbon) and the corresponding 4XNU-template (grey ribbon). The ligands (nisoxetine) are colored purple and blue, respectively, with an RMSD equal to 1,12 Å. Only some binding site residues, 4Å from the cocrystallized ligand, are viewed (labeled in cursive) for simplicity. The ions are illustrated as spheres, where sodium is purple and chloride is sea green. In the illustration, the salt bridge between Asp75 and the protonated amine (in nisoxetine) is marked with pink dashed lines.*

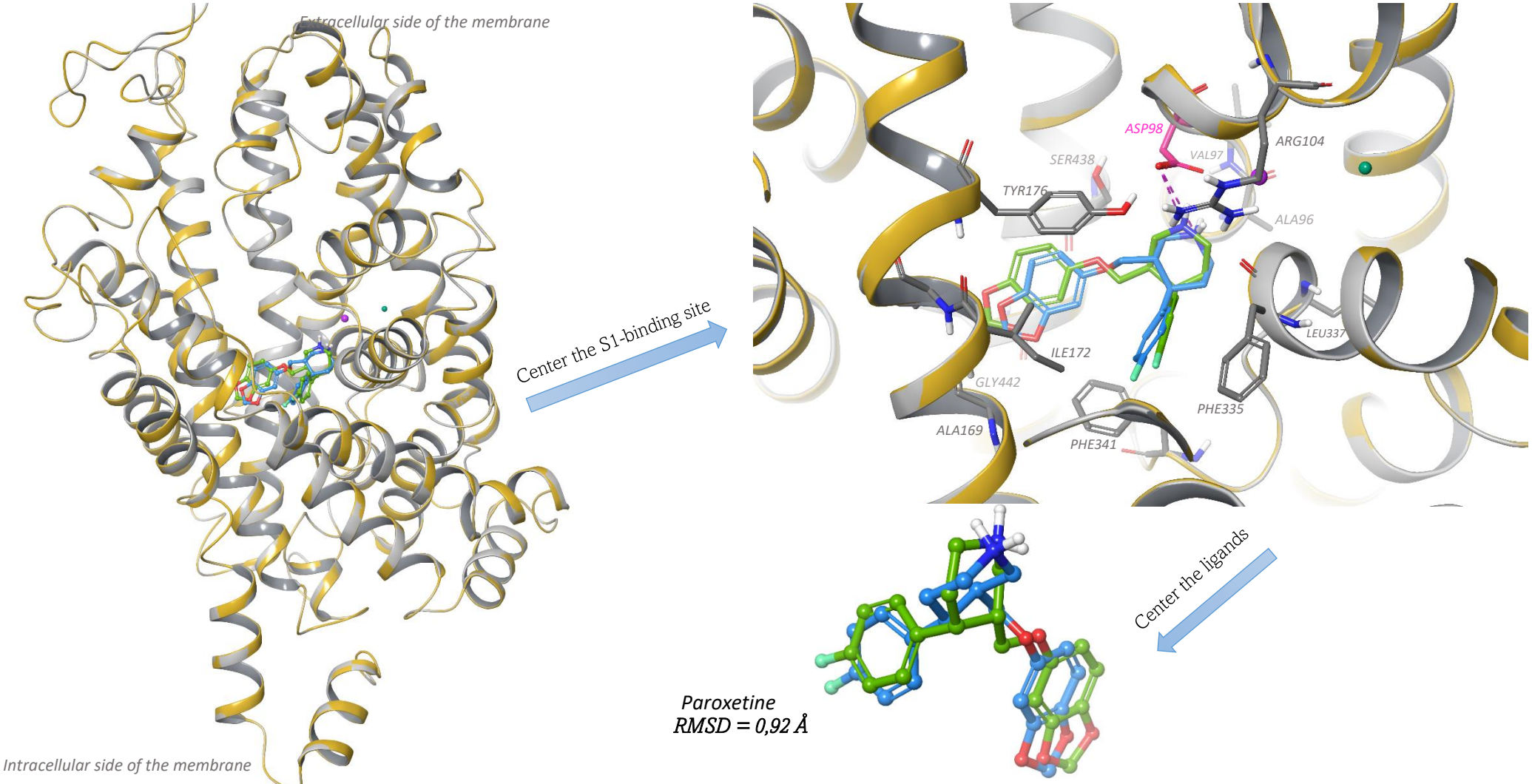

Figure 20: *Overview of the superposition of the outward-facing hSERT- model based on 5I6X (yellow ribbon) and the corresponding 5I6X-template (grey ribbon). The ligands (paroxetine) are colored green and blue, respectively, with an RMSD equal to 0,92 Å. Only some binding site residues, 4Å from the cocrystallized ligand, are viewed (labeled in cursive) for simplicity. The ions are illustrated as spheres, where sodium is purple and chloride is sea green. In the illustration, the salt bridge between Asp98 and the protonated amine (in paroxetine) is marked with pink dashed lines.*

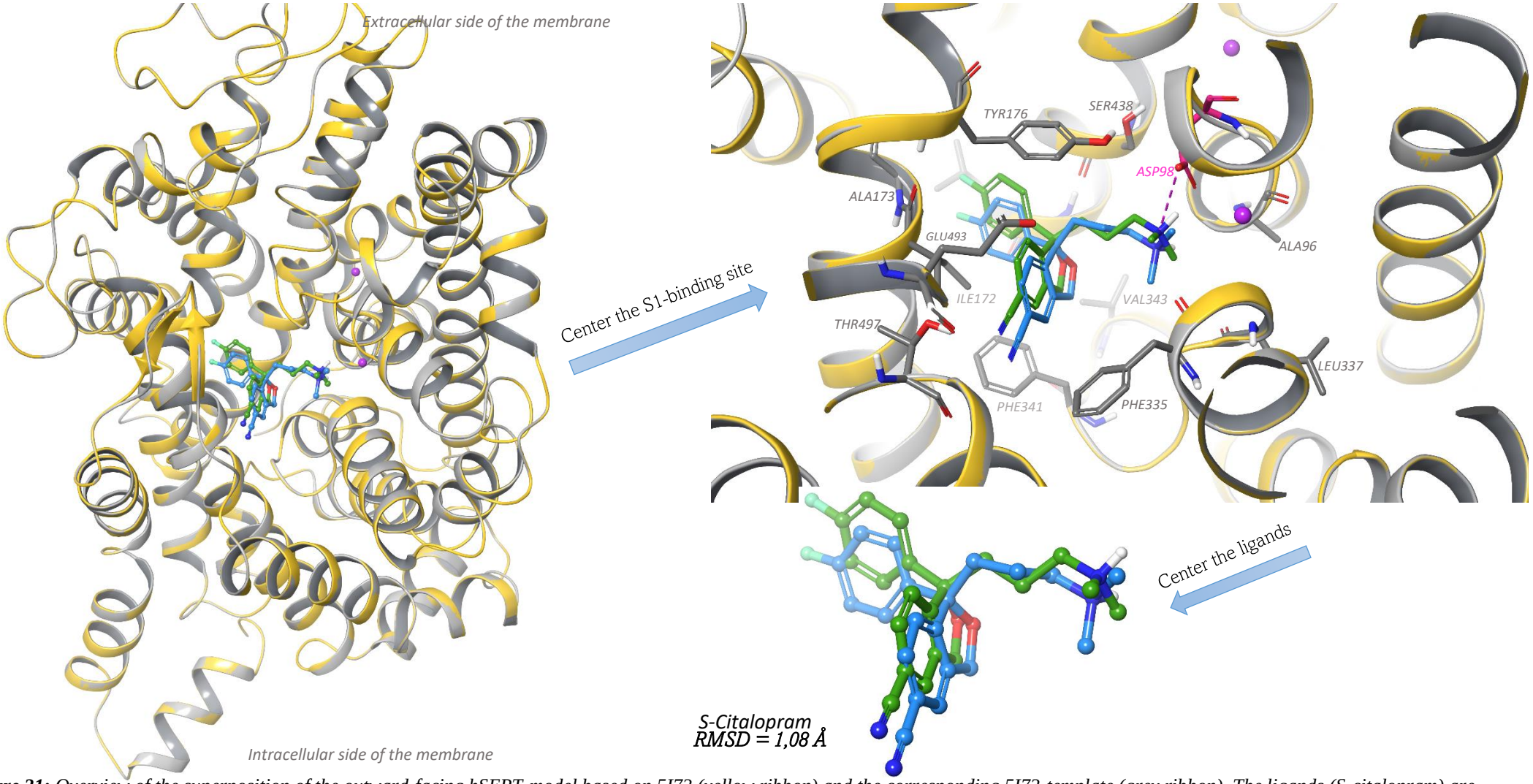

Figure 21: *Overview of the superposition of the outward-facing hSERT-model based on 5I73 (yellow ribbon) and the corresponding 5I73-template (grey ribbon). The ligands (S-citalopram) are colored green and blue, respectively, with an RMSD equal to 1,08 Å. Only some binding site residues, 4Å from the cocrystallized ligand, are viewed (labeled in cursive) for simplicity. The ions are illustrated as spheres, where sodium is purple and chloride is sea green. In the illustration, the salt bridge between Asp98 and the protonated amine (in S-citalopram) is marked with pink dashed lines.*

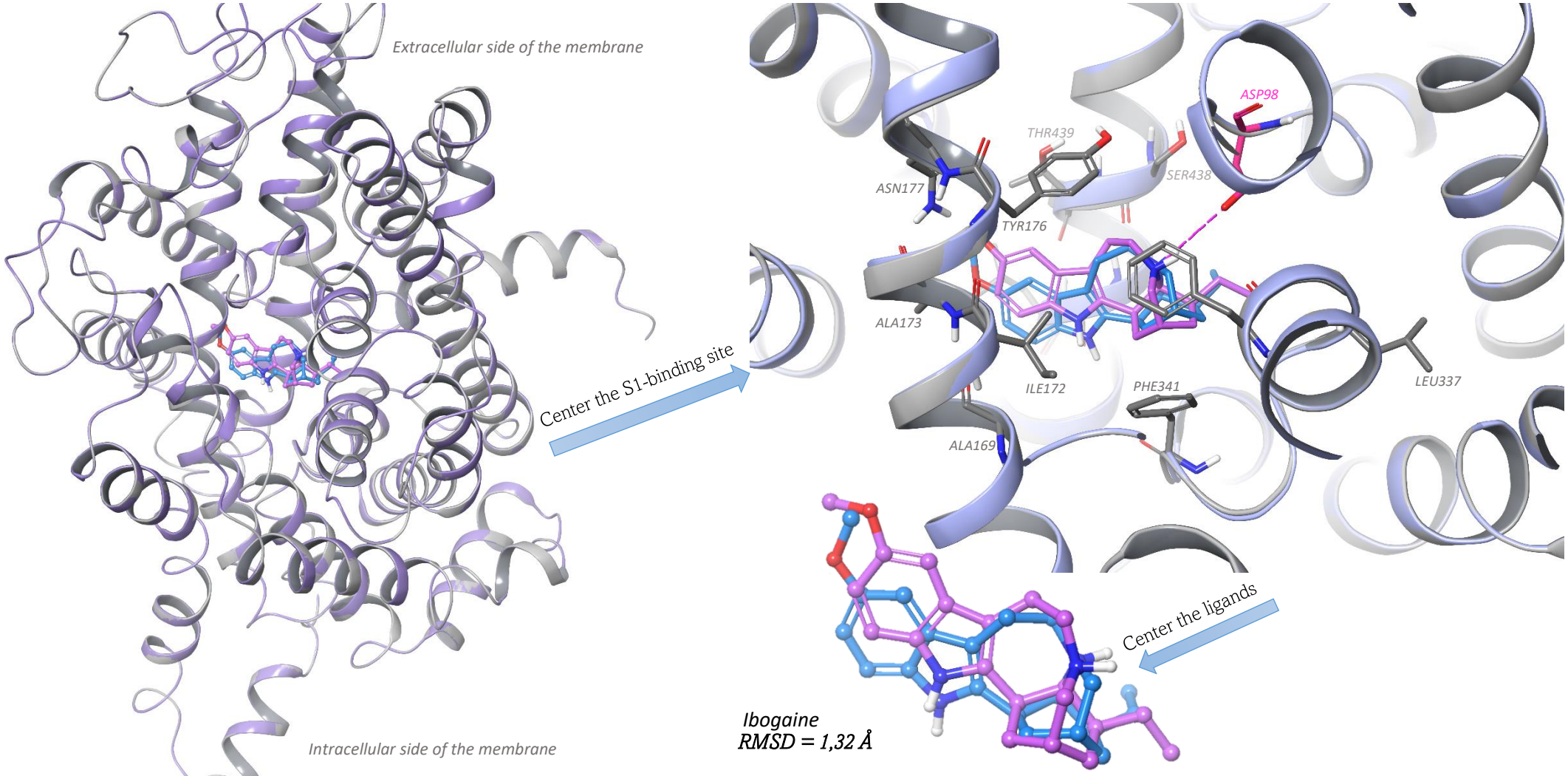

Figure 22: *Overview of the superposition of the inward-facing hSERT-model based on 6DZZ (light purple ribbon) and the corresponding 6DZZ-template (grey ribbon). The ligands (ibogaine) are colored purple and blue, respectively, with an RMSD equal to 1,32 Å. Only some binding site residues, 4Å from the cocrystallized ligand, are viewed (labeled in cursive) for simplicity. In the illustration, the salt bridge between Asp98 and the protonated amine (in ibogaine) is marked with pink dashed lines. The ions were not solved in the 3D structure of the 6DZZ-template (resolution: 3.60 Å).*

Moreover, mainly all the transporter models generated in this study were in an outward-facing conformation. Indeed, only hSERT was generated in an inward-facing conformation (based on the PDB-code: 6DZZ), meaning that the analyses performed on the inward-facing conformation (both the IFD calculations and MD simulations) are based on hSERT, and not hNET and hDAT in this study. This is important to take into account, even though some of the included substances are more selective for the inward-facing conformation of the latter transporters. However, more of this will be discussed in the next chapters.

The structural differences in the conformation between the outward (PDB-template: 5I6X) - and inward-facing (PDB-template: 6DZZ) hSERT are shown in figure 23. From the illustration, it is possible to observe that binding of ligands (in this case: the typical inhibitor paroxetine) that bind and block hSERT in an outward-facing conformation, induces a more tightly packet conformation of the transporter. This applies especially in the regions near the S1-binding site. On the other hand, binding of ligands that prefer to bind hSERT in an inward-facing conformation (in this case: the atypical inhibitor ibogaine), induce a "wider" spread of the TMHs. The conformation of hSERT observed upon binding to paroxetine and ibogaine (figure 23), can be seen in the light of the three-step translocation mechanism described in chapter 1.5 (see figure 8).

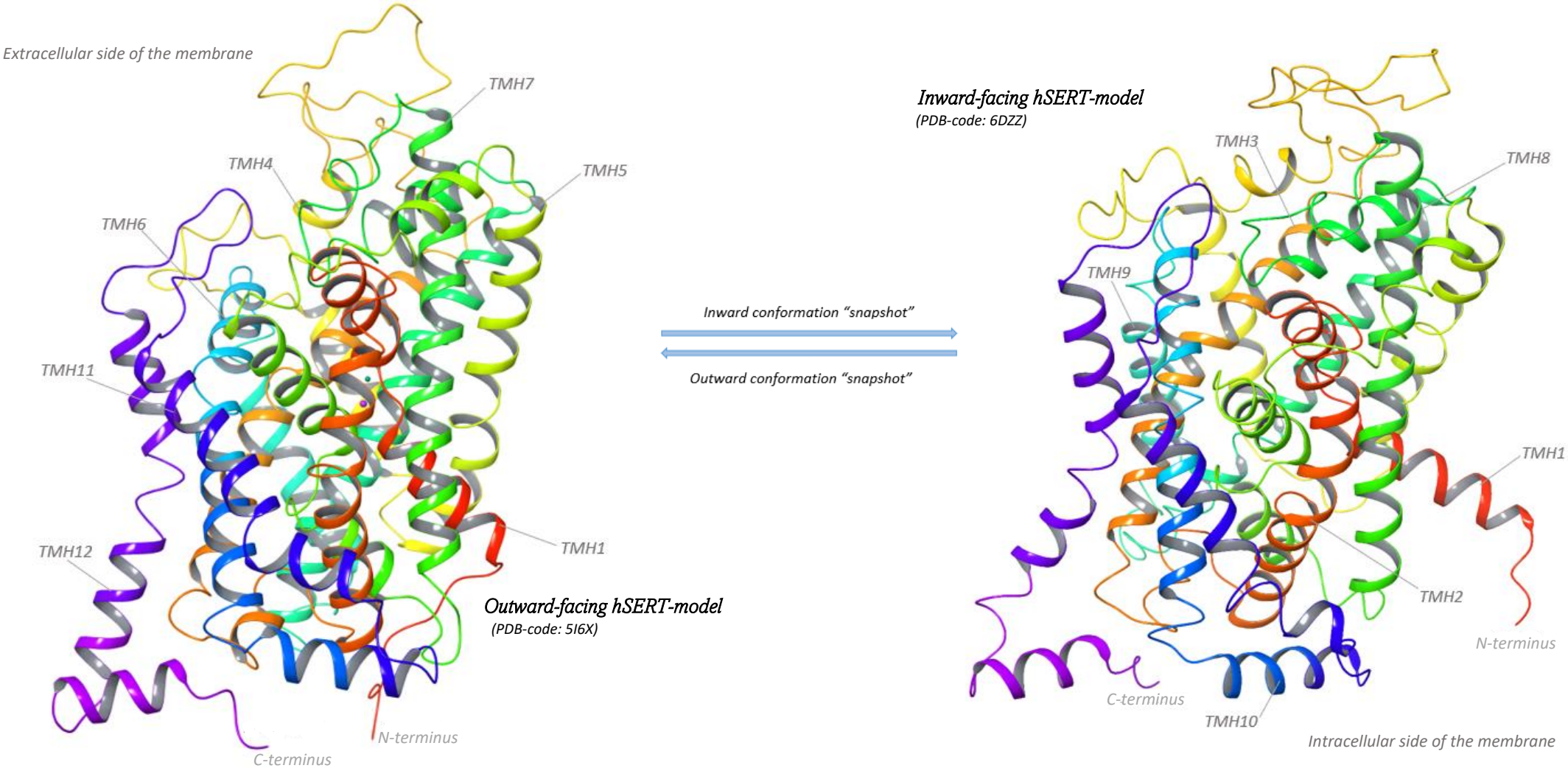

Figure 23: *3D representation of the hSERT models based on, respectively, the PDB-templates 5I6X (resolution: 3.14 Å) and 6DZZ (resolution: 3.60 Å) for comparison of the hSERT-conformation upon binding to a typical inhibitor (here: paroxetine) and atypical inhibitor (here: ibogaine). The ligands are not displayed in this illustration. In the 5I6X-based model, the sodium ion is colored purple, while the chloride ion is colored sea green. Each TMH has the same color code in both structures.*

4.2 Induced fit docking calculations

As described in earlier chapters, the IFD procedures confer flexibility to the sidechains in the MATs, as well as the ligands are allowed to adapt into the binding pocket by inducing conformational changes into the target transporter protein. Hence, intermolecular interactions between the ligand and S1-site can occur and be observed (118).

In this study, all 23 ligands were docket into the S1- site of each MAT-model by induced fitting. The intrinsic activity of each ligand (i.e., if the substance act as an inhibitor or substrate), and data on the potency of the ligands towards each MAT are summarized in table 4. Included in the table are the DAT/SERT- and DAT/NET-ratios, showing the ligands selectivity and preference towards DAT, SERT, and NET. In addition, the best IFD-scores (kcal/mol) from the docking studies, and the stereochemistry of the ligand in these complexes are profiled in table 5-8.

In general, the docking score represent the binding free energy. Hence, poses with greater negative magnitude of free energy are considered as the most stable protein-ligand complexes. Based on this, it can be stated that lower scores correspond to "tighter" and more energetically favorable interactions between a ligand and the protein (118, 170, 171, 172).

Moreover, two different measurements were applied to describe the relative potency of the included ligands toward each MAT. In the literature, the potency of the psychostimulants is usually given as the half maximal inhibitory concentration (IC_{50}), while antidepressants and the other included substances (i.e., the non-stimulant atomoxetine, antidepressants, and research standards) are given by the K_i.

Both IC_{50} and K_i are used to compare the relative potency of substances. As a general rule, smaller values indicate that a lower concentration of the specific substance is needed to execute its effect on the target, meaning that the potency is greater. However, there is a difference in these two measurements: while K_i is a constant value for a given substance (i.e., independent of the concentration of the substance), IC_{50} is a relative value (i.e., the value depends on the concentration of the substance used in the assay) (173).

Therefore, IC_{50} gives information about a substance's potency, by providing a measurement of how much of the substance that is required to inhibit a biological process by half. Implying that lower IC_{50} indicates that lower concentrations of the ligand are needed to inhibit the

function of its target with 50 % (174). Four different studies (175, 176, 177, 178, 179), all contributed by some of the same authors (Liechti M.E and Hoener M.C et.al.), were the basis for the IC_{50}-values given in table 4. In all the studies the measurements of the monoamine uptake transport inhibition were, superior, assessed in the human embryonic kidney 293 that expressed the human MATs. The methods were performed according to two previous studies by Tatsumi et.al., 1997 (180) and Hysek et.al., 2012 (181) – making the data more homogenous. On the contrary, IC_{50} for the atypical inhibitor ibogaine was obtained from Bhat et.al (182) .This study was also performed in the human embryonic kidney 293 expressing hSERT and hDAT, but the method used to determine IC_{50} differed from the four studies used for the other included substances. For information, the 95 % confidence intervals of the measurements are not included in table 4.

The inhibition constant (K_i), on the other hand, is reflective of the binding affinity. Meaning that lower K_i indicates a greater ability for a ligand to bind its target, besides that lower concentrations of the ligand are required to exert the desired effect (173, 183). The K_i-values provided in table 4 were retrieved from the PDSP-database. (144). However, some of the values are from other species than humans (marked with an asterisk). For these exceptions, the K_i (nM) based human MATs are additionally listed in the table for comparison. The latter data were retrieved from the following review article by Torres G.E et.al. (184).

Table 4: *Intrinsic activity, affinity data, and IFD-scores of the included ligands in this study. Included in the table is the DAT/SERT- and DAT/NET ratios.*

Ligand	**Intrinsic property**	**DAT** IC_{50} *(μM)* ***Ki*** *(nM)*	**SERT** IC_{50} *(μM)* ***Ki*** *(nM)*	**NET** IC_{50} *(μM)* ***Ki*** *(nM)*	**DAT/SERT**	**DAT/NET**	**Source of affinity data** *(IC_{50} and K_i)*
DA	Substrate	67-1770 nM	1000 nM*	323 nM	0.56-15*	0.18-4.8*	PDSP
NE	Substrate	8500-10000 nM	1000 nM*	63.9 nM*	0.10-0.12*	0.0064-0.0075*	PDSP
5-HT	Substrate	10000 nM	180-552.2 nM*	3013-10000 nM*	0.018-0.055*	0.30-1.0*	PDSP
Amphetamine	Substrate	1.3 μM	45 μM	0.07 μM	35	0.054	(175)
Methamphetamine	Substrate	1.1 μM	18 μM	0.14 μM	16	0.13	(175)
Cocaine	Typical inhibitor	0.768 μM	2.37 μM	0.451 μM	3.1	0.59	(176)
Mephedrone	Substrate	3.31 μM	4.64 μM	0.254 μM	1.4	0.077	(176)
α-PVP	Typical inhibitor	0.04 μM	>100 μM	0.02 μM	~2500	0.50	(175)
PMMA	Typical inhibitor	49 μM	1.77 μM	1.2 μM	0.036	0.024	(177)
MMAI	Substrate	193 μM	0.68 μM	3.6 μM	0.0035	0.019	(179)
MDMA	Substrate	17 μM	1.36 μM	0.45 μM	0.080	0.026	(177)
MDPV	Typical inhibitor	0.05 μM	9.6 μM	0.04 μM	192	0.80	(175)
Methylphenidate	Typical inhibitor	0.13 μM	274 μM	0.12 μM	2107	0.92	(178)
Atomoxetine	Typical inhibitor	1451 nM	77 nM	5.0 nM	0.053	0.0034	PDSP
Mazindol	Typical inhibitor	15.4-60 nM	49.3-272 nM*	0.46-1.93 nM	3.2-4.5*	0.030-0.032	PDSP
		27.6 nM	153 nM	3.2 nM	5.5	0.12	(184)
Paroxetine	Typical inhibitor	268- 963 nM	0.06-0.83 nM	40-328 nM	0.00022-0.00086	0.15-0.34	PDSP
Nisoxetine	Typical inhibitor	334-560 nM*	610 nM*	0.46-3.4 nM*	1.09-1.83*	0.0061-0.0014*	PDSP
		477 nM	383 nM	5.1 nM	0.80	0.012	(184)
Citalopram	Typical inhibitor	>10000 nM	1.13-19 nM	4070- >10000nM	~0.00011-0.0019	~0.41-1.0	PDSP

Clomipramine	Typical inhibitor	2190-3020 nM	0.14-0.28 nM	38-53.7 nM	$6.4 \cdot 10^{-5}$-$9.3 \cdot 10^{-5}$	0.017-0.018	PDSP
β-CFT	Typical inhibitor	26.1 nM	127 nM	31.9 nM	4.9	1.2	(184)
Vanoxerine	Atypical inhibitor	-	-	-			
Ibogaine	Atypical inhibitor	22.1 μM	8.2 μM	-	0.37		(182)
JHW 007 (Axial tNH)	Atypical inhibitor	-	-	-			
JHW 007 (Equatorial tNH)	Atypical inhibitor	-	-	-			

For IC_{50}, the 95 % confidence intervals are not stated in the table. The source for the given values is, however, linked to the right in the table.
PDSP K_i -intervals represent values from different sources, stated by the PDSD K_i.
PDSD K_i-values based on other species than human is marked with an asterisk (*). DA bound to SERT: rat brain. 5-HT bound to SERT: rat brain. NE bound to SERT: rat brain. NE bound to NET: whole brain except for cerebellum in rats. 5-HT bound to NET: whole brain except for cerebellum in rats. Nisoxetine bound to DAT = range in striatum in rats. Nisoxetine bound to SERT = rat brain. Nisoxetine bound to NET = range given from forebrain (lowest value) to temporal cortex (highest value) in rats. Mazindol bound to SERT = range given from frontal cortex (lowest value) to the whole brain (except for the cerebellum) (highest value) in rats. For some of these exceptions, the available K_i -values based human MATs (retrieved from (184) are additionally listed in the table for comparison, including the ratio calculations.
Note that the IC_{50}-values of ibogaine was determined by another method (182).
Substances where no K_i or IC_{50} was found, are marked with a hyphen (-).

In table 4, ratios >1 mean that the substance had higher selectivity for DAT than SERT in the DAT/SERT calculations, and higher selectivity for DAT in the DAT/NET calculations. The opposite applies to ratios < 1. The ratios are expressed as $1/IC_{50}$ DAT:$1/IC_{50}$ SERT and $1/IC_{50}$ DAT:$1/IC_{50}$ NET. Substances with high ratios (>10) are associated with dopaminergic effects, and high abuse potential. This classification system is according to Rudin et.al (185). The results from table 4 will be put more into context in chapter 5.2.

Table 5: *Intrinsic properties, the best IFD-score and stereochemistry of the ligands in the outward-facing hDAT based on the 4XP1 (left)- and 4XP4-template (right).*

Ligand	**Intrinsic property**	**IFD Score** *(Kcal/mol)*	**Stereochemistry in docked ligand**
DA	Substrate	-7.49	-
NE	Substrate	-8.90	R
5-HT	Substrate	-8.13	-
Amphetamine	Substrate	-8.13	R
Methamphetamine	Substrate	-7.66	R
Cocaine	Typical inhibitor	-7.68	**
Mephedrone	Substrate	-7.74	R
α-PVP	Typical inhibitor	-7.60	S
PMMA	Typical inhibitor	-7.72	R
MMAI	Substrate	-8.59	S
MDMA	Substrate	-8.33	R
MDPV	Typical inhibitor	-9.00	S
Methylphenidate	Typical inhibitor	-7.83	1: R & 2: S
Atomoxetine	Typical inhibitor	-8.55	R
Mazindol	Typical inhibitor	-10.37	R
Paroxetine	Typical inhibitor	-10.08	1: S & 2: S
Nisoxetine	Typical inhibitor	-8.68	S
Citalopram	Typical inhibitor	-10.16	R
Clomipramine	Typical inhibitor	-9.65	-
β-CFT	Typical inhibitor	-8.80	**

Ligand	**Intrinsic property**	**IFD Score** *(Kcal/mol)*	**Stereochemistry in docked ligand**
DA	Substrate	-7.22	-
NE	Substrate	-8.80	R
5-HT	Substrate	-7.51	-
Amphetamine	Substrate	-7.68	R
Methamphetamine	Substrate	-7.41	R
Cocaine	Typical inhibitor	-8.06	**
Mephedrone	Substrate	-6.89	R
α-PVP	Typical inhibitor	-7.43	S
PMMA	Typical inhibitor	-7.64	R
MMAI	Substrate	-8.55	S
MDMA	Substrate	-8.64	R
MDPV	Typical inhibitor	-8.86	S
Methylphenidate	Typical inhibitor	-7.82	1: S & 2: S
Atomoxetine	Typical inhibitor	-8.75	R
Mazindol	Typical inhibitor	-9.40	S
Paroxetine	Typical inhibitor	-10.31	1: R & 2: R
Nisoxetine	Typical inhibitor	-8.33	R
Citalopram	Typical inhibitor	-10.35	R
Clomipramine	Typical inhibitor	-10.63	-
β-CFT	Typical inhibitor	-8.71	**

Stereochemistry: Ligands with no stereocenters are marked with hyphen (-). Ligands with a predetermined configuration, as described in the methods, are marked with two asterisks (**).

Table 6: *Intrinsic properties, the best IFD- score and stereochemistry of the ligands in the outward-facing hDAT based on the 4XP6 (left)- and 4XP9-template (right).*

Ligand	**Intrinsic property**	**IFD Score** (*Kcal/mol)*	**Stereochemistry in docked ligand**
DA	Substrate	-6.93	-
NE	Substrate	-9.58	R
5-HT	Substrate	-8.23	-
Amphetamine	Substrate	-7.86	S
Methamphetamine	Substrate	-7.29	S
Cocaine	Typical inhibitor	-8.06	-
Mephedrone	Substrate	-7.55	S
α-PVP	Typical inhibitor	-8.16	R
PMMA	Typical inhibitor	-7.64	S
MMAI	Substrate	-8.57	S
MDMA	Substrate	-7.97	S
MDPV	Typical inhibitor	-9.81	R
Methylphenidate	Typical inhibitor	-7.85	1: S & 2: S
Atomoxetine	Typical inhibitor	-8.93	R
Mazindol	Typical inhibitor	-10.26	R
Paroxetine	Typical inhibitor	-10.20	1: R & 2: R
Nisoxetine	Typical inhibitor	-8.85	R
Citalopram	Typical inhibitor	-10.76	R
Clomipramine	Typical inhibitor	-11.13	-
β-CFT	Typical inhibitor	-8.63	**

Ligand	**Intrinsic property**	**IFD Score** (*Kcal/mol)*	**Stereochemistry in docked ligand**
DA	Substrate	-7.23	-
NE	Substrate	-9.80	S
5-HT	Substrate	-8.78	-
Amphetamine	Substrate	-7.75	S
Methamphetamine	Substrate	-6.98	R
Cocaine	Typical inhibitor	-7.53	*
Mephedrone	Substrate	-6.60	S
α-PVP	Typical inhibitor	-7.07	R
PMMA	Typical inhibitor	-7.29	S
MMAI	Substrate	-8.60	R
MDMA	Substrate	-7.65	S
MDPV	Typical inhibitor	-8.63	S
Methylphenidate	Typical inhibitor	-7.38	1: R & 2: S
Atomoxetine	Typical inhibitor	-7.86	S
Mazindol	Typical inhibitor	-9.54	R
Paroxetine	Typical inhibitor	-10.21	1: R & 2: S
Nisoxetine	Typical inhibitor	-8.55	S
Citalopram	Typical inhibitor	-10.27	S
Clomipramine	Typical inhibitor	-10.81	-
β-CFT	Typical inhibitor	-6.00	**

Stereochemistry: Ligands with no stereocenters are marked with hyphen (-). Ligands with a predetermined configuration, as described in the methods, are marked with two asterisks (**).

Table 7: *Intrinsic properties, the best IFD-score and stereochemistry of the ligands in the outward-facing hSERT based on the 5I6X (left)- and 5I73-template (right).*

Ligand	**Intrinsic property**	**IFD Score** (*Kcal/mol)*	**Stereochemistry in docked ligand**
DA	Substrate	-6.84	-
NE	Substrate	-8.16	R
5-HT	Substrate	-8.99	-
Amphetamine	Substrate	-7.59	S
Methamphetamine	Substrate	-7.41	R
Cocaine	Typical inhibitor	-7.58	**
Mephedrone	Substrate	-6.80	S
α-PVP	Typical inhibitor	-7.26	R
PMMA	Typical inhibitor	-7.47	R
MMAI	Substrate	-8.34	R
MDMA	Substrate	-8.28	S
MDPV	Typical inhibitor	-7.87	S
Methylphenidate	Typical inhibitor	-7.43	1: S & 2: R
Atomoxetine	Typical inhibitor	-8.96	R
Mazindol	Typical inhibitor	-10.38	R
Paroxetine	Typical inhibitor	-10.36	1: R & 2: R
Nisoxetine	Typical inhibitor	-9.02	R
Citalopram	Typical inhibitor	-10.94	R
Clomipramine	Typical inhibitor	-9.60	-
β-CFT	Typical inhibitor	-8.20	**

Ligand	**Intrinsic property**	**IFD Score** (*Kcal/mol)*	**Stereochemistry in docked ligand**
DA	Substrate	-7.32	-
NE	Substrate	-8.53	S
5-HT	Substrate	-8.60	-
Amphetamine	Substrate	-7.69	S
Methamphetamine	Substrate	-6.71	R
Cocaine	Typical inhibitor	-7.95	**
Mephedrone	Substrate	-7.18	S
α-PVP	Typical inhibitor	-7.69	S
PMMA	Typical inhibitor	-6.96	S
MMAI	Substrate	-7.95	R
MDMA	Substrate	-7.58	S
MDPV	Typical inhibitor	-7.67	S
Methylphenidate	Typical inhibitor	-6.80	1: R & 2: S
Atomoxetine	Typical inhibitor	-8.80	R
Mazindol	Typical inhibitor	-9.71	R
Paroxetine	Typical inhibitor	-10.17	1: R & 2: S
Nisoxetine	Typical inhibitor	-8.81	R
Citalopram	Typical inhibitor	-10.21	S
Clomipramine	Typical inhibitor	-10.30	-
β-CFT	Typical inhibitor	-7.32	**

Stereochemistry: Ligands with no stereocenters are marked with hyphen (-). Ligands with a predetermined configuration, as described in the methods, are marked with two asterisks (**).

Table 8: *Intrinsic properties, the best IFD- score and stereochemistry of the ligands in the outward-facing hNET based on the 4XNU-template (left), and the inward-facing hSERT based on the 6DZZ-template (right). In the right table only ligands that bind the inward-facing conformation of the MATs are shown.*

Ligand	**Intrinsic property**	**IFD Score** (*Kcal/mol)*	**Stereochemistry in docked ligand**
DA	Substrate	-7.10	-
NE	Substrate	-8.52	S
5-HT	Substrate	-7.57	-
Amphetamine	Substrate	-7.58	R
Methamphetamine	Substrate	-6.83	S
Cocaine	Typical inhibitor	-7.57	**
Mephedrone	Substrate	-6.96	S
α-PVP	Typical inhibitor	-7.00	S
PMMA	Typical inhibitor	-6.69	S
MMAI	Substrate	-8.04	R
MDMA	Substrate	-7.63	R
MDPV	Typical inhibitor	-7.61	S
Methylphenidate	Typical inhibitor	-6.53	1: S & 2: S
Atomoxetine	Typical inhibitor	-8.18	S
Mazindol	Typical inhibitor	-9.28	R
Paroxetine	Typical inhibitor	-10.39	1: S & 2: R
Nisoxetine	Typical inhibitor	-8.41	R
Citalopram	Typical inhibitor	-9.60	R
Clomipramine	Typical inhibitor	-10.32	-
β-CFT	Typical inhibitor	-7.84	**

Ligand	**Intrinsic property**	**IFD Score** (*Kcal/mol)*	**Stereochemistry in docked ligand**
DA	Substrate	-7.67	-
NE	Substrate	-8.62	R
5-HT	Substrate	-8.04	-
Vanoxerine	Atypical inhibitor	-10.83	-
JHW 007 (Axial tNH)	Atypical inhibitor	-9.80	S**
JHW 007 (Equatorial tNH)	Atypical inhibitor	-9.80	**
Ibogaine	Atypical inhibitor	-8.60	**

Stereochemistry: Ligands with no stereocenters are marked with hyphen (-). Ligands with a predetermined configuration, as described in the methods, are marked with two asterisks (**).

In general, the affinity between a ligand and protein is related to the formation of intermolecular interactions in the binding site. In this study, lower concentrations of both the measured IC_{50} and K_i denote that the given substance has higher potency to the specific MAT. Furthermore, the force field based (OPLS4) IFD-calculations contributed to calculate the docking scores based on, amongst others, the interactions in each pose generated by the IFD-application (Schrödinger release 2022-3) – see chapter 1.8.2. As a thumb rule, greater negative magnitude of the docking score resembles a more energetically stable protein-ligand complex (186).

By that, it was further of interest to choose some ligands that, according to literature and the results from table 4-8, appears to be more selective for one MAT, as well have the ability to create a stable MAT-ligand complex (i.e., in terms of potency and docking score). From there, differences in both the binding mode and formation of intermolecular interactions in the MATs could be examined. In chapter five, these results will be discussed more conforming to available literature.

Figure 24-29 reports the predicted docking poses of nisoxetine, atomoxetine, methylphenidate, MDPV, MMAI, paroxetine, and MDMA. The binding mode of the atypical inhibitors vanoxerine and ibogaine in the inward-facing hSERT are shown in figure 32. In addition, the binding mode of the non-selective typical inhibitor cocaine is included (figure 31). The ligand-MAT complexes with the best docking scores were chosen from the docking studies (table 5-8).

In each illustration, the 3D representations of the generated poses are viewed from approximately the same angle to make the complexes more comparable, with residues encircling the ligand at a 3Å distance in the S1-site. These 3D figures of the binding pocket are included for comparison of the orientation of the ligands, with respect to the surrounding residues, in each MAT. Remarkably, all the ligands placed their protonated amine near Asp in TMH1 (hNET: Asp75; hDAT: Asp79; hSERT: Asp98). The interactions are demonstrated as dashed lines, colored by type of interaction, respectively: salt-bridge (pink), hydrogen-bond (yellow), cation-pi interaction (green), and pi-pi-stacking (blue). Van der Waals (vdW) interactions exist among all atoms, both in the ligand and protein, and is not displayed in the figures. Finally, the stereochemistry of the ligands is as stated in the ligand-MAT complexes in table 5-8.

Accompanying to the figures in this section are figure S7 in the supplementary material, and table 9 in this section. Figure S7 demonstrates a multiple sequence alignment of the three human MAT-sequences from UniProtKB, dDAT (PDB-code: 4XP1), and the ts3-construct of hSERT (PDB-code: 5I6X). Differences in amino acids in the S1-site can be observed from this figure. In addition, table 9 provides an overview of conserved and divergent (also termed non-conserved) residues in each MAT. In this table, only the residues observed in figure 24-32 are shown, meaning residues within 3 Å from the ligand in the S1-site. However, a distance of 3Å was enough to observe all the occurring interactions in each ligand-MAT complex. In total, these results contribute to getting a better understanding of preference towards each MAT. The figures in this section will be described more in chapter 5.2.

In the S1-site of each model, TMH1, TMH6, and TMH8 constituted subsite A - some observed residues in this area were Asp75, Phe72, Ala73, Ser318, and Ser419 in **hNET** (**hDAT:** Asp79, Phe76, Ala77, Ser321, Ser422**; hSERT:** Asp98, Tyr95, Ala96, Ser336, Ser438). Subsite B contained TMH3 and TMH8 – some residues in this subsite were Val148, Ser420, and Gly423 in **hNET** (**hDAT**: Val152, Ala423, Gly426**; hSERT:** Ile172, Thr439, Gly442). Finally, TMH3, TMH6, and TMH10 formed subsite C – some observed residues in this subsite were Phe317, Phe323, Ala477, Gly478, and Ile481in **hNET** (**hDAT:** Phe320, Phe326, Ala480, Gly481, Ile484**; hSERT:** Phe335, Phe341, Thr497, Gly498, Val501).

Table 9: *Corresponding amino acid residues in hNET, hDAT, and hSERT belonging to the S1-site. Residues with a distance within 3 Å from the ligands illustrated in figure 24-32 are only shown. Conserved residues are demonstrated in cursive, while divergent residues are demonstrated in cursive bold (red) letters.*

Region	Position in the alignment	hNET	hDAT	hSERT
TMH1	Divergent	***Phe72***	***Phe76***	***Tyr95***
TMH1	Conserved	*Ala73*	*Ala77*	*Ala96*
TMH1	Conserved. Salt bridge.	*Asp75*	*Asp79*	*Asp98*
TMH1	Divergent	***Ala77***	***Ala81***	***Gly100***
TMH1	Conserved	*Arg81*	*Arg85*	*Arg104*
TMH1	Conserved	*Phe110*	*Phe114*	*Phe133*
TMH3	Divergent	***Val141***	***Val145***	***Ile165***
TMH3	Conserved	*Ile144*	*Ile148*	*Ile168*
TMH3	Divergent	***Ala145***	***Ser149***	***Ala169***
TMH3	Divergent	***Leu146***	***Leu150***	***Phe170***
TMH3	Divergent	***Val148***	***Val152***	***Ile172***
TMH3	Divergent	***Gly149***	***Gly153***	***Ala173***
TMH3	Divergent	***Tyr151***	***Phe155***	***Tyr175***
TMH3	Conserved	*Tyr152*	*Tyr156*	*Tyr176*
TMH3	Conserved	*Asn153*	*Asn157*	*Asn177*
TMH6	Divergent	***Phe316***	***Cys319***	***Phe334***
TMH6	Conserved	*Phe317*	*Phe320*	*Phe335*
TMH6	Conserved	*Ser318*	*Ser321*	*Ser336*
TMH6	Conserved	*Leu319*	*Leu322*	*Leu337*
TMH6	Conserved	*Gly320*	*Gly323*	*Gly338*
TMH6	Divergent	***Ala321***	***Val324***	***Pro339***
TMH6	Conserved	*Phe323*	*Phe326*	*Phe341*
TMH6	Conserved	*Val325*	*Val328*	*Val343*
TMH6	Conserved	*Leu326*	*Leu329*	*Leu344*
TMH6	Conserved	*Phe329*	*Phe332*	*Phe347*
TMH7	Conserved	*Thr346*	*Thr349*	*Thr364*
TMH8	Conserved	*Ser419*	*Ser422*	*Ser438*
TMH8	Divergent	***Ser420***	***Ala423***	***Thr439***
TMH8	Divergent	***Gly422***	***Gly425***	***Ala441***
TMH8	Conserved	*Gly423*	*Gly426*	*Gly442*
TMH8	Divergent	***Met424***	***Met427***	***Leu443***
TMH10	Divergent	***Ala477***	***Ala480***	***Thr497***

TMH10	Conserved	*Gly478*	*Gly481*	*Gly498*
TMH10	Divergent	***Ile481***	***Ile484***	***Val501***
TMH10	Conserved	*Leu482*	*Leu485*	*Leu502*

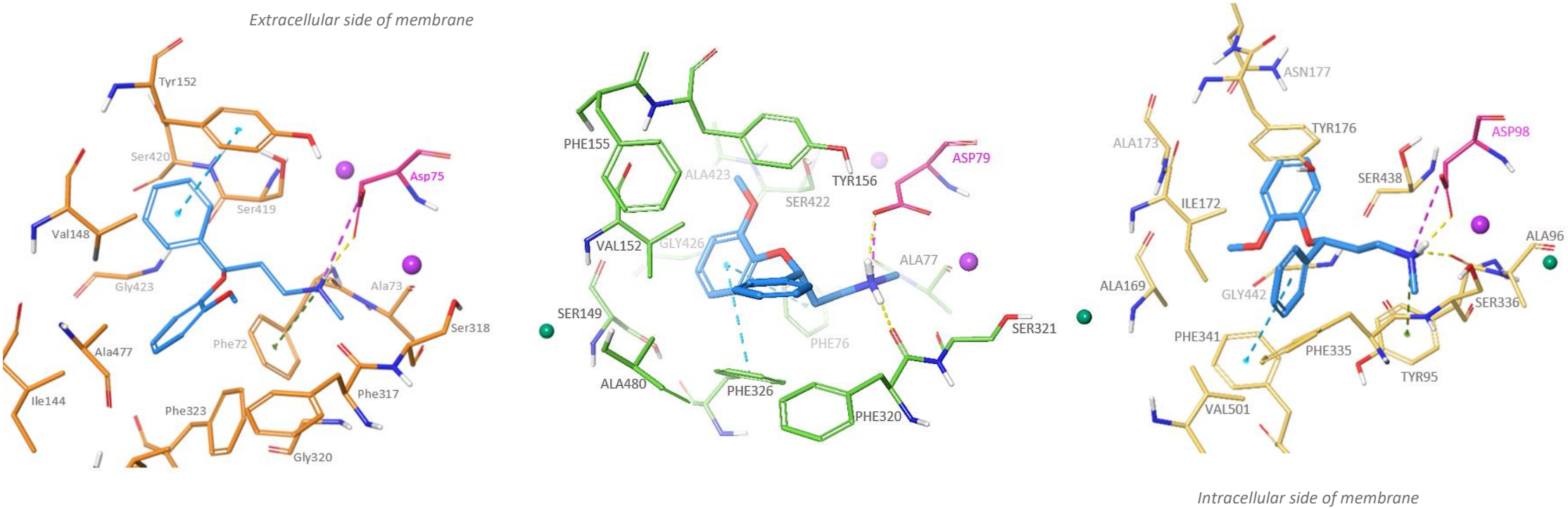

Figure 24: *3D overview of the intermolecular interactions between nisoxetine (blue) and the residues (3Å from ligand) in the S1-site of hNET (orange) based on 4XNU, hDAT (green) based on 4XP6, and hSERT (yellow) based on 5I6X. The poses with the best IFD-score are illustrated: -8.41 kcal/mol (nisoxetine-hNET); -8.85 kcal/mol (nisoxetine-hDAT); and -9.02 kcal/mol (nisoxetine-hSERT). Nisoxetine is defined as an sNRI (typical inhibitor of NET) with a high potency for NET, K_i = 0.46 – 3.4 nM in rats (range given from the forebrain to temporal cortex) and 5.1 nM in humans. For comparison K_i (DAT) is 334-560 nM in rat-striatum (PDSP) and 477 nM in humans, while K_i (SERT) is 610 nM in the rat-brain and 383 nM in humans (see table 4). Note that a cation-π interactions with Phe76 also was created between nisoxetine and hDAT, but is difficult to see in the figure.*

In the figure, sodium ions are colored purple, while chloride is sea green. The interactions are displayed as dashed lines, colored by type of interaction: salt-bridge (pink), hydrogen-bond (yellow), cation-pi interaction (green), and pi-pi-stacking (blue). Van der Waals (vdW) interactions exist among all atoms and are not displayed in the figure.

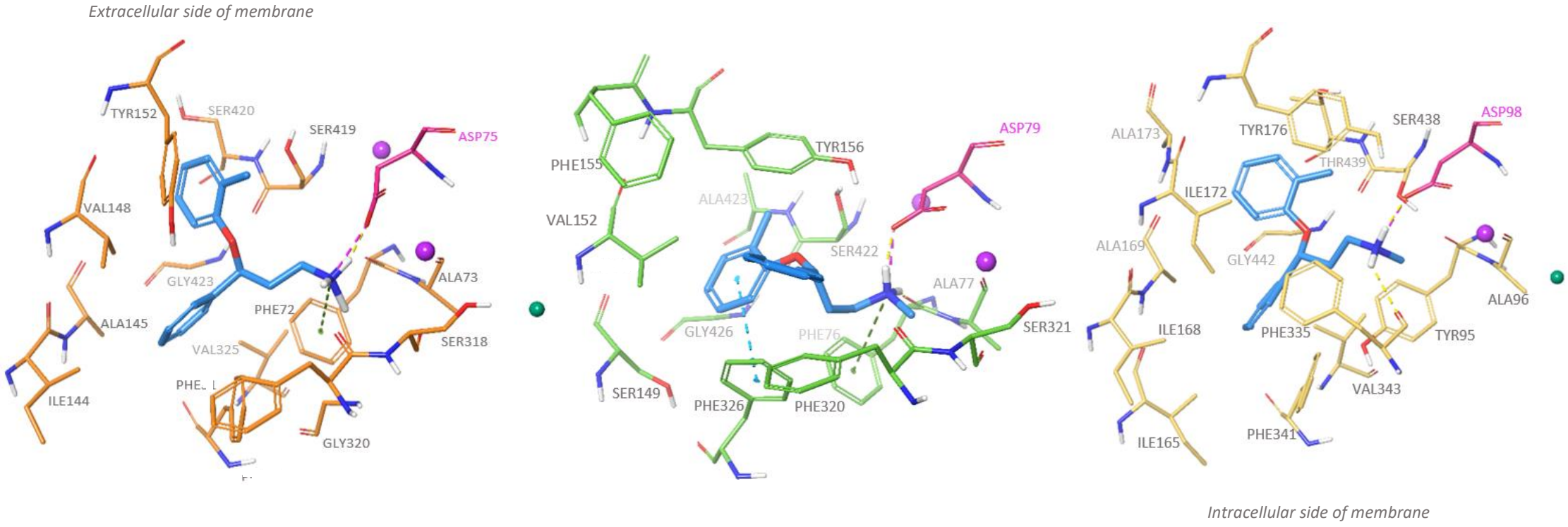

Figure 25: *3D overview of the intermolecular interactions between atomoxetine (blue) and the residues (3Å from ligand) in the S1-site of hNET (orange) based on 4XNU, hDAT (green) based on 4XP6, and hSERT (yellow) based on 5I6X. The poses with the best IFD-score are illustrated: -8.18 kcal/mol (atomoxetine-hNET); -8.93 kcal/mol (atomoxetine-hDAT); and -8.96 kcal/mol (atomoxetine-hSERT). Atomoxetine is a therapeutic non-stimulant, sNRI (typical inhibitor of NET), with a high potency for NET: K_i = 5.0 nM. For comparison K_i (DAT) is 1451 nM, while K_i (SERT) is 77 nM (see table 4).*

In the figure, sodium ions are colored purple, while chloride is sea green. The interactions are displayed as dashed lines, colored by type of interaction: salt-bridge (pink), hydrogen-bond (yellow), cation-pi interaction (green), and pi-pi-stacking (blue). Van der Waals (vdW) interactions exist among all atoms and are not displayed in the figure.

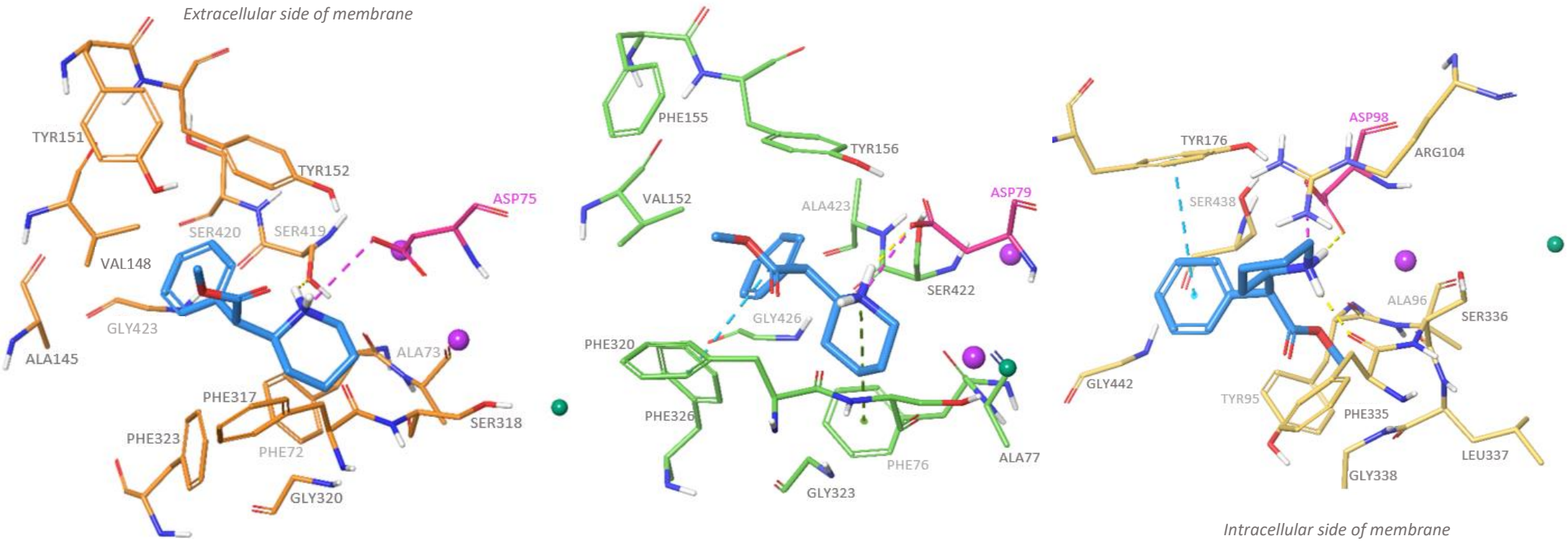

Figure 27: *3D overview of the intermolecular interactions between methylphenidate (blue) and the residues (3Å from ligand) in the S1-site of hNET (orange) based on 4XNU, hDAT (green) based on 4XP1, and hSERT (yellow) based on 5I6X. The poses with the best IFD-score are illustrated: -6.53 kcal/mol (methylphenidate-hNET); -7.83 kcal/mol (methylphenidate-hDAT); and -7.43 kcal/mol (methylphenidate-hSERT). Methylphenidate is a therapeutic psychostimulant with high potency (act as a typical inhibitor) for DAT and NET: IC_{50} (DAT) = 0.13 μM and IC_{50} (NET)= 0.12 μM. For comparison IC_{50} (SERT) is 274 μM (see table 4).*

In the figure, sodium ions are colored purple, while chloride is sea green. The interactions are displayed as dashed lines, colored by type of interaction: salt-bridge (pink), hydrogen-bond (yellow), cation-pi interaction (green), and pi-pi-stacking (blue). Van der Waals (vdW) interactions exist among all atoms and are not displayed in the figure.

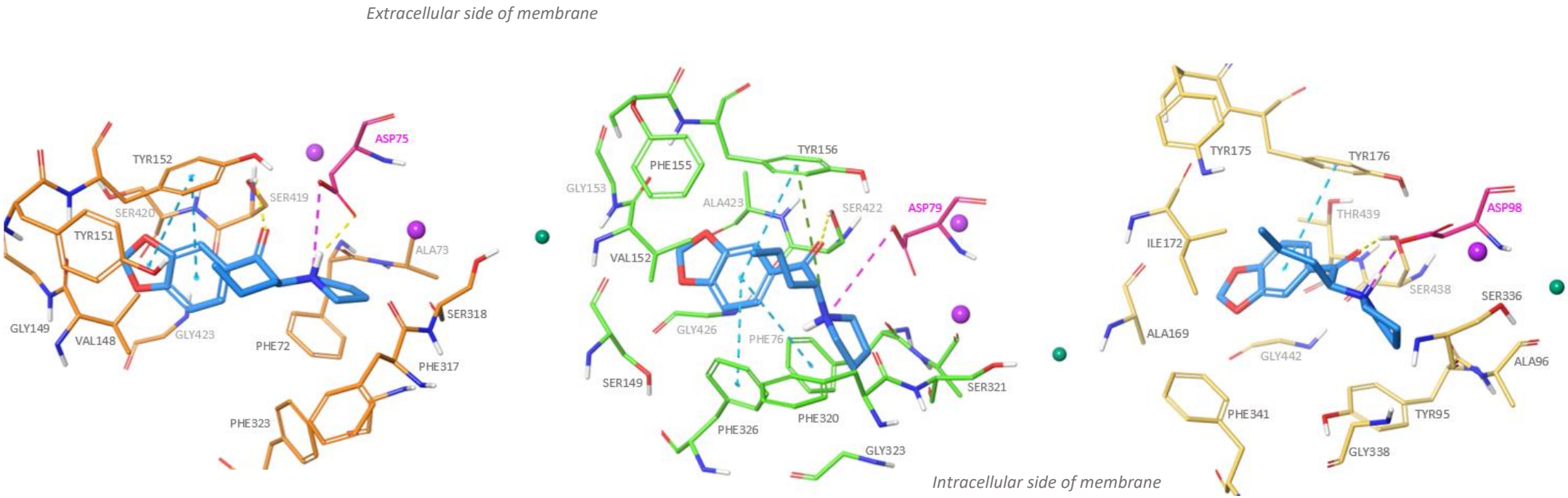

Figure 27: *3D overview of the intermolecular interactions between MDPV (blue) and the residues (3Å from ligand) in the S1-site of hNET (orange) based on 4XNU, hDAT (green) based on 4XP6, and hSERT (yellow) based on 5I6X. The poses with the best IFD-score are illustrated: -7.61 kcal/mol (MDPV-hNET); -9.81 kcal/mol (MDPV-hDAT); and -7.87 kcal/mol (MDPV-hSERT). MDPV is an NPS with especially high potency (act as a typical inhibitor) for DAT and NET: IC_{50} (DAT) = 0.05 μM and IC_{50} (NET)= 0.04 μM, compared to SERT where the potency is IC_{50} = 9.6 μM (see table 4).*

In the figure, sodium ions are colored purple, while chloride is sea green. The interactions are displayed as dashed lines, colored by type of interaction: salt-bridge (pink), hydrogen-bond (yellow), cation-pi interaction (green), and pi-pi-stacking (blue). Van der Waals (vdW) interactions exist among all atoms and are not displayed in the figure.

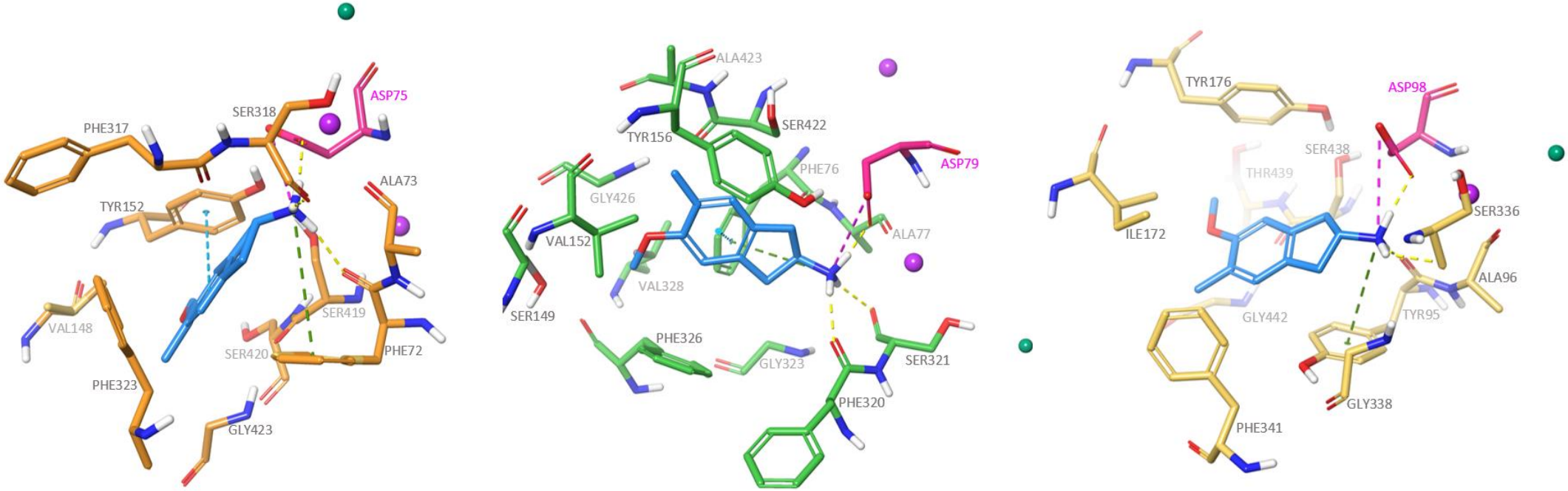

Figure 28: *3D overview of the intermolecular interactions between MMAI (blue) and the residues (3Å from ligand) in the S1-site of hNET (orange) based on 4XNU, hDAT (green) based on 4XP9, and hSERT (yellow) based on 5I6X. The poses with the best IFD-score are illustrated: -8.04 kcal/mol (MMAI-hNET); -8.60 kcal/mol (MMAI-hDAT); and -8.34 kcal/mol (MMAI-hSERT). MMAI is a research standard, with especially high potency (act as a substrate) for SERT: IC_{50} (SERT) = 0.68 μM. For comparison the IC_{50} (DAT) = 193 μM and IC_{50} (NET)= 3.6 μM.*

In the figure, sodium ions are colored purple, while chloride is sea green. The interactions are displayed as dashed lines, colored by type of interaction: salt-bridge (pink), hydrogen-bond (yellow), cation-pi interaction (green), and pi-pi-stacking (blue). Van der Waals (vdW) interactions exist among all atoms and are not displayed in the figure.

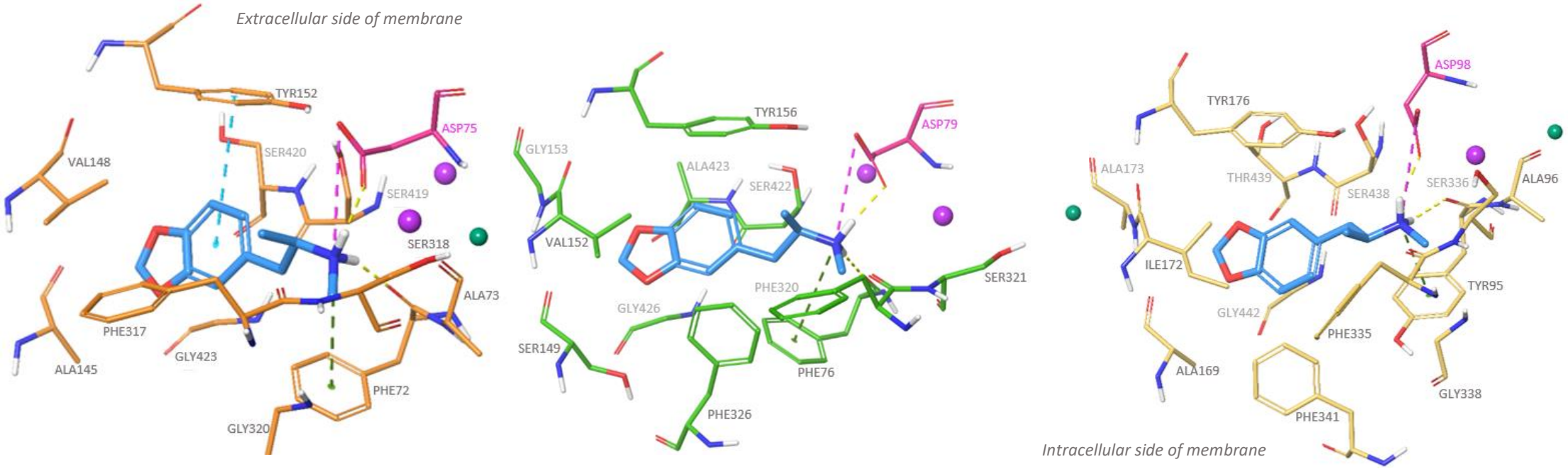

Figure 29: *3D overview of the intermolecular interactions between MDMA (blue) and the residues (3Å from ligand) in the S1-site of hNET (orange) based on 4XNU, hDAT (green) based on 4XP4, and hSERT (yellow) based on 5I6X. The poses with the best IFD-score are illustrated: -7.63 kcal/mol (MDMA-hNET); -8.64 kcal/mol (MDMA-hDAT); and -8.28 kcal/mol (MDMA-hSERT). MDMA is a traditional illicit stimulant with high potency (act as a substrate) for SERT and NET: IC_{50} (SERT) = 1.36 μM and IC_{50} (NET)= 0.45 μM. For comparison the IC_{50} (DAT) = 17 μM (see table 4).*

In the figure, sodium ions are colored purple, while chloride is sea green. The interactions are displayed as dashed lines, colored by type of interaction: salt-bridge (pink), hydrogen-bond (yellow), cation-pi interaction (green), and pi-pi-stacking (blue). Van der Waals (vdW) interactions exist among all atoms and are not displayed in the figure.

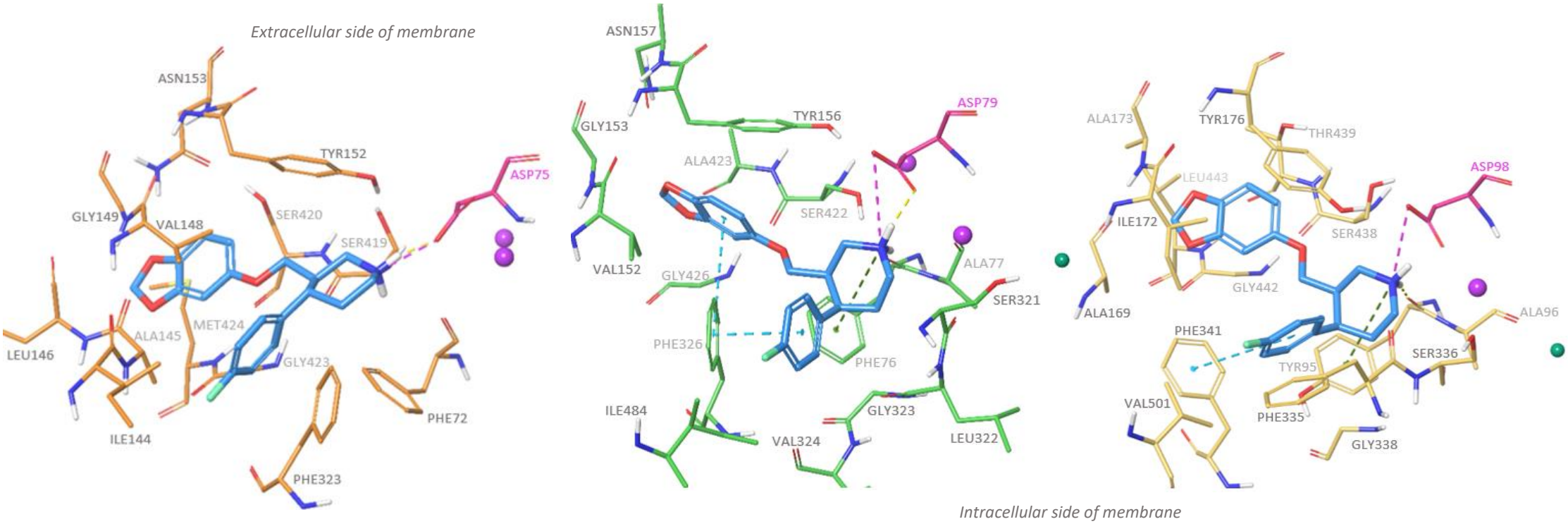

Figure 30: *3D overview of the intermolecular interactions between paroxetine (blue) and the residues (3Å from ligand) in the S1-site of hNET (orange) based on 4XNU, hDAT (green) based on 4XP4, and hSERT (yellow) based on 5I6X. The poses with the best IFD-score are illustrated: -10.39 kcal/mol (paroxetine-hNET); -10.31 kcal/mol (paroxetine-hDAT); and -10.36 kcal/mol (paroxetine-hSERT). Paroxetine is an antidepressant (SSRI) with high potency (act as a typical inhibitor) for SERT: K_i (SERT)= 0.06-0.83 nM. For comparison Ki (DAT) =268-963 nM and Ki (NET)= 40-328 nM (see table 4).*

In the figure, sodium ions are colored purple, while chloride is sea green. The chloride ion in hNET is cropped out from the figure for a better view of the binding site residues. The interactions are displayed as dashed lines, colored by type of interaction: salt-bridge (pink), hydrogen-bond (yellow), cation-pi interaction (green), and pi-pi-stacking (blue). Van der Waals (vdW) interactions exist among all atoms and are not displayed in the figure.

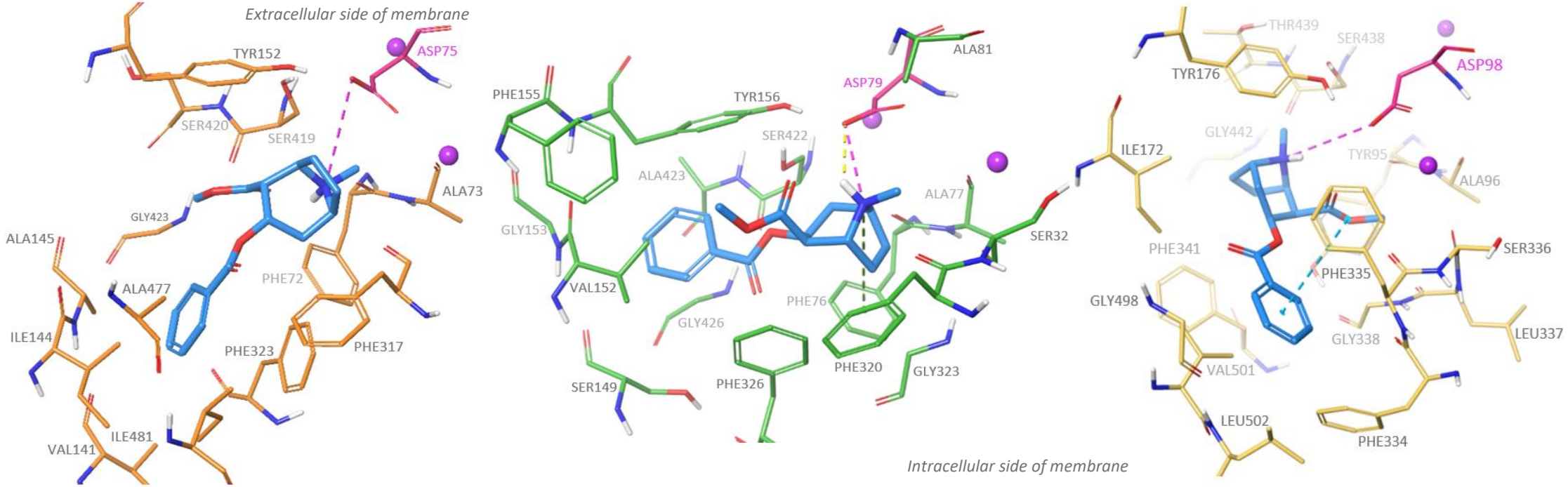

Figure 31: *3D overview of the intermolecular interactions between cocaine (blue) and the residues (3Å from ligand) in the S1-site of hNET (orange) based on 4XNU, hDAT (green) based on 4XP4, and hSERT (yellow) based on 5I73. The poses with the best IFD-score are illustrated: -7.57 kcal/mol (cocaine-hNET); -8.06 kcal/mol (cocaine-hDAT); and -7.95 kcal/mol (cocaine-hSERT). Cocaine is a non-selective traditional illicit psychostimulant, with relatively high potency for all the MATs (acting as a typical inhibitor): IC_{50} (DAT) = 0.768 μM; IC_{50} (SERT)=2.37 μM; and IC_{50} (NET)= 0.451 μM (see table 4).*

In the figure, sodium ions are colored purple, while chloride is sea green. The chloride ion in hNET and hDAT is cropped out from the figure for a better view of the binding site residues. The interactions are displayed as dashed lines, colored by type of interaction: salt-bridge (pink), hydrogen-bond (yellow), cation-pi interaction (green), and pi-pi-stacking (blue). Van der Waals (vdW) interactions exist among all atoms and are not displayed in the figure.

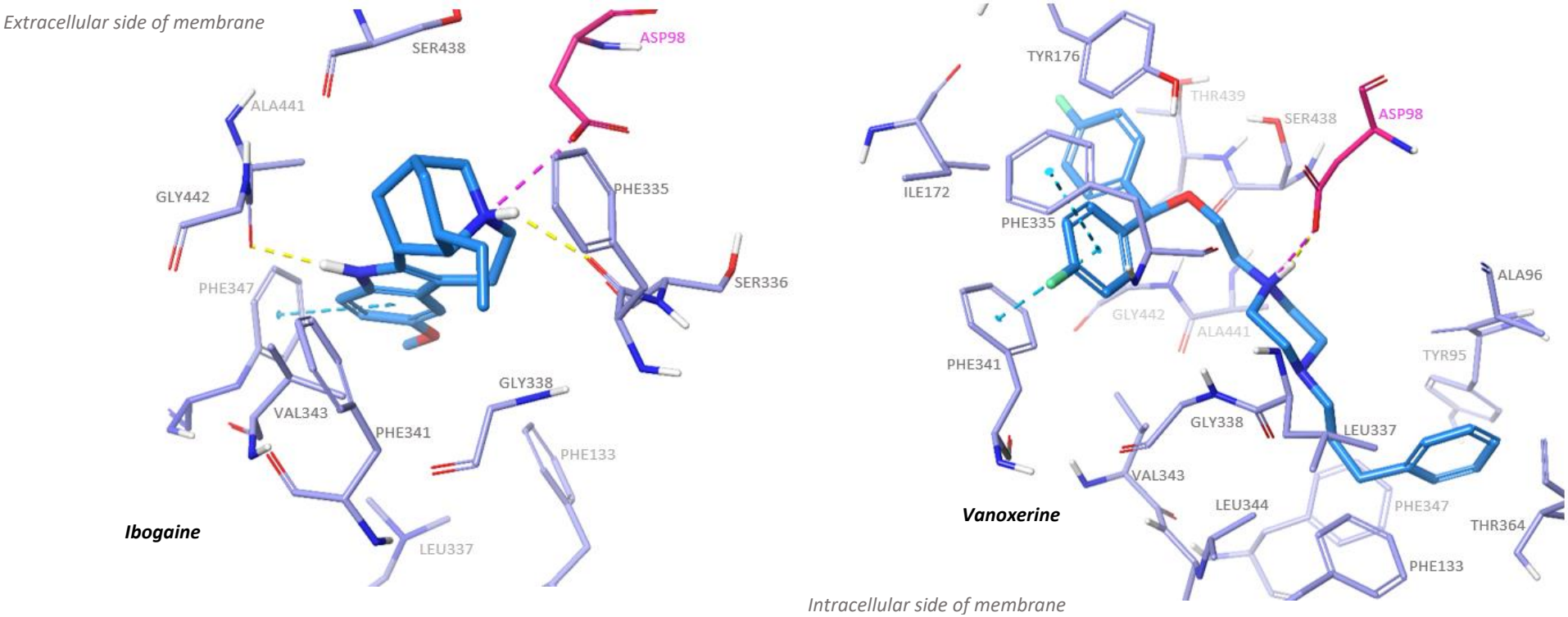

Figure 32: *3D overview of the intermolecular interactions between, respectively, ibogaine (blue, to the left) and vanoxerine (blue, to the right), and the residues (3Å from ligand) in the S1-site of the inward-facing hSERT (light purple) based on the 6DZZ-template from PDB. There were no ions in the 6DZZ-template, therefore no ions are shown in the model-figures. The interactions are displayed as dashed lines, colored by type of interaction: salt-bridge (pink), hydrogen-bond (yellow), cation-pi interaction (green), and pi-pi-stacking (blue). Van der Waals (vdW) interactions exist among all atoms and are not displayed in the figure.*

Both ibogaine and vanoxerine are considered atypical inhibitors: ibogaine is an atypical SERT-inhibitor (83), while, vanoxerine is an atypical DAT-inhibitor (97, 187). The poses with the best IFD-score are illustrated in the figure: -8.60 kcal/mol (ibogaine-hSERT) and -10.83 kcal/mol (vanoxerine-hSERT). Ibogaine have relatively high potency for SERT (IC_{50} = 8.2 µM), and moderate for DAT (IC_{50} = 22.1 µM). No data on the potency of vanoxerine towards each MATs were found during this project (see table 4).

4.3 Molecular dynamics simulations

Five all-atom MD simulations were performed to further evaluate the dynamics during the stabilization and creation of intermolecular interactions upon binding to the MATs.

The following five systems were studied: “nisoxetine in complex with the outward-facing hNET (model based on the PDB-structure 4XNU)”, “methylphenidate in complex with the outward-facing hDAT (model based on the PDB-structure 4XP4)”, “MDMA in complex with the outward-facing hSERT (model based on the PDB-structure 5I6X)”, “vanoxerine in complex with the inward-facing hSERT (model based on the PDB-structure 6DZZ)”, in addition, “vanoxerine in complex with the outward-facing hSERT (model based on the PDB-structure 5I6X)” was studied. The latter system was created to compare the binding mode of vanoxerine in the outward-and inward- facing conformation of hSERT, to further explore determinants for selective binding to a particular conformation of SERT.

4.3.1 Stability analysis of the ligand-protein complexes

The stability of a protein and ligand during an MD simulation is relative to the conformational deviations established throughout the trajectories. To indicate the stability of the five complexes, RMSD was measured for both the ligands and MATs all over the simulations. The root mean square fluctuations (RMSF) was also calculated for the transporters only. Both the RMSD- and RMSF values, based on the alpha-carbons (C_α), were retrieved from the *Simulation Interactions Diagram panel* in Maestro (Schrödinger release 2022-3).

Protein (based on C_α) RMSD measures the average differences in the displacement of the alpha-carbons for a given frame relative to the initial reference frame. Ligand RMSD, however, measures how stable a ligand is with respect to the protein (and its binding pocket). Moreover, the RMSF reflects the fluctuations and changes in local areas of a protein during a simulation. As a thumb rule, smaller deviations and less fluctuation indicate more stability: values of the order 1-3 Å are “acceptable” for a system that has reached equilibrium (122).

4.3.2.1 Root mean square deviation (RMSD) plots

The plots below, figure 33 and 34, display the evolution of the RMSD of the MATs (left Y-axis, blue graphs) and ligands (right Y-axis, violet) throughout the 100 ns long simulation for each of the five MD systems, with respect to the conformation in the reference frame. Moreover, the Protein RMSD is calculated based on the MATs carbon-alpha (Cα) backbone, while the Ligand RSMD is determined based on the ligand heavy atoms. Considering the Protein RMSD, significantly higher values of the Ligand RMSD imply that the ligand has diffused from its initial location in the S1-pocket.

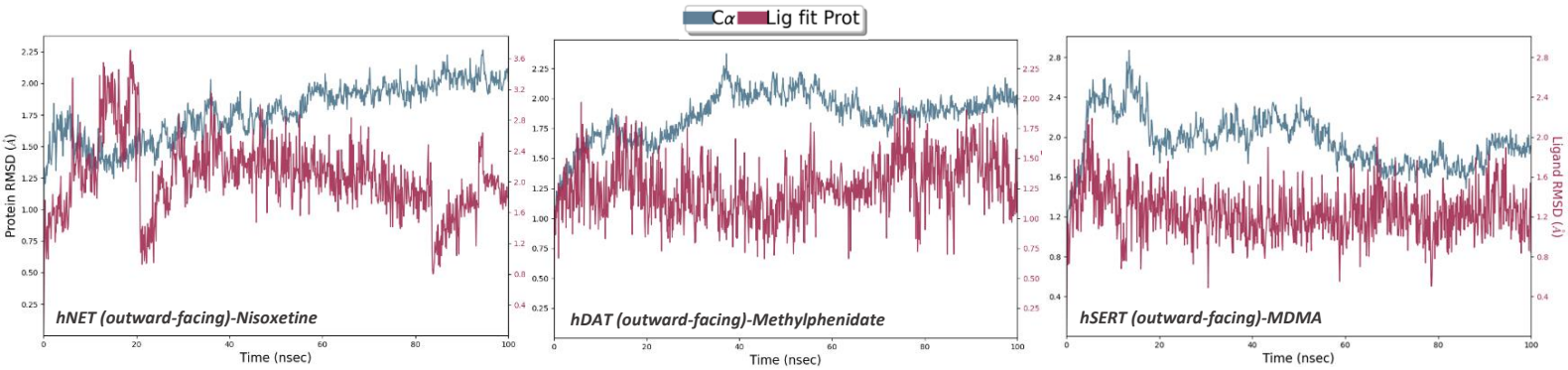

Figure 33: *RMSD analysis of the MD simulation trajectory. From the left: RMSD plot of hNET (model based on the PDB-template 4XNU)-nisoxetine complex, hDAT (model based on the PDB-template 4XP4)-methylphenidate complex, and hSERT (based on the PDB-template 5I6X)- MDMA complex. The MAT-RMSD (blue graphs) is calculated based on the Cα, with respect to the reference frame. The Ligand RMSD (violet graphs) is calculated based on the ligand heavy atoms, concerning the protein ("Lig fit Prot") and the initial position of the ligand.*

The RMSD of hNET profiled an increasing tendency from the beginning of the simulation, with an exception in the period from 5.80 ns to 14.90 ns. The highest peak was reached 94.70 ns into the simulation, where the RMSD equaled 2.16 Å. hNET attained a stable conformation after approximately 56.90 ns, where the mean RMSD was 1.90 Å. Nisoxetine, on the other hand, displayed a rise in the RMSD from already frame 1. The climax was reached at RMSD 3.71 Å (18.70 ns from onset), while the first great deviation from the initial conformation of nisoxetine concerning the S1-pocket happened after 6.20 ns (RMSD 3.30 Å). At this time, it seemed like nisoxetine slightly diffused from its initial position in the S1-pocket. Interestingly, the RMSD fell to 1.38 Å after 21.10 ns before attaining a mean value around RMSD 2.28 Å from 32.20 ns to 83.40 ns. However, this "cycle" was interrupted from about 83.80 ns (RMSD 0.80 Å) towards the end of the simulation. The simulation was not long enough to observe the reach of the "real" equilibrium of the nisoxetine.

The hDAT similarly profiled a rising trend in the RMSD throughout the trajectories, when bound to methylphenidate. The peak RMSD (2.37 Å) was achieved around 37.20 ns before the protein emerged at the equilibrium around 1.92 Å - and persisted throughout the run time. The highest value in this period was 2.17 Å (at 47.30 ns). Though, there was a slight decrease in RMSD between 14.20 (RMSD 1.66 Å) ns to 22.20 ns (RMSD 1.58 Å). Moreover, methylphenidate outlined a relatively stable conformation throughout the simulation, where the RMSD fluctuated around 1.30 Å from start to end. Overall, the ligand seemed to stay in the same position in the binding pocket during the whole simulation.

The outward-facing hSERT bound to MDMA reached the highest RMSD at 2.71 Å (13.70 ns from onset). The protein was already stabilized around 17.90 ns into the simulation, and the RMSD fluctuated around 1.97 Å at equilibrium during the trajectories. The highest value in this interval was 2.29 Å (at 50.60 ns). MDMA was distinctly stable throughout the trajectories, where the equilibrium appeared to be attained around 0.20 ns to 0.30 ns into the simulation (average RMSD around 1.20 Å). The supreme value was RMSD 1.84 Å (5.40 ns) in the stable state, meaning that MDMA was positioned in the same place for the entire 100 ns.

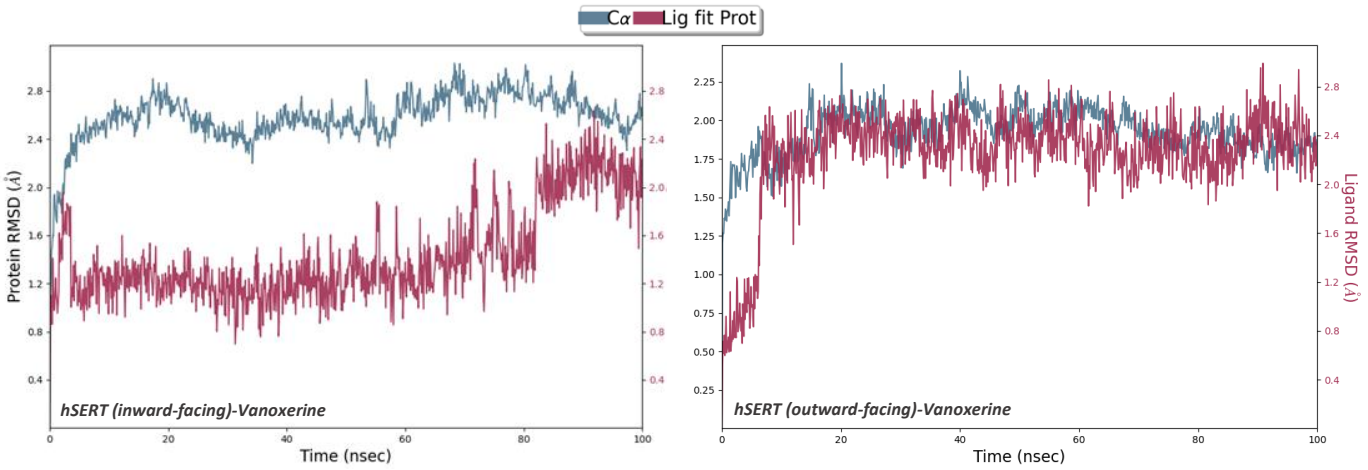

Figure 34: *RMSD analysis of the MD simulation trajectory. The MAT-RMSD (blue graphs) is calculated based on the Cα, with respect to the reference frame. The Ligand-RMSD (violet graphs) is calculated based on the ligand heavy atoms, concerning the protein ("Lig fit Prot") and the initial position of the ligand. To the left: RMSD plot of hSERT (model based on the the PDB-template 6DZZ)-vanoxerine complex. To the right: hSERT (model based on PDB-template 5I6X)- vanoxerine complex.*

The inward-facing hSERT appeared to be stable during the entire course of the simulation. Approximately 3.80 ns from the onset the RMSD oscillated around 2.58 Å. In this interval, the highest value was 3.03 Å (68.30 ns into the simulation). Vanoxerine also happened to be stable during the first 82.00 ns of the simulation (mean RMSD 1.22 Å), with a peak at RSMD 2.23 Å (at 71.80 ns). After 82.00 ns, vanoxerine was slightly further displaced compared to

the reference structure. The RMSD fluctuated therefore around 2.1 Å from that time to the end of the simulation. However, the Ligand RMSD was in general lower than the Protein RMSD, meaning that vanoxerine mainly kept the same position in the S1-pocket throughout the simulation.

Finally, in the last system both the outward-facing hSERT and vanoxerine were fairly stable during the simulation.

Contrasting the inward-facing conformation of hSERT, the RMSD fluctuated at a lower value for this system (around 1.78 Å). By that, the outward-facing conformation bound to vanoxerine underwent less conformational changes during the simulation - compared to the inward-facing hSERT. The highest RMSD (2.27 Å) was reached 20.10 ns from the onset. Vanoxerine, however, stabilized after around 6.70 ns (mean RMSD 2.4 Å). During the equilibrium, the peak RMSD (2.99 Å) was reached 90.90 ns toward the simulation's end. Like the other systems, the Ligand RMSD was not significantly higher than the Protein RMSD, meaning that vanoxerine was positioned in the same location in the S1-pocket during the whole course of the simulation.

4.3.2.2 Root mean square fluctuation (RMSF) plots

The flexibility of the individual amino acid residues is assessed in the Protein RMSF plots below (figure 35 and 36). These plots point to parts of the MATs that may contribute to the molecular motion of the systems, and indicate areas of the MATs that are more mobile upon binding. Highlighted as green vertical bars are the residues that interact and "enclose" the ligands, implying the stability of these residues during the course of the simulation. The secondary structure elements are also outlined, where helices, β-sheets, and loop areas are shown in a salmon red-, blue- and white color, respectively. Generally, loops are more structurally flexible than helices and β-sheets (188).

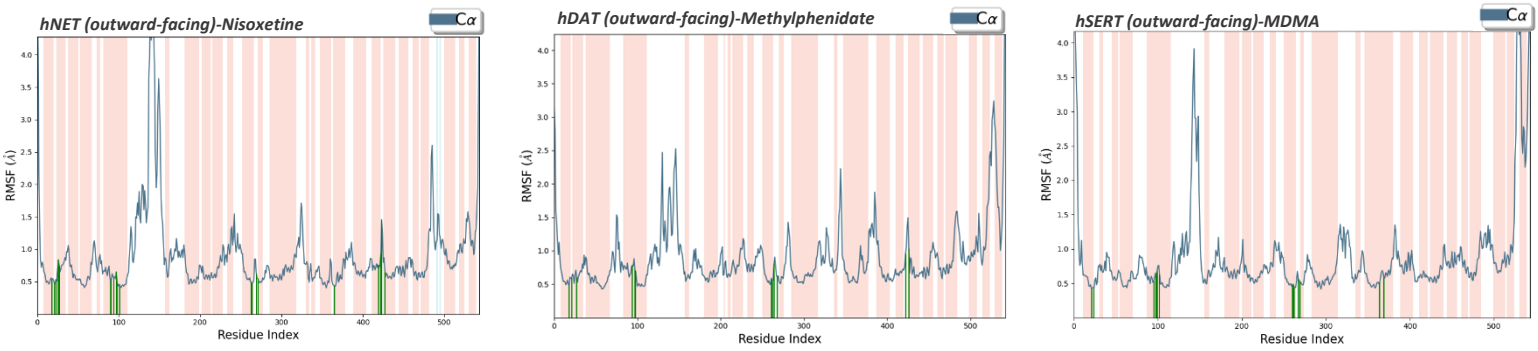

Figure 35: *RMSF analysis of the MD simulation trajectory. The Protein RMSF (blue graphs) is calculated based on the carbon-alphas of each MAT, concerning the reference frame. Amino acids that interact with the ligand are marked with green vertical bars. Colored in white, salmon pink, and blue are the loops, helices, and β-sheets, respectively. From left: RMSF plot of hNET (based on the PDB code 4XNU)-nisoxetine complex, hDAT (based on PDB code 4XP4)-methylphenidate complex, and hSERT (based on PDB code 5I6X)- MDMA complex. Peaks indicate areas in the MAT that fluctuate the most.*

The RMSF plot of nisoxetine in complex with hNET indicated that the areas near the N-and C- terminus oscillated the most during the simulation. Throughout the 100 ns, Gln54 and Glu597, near the N-and C-terminus respectively, fluctuated with RMSF values equal to 5.30 Å and 5.90 Å from their initial position. Moreover, the loop areas also showed high mobility, with a peak RMSF at 4.35 Å (Gly194). Nonetheless, the residues in contact with nisoxetine profiled great stability with a max value at 1.23 Å (Gly478). The mean RMSF fluctuated around 0.52 Å for residues in the secondary structures, disregarding the peaks observed in the loop regions.

The outward-facing hDAT bound to methylphenidate also revealed most fluctuations in the N-and C- terminus regions. Gln58 near the N-terminus reached an RMSF at 3.15 Å, while Asp600 close to the C-terminus deviated with 5.62 Å from its initial position. As expected, the loop areas fluctuated more than the other secondary structures, where the peak approached an RMSF at 3.24 Å (Ser586). However, the other residues in the loops had all an RMSF under 3.0 Å, indicating that the loops moved slightly concerning the initial position. Residues in contact with methylphenidate had minor fluctuations, where the highest observed value was at 1.03 Å (Ile484). Besides the peaks, the mean RMSF stabilized around 0.53 Å.

Likewise, the outward-facing hSERT bound to MDMA confirmed slight fluctuations during the simulation. The greatest oscillations were observed in the terminal areas (RMSF 4.25 Å for Leu74 and 5.46 Å for Pro617 near the N- and C- terminus, respectively). In the loops, Pro601 (RMSF at 4.0 Å) and Asn217 (RMSF at 3.92 Å) similarly showed high fluctuations, however, most of the residues in the loops had an RMSF under 3.0 Å. Nevertheless, the residues in contact with MDMA were fairly stable during the 100 ns and reached a max RMSF at 0.67 Å (Ala173). The mean RMSD was 0.50 Å, discounting the few maximum peaks found in the loop regions.

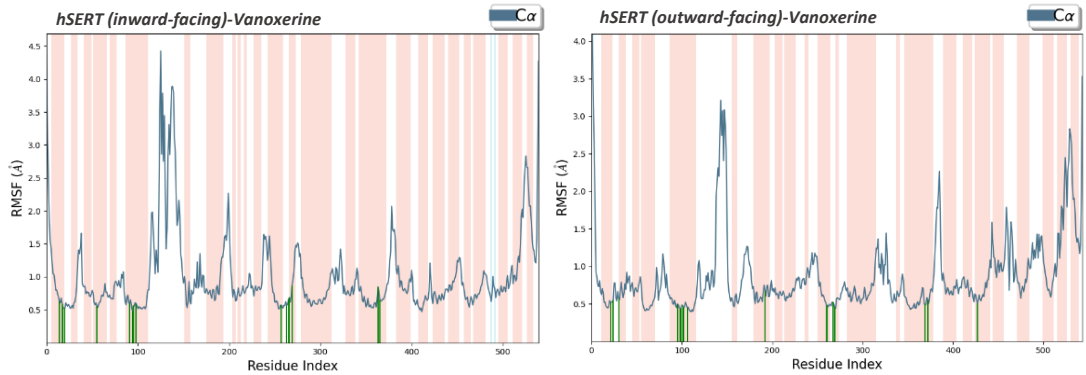

Figure 36: *RMSF analysis of the MD simulation trajectory. The Protein RMSF (blue graphs) is calculated based on the carbon-alphas of each MAT, concerning the reference frame. Amino acids that interact with the ligand are marked with green vertical bars. Colored in white, salmon pink, and blue are the loops, helices, and β-sheets, respectively. To the left and right, respectively: RMSF plot of hSERT (model based on the PDB-template 6DZZ)-vanoxerine complex, and hSERT (model based on PDB-template 5I6X)- vanoxerine complex. Peaks indicate areas of the MATs that fluctuate the most.*

The fluctuation of hSERT bound to vanoxerine was fairly similar in both the inward-and outward-facing conformation throughout the simulations. Understandably, the areas near the terminals underwent the most fluctuations. In the inward-facing conformation, the RMSF approached 4.47 Å for Glu78 (near the N-terminus) and 4.47 Å for Pro617 (near the C-terminus). Comparable the highest RMSFs were 4.36 Å for Leu74 and 3.53 Å for Pro617 in the terminal areas in the outward-facing conformation. Similar to the other three systems, the loop regions displayed great mobility: Ser203 (inward-facing conformation) reached a peak at 4.43 Å, and Asn217 (outward-facing conformation) had a peak RMSF at 3.21 Å, respectively. Nonetheless, the average RMSF stabilized around 0.70 Å (inward-facing hSERT) and 0.55 Å (outward-facing hSERT). As expected, the residues in contact with vanoxerine were stable in both systems, where the highest values were 2.66 Å (Lys605, inward-facing conformation) and 0.57 Å (Arg104, outward-facing conformation).

4.3.2 Visualization of the dynamic behavior of the ligand-protein complexes based on selected frames throughout the MD trajectories

Each of the five MD simulations was successfully run for 100 ns (at a constant temperature and pressure ensemble, respectively 300 K and 1.01325 bar), where 1001 frames were produced for each simulation. To be able to visualize the dynamic behavior and motions during this period, five timeframes were retrieved from each simulation: frame 1 (dark blue), 251 (lilac), 501 (white), 751 (beige), and 1001 (red). By that, the position and orientation of the ligands in the S1-site, development of intermolecular interactions, and flexible conformational changes of the ligands and MATs could be investigated. Figure 37 displays the dynamic and conformational transition based on the five frames. Note that frame one was the starting structure.

However, these frames only represent the "in the moment" dynamics of the ligands and MATs at the exact time the snapshots were captured. Hence, the selected frames are not representative of the whole 100 ns long simulation– they rather give a simplified overview.

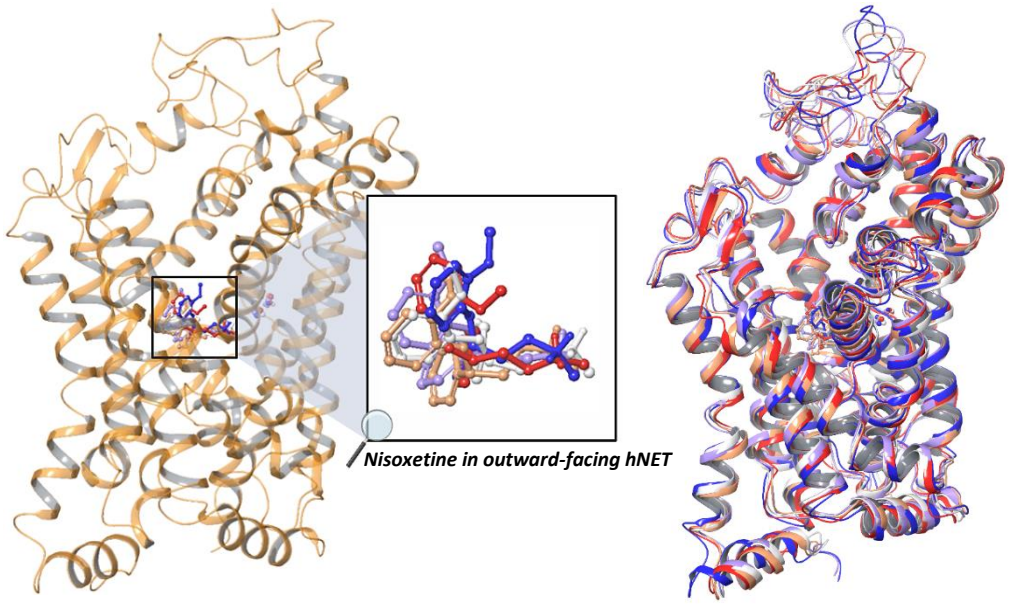
Nisoxetine in outward-facing hNET

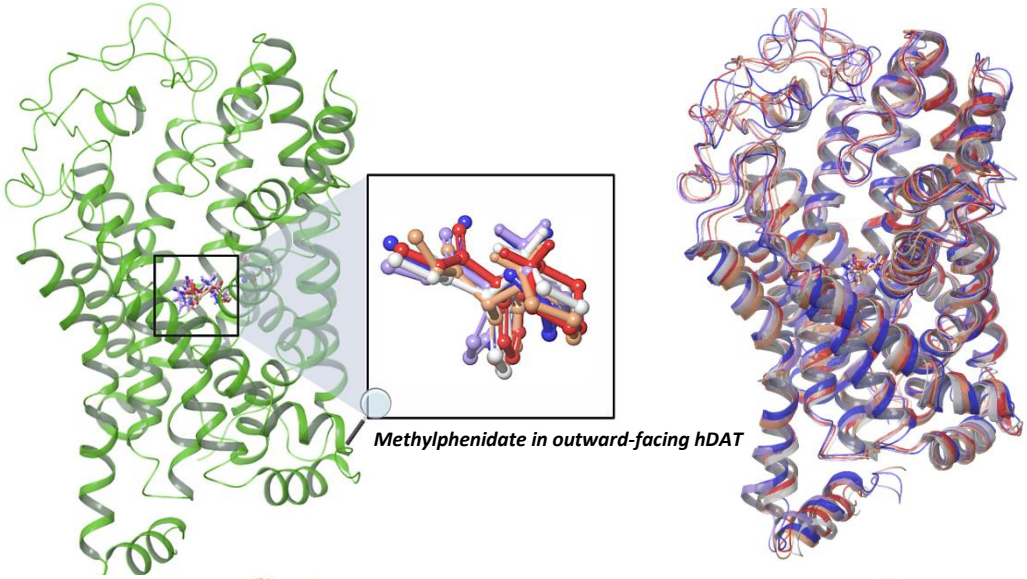
Methylphenidate in outward-facing hDAT

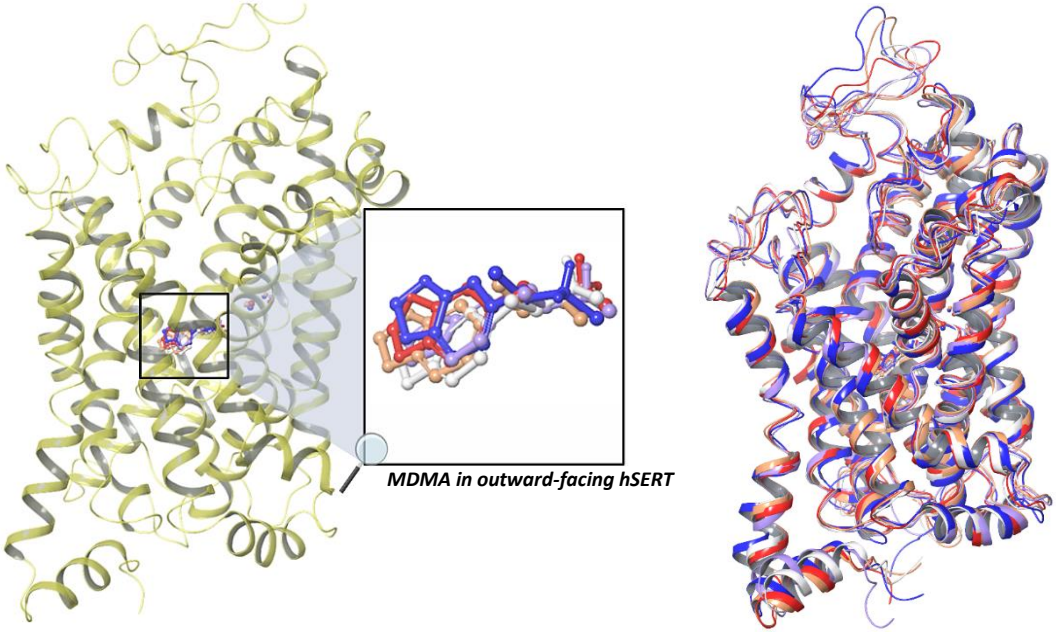
MDMA in outward-facing hSERT

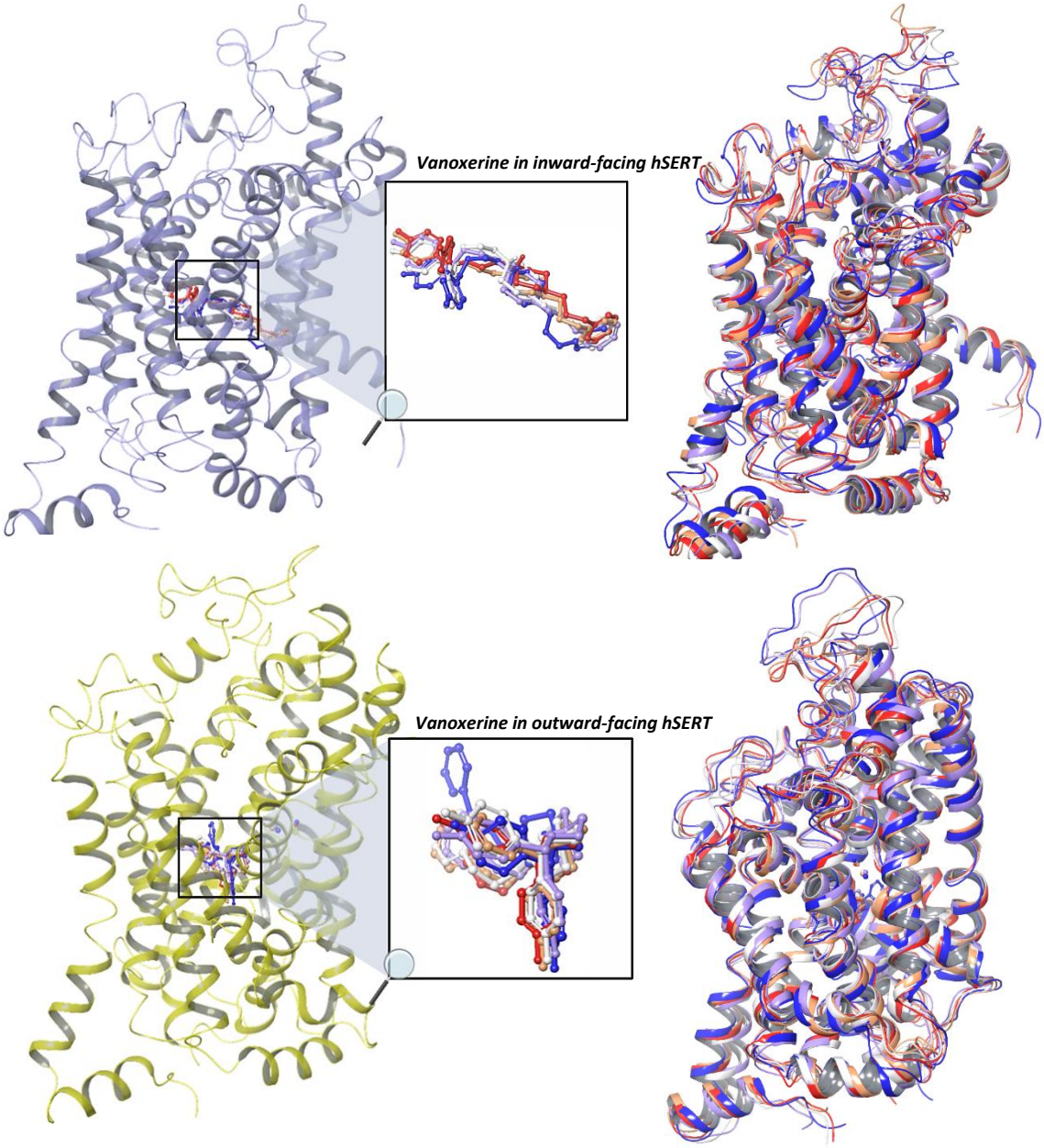

Figure 37: *To the left: The selected ligands in complex with the models of the human MATs (with the best IFD-scores) from the IFD-studies, respectively: hNET (orange); hDAT (green); the outward-facing hSERT (yellow); and the inward-facing hSERT (light purple). The ligands from frame 1 (dark blue), 251 (lilac), 501(white), 751(beige), and 1001 (red) from the 100 ns long simulations are superimposed for comparison of the orientation and placement in the S1- pocket in the five snapshots. The ions crucial for the activity of the MATs are displayed with the same color codes as the belonging frame but are not centered. See previous figures for a better view of the sodium- and chloride ions. To the right: Superposition of all the ligand-MAT complexes from the five different frames (same color codes as the ligands), for observation of the dynamics upon binding to the MATs. The figures are created in Maestro (Schrödinger release 2022-3) and edited with Biorender.com.*

During MD simulations, the proteins and ligands undergo conformational changes to create a more specific and energetically favorable binding mode (Schrödinger release 2022-3). The goal is, hence, to produce the most energetically stable ligand-MAT complex through dynamic adaptions.

Based on the five created systems, nisoxetine in hNET profiled extensive conformational changes compared to the other systems. The protonated amine group was situated in nearly the same place during the simulation, while the position of the aromatic rings, however, varied more. Interestingly, gradual conformational alterations were observed from frame 1 to 751, but the final location of the functional groups (frame 1001) was fairly analogous to frame 1 in the end. On the other hand, the systems involving methylphenidate and MDMA captured minor deviations in the orientation in the S1-site and conformational changes - concerning the initial reference. The relative stable conformations of the ligands were also reflected in the detected interactions with hDAT and hSERT through the simulations (see section 4.3.3), respectively.

The adaptions of vanoxerine in the outward- and inward-facing hSERT were highly distinct (see figure 37) compared to one another. This was especially observed in the location of the monosubstituted aromatic ring (and the attached propyl-chain) of vanoxerine. Nevertheless, in each system, vanoxerine itself was relatively stable. The orientation and conformation were mainly the same in all five frames, with particularly slight deviations between frame 251, 501, 751, and 1001.

Furthermore, modest changes in the overall conformation of the secondary structures (except for the flexible loops) in the MATs were observed. A reason may be that the complexes generated from the IFD were applied as a starting point for the MD simulations. The ligands were already bound to the S1-site, and the entrance to the binding pocket was locked in either an outward- or inward-facing conformation. Thus, the first dynamic steps of the three-step mechanism upon binding to the MATs were not viewed – where great conformational changes from an inactive to active transporter arise.

The intermolecular interactions in each ligand-MAT complex were further examined between the ligand, residues, and water molecules within 6 Å in the S1-binding site. However, note that intramolecular interactions between ions and residues in larger circumferences also

occurred and contributed to the stabilization. Van der Waals interactions (vdW) appeared between all atoms too.

In the nisoxetine-hNET system, the same intermolecular interactions mainly remained in all five snapshots. Throughout the frames, a salt bridge between the protonated amine in nisoxetine and Asp75 (TMH1) persisted. Polar hydrogen bonds (H-bonds) were also profiled: an H-bond between the amine in nisoxetine and Phe317 (TMH6) was observed in all the frames- except for frame 251, where an H-bond was established with Ser318 (TMH6) instead. In the same way, an H-bond between the amine and Asp75 was additionally seen in all the frames - excluding frame 501, where only the H-bond with Phe317 was present. Interestingly, a cation-π interaction with Phe72 (TMH1) occurred in all frames, apart from frame 1001. In only frame 1 and 1001, however, a cation-π interaction with Phe323 (TMH6) was also detected –including a π-π stacking with Tyr152 (TMH3) (frame 1: with the monosubstituted aromatic ring. Frame 1001: with the disubstituted aromatic ring). In frame 1, the monosubstituted aromatic ring also formed a π-π interaction with Phe72. Lastly, the methylether-oxygen in nisoxetine and Asp75 created an H-bond with the same water molecule in frame 751.

Similarly, the protonated secondary amine in methylphenidate created a salt bridge with Asp79 (TMH1) in all the frames. However, hydrophobic interactions were mostly dominating in this system. In frame 251, 501, 751, and 1001 a π-π interaction between the aromatic ring in methylphenidate and Phe326 (TMH6) was established. This kind of hydrophobic interaction were additionally formed with Tyr156 (TMH3) in all frames, except for frame 251. Besides, a π-π stacking with Phe76 (TMH1) was also detected in frame 501 and 751. Further, the amine established H-bonds with Asp79 and Phe320 (TMH6) in, respectively, frame 251 and 501. A water molecule (frame 251) also created H-bonds with the amine in methylphenidate and Phe320. Lastly, a cation-π interaction with Phe76 was exclusively observed in frame 1.

MDMA profiled minimal conformational changes and had thus virtually the same position in the S1-site during the simulation. By that, the established intermolecular interactions with hSERT were identical in frame 251, 501, 751, and 1001. Asp98 (TMH1) formed a salt bridge and H-bond with the positively charged amine in MDMA in all frames. Tyr95 (TMH2) was also included by creating an H-bond and cation-π interaction with the amine (however, the H-bond with Tyr95 was not present in frame 1). Frame 1 additionally had three interactions: an

H-bond between the protonated amine and Phe335 (TMH6), and one cation-π interaction with Phe341 (TMH7) and Phe335 each.

As expected, a salt bridge between vanoxerine (in the inward-facing hSERT) and Asp98 was present in all five frames. A polar H-bond was also established (frame 251, 501, 751, and 1001), comprising the protonated amine in vanoxerine and Asp98. In the two first snapshots, the amine group additionally formed an H-bond and cation-π interaction with Phe335 (TMH6). The cation-π interaction was also detected in frame 501. Hydrophobic interactions also occurred in form of a π-π interaction between Phe341 (TMH7) and the adjacent disubstituted aromatic ring in vanoxerine (in frame 751, the interaction included the other disubstituted aromatic ring). In the last three snapshots, a π-π interaction between Phe347 (TMH8) and the monosubstituted aromatic ring in vanoxerine was present too. Lastly, disubstituted aromatic ring additionally profiled π-π stacking with Phe335 in frame 751. In only frame 751, a water molecule created a H-bond with the secondary, neutral, amine in vanoxerine.

In the outward-facing hSERT, vanoxerine notable formed a salt bridge with Asp98 (TMH8) in only frame 251. Instead, a cation-π interaction with Tyr95 (TMH2) was profiled in all five frames. Aromatic π-π interactions were, however, observed in all frames but comprising different residues. In only frame 1, a π-π interaction was observed between the disubstituted aromatic ring and the nearby Phe334 (TMH6). This type of interaction was rather created with Tyr175 (TMH3) and the other disubstituted aromatic ring in the two next frames. Moreover, a π-π interaction was investigated comprising the disubstituted aromatic ring and adjacent Phe341 (TMH7) – and not Tyr175 or Phe334 – in the two last frames. In frame 751, the other disubstituted aromatic ring also created an aromatic interaction with Tyr176 (TMH3).

Overall, the marginal differences in the conformation and position of the ligands appeared to result in only a few variations in the type of occurring intermolecular interactions - during the stabilization of the ligand-MAT complexes. The orientation of the ligands was virtually the same throughout the 100 ns long simulation, and the MATs also underwent slight conformational changes.

4.3.3 Investigation of ligand-protein interactions

Interactions between the ligand and MATs were monitored and conducted by the *Simulation Interactions Diagram Panel* (Schrödinger release 2022-3) in Maestro. This module creates a graphical visualization of the dynamic behavior and occurring intermolecular interactions in the complexes. Thus, the diagram indicates contacts that may be important for stabilizing a ligand-MAT complex. The interaction diagrams for the five systems are demonstrated in figure 38-42.

The stacked bar charts present the fraction of time a specific residue was engaged in an interaction during the 100 ns long simulations. Desmond (Schrödinger release 2022-3) categorizes the intermolecular interactions into four types: H-bonds (green), hydrophobic interactions (lilac), ionic interactions (hot pink), and water bridges (blue). The hydrophobic interactions are further classified into three subtypes: cation-π-, π-π-, and other non-specific interactions (i.e., involving a hydrophobic residue and aliphatic- or aromatic groups in the ligand). In addition, a schematic overview of the ligand-protein contacts that were maintained in more than 30.0 % of the simulation time is displayed. A residue that was engaged in several contacts, of the same type or different types, may have values close to, or higher than, 1.0 or 100 %.

Note that, the Simulation Interaction Diagram Panel (Schrödinger release 2022-3) only reports an ionic interaction if the same functional donor- or acceptor group not already is engaged in an H-bond. In the four first MD simulations (figure 38-41), both the positive amine in the ligand and Asp in TMH1 were involved in H-bonds mainly through the whole simulation, meaning that figure 38-41 only displays the salt bridges when the H-bond was not present. However, the salt bridge *was present in all frames* during the entire 100 ns long simulation for the four first systems (figure 38-41). Only the vanoxerine-hSERT (outward-facing) complex did not create an H-bond during the simulation, which means that figure 42 shows the “true” percentage presence of the salt bridge.

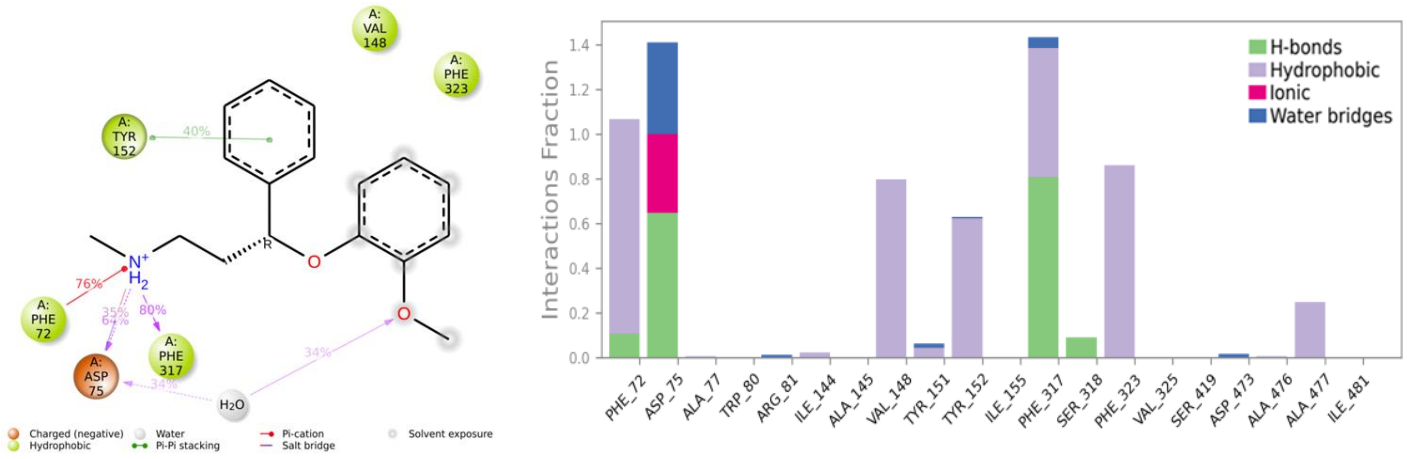

Figure 38: *To the left: Schematic diagram of the interactions in the nisoxetine-hNET complex during the 100 ns long simulation. Only contacts occurring more than 30.0 % throughout the simulation are shown. To the right: Stacked bar chart of the hNET-nisoxetine interactions during the simulation. H-bonds are shown in green, ionic interactions in hot pink, hydrophobic interactions are represented in lilac, and water bridges in blue.*

The protonated amine group appeared to play a key role in nisoxetine. Throughout the simulation, the amine was engaged in an H-bond with Phe317 and Asp75 for 80 % and 64 % of the time, respectively. The crucial ionic interaction was preserved in the entire simulation, however, due to the presence of the H-bond interaction between the amine and Asp75 the Interaction Diagrams only displayed the salt bridge as having 35 % existence. Moreover, the amine also maintained a cation-π interaction with Phe72 for 76 % of the entire simulation. In addition, a π-π interaction involving Tyr152 was established 40 % of the time (figure 38), as well as several hydrophobic interactions (lilac bars) were maintained over 30 % of the simulation, this included the following residues: Val148 (approximately 80 %), Phe323 (slightly over 80 %), Phe317 (approximately 60 %), and Ala477 (approximately 30 %). Lastly, water molecules also contributed to stabilize the nisoxetine-hNET complex by situating water bridges with some of the binding-site residues and nisoxetine (figure 38). In 34 % of the trajectories, two water bridges were created with Asp75 and the methylether-oxygen of nixoxetine.

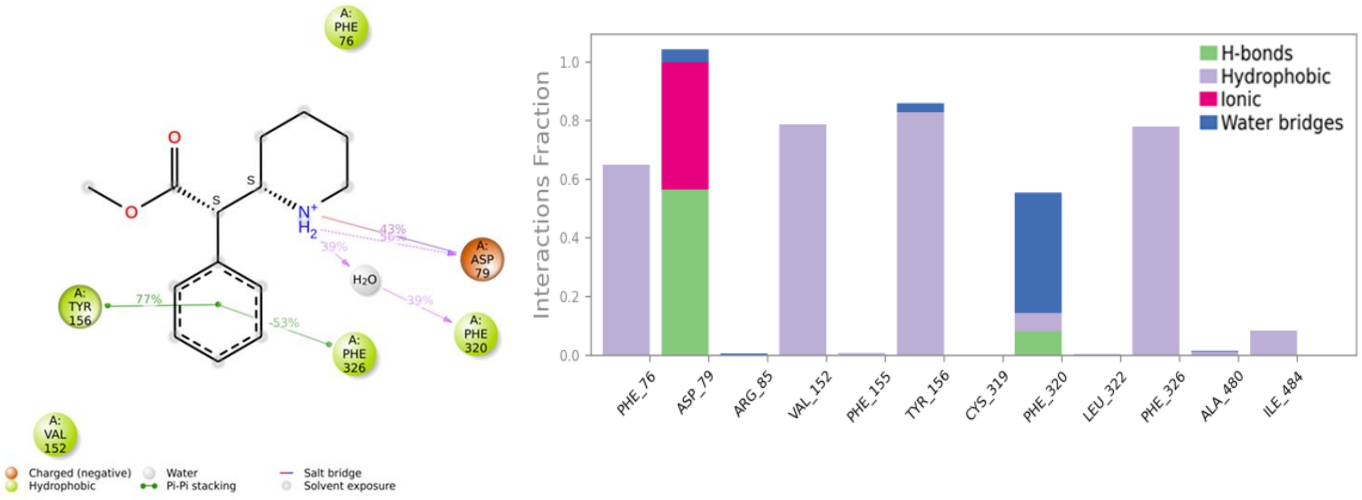

Figure 39: *To the left: Schematic diagram of the interactions in the methylphenidate-hDAT complex during the 100 ns long simulation. Only contacts occurring more than 30.0 % throughout the simulation are shown. To the right: Stacked bar chart of the hDAT-methylphenidate interactions during the simulation. H-bonds are shown in green, ionic interactions in hot pink, hydrophobic interactions are represented in lilac, and water bridges in blue.*

In the methylphenidate-hDAT system, a salt bridge and H-bond were engaged between Asp79 and the positively charged amine in methylphenidate for 100 % and 56 % of the simulation, respectively. However, owing to the concurrent occurring H-bond with Asp79, the Interaction Diagram only displayed the ionic interaction as having 43 % presence (figure 39). The aromatic ring in methylphenidate also participated in a π-π interaction with Tyr156 for 77 % of the trajectories, and Phe326 for 53 %. Other hydrophobic interactions (lilac bars) that retained over 30 % of the time included: Phe76 (slightly over 60 %) and Val152 (slightly under 80 %). Besides, the amine in methylphenidate also created a water bridge for 39 % of the period- in addition, the same water molecule interacted with Phe320 in terms of a water bridge also 39 % of the time.

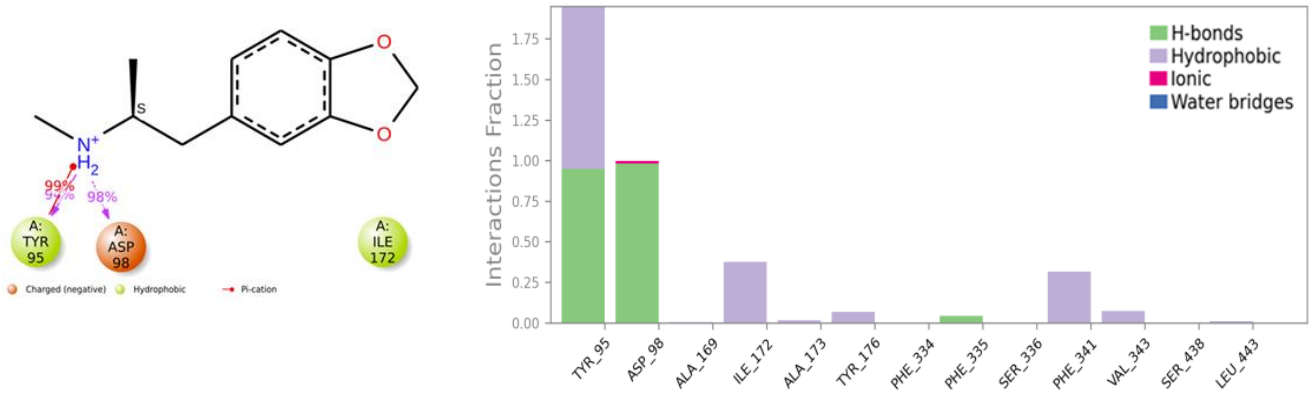

Figure 40: *To the left: Schematic diagram of the interactions in the MDMA-hSERT (outward-facing) complex during the 100 ns long simulation. Only contacts occurring more than 30.0 % throughout the simulation are shown. To the right: Stacked bar chart of the hSERT (outward-facing)-MDMA interactions during the simulation. H-bonds are shown in green, ionic interactions in hot pink, hydrophobic interactions are represented in lilac, and water bridges in blue.*

The same interactions mainly persisted throughout the whole MD simulation in the MDMA-hSERT system – as previously described. Interestingly, an H-bond and salt bridge were preserved for 98 % and 100 % of the time. The ionic interaction was only reported as ~ 1 % in the Interactions Diagrams due to the simultaneously occurring H-bond with Asp98. Moreover, Tyr95 participated to stabilize the complex by engaging an H-bond and cation-π interaction with the positive amine for, respectively, 94 % and 99 % of the period. Likewise, Ile172 maintained hydrophobic interactions with MDMA in around 38 % of the 100 ns.

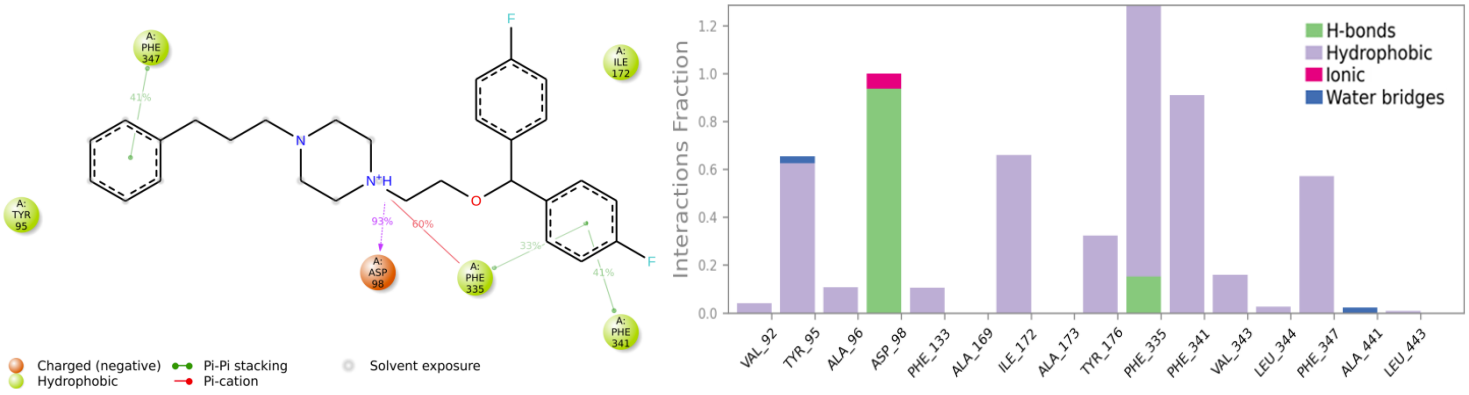

Figure 41: *To the left: Schematic diagram of the interactions in the vanoxerine-hSERT (inward-facing) complex during the 100 ns long simulation. Only contacts occurring more than 30.0 % throughout the simulation are shown. To the right: Stacked bar chart of the hSERT (inward-facing)-vanoxerine interactions during the simulation. H-bonds are shown in green, ionic interactions in hot pink, hydrophobic interactions are represented in lilac, and water bridges in blue.*

Similarly, the protonated amine in vanoxerine maintained an H-bond with Asp98 (in the inward-facing hSERT) during 93 % of the simulation time, while a salt bridge occurred for 100 %. Owing to the concurrent H-bond and ionic interaction between Asp98 and the amine in vanoxerine, the Interaction Diagram only displayed the salt bridge as having a ~ 6 % presence. Additionally, several hydrophobic interactions were observed: one of the aromatic rings substituted with fluor (figure 41) maintained two π-π interactions with both Phe335 (33 % of the time) and Phe341 (41 % of the time). The monosubstituted aromatic ring also preserved a π-π interaction with Phe347 for 41 % of the simulation time. Other hydrophobic contacts (lilac bars) that remained over 30 % of the simulation included: Tyr95 (slightly over 60 %), Ile172 (slightly over 60 %), Tyr176 (slightly over 30 %), and Phe341 (around 50 %). Also, a cation-π interaction engaging the protonated amine in vanoxerine and Phe335 was detected in 60 % of the trajectories.

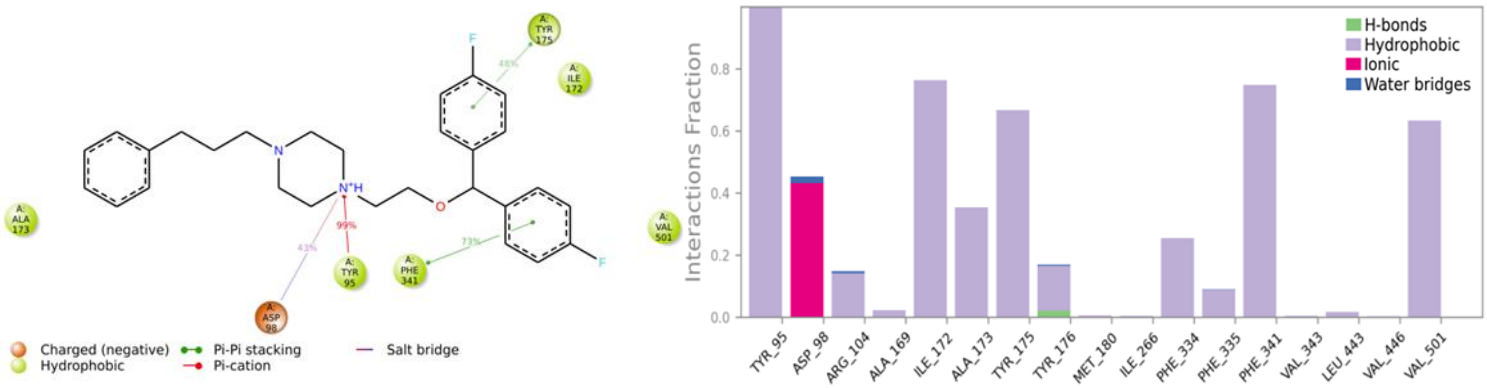

Figure 42: *To the left: Schematic diagram of the interactions in the vanoxerine-hSERT (outward-facing) complex during the 100 ns long simulation. Only contacts occurring more than 30.0 % throughout the simulation are shown. To the right: Stacked bar chart of the hSERT (outward-facing)-vanoxerine interactions during the simulation. H-bonds are shown in green, ionic interactions in hot pink, hydrophobic interactions are represented in lilac, and water bridges in blue.*

In contrast to vanoxerine in the inward-facing hSERT, the salt bridge maintained 43 % of the simulation time in the outward-facing conformation. The positively charged amine in vanoxerine was, on the other hand, involved in a cation-π interaction with Tyr95 that was preserved 99 % of the time. Further, both aromatic rings (substituted with fluor) were involved in π-π interactions with Tyr175 (48 % of the time) and Phe341 (73 % of the time), respectively (figure 42). Like the other systems, hydrophobic interactions (lilac bars) also occurred throughout the trajectories, involving the following residues: Ile172 (slightly under

80 % of the time), Ala174 (slightly under 40 % of the time), Phe334 (slightly under 30 % of the time), and Val501 (slightly over 60 % of the time).

5 Discussion

This study aimed to get a greater understanding of determinants for preferred and selective binding to the human MATs, at a molecular level. To manage this, models of each of the human transporters (i.e., homology models of hDAT and hNET, in addition to models of hSERT), based on the corresponding human target sequences from UniProtKB, were first built. This made it possible to observe residues in the S1-pocket of the MATs, and to further get a deeper knowledge of how divergent and conserved residues contribute to selectivity towards each MAT- through creation of specific intermolecular interactions. IFD and MD simulations were, additionally, used to accomplish this and to obtain information on affinity and IFD-scores, occurring interactions, and binding poses in the most energetically favorable ligand-MAT complexes. In this study, it was of particular interest to examine distinct psychostimulants and a selection of other substances interacting with the MATs (i.e., antidepressants, atypical inhibitors, a non-stimulant, and some research standards). Thus, structural features of the ligands were also observed regarding selectivity for the MATs.

5.1 Monoamine transporter models and validation of the output

Biological 3D structures are valuable in gaining knowledge about, amongst others, folding, biochemical activity, and binding specificities of proteins (101, 102). In the present study, the 3D models of the human MATs made it possible to map residues in the S1-site of hDAT, hNET, and hSERT. Eight MAT-models were in total made: four outward-facing hDAT-models (based on the PDB-templates 4XP1, 4XP4, 4XP6, and 4XP9), one outward-facing hNET-model (based on the PDB-template 4XNU), two outward-facing hSERT-models (based on the PDB-templates 5I6X and 5I73), and one inward-facing hSERT-model (based on the PDB-template 6DZZ). This was described more detailed in earlier chapters. The TMHs and residues (see chapter 4.2) that formed the primary binding site of each generated model, agreed to earlier publications regarding the primary binding site (187, 189), as well as the orientation of the corresponding residues (and ligands) were the same as the experimentally determined template-structures from PDB used to generate the MAT-models (145, 146, 148, 169).

Note that the binding and preference for the S2-site or other allosteric sites not will be discussed in this thesis, although it is known that binding to allosteric sites modulates the S1-site, and vice versa (53, 187, 189).

The Protein BLAST (table 1) and sequence alignment (figure S1 and S3) from MSV (Schrödinger, release 2022-3) both revealed that the percentage sequence identity between dDAT (template) and the target sequences hNET and hDATs, was more than 50 %. Thus, these proteins were homologous and had the same overall folding. Favorable for this study, was that binding site residues, in general, are more conserved than residues outside the binding site (103, 104). Nevertheless, it is important to count that a homology around 50 % at an amino acid level, does not mean that the structural information of dDAT directly can be extrapolated to hNET and hDAT (187).

The outward-facing models of hSERT were, on the other hand, built based on templates of hSERT with only a few mutations (i.e., the PDB-structures 5I6X and 5I73 were ts3-constructs of hSERT), while the inward-facing hSERT was based on an N-and C terminus truncated wild-type hSERT (PDB-code: 6DZZ). This was described in more detail in chapter 3.3. Thus, it was expected that the percentage identity was high: both Protein BLAST (table 1) and the alignment (figure S2) revealed more than 95 % identity to the 5I6X- and 5I73-templates, and 100 % identity to the 6DZZ-template. Again, the hSERT-models were not homology models due to that they, in principle, were built on hSERT-templates.

An important consideration when using templates from PDB is the resolution of the solved 3D structures. The resolutions of all the solved templates were more than 2.80 Å (see table 1), however, as explained by Ortore et.al (187) these resolutions are not high enough to ensure exact structural folding, sidechain rotamers, and it may be hard to distinguish between NH- and O-atoms – as well as hydrogen atoms may be missing. As described in chapter 4.1, the resolution of the PDB-templates 5I6X and 5I73 was not high enough to solve the Na2-and chloride site, respectively. Similarly, none of the ions were solved in the PDB-template 6DZZ. In addition, the β-turn between TMH11 and TMH12 was either not identified in the hSERT-models based on 5I6X and 6DZZ (145, 146). Consequently, it is limited how well the Protein Preparation Wizard prepares the templates for further modeling, this includes the refinement performed by MSV (Schrödinger, release 2022-3) before building the models.

Moreover, the quality of the models was validated by generating Ramachandran Plots (see figure 14), and by assessing the predictability of the models (figure 15-22). Regarding the stereochemical quality, table 3 reported that all the models of the outward-facing MATs had more than 90 % of the residues in the allowed, most favorable, area in the belonging Ramachandran Plots. The inward-facing hSERT model had 87,8 % of all the residues in the most favorable region. According to PROCHECK (156) a model, based on templates with resolutions ≥ 2.0 Å, is defined as good if greater than 90 % of the residues are in the allowed region. All the outward-facing MAT-models fulfilled this criterion, and the inward-facing hSERT model was also close to 90 %.

As described in earlier chapters, it is not favorable to have residues in disallowed regions, owing to that unfavorable phi-and psi angles of sidechains lead to a higher degree of steric stress -leading to a less energetically favorable protein model. Less than 1 % of the residues in each model were in the disallowed area (see table 3 and figure 14). Beneficial for this study was that all these residues were positioned in extra-and intracellular loop areas far from the orthosteric binding site – and not in the S1-site. In the hDAT-models, this comprised: IL1 (Ile137 and Lys139) and EL2 (Ser198, Ser201, and Ala214), while the "disallowed" residues were placed in EL2 (Lys204 and His199) in the hNET-models. For hSERT only the models based on the templates 6DZZ and 5I6X had residues in the disallowed area, comprising IL4 (His456) and EL6 (Tyr570), respectively.

To further evaluate the models, the ligands from the study were redocket into the S1-pocket of the MAT-models – and superimposed to the cocrystallized ligands (see chapter 4.1). Figure 15-22 showed that the redocked ligands overlapped well with the corresponding ligands from the PDB-templates; the ligands had the same pose as in the experimentally determined 3D structures. Accordingly, the RMSD-values were all lower than 2.0 Å (range given from 0.30-1.32 Å) as displayed in figure 15-22, which supports these findings (160). Once again, the RMSD for the superposition of the MAT-models to their corresponding template was not calculated, however, figure 15-22 implies great overlap of the secondary structures. The greatest differences were observed in the loops. This was expected due to that loops (and turns) distantly from the binding sites, in general, are less conserved compared to residues in helices and β-strands. However, IL's and EL's are flexible, and these regions do not affect the S1-site significantly (104, 188). More about the structural stability of the MAT-models will be discussed in chapter 5.3.

Overall, the models generated in the present study had a high enough quality to further perform IFD and MD simulations. As discussed earlier, the quality of a model is dependent on the quality of the templates used to generate the model. Owing to that the *overall* sequence identities of the homology models of hNET and hDAT were slightly over 50 %, there will be some uncertainties in them. Yet, the binding site residues are more conserved than non-binding site residues (41). However, since there are no experimentally 3D structures of hDAT and hNET yet, these models are valuable in getting a deeper insight and understanding of S1-site of these two MATs, as well as to suggest ligand-MAT interactions and dynamic behavior (101, 190). According to Robinson et.al (190), the accuracy of models with sequence identity greater than 90 % is comparable to experimentally mapped structures. In this study, this was applicable to the hSERT-models.

5.2 Induced fit docking

In this study, IFD was applied to generate the most energetically favorable poses of the included ligands bound to each of the human MAT-models. The IFD-studies made it possible to predict the most favorable orientation of the ligands in the S1-pocket of hNET, hDAT, and hSERT with respect to the ionic interaction with Asp in TMH1 (hNET: Asp75; hDAT: Asp79; hSERT: Asp98). Additionally, the poses gave an overview of the residues surrounding the ligands (within 3 Å) in each MAT, hence, both the binding mode and key residues for selectivity and preferences to a specific MAT could be examined.

The best poses were mainly selected based on the docking scores. However, scoring functions are simplifications of the binding free energy (see equation 1) of a system. Many physical interactions and entropic effects (i.e., flexibility and dynamics of the protein and ligand) are excluded: this includes interactions involving solvents. The effect of water molecules is important, due to that protein-ligand recognition and binding take place in an aqueous environment. In fact, a water molecule can engage in three to four H-bonds with surrounding molecules and the ligand, which also contribute to the overall binding energy- and docking score. The scorings are hence approximations of the reality (113, 118). Moreover, the docking scores were estimated based on force fields. In this study, the most recent OPLS4 force field was applied for these calculations: however, force field calculations (see section 1.8.4) are also mathematical approaches, thus comprise inaccuracies. This is described more in chapter 5.3.

Before running the IFD, a grid box (total size: 20 $Å^3$), with the cocrystallized ligands from the PDB-structures as the selected centroids, was generated to specify the binding site where the ligands from the present study should be docket by induced fitting (see chapter 3.4.2) (116). A large grid size was set to incorporate the ligands in the S1-site, comprising important residues in the binding region. On the other hand, large enclosing boxes can include irrelevant regions, leading to more uncertainties in the docking score calculations. Additionally, constraints in terms of a grid box, may not encompass all the conformational changes of the MATs and ligands – owing that the obtained information is from after the ligands are positioned in the desired binding site.

Besides, the ligands were limited to the S1-site (defined by the grid-box), meaning possible interactions with allosteric sites (e.g., S2-and S3- sites), simultaneous binding to the allosteric vestibular (S2-) site, or interactions with EL4 which act as a "gatekeeper" for entry of substances to the MATs, not was taken into account. These sites are also suggested to play a role in selectivity and binding to the MATs. However, note that the grid box was set to 20 $Å^3$, while the S2-site is suggested to be located around 13 Å above the S1-site (97, 191, 192).

Lastly, unlike standard rigid docking, IFD allows a flexible ligand to be docket into a mobile protein, which is a better approach to the dynamic nature of ligands and proteins (116). This was described in detail in chapter 1.8.2.

5.2.1 General considerations on selectivity and preference for the monoamine transporters

In CNS, the MATs are targets for psychostimulants, antidepressants, non-stimulants, and several other substances – such as research standards. These substances act as substrates, typical inhibitors, or atypical inhibitors for the transporters – as described in earlier sections (49). The affinity data (note that some of the data in table 4 are from other species than humans) and IFD- scores generated in this study, do not give information about these intrinsic properties but are important in obtaining knowledge about the selectivity a substance has towards each MAT, in terms of IC_{50} and K_i.

In this section selectivity and preferences for the MATs is systematically classified concerning IC_{50} and K_i. However, only the ligands that had relatively high preference for either NET, DAT, or SERT will be described here, in addition to cocaine. The ratios are classified according to the same classification system as described by Rudin et.al (185):

DAT/SERT ratios (>1) indicate that a substance has more preference for DAT, while low DAT/SERT ratios (<1) indicate that the preference is higher for SERT. The same system applies to the DAT/NET ratios. A high ratio is typically by 10-fold difference, i.e., high ratios are >10, while low ratios are <0.10 (175, 185, 193). Generally, potency for a MAT can also be categorized into high ($IC_{50} \leq 1$ μM), moderate (1 μM < IC_{50} <10 μM), and low ($IC_{50} \geq 10$ μM) (194). Similar classification can be used for K_i: high ($K_i \leq 1$ nM)-, moderate ($10 \leq K_i <$ 100 nM)-, and low ($K_i \geq 100$ nM) potency, based on results from: (195, 196).

High potency for DAT corresponds to a stimulation of the mesolimbic system associated with reward, motivation, and emotions, but also increased risk for abuse (i.e., incentive salience) and addiction (see chapter 1.3). These effects are often referred to as amphetamine-like effects (177). However, among the included substances, α-PVP and MDPV (NPSs) showed the highest potency for both DAT (IC_{50} = 0.04 μM and IC_{50} = 0.05 μM, respectively) and NET (IC_{50} = 0.02 μM and IC_{50} = 0.04 μM, respectively) compared to SERT (IC_{50} >100 μM and IC_{50} = 9.6 μM, respectively). Similar potencies for these two stimulants were expected, due to that α-PVP is structurally analogous to MDPV – the only difference is the lack of the 3,4-methylenedioxy ring on α-PVP (see figure 12). As reported in table 4, the DAT/SERT ratios were remarkably ∼2500 for α-PVP and ∼192 for MDPV, pointing out high selectivity towards DAT compared to SERT.

On the other hand, the traditional illicit stimulant MDMA is associated with serotonergic-like effects by acting at SERT (IC_{50} = 1.36 μM), however, the potency for NET is also high (IC_{50} = 0.45 μM) (table 4) (177). Structurally, MDMA is also fairly similar to NE. Acute effects of MDMA due to increased transmission of 5-HT and NE comprise a “deeper self-reflection” or “touching within” (i.e., entactogenic properties), yet, prolonged use and high doses are related to adverse side effects such as neurotoxicity (e.g., serotonergic toxicity involving seizures, serotonergic syndrome, and hyperthermia) (197, 198, 199). As revealed from table 4, the potency for DAT was relatively low (IC_{50} = 17 μM) – implicating a lower abuse potential. Thus, the preference for DAT was 13-fold and 38-fold lower compared to SERT and NET, respectively. Interestingly, the research standard MMAI showed especially high potency for SERT (IC_{50} = 0.68 μM), but also some for NET (IC_{50} = 3.6 μM), compared to DAT (IC_{50} = 193 μM). Hence, MMAI is reported to have MDMA-similar effects (179, 199).

Moreover, both methylphenidate and atomoxetine are, as described in previous chapters, used in the treatment of ADHD (66). Both substances act as typical inhibitors but show different

preferences for the MATs. Methylphenidate provided high and similar potency for both DAT (IC_{50} = 0.13 μM) and NET (IC_{50} = 0.12 μM) relative to SERT (IC_{50} = 274 μM). Due to the high potency for DAT (DAT/SERT ratio: 2107), methylphenidate is classified as a therapeutic *stimulant*, causing desired clinical effects such as amplified attention and concentration (reward-related learning), however, the rise in dopaminergic neurotransmission can, amongst others, also increase the side-effects such as the risk of addiction, insomnia, and loss of appetite (66, 67). In contrast, atomoxetine had mainly only preference for NET, with accordingly much higher potency for NET compared to the two other MATs (table 4). Owing to the lower potency for DAT (DAT/NET ratio: 0.0034), this therapeutic drug is classified as a *non-stimulant*. However, elevated noradrenergic transmission in the treatment of ADHD is reported to exert effects on performance, attention, and impulsive control (200, 201). The potency for SERT was also low for atomoxetine (DAT/SERT ratio: 0.053), indicating a weak interaction with SERT.

Similar to atomoxetine, the research standard nisoxetine had high selectivity for NET. The DAT/NET ratio was 0.0061-0.0014 (rat data) and 0.012 (human data), and the DAT/SERT ratio was 1.09-1.83 and 0.80 from, respectively, the rat-and human data (table 4). Hence, there was not any significant difference in the preference between DAT and SERT.

As expected, the two included SSRIs had high selectivity for SERT. The DAT/SERT ratio for paroxetine was notable $2.2 \cdot 10^{-4}$- $8.6 \cdot 10^{-4}$. Citalopram also exhibited a similar preference: the DAT/SERT ratio was $\sim 1.1 \cdot 10^{-4}$-$1.9 \cdot 10^{-3}$ (table 4). The low potency at DAT explains why SSRIs are not addictive and therefore have low abuse potential. Hence, the therapeutic effects of SSRIs in, for instance, treatment of clinical depression can partly be explained by the increased serotonergic activity, leading to amongst others a feeling of well-being (see chapter 1.7) (202). Clomipramine had, furthermore, remarkably high preference for SERT (DAT/SERT ratio: $6.4 \cdot 10^{-5}$-$9.3 \cdot 10^{-5}$) and NET (DAT/NET ratio: 0.017-0.018) compared to DAT (table 4) (203).

Finally, while the mentioned substances displayed high preference for one or two MATs, cocaine is classified as a non-selective MAT inhibitor (176). The ratios were: 3.1 (DAT/SERT) and 0.59 (DAT/NET), as stated in table 4. Nevertheless, the potency towards SERT was the lowest with IC_{50} = 2.37 μM, while IC_{50} was 0.768 μM and 0.451 μM for DAT and NET, respectively.

Moving further, atypical inhibitors are suggested to bind the MATs in a different manner than the typical inhibitors. The background for this is much due to the distinct behavioral profiles: atypical DAT inhibitors (such as vanoxerine) tend to have a slower onset and gradually increase (long-lasting) extracellular levels of DA, while the typical inhibitors can cause rapidly elevated levels of DA – hence the addictive potential. The atypical inhibitors have, in contrast, shown anti-addictive properties (96, 97, 187, 204, 205). In this study, the atypical inhibitors were included to identify determinants for binding to an inward-facing conformation of the MATs. Likewise, JHW007 is stated to act as an atypical DAT-inhibitor (164, 206). Consequently, the equatorial tnH isomer of JHW007 stabilizes the inward-facing conformation of DAT better than the axial isomer (see figure S6) (164). This differs from trends observed in typical inhibitors, like cocaine and β-CFT, that possess an axial conformation of the tnH group (see figure 12)- and stabilize the outward-facing DAT (164). Unfortunately, the affinity data in terms of Ki and IC_{50} were not accessible for these atypical inhibitors during this study. On the contrary, some studies (146, 207, 208) regarding the binding of ibogaine in the inward-facing SERT underpins ibogaine's preference for SERT. According to table 4, ibogaine had relatively high potency for SERT (8.2 μM), while the potency for DAT was relatively low (IC_{50} = 22.1 μM).

5.2.1.1 Context between IFD-scores and selectivity

The results from the IFD exhibited no clear correlation between selectivity for a MAT and the IFD-scores for the generated poses. By that, the scores could not support the ligand's preference for either DAT, SERT, or NET. For instance, MMAI profiled high preference towards SERT and NET compared to DAT, while the IFD-scores were between -8.55 kcal/mol (4XP4) and -8.60 kcal/mol (4XP9) in the MMAI-hDAT poses, -8.34 kcal/mol (5I6X) and -7.95 kcal/mol (5I73) in the MMAI-hSERT poses, and -8.04 kcal/mol (4XNU) in the MMAI-hNET pose (see table 5-8). This observation may be due to that the S1-pocket is lined between the unwound TMH1 and TMH6 that provide flexibility to the S1-pocket (crucial for the three-step mechanism) in MATs (57). Thus, MATs have a great ability to accommodate different ligands and adapt to them by induced fitting. Nevertheless, calculations of IFD-scorings are complex and involve several more factors than only the creation of intermolecular interactions in the binding pocket (see chapter 1.8.2). According to Yang et.al (209), the inadequate understanding of the complexity in the formation of

interactions and inaccuracy in scoring methods is a limitation in predicting true binding affinities (and scorings).

Additionally, as previously touched into, all the ligands in the present study were docket into the S1-site defined by a 20 $Å^3$ grid with the co-crystallized ligands as the centroid, while the S2 site is suggested to be around 13 Å from the orthosteric site – leading to that these two sites may overlap. For instance, an MD simulation by Cheng et.al (49) revealed that cocaine diffuses and settles close to the S2-site, due to the large size it was proposed that translocation deep into the S1-site was hindered. Further, S-citalopram has shown the ability to bind the S2-site at a low affinity, where binding to the vestibular (S2-) site is reported to affect the affinity for the S1-site (and vice versa): as explained in the 1.5.2, dissociation of S-citalopram in the S1-site is delayed if the S2-site is occupied at the same time, while binding to the S1-site enhance binding to the S2-site. In total, the IFD-method did not consider how binding to allosteric sites can accommodate the binding mode in the S1-site, as well as larger ligands are suggested to be able to stabilize in allosteric sites. Thus, due to the approximations made in the IFD in this study, it was hard to draw a correlation between the scorings and selectivity ratios (53, 189, 191, 210).

The results represented in table 5-8 showed that the stimulants, generally, had IFD-scores around -7.00 kcal/mol to -8.00 kcal/mol, while the other included substances had IFD-scores in the area from slightly higher than 8.00 kcal/mol to around -10.00 kcal/mol. Based on this data, it appeared that the stimulants that bound the MATs with potencies in the micromolar range (i.e., the IC_{50} values were in the micromolar range) correspondingly had lower IFD-scores - compared to the other substances that, in general, had higher potency for each MAT (i.e., K_i values were in the nanomolar-range). Thus, implying that higher potency for the MATs was associated with higher IFD-scores. Some ligands had high scores that stood out: in the outward-facing MATs, mazindol, paroxetine, citalopram, and clomipramine had scores around -10.00 kcal/mol in all three MATs – these substances had K_i values in the nanomolar range (see table 4). In addition, vanoxerine and JHW007 had similar scores in the inward-facing hSERT (see table 5-8 for exact IFD-scores). Interestingly, some similar structural features can be observed for these substances (see figure 12): all of them are highly hydrophobic ring-systems (comprising at least two aromatic moieties) substituted with halogens (i.e., fluorine or chlorine), thus, indicating that these large molecules form several favorable interactions with residues in the binding pocket. These features will be discussed in

chapter 5.2.1.2. On the other hand, MDPV had IFD-scores equal to -9.81 kcal/mol and -9.00 kcal/mol in the hDAT-models based on PDB-structures 4XP6 and 4XP1, respectively -where the IC_{50} was measured in the micromolar range (see table 4). MMAI, likewise, had IFD-scores around -8.00 kcal/mol in all MATs – the IC_{50} was also in the micromolar range.

5.2.1.2 Structure-activity relationship: context between stereochemistry in the IFD-poses, structural features and selectivity towards the MATs

The IFD-studies demonstrated either no obvious trend between selectivity, IFD-score, and the stereochemistry in each of the docket ligands (see table 5-8). Meaning that there were not any significant differences in the obtained IFD-scores with respect to the stereochemistry in the ligands – therefore no correlations to selectivity could either be detected. Again, this can be explained by the same reasons as in section 5.2.1.1. However, stereochemistry can alter both action and potency toward a target. Accordingly, the (S)-isomer of MDPV is shown to be over 100-fold more potent than the (R)-enantiomer at DAT (211), while for nisoxetine the (R)-isomer is more potent than the (S)-enantiomer at NET (212). Unfortunately, the affinity data in table 4 did not account for the stereochemistry of the included ligands, making it difficult to discuss stereochemistry as a determinant for selectivity for a specific MAT further in this thesis.

On the other hand, several SAR-studies have been performed over the years, suggesting structural features which are important towards selectivity for each MAT. These features will briefly be pointed out in this section, and in the next section (chapter 5.2.2) interactions created in the S1-pocket of hNET, hDAT, and hSERT with be examined – giving an insight into the importance of these features (and, of course, binding site residues) in the "chose" of selectivity to either a serotonergic (low DAT/SERT ratio)-, dopaminergic (high DAT/SERT-ratio)-, or noradrenergic (low DAT/NET ratio) pharmacology. Most of the studies on SAR for substances that bind the MATs are done with amphetamine and MDMA (figure 12) as starting structures to explore structural properties that enhance or decrease the preference for, respectively, DAT and SERT. Consequently, only a few similar studies on NET have been performed.

As previously mentioned, amphetamine and methamphetamine are traditional illicit stimulants that early were discovered for their stimulating effects (high potency for DAT). For psychostimulants, the addition of para (3,4 or 4)-substituents on the aromatic moiety is

suggested to enhance the preference for SERT-binding (175, 177). This is consistent with the affinity data represented in table 4, for instance: PMMA only has a methyl-ether group (para-position) in difference from methamphetamine, however, the potency for DAT was 45-fold lower compared to methamphetamine (see table 4 for ratios and figure 12). A general consideration is that the larger the aryl-substituent is, the more likely the selectivity shifts towards SERT. An homology modeling study (213) showed that NPSs with hydrophobic bulky aspects in para-position accommodated better to hSERT than hDAT, while polar substitutions in the para-position played a role in hDAT-selectivity.

Hence, the addition of 3,4-methylenedioxy groups to aromatic moieties (i.e., benzodioxole) is also associated with a shift from DAT- to SERT-selectivity (175, 177, 211). This may originate from structural similarity to MDMA (figure 12), which only possesses the two-oxygen ring system in difference from methamphetamine: as observed in table 4, MDMA had 13-fold higher potency for SERT than methamphetamine, but 16-fold lower potency for DAT (table 4), where the DAT/SERT ratios were 0.080 and 16, respectively. A corresponding finding was observed between MDPV and its derivate α-PVP, where the latter NPS lack the 3,4-methylenedioxy group (figure 12): MDPV had a 10-fold higher potency for SERT than α-PVP (table 4), including that the DAT/SERT ratio was much higher for α-PVP (DAT/SERT ratio: 192 and ∼2500, respectively). However, in total both substances still had high preference for DAT compared to SERT (table 4). From the IFD-poses in this study, the benzodioxole appeared to play an important role in MDMA, MMAI and paroxetine's preference for hSERT compared to hDAT (see section 5.2.2).

On the other hand, β-keto groups are proposed to be an important contributor for increasing potency at DAT and the DAT/SERT ratio (211, 214). This group is seen in both mephedrone, MDPV, and α-PVP which all had high potency at DAT compared to SERT. Mephedrone, however, also had relatively high potency at SERT too, which may be due to the para-methyl group in the aromatic ring. Nonetheless, methylphenidate has some structural similarities to α-PVP (figure 12) and may explain its high selectivity for DAT compared to SERT. Reported for methylphenidate is that the ester-group may be important for DAT-binding, while the β-substituent on the ester can vary. However, the potency can be affected: removement of the ester-group is reported to reduce the potency for DAT by 4-fold. Accordingly, longer alkyl-chains on the ester reduce DAT-selectivity (215, 216). Based on the IFD-poses of

methylphenidate (see chapter 5.2.2), the methyl ester seemed to play a role in methylphenidate's higher preference for hDAT and hNET compared to hSERT.

From previous chapters, it is known that bigger molecules are associated with inhibitor properties, while smaller molecules are related to substrate properties. A general trend is that inhibitors of DAT typically have a tertiary amine and an extended (or large) α-sidechain attached to the amine. For the latter feature, the amine can be primary, secondary, or tertiary – however, the selectivity for DAT will also increase in the same order. In, for instance, the IFD-poses of MDPV from this study (see section 5.2.2) the α-propyl group attached to the amine appeared to be important in MDPV's preferences for the MATs. On the contrary, simple primary amines (or N-methyl secondary amines) are linked to substrates in general (211). This trend was also observed for the included ligands in this study (see figure 12).

Substances with a "mixture" of typical features for both SERT and DAT preferences are, hence, expected to exhibit both dopaminergic- and serotonergic-like effects. According to Liechti (217) and Simmler et.al (176) this is, amongst other, seen for mephedrone which is a *cocaine-MDMA-mixed β-keto-amphetamine* and cocaine (see figure 12 and table 4). In the IFD-poses from the present study, cocaine appeared to favor the binding in both hNET, hDAT, and hSERT (see section 5.2.2).

Moreover, a study (187) profiled additional structural features that may indicate SERT-selectivity. This includes a piperidine (or an amine that can be protonated), aromatic moieties (hydrophobic feature) substituted with, amongst others, 4-fluorine, 2-fluorine, or a 3,4-methylenedioxy group, and a methoxy spacer. Some of these features were seen in the highly SERT-selective paroxetine and citalopram in this study (table 4). In paroxetine, both the 4-fluorine-substition and 3,4-methylenedioxy group appeared to be important for its high preference for hSERT compared to hNET and hDAT – in the present study (see section 5.2.2). However, citalopram is also known to bind the allosteric S2-site of SERT, which may explain the slightly different structural features compared to paroxetine - this includes, for instance, the cyano-group which is reported to be important for binding to the S2-site (210).

There are not many studies available on the SAR for ligands binding to NET. However, some similar structural features (figure 12) were observed between the highly selective NET-inhibitors atomoxetine and nisoxetine (see table 4). Both compounds have two aromatic moieties that branch from a central chiral carbon, and ortho-substitution in one of the

aromatic rings. A study by Penmatsa et.al (169) also reported ortho-substitutions in aromatic moieties as important for NET-selectivity – and shifts the selectivity from DAT-recognition. The ortho-substitution in both atomoxetine and nisoxetine appeared to play an important role in these substances' high selectivity for hNET compared to hDAT and hSERT, in the present study too (see section 5.2.2).

Finally, the atypical inhibitors differ structurally from the typical inhibitors and substrates. Due to that the atypical inhibitors are widely structurally heterogeneous, there are a lack of available studies on their SAR and pharmacophore. Interestingly, they are, however, proposed to bind the inward-facing conformation of the MATs, and thus profile similar behavioral effects (187, 206, 218). The binding mode in the S1-site may play a key role here (see section 5.2.2). Nonetheless, from figure 12 it can be observed that JHW007 and vanoxerine are structurally related: both possess two aromatic groups substituted with fluorine and comprise an ether-group. As discussed by Reith et.al (97), benztropine analogs with the addition of diphenylethers (like JHW007, and similar to vanoxerine) have been shown to act as atypical inhibitors binding the inward-facing conformation of the MATs. Thus, increasing the neurotransmission without causing any stimulating effects.

As an important note, several factors affect the structure-design of a substance that acts in the CNS. In this section, only the pharmacodynamic aspects were viewed, but the ability for a substance to "reach" CNS by, for instance, both having the ability to cross pharmacokinetic barriers in the body and penetrate BBB is also important for the overall potency, actions, pharmacological effects and side-effects (211).

5.2.2 Protein-ligand interactions and binding mode of selected ligand-protein complexes

The human MATs share around 50 % overall sequence identity, meaning that these transporters are structurally related and have the same overall fold. Although the S1-site residues among the MATs are highly conserved, divergent key residues contribute to explaining selectivity towards hNET, hDAT, and hSERT. In addition, distinct ligands induce different conformational changes to each MAT, implying that altered position of the residues in the binding pocket also affects selectivity (187, 191). As mentioned earlier, the multiple sequence alignment provided in figure S7 (supplementary material) and table 9 shows divergent and conserved amino acids in the MATs.

The intermolecular interactions and binding mode of the complexes represented in figure 24-32, will in this chapter be examined more deeply. Finally, the crucial salt bridge with Asp in TMH1 (hNET: Asp75; hDAT: Asp79; hSERT: Asp98) was formed in all complexes reported in table 5-8, reinforcing its importance for recognition.

5.3.1 Binding mode and interactions of atomoxetine and nisoxetine:

Four types of interactions with nisoxetine occurred in all MATs (figure 24): the crucial salt bridge with Asp in TMH1, H-bonds, π-π interaction and cation-π interaction. Asp in TMH1 (hNET: Asp75; hDAT: Asp79; hSERT: Asp98) engaged in an H-bond and salt bridge with nisoxetine in all poses. Further, the corresponding non-conserved Phe72 (hNET): Phe76 (hDAT): and Tyr95 (hSERT) in TMH1 also participated in a cation-π interaction in the three MATs. This residue was also engaged in an H-bond with the protonated amine in nisoxetine in hNET and hSERT. In hDAT Phe320 (TMH6) rather created a H-bond with the protonated amine group, while Phe76 participated in a π-π interaction. Further, the corresponding Phe326 (hDAT) and Phe341 (hSERT) in TMH6 formed a π-π interaction with nisoxetine, while Tyr152 (TMH3) also engaged in another π-π interaction in hDAT. Consequently, this implies that these residues are important for stabilization and recognition in MATs – and binding of nisoxetine. In total most interactions were created in the hDAT-complex. These extra interactions may explain the slightly higher IFD-scores, reported in table 5-8, of the nisoxetine-hDAT (score: -8.85 kcal/mol)- and nisoxetine-hSERT (score: -9.02 kcal/mol) complexes compared to nisoxetine-hNET (score: -8.41 kcal/mol).

Owing to that the NET-selectivity of nisoxetine is high compared to DAT (DAT/NET ratio: 0.0061-0.0014 from rat data, and 0.012 from human data) and SERT (DAT/SERT ratio: 1.09-1.83 from rat data, and 0.80 from human data), other determinants than these interactions may take part in the explanation for its selectivity.

As previously mentioned, the ortho-substitution (figure 12) possessed in nisoxetine and atomoxetine is a purposed determinant for the high selectivity for NET (192). The IFD-poses revealed that the residues surrounding the ortho-methoxy group in nisoxetine were different in the three nisoxetine-complexes (figure 24). In hNET the ortho-methoxy group was placed among hydrophobic residues, comprising Phe323, Ala145, Ala477 (hDAT: Phe326, Ser149, Ala480) – away from the hydrophilic residues in TMH8 (Ser419 and Ser420), and Tyr151 (hDAT: Phe155). In hDAT, the methoxy group was kept in the region comprising Ala423

and Phe155 – closer to the conserved polar Ser422 (TMH8). It would have been expected that a relatively polar methoxy group would favor a combination of a hydrophilic and hydrophobic environment, however, according to Andersen et.al (192) it appears that specific residues in subsite C are key determinants for NET-selectivity. In the same study, the mutation of Ala145 and Ala426 to the corresponding hDAT-residues (Ser149 and Ser429) reduced the potency of nisoxetine for NET significantly (up to 168-fold). Meaning that the non-conserved Ser149 and Ser429 are expected to create unfavorable interactions with nisoxetine. However, Ser429 (hDAT) or Ala426 (hNET) were not observed within 3 Å from the ligand in the S1-pocket in the present study. The binding mode of nisoxetine from this study, yet, agrees with the findings by Ortore et.al (187), which also claim that the "shift" of the methoxyphenyl ring in nisoxetine in hDAT weakens the salt bridge between nisoxetine and Asp79 (TMH1). In this study, the distance from the protonated amine to Asp75 (hNET) was 1.69 Å, while the distance was 3.20 Å to Asp79 (hDAT), implying a stronger interaction in hNET.

In hSERT, the methoxyphenyl of nisoxetine was placed closer to subsite B than C. Non-conserved residues also seemed to disfavor the binding in hSERT compared to hNET (figure 24). The non-conserved polar Thr439 (hNET: Ser420; hDAT: Ala423) in TMH8 can be a part of the explanation. However, the region between subsite A and B in hSERT and hNET were fairly similar in "polarity", making it difficult to explain the role of Thr439 alone in the higher NET-preference. In hNET the non-substituted aromatic moiety was placed near the polar TMH8-residues.

Furthermore, the bulky size of Ile172 (TMH3) in hSERT (hNET: Val148; hDAT: Val152) may be involved in explaining the high selectivity for NET compared to SERT. In a study (219) where Val148 in hNET was mutated to Ile, approximately 30 % of the transporter activity was retained compared to the wild type – indicating that this residue is a key determinant for NET-selectivity. Another suggestion is that the bulky Ile172 in hSERT sterically hinders the substituted aromatic ring from completely stabilizing in the hydrophobic pocket containing Phe335, Phe341, Ala169, and Ile172. Interestingly, Ortore et.al (187) explained that Ile172 in the hydrophobic cavity clashes with the aromatic system in nisoxetine, leading to that the protonated amine in nisoxetine is at a 5 Å distance from Asp98. In this study, the corresponding distance was 3.51 Å – both higher than detected in hNET and hDAT. Moreover, the polar OH-group in Tyr95 (TMH1) of hSERT may also play

a role in the stabilization of the non-substituted, non-polar, aromatic moiety of nisoxetine (hNET: Phe72; hDAT: Phe76) (see figure 24). Yet, the mutation Tyr95Ala has been shown cause a 6-fold loss of potency towards hSERT for nisoxetine – indicating that this residue is important for binding to SERT (219). This was, however, expected due to that Tyr95 was participated in a stabilizing cation-π interaction with the protonated amine of nisoxetine (figure 24).

In all three MATs, the amine of nisoxetine was positioned in approximately the same place (subsite A) and was stabilized by several interactions (see figure 24). This region consisted of mainly conserved residues.

Similar discoveries were found for atomoxetine (figure 25). To create a stable complex, both the salt bridge and H-bond with the crucial Asp in TMH1 were retained in each complex. Nevertheless, while atomoxetine-hNET only had one extra cation-π interaction with Phe72 (TMH1) compared to the two other MATs, atomoxetine was engaged in both an H-bond and cation-π interaction with the corresponding Phe76 in hDAT – in addition to a π-π interaction with the conserved Phe326. In hSERT, only an extra H-bond with the conserved Phe335 was formed. This contributed to explaining the differences in the IFD-scores observed in table 5-8: atomoxetine-hNET (score: -8.93 kcal/mol), atomoxetine-hDAT (score: -8.96 kcal/mol), and atomoxetine-hSERT (score: -8.18 kcal/mol).

As observed in figure 25, the binding mode of atomoxetine in hDAT and hSERT was similar to that seen for nisoxetine. Hence, the high preference for NET compared to DAT and SERT, can be explained by the same suggestions as for nisoxetine. However, a remarkable difference was detected between the substituted aromatic moieties of nisoxetine and atomoxetine. The methyl (ortho)-substituted aromatic ring in atomoxetine was not positioned in the most hydrophobic region of hNET. This phenomenon may be due to the smaller size of methyl compared to the methoxy group in nisoxetine. Yet, possible hydrophobic interactions between the conserved Tyr152 and non-conserved Tyr151 in TMH3 of hNET (see table 9), and the methyl-substituted aromatic moiety can be favorable during stabilization of atomoxetine. Similar binding mode was observed in a molecular dynamics study by Zheng et.al (220). The fact that this ortho-substituted aromatic ring not was placed in the "favorable" region in subsite C, and the fewer intermolecular interactions, may explain why atomoxetine has a slightly lower potency for NET compared to nisoxetine (see table 4). On the other hand,

the polar sidechain of Ser419 was “moved” away from the methyl-group in atomoxetine, and the non-substituted aromatic ring was placed in the hydrophobic region (subsite C) of hNET.

Interestingly, the non-conserved Gly149 in TMH3 of hNET (hDAT: Gly153; hSERT: Ala173) has shown to be important for NET-selectivity. According to a study by Sørensen et.al (219), the mutation Gly149Ala in hNET displayed a 4-6-fold decrease in the NET-potency of atomoxetine and nisoxetine. The findings included that Ala173 appeared to decrease the flexibility for the ligands to “shape” into the S1-pocket of SERT, but the mutation increased the hydrophobicity which was an advantage for ligands that prefer SERT. In the present study, only Ala173 was observed to be within a 3 Å distance from atomoxetine and nisoxetine in the hSERT-complexes. Gly149 (hNET) and Gly153 (hDAT) was, on the contrary, not observed in the IFD-poses, meaning that they were further away from the ligands – therefore Ala173 may have caused more steric hindrance, or reduced the flexibility, in the hSERT-complexes.

5.3.2 Binding mode and interactions of methylphenidate and MDPV:

Methylphenidate exhibited high selectivity for NET and DAT compared to SERT (table 4). In all the complexes (figure 26) the salt bridge with the crucial Asp in TMH1 was formed, reinforcing its importance for recognition. H-bonds with the protonated amine were also created in all MATs, but engaged different residues: Ser419 (hNET), Asp79 (hDAT), and Asp98 besides Phe335 (hSERT). In total, the occurring interactions could not entirely explain methylphenidates preferences for the MATs, owing to that several more interactions were observed in hDAT and hSERT than hNET. The number of created interactions was, on the other hand, reflected in the IFD-scores (table 5-8) for each complex: methylphenidate-hNET (score: -6.53 kcal/mol), methylphenidate-hDAT (score: -7.83 kcal/mol), and methylphenidate-hSERT (score: -7.43 kcal/mol).

Interestingly, the poses of methylphenidate (figure 26) exposed that the piperidine ring was in a favorable chair conformation in hNET and hDAT, while the conformation of the ring system in hSERT appeared to be “tight” packet – thus was exposed to more steric stress. This unfavorable conformation of the piperidine in hSERT may indicate methylphenidate’s higher preference for DAT and NET compared to SERT. Moreover, SAR-studies on methylphenidate point out, as mentioned in section 5.2.1, that secondary amines with extended α-chains in inhibitors favor DAT-binding (211). This was observed for the hDAT-

and hNET-complexes in the present study. The environment surrounding the piperidine was also similar in hNET and hDAT, however, an extra cation-π interaction with Phe76 (TMH1) was seen in hDAT and not hNET (nor hSERT).

The aromatic moiety and methyl ester of methylphenidate (figure 26) were placed in regions mainly comprised of non-polar residues in hSERT, which may have contributed to stabilizing the complex through hydrophobic interactions. The aromatic moiety created a stabilizing edge-to-face π-π interaction with Tyr176 (TMH3). Within 3 Å, Ser438 (TMH8 in hSERT) was the only observed polar residue, but this conserved residue was seen in all complexes – indicating that it not may have been important for determining the selectivity-preferences of methylphenidate (table 4). However, the relatively polar methyl ester (221) was in contrast to hNET and hDAT placed in the same hydrophobic region (in subsite A). Only the non-conserved Tyr95 in TMH1 (hNET: Phe72; hDAT: Phe76) contributed to a small polar surface through the hydroxy-group. Hence, the unfavorable environment for the methyl ester may play a role in the higher preference for DAT and NET compared to SERT. Unfortunately, during this present project, no other studies on the binding mode of methylphenidate in MATs were found.

Further, the aromatic moiety and methyl ester pointed in the same direction (between subsites B and C) in hNET and hDAT – as observed in figure 26. In hNET both the polar Ser420 (hDAT: Ala423; hSERT: Thr439), conserved Ser419 in TMH8, and the hydroxy-group of Tyr151 (hDAT: Phe155; hSERT: Tyr175) (TMH3), were surrounding the relatively polar methyl ester group. Hence, the more hydrophilic environment may have been favorable for this functional group. Including that, the methyl ester may have had the ability to create stabilizing H-bond with the polar residues during the stabilization of the complex (221). Similarly, the methyl ester also interacted with the non-conserved Ser149 in hDAT (hNET: Ala145; hSERT: Ala169). For both MATs, the aromatic moiety interacted with non-polar residues in the same area (between subsites B and C). In total, this region was slightly more hydrophobic in hDAT than hNET, due to non-conserved residues such as Ala423 (hDAT; hNET: Ser420; hSERT: Thr439). Interestingly, the aromatic moiety seemed to be moved away from the non-conserved Ser149 in hDAT - reducing the polar contacts with this residue. In addition, methylphenidate created a favorable π-π interaction with Phe320 (TMH6). In hNET, the corresponding Phe323 was further away from the aromatic moiety, thus no

aromatic interaction was observed. Nonetheless, the selectivity towards DAT and NET is similar for methylphenidate compared to SERT (see table 4).

MDPV also showed high preference for both DAT and NET compared to SERT (DAT/SERT ratio: 192 and DAT/NET ratio: 0.8), as seen in table 4.

From this study, the n-propyl group (extended α-sidechains) in MDPV was placed in between subsite B and C (closer to subsite C) in both hNET, hDAT, and hSERT, hence, interacting mainly through hydrophobic interactions. The IFD-poses (figure 27) further revealed that some residues in this region were the conserved Phe320, Phe326 (TMH6), and non-conserved Val152 (TMH3) in hDAT (hNET: Val148; hSERT: Ile172) - indicating that the Val (subsite B) in hNET and hDAT may play a role in the higher preference for these two MATs compared to SERT. Interestingly, Steele et.al (222), also reported other residues (not shown from the angle in figure 27) that contributed to stabilizing the n-propyl chain: important residues interacting with the n-propyl chain were: Ile484 and Ala480 (TMH10) in hDAT. These amino acids are conserved in hNET, while in hSERT the corresponding residues are: Val501 and Thr497 (table 9). Owing that hydrophobic interactions are favorable for stabilizing the n-propyl chain, the bulkier size of Ile484 may be able to create more non-polar contacts in hDAT and hNET, besides, less favorable interactions with the polar Thr497 are created in hSERT. Consequently, this may contribute to explain the higher selectivity for both NET and DAT compared to SERT (table 4).

Furthermore, the benzodioxole group of MDPV was placed in subsite B in hNET and hDAT, while it "tilted" slightly towards subsite C in hSERT – leading to that the polar 3,4-methylenedioxy group was positioned closer to the bulky Ile172 (TMH3) in hSERT. Hence, the polar 3,4-methylenedioxy group was not placed close to polar residues in TMH8 (i.e., Ser438 and Thr439), where favorable hydrophilic interactions could occur- and potentially H-bonds. In hNET, the benzodioxole was buried among both polar and hydrophobic residues that could interact with this moiety: Tyr151, Tyr152, Ser419, Ser420 (hSERT: Tyr175: Ile172: Ser438: Thr439) – in hDAT, the corresponding residues were mainly hydrophobic (hDAT: Phe155: Tyr156: Ser422: Ala423). Remarkably, the 3,4-methylenedioxy group created a π-π interaction with Tyr152 in hNET, which was not observed in the two other poses (figure 27). Interestingly, Steele et.al (222) pointed out that Ser149 in hDAT (hNET: Ala145; hSERT: Ala169) created favorable polar interactions with the benzodioxole tail group of MDPV, by explaining that theoretically H-bonds could be formed. On the other

hand, the polar 3,4-methylenedioxy ring has shown to not be a major determinant contributing to MDPV's high preference for DAT (table 4) (211, 222). In this study, the bezodioxole group seemed to be "moved away" from Ser149 in hDAT (see figure 27).

Nonetheless, the aromatic ring of the benzodioxole group created more intermolecular interactions in the hDAT-complex (i.e., π-π interaction with Phe76, Tyr176, Phe326) than in hNET and hSERT. These interactions may, in total, contribute to stabilizing the benzodioxole group in hDAT. However, in all three poses, the aromatic ring interacted with the corresponding, conserved, Tyr in TMH3 (hDAT: Tyr176; hNET: Tyr152; hSERT: Tyr176), indicating that this residue is important for the recognition and stabilization of MDPV in MATs.

Based on the IFD-poses of MDPV, the β-keto group in MDPV had the ability to create an H-bond with the conserved Ser in TMH8 (hNET: Ser419; hDAT: Ser422; hSERT: Ser438) in all three MATs. Close to this group was also the non-conserved hydrophobic Ala423 in hDAT, while the corresponding residues in hNET (Ser420) and hSERT (Thr439) were polar. By that, the poses did not entirely explain why the β-keto group has been shown to be important for increasing the potency at DAT, and hence the DAT/SERT ratio, yet the non-polar Ala423 in hDAT may role (211, 214, 222).

Finally, the pyrrolidine ring containing the protonated amine was placed in subsite A in all MAT-complexes, forming the crucial salt bridge with Asp in TMH1 (hNET: Asp75; hDAT: Asp79; hSERT: Asp98). As observed in figure 27, the same Asp also created an H-bond with the protonated amine in hNET and hSERT, while the amine rather was engaged in an H-bond with Tyr156 in hDAT. Again, the intermolecular interactions were not reflected by the IFD-scores: -9.81 kcal/mol (MDPV-hDAT complex), -7.87 kcal/mol (MDPV-hSERT complex), and -7.61 kcal/mol (MDPV-hNET complex).

5.3.3 Binding mode and interactions of MDMA, MMAI and paroxetine:

MDMA had high preference for SERT and NET compared to DAT (table 4). Similar to nisoxetine and atomoxetine the intermolecular interactions did not give much information about the selectivity-profile of MDMA. As seen in figure 29, all complexes formed a salt bridge and H-bond with Asp in TMH1 (hNET: Asp75; hDAT: Asp79; hSERT: Asp98). In addition, an H-bond and cation-π interaction with the non-conserved Phe72 (hNET): Phe76

(hDAT): and Tyr95 (hSERT) in TMH1 was created. Thus, indicating that these residues are important for MDMA-recognition. Only in the hNET an extra π-π interaction with the conserved Tyr152 was observed, which may explain the slightly higher selectivity for NET compared to SERT and DAT (see table 4). However, the IFD-scores in table 5-8 did not reflect the number of interactions in each complex: MDMA-hNET (score: -7.63 kcal/mol), MDMA-hDAT (score: -8.64 kcal/mol), and MDMA-hSERT (score: -8.28 kcal/mol).

Moreover, in the S1-pocket of hNET and hSERT (figure 29), two residues appeared to stabilize the benzodioxole tail group of MDMA by having the ability to create H-bonds with the oxygens of the polar 3,4-methylenedioxy-group and stabilize the aromatic moiety through hydrophobic interactions: this comprised the non-conserved Tyr151 in TMH3 (hSERT: Tyr175; hDAT: Phe155), and Ser420 in TMH8 (hSERT: Thr439; hDAT: Ala423) of hNET. Including, the region between subsite B and C in hNET and hSERT involved more hydrophobic residues than hDAT. A key residue here was the polar non-conserved Ser149 in TMH3 of hDAT (hNET: Ala149; hSERT: Ala169). These findings are in accordance with the findings by Islas et.al (223).

MMAI exhibited especially high preference for SERT compared to DAT, yet, the preference for NET was also high in comparison to DAT (table 4), however, there were no available studies on its binding mode or other aminoindane-analogs. Nonetheless, the interactions in the IFD-poses (figure 28) could not reflect selectivity preferences for MMAI, especially since fewest interactions were observed in the MMAI-hSERT complex. Like MDMA, a salt bridge and H-bond with the crucial Asp in TMH1 appeared to be important in stabilizing MMAI. Additionally, a cation-π interaction with the non-conserved Phe (hNET: Phe72; hSERT: Phe76) and Tyr95 (hSERT) in TMH1, and an H-bond with the conserved Ser in TMH6 (hNET: Ser318; hDAT: Ser321; hNET: Ser336), were observed in all complexes. The extra interactions in hDAT and hNET were neither reflected in the IFD-scores in table 5-8: hNET (-8.04 kcal/mol), hDAT (-8.60 kcal/mol) and hSERT (-8.34 kcal/mol).

The IFD-poses revealed that MMAI induced different conformational changes in the MATs, which could be observed by the distinct placement of corresponding residues (see figure 28 and table 9). Thus, the orientation of the methoxy-substituent was directed to the non-conserved Tyr in TMH3 in both hNET (Tyr151) and hSERT (Tyr175), while in hDAT the aromatic methyl-group was directed to the corresponding Phe155. Interestingly, in hSERT the methoxy group was placed in a region consisting of both polar and hydrophobic residues

(see figure 28). This region was, amongst others, provided by TMH3 (Ile172 and Tyr175) and TMH8 (Thr439 and Ser438). It appeared, similar to the benzodioxole tail of MDMA, that this environment may have been favorable for the relatively polar methoxy group. Hence, the polar surrounding residues may act as H-bond donors during the stabilization of MMAI, by interaction with the lone electron pair on the methoxy group oxygen (224). Additionally, the methyl-substituent was stabilized in a hydrophobic region in hSERT (comprising Phe341, Ala169, Phe170, and Ile172). The bulky size non-conserved Ile172 may also play a role in the stabilization of MMAI. Unfortunately, no studies on the binding mode of MMAI were found, making it difficult to support these findings furthermore.

In hNET, the methoxy group of MMAI was in contrast "moved away" from the polar residues Ser420 and Ser419 (hSERT: Thr439 and Ser438), due to a different placement of TMH8. Thus, it was positioned in a slightly more hydrophobic environment: this orientation, however, of the aromatic moiety allowed the formation of a π-π interaction with Tyr152 in hNET, which was not observed in hSERT. Owing the slightly lower potency for NET compared to SERT (table 4), the region in hSERT consisting of both polar and hydrophobic residues may be important for MMAIs preference for SERT. Contrasting the other MATs, mainly non-polar residues surrounded MMAI within a 3 Å distance in hDAT. This hydrophobic environment would overall be expected to also be favored by MMAI. However, an eye-catching difference from hNET and hSERT was that the S1-pocket in hDAT appeared to be more "tightly packet", which may have caused more steric stress. Including, the methoxy group were placed in a hydrophobic environment.

Moving further, paroxetine is a typical inhibitor with high selectivity for SERT. All paroxetine-complexes (see figure 30) formed a salt bridge and H-bond with the conserved and crucial Asp in TMH1, however, hydrophobic interactions were only formed in the hDAT and hSERT. Remarkably, all complexes still had high IFD-scores: -10.39 kcal/mol (paroxetine-hNET), -10.31 kcal/mol (paroxetine-hDAT), and -10.36 kcal/mol (paroxetine-hSERT). The IFD-poses discovered that the orientation of paroxetine was approximately the same in all complexes: the para-fluor aromatic moiety was placed in subsite C, the benzodioxole tail group was positioned in subsite B, and the protonated amine moiety was placed in subsite A. This agrees with the findings by Coleman et.al (225) and Zeppelin et.al (52). Therefore, some key residues in each subsite may explain the high selectivity for hSERT compared to the two other MATs.

In hSERT the benzodioxole tail group of paroxetine seemed to be stabilized by both hydrophilic- and hydrophobic residues (i.e., Ile172, Tyr175, Tyr176, Leu443, Thr439, Ser438), like MDMA. The corresponding moiety was in hNET also buried in the same environment but closer to subsite C: Val148, Tyr151, Tyr152 (TMH3); Met424, Ser420, and Ser419 (TMH8). The distance from the polar residues were approximately the same in hNET and hSERT, yet a key difference was the less bulky Leu443 in hSERT compared to Met424 in hNET (hDAT: Met427), which may contribute to the selectivity for SERT. Consequently, subsite B of hDAT comprised mainly of hydrophobic residues. Key residues were the non-conserved Phe155 (hNET: Tyr151; hSERT: Tyr175), and Ala423 (hNET: Ser420; hSERT: Thr439). The polar Ser422 (TMH8) in hDAT was also too far away from the 3,4-methylenedioxy group (7.89 Å) to be able affect this group significantly. Thus, the more hydrophobic environment surrounding the benzodioxole and methoxy spacer in hDAT, may contribute to the lower preference for this transporter compared to hSERT .

The fluorophenyl moiety (figure 30) was placed in a hydrophobic region between subsites B and C in the three complexes. Interestingly, the conformation of Phe326 in TMH6 (hDAT) made paroxetine able to create two π-π interactions (edge-to-face and sandwich type) with this residue. This was not observed for the corresponding conserved residue in hNET, yet, in hSERT an edge-to-face π-π stacking was formed with Phe341 (TMH6). According to Ortore et.al (187), the small polar surface of the non-conserved Thr497 (TMH10) in hSERT (hNET: Ala477; hDAT: Ala480) seems to be able to receive fluor-substituents better, which contributes to the overall stabilization in hSERT. Therefore, another suggestion is that the non-conserved Tyr95 (hNET: Phe72; hDAT: Phe76) also provide polar stabilization, owing to the formation of possible H-bonds with fluor during stabilization of the complex.

Regardless, the protonated amine (both in MDMA, MMAI, and paroxetine) was positioned in subsite A in all MATs, and most of the intermolecular interactions were engaged with this group. Finally, paroxetine compared to MDMA and MMAI occupied the S1-pocket to a larger extent, due to its larger size – thus explaining why it is an inhibitor and not a substrate.

5.3.4 Binding mode and interactions of cocaine:

Cocaine is a non-selective MAT-inhibitor (table 4). In the IFD-poses (figure 31) from this study, the aromatic ring of cocaine appeared to be buried in a hydrophobic region between subsites B and C. While this moiety was placed more towards subsite C in hNET and hSERT,

it appeared to have moved away from the non-conserved polar Ser149 in TMH3 of hDAT (hNET: Ala145; hSERT: Ala169) – hence the aromatic moiety was placed more towards subsite B. However, the aromatic ring of cocaine was in all MATs surrounded and stabilized by hydrophobic residues, and as proposed by mutational studies (226, 227, 228), the TMH3 residues Val152 (hDAT; hNET: Val148) and Ile172 (hSERT) have all been shown to be important for cocaine-recognition (see figure 31) – although these residues not are conserved in the SLC6 transporter family. Interestingly, only in hSERT, the aromatic ring formed a favorable π-π interaction with the conserved Phe335 (TMH6).

In all complexes (figure 31), the tropane ring was directed towards Asp in TMH1 (hNET: Asp75; hDAT: Asp79; hSERT: Asp98). In hDAT, the protonated amine also created a cation-π interaction (Phe76 in TMH1) and an H-bond (Asp79) that was not observed in the two other MATs, although the distances to the corresponding residues (hNET: Phe72; hSERT: Tyr95) was approximately the same. However, the IFD-scores were around -8.00 kcal/mol in all three poses (table 5-8). Overall, the environment surrounding the tropane ring was similar in all MATs. Further, the methyl ester was close to a small polar surface in all complexes. However, the methyl ester was in hNET closer to both the non-conserved Ser420 (hDAT: Ala423; hSERT: Thr439) in TMH8 and conserved Ser149 in TMH3, leading to a more favorable polar environment for this functional group (221).

The binding modes detected in this study were in accordance with other studies on cocaine (148, 226, 227). On the other hand, the pose of cocaine in hSERT was not the same as proposed by Koldsø et.al (229), which found that all IFD-poses of cocaine bound to hSERT had the same orientation as in hDAT – both in the placement of the aromatic moiety and tropane ring. Unfortunately, no other studies on the cocaine-hSERT binding mode or interactions were found: Zepplin et.al (52) also used the results from Koldsø et.al as the basis for their cocaine-hSERT studies. Consequently, the methods differed from the ones applied in the present study. The hSERT-model was a homology model based on LeuT (PDB-code: 2A65), and the IFD-procedure differed from the IFD protocol by Schrödinger (116): according to Koldsø et.al (229) the default H-bond cut-off was increased from -0.05 kcal/mol to 0.00 kcal/mol (i.e., the criterion of minimum one H-bond in a given pose was removed) – leading to that cocaine not entirely could bind inside the S1-pocket (229). Note that the overall sequence identity is ~20-25 % between LeuT and the human MATs, which is lower

compared to the overall sequence identity between dDAT (template in this study) and the human MATs (~50 %) (42).

5.3.5 Binding mode and interactions of ibogaine and vanoxerine:

The IFD-poses of ibogaine and vanoxerine (figure 32) in the inward-facing hSERT showed that Phe335 (TMH6), Phe341 (TMH6), Phe347 (TMH6), and Ala441 (TMH8) had moved tighter into the S1-site compared to the complexes with the outward-facing hSERT (see also figure 23). This conformational change was expected, due to that the tilting of TMH6 and TMH8 results in a block of the release of the atypical inhibitors to the extracellular side of the membrane (146). The movement of Phe335 (TMH6) closer to Tyr176 (TMH3) leads to a closure of one of two extracellular gates (see chapter 1.5). Owing to that figure 32 only displays residues within 3 Å from the ligands, the extracellular gate created between Arg104 (TMH1) and Glu493 (TMH10) is not shown – but this gate was observed in both poses.

Ibogaine and vanoxerine had both high IFD-scores (-8.80 kcal/mol and -10.83 kcal/mol, respectively) as observed in table 8. Interestingly, vanoxerine had a better score although it is suggested to be DAT-selective, while ibogaine has a higher preference for SERT (182, 187, 205). Again, the IFD-scores did not have any clear correlation to the ligands selectivity, however, the higher score for vanoxerine may be due to that the bigger size of vanoxerine induced more interactions or contacts in the S1-pocket. Nontheless, each of the complexes (figure 32) created the crucial salt bridge with Asp98 (TMH1), in addition to H-bonds and π-π interactions. Owing to the different structures of the substances and occupation in the S1-pocket, different residues were involved in the latter interactions. Consequently, atypical inhibitors do not have an "overall" SAR, owing to that this group of substances is heterogenous (see section 5.2.1). Nonetheless, looking deeper into the S1-pocket it was possible to detect some similar residues that may have contributed to stabilizing each of the substances in the inward-facing hSERT.

In both complexes, Phe335 (TMH6) appeared to stabilize the ligands by creating a hydrophobic environment for the relatively non-polar vanoxerine and ibogaine – indicating that this is a key residue for stabilization in the inward-facing conformation. Consequently, this residue was also engaged in a π-π interaction with one of the fluorophenyl moieties in vanoxerine, and H-bond (through the backbone) with the protonated amine in ibogaine (figure 32). Furthermore, in both poses mainly hydrophobic residues surrounded the ligands,

which may have contributed to further stabilize them. Thus, the aromatic moieties were stabilized through π-π interactions: in ibogaine the aromatic moiety interacted with Phe347 (TMH6), and in vanoxerine one of the fluorophenyl rings interacted with both Phe341 (TMH6) and Phe335 (TM6). In an environment of lipophilic residues, the neutral amine of ibogaine was also stabilized by an H-bond with the backbone of Ala441 (TMH8), which may also explain ibogaine's stabilization in the inward-facing hSERT. Ala441 was also placed near vanoxerine. Vanoxerine, on the other hand, formed an H-bond with Asp98 (TMH1).

These findings are in agreement with a study by Coleman et.al (146) regarding ibogaine. Also, an interesting point by Jacobs et.al (207), was that ibogaine structurally is similar to 5-HT. However, due to the bigger size of ibogaine, it rather acts as an inhibitor at hSERT than a substrate. According to Coleman et.al (146), ibogaine has a 10-fold lower binding to the outward-facing hSERT, reinforcing that ibogaine binds the inward conformation. The unique behavior of ibogaine is also suggested to be due to interactions with a possible S3-site, sited slightly below the S1-site (97). This will, nonetheless, not be discussed in this thesis. There were unfortunately not any studies regarding the binding mode of vanoxerine in the inward-facing hSERT (or hDAT), making it challenging to compare the findings in this study to other discoveries. However, two studies (97, 204) have pointed out the diphenyl-methoxy group of vanoxerine as an important structural determinant for its atypical binding profile. From the IFD-pose of vanoxerine in hSERT, in this study, it was observed that all the aromatic moieties of vanoxerine was placed among favorable hydrophobic cavities. The IFD-score was also high. In section 5.3, the interactions between vanoxerine in both the outward-facing and inward-facing hSERT will be examined more.

5.3 Molecular dynamics simulations

MD simulations were the last part of this study. Contrasting the IFD-poses, these simulations gave insight into intermolecular interactions that were important during the stabilization of ligand-MAT complexes and provided information about the orientation of the ligands in the S1-site. Hence, MD simulations were valuable in gaining more knowledge about selectivity for a specific MAT, based on contact frequencies of the occurring interactions and stability.

The advantages of simulations are that they provide the dynamic behavior of a system concerning the orientation in the lipid bilayer, rather than a still image, giving a higher reliability and biological context. Additionally, MD simulations capture the motion of every atom at any point of time. This is difficult to obtain in experimental methods. However, it is important to note the limitations of this computational method. Firstly, the accuracy of the simulation is dependent on the quality of the protein models (or experimental determined structure) used in the study (121). Furthermore, MD simulations are calculated based on the selected force field for the system. In this study, the latest force field, OPLS4, was applied to all the systems. OPLS4 has improvements in terms of, amongst others, a more precise representation of water solvation and hydration, as well as progressed performance in predicting ligand-protein binding affinities. Nevertheless, force fields are based on approximations, hence they are not perfect or entirely accurate (121, 230).

Another limitation is the simulation timescale. It is desired to capture important biomolecular processes – such as the binding of ligands and conformational alterations. In this study, the time step size was set to two femtoseconds: typically, structural alterations of proteins happen in timescales around nano-or microseconds. Besides, the simulations were run for 100 ns, which was long enough to see the stabilization of the ligand-MAT complexes from the IFD. On the other hand, if the time step size is not short enough to "catch" fast molecular movements, important molecular events can be missed. Including, longer time steps may induce less stability to the system (121).

Lastly, MD simulations may be time consuming, but this is in advantage of the valuable dynamic information provided by this molecular method. MD simulations are more and more used to both understand experimental results and to guide experimental work – in addition, this theoretical approach can generate hypotheses for further experimental work (121).

5.3.1 Stability analysis of the ligand-protein systems

Both RMSD- and RMSF plots were used to evaluate the stability and structural alterations in the five generated ligand-MAT complexes, as described in section 4.3.2. The RMSF plots also revealed the structural stability and mobility in the binding site.

Overall, the RMSD plots of the nisoxetine-hNET-, methylphenidate-hDAT-, and MDMA-hSERT (outward-facing) complexes (see figure 33), were relatively stable during the entire simulation. However, a general consideration was that the Ligand RMSDs upon stabilization generally were lower than the Protein RMSD, meaning that the ligands were in the same position during the simulation and that greater deviations arose in the MATs – concerning the reference structure. This was expected, due to that proteins conform to ligands by induced fitting – to make the most energetically favorable complex. Yet, ligands also accommodate the binding pocket (115, 116, 117). The greatest deviations were detected at the beginning of the simulations, nonetheless, the mean RMSD were lower than 3.0 Å in all systems (122), implying that slight deviations from the initial conformation occurred. In total, all the systems reached equilibrium, but nisoxetine (figure 33) seemed to have some outlier Ligand RMSD-values from around 83.80 ns, and the simulation was not long enough to observe if these values "just" were outliers or if nisoxetine deviated more from the initial reference structure.

Moreover, the observations from the RMSF plots (see figure 35) were in consonance with the knowledge about secondary structures (188): the most flexible regions were in the loop- and terminus areas in all five systems. Additionally, the S1-site residues in contact with the ligands showed relatively rigid behavior (mean RMSF was lower than 1.0 Å), indicating that these residues were stabilized through intermolecular interactions with the ligands.

In the systems with vanoxerine, similar tendencies were observed (see figure 34 and 36). Interestingly, the Ligand RMSD for vanoxerine in the outward-facing hSERT was much higher than in the inward-facing hSERT, in the first 82.00 ns of the simulation (figure 34). Thus, this indicated that vanoxerine in the first conformation underwent more conformational changes before stabilizing. In both systems, on the other hand, the Ligand RMSDs were lower than 3.0 Å. Lastly, the inward-facing hSERT bound to vanoxerine had both slightly higher RMSF and Protein RMSD compared to the outward-facing hSERT. No stability studies on vanoxerine were found by the time of this project, yet the higher degree of

flexibility and conformational change may be due to that the S1-pocket had to adapt to a "extended" conformation of vanoxerine. In the outward-facing hSERT, vanoxerine had a more "compact" conformation, thus, it did not occupy as large space in the S1-site. This will be discussed more in the next chapter.

As mentioned earlier, an important note is that great conformational changes occur during the three-step mechanism upon binding to the MATs (41). The MD simulations did not capture these events, due to that the poses from the IFD were used for the simulations. Consequently, the ligands were already bound to the MATs, and from the IFD-procedures the most favorable poses were chosen. Hence, intermolecular interactions were also created in each pose, which also may have contributed to "holding" the ligands in a stable position in the S1-site – and overall stabilizing the complexes. Unfortunately, no ligand-free systems were created, therefore, the conformational changes in the bound MATs could not be compared to their usual dynamic behavior.

5.3.2 Protein-ligand interactions during molecular dynamics simulations

In this study, it was interesting to further examine residues that contributed to the overall stability through intermolecular interactions with the ligands that persisted for more than 30 % of the simulation. This was described in more detail in section 4.3.3. These residues may be determinants participating in the explaining of a ligand's preference for a specific MAT. The following three systems of the outward-facing MATs were studied through MD simulations: nisoxetine in hNET (DAT/NET ratio: <0.10), methylphenidate in hDAT (DAT/SERT ratio >10), and MDMA in hSERT (DAT/SERT ratio: <0.10) – giving a deeper insight into interactions in each MAT bound to ligands that showed high preference for them compared to the other MATs, respectively (see table 4). However, it would also have been interesting to run MD simulations of these ligands in all three MATs in the future, to observe if there are any differences in the persistence of the interactions and stabilization in the S1-pocket – which overall also contribute to the knowledge of a substance's selectivity. Moreover, vanoxerine in both the inward- and outward-facing hSERT was also studied through MD simulations.

As observed from figure 37 slight conformational changes occurred in the transporters and ligands throughout the simulations, as well as the ligands mainly were in the same position in all frames. Thus, it was expected that specific interactions with some key residues were

maintained more than 30 % of the simulation time - to “keep the ligands stable”. In all systems, except for vanoxerine bound to the outward-facing hSERT, the ability to maintain the salt bridge with Asp (hNET: Asp75; hDAT: Asp79; hSERT: Asp98) throughout the 100 ns was seen. This ionic interaction is, as described earlier, essential for binding to the MATs (41, 42, 51, 231). This will be discussed more in this section.

In the nisoxetine-hNET system (figure 38), the same interactions as detected in IFD-pose (figure 24) were maintained more for than 30 % of the entire simulation – comprising an H-bond with Asp75 (TMH1), cation-π interaction with Phe72 (TMH1), and π-π interaction with Tyr152 (TMH3). Again, these interactions appear to be important for recognition and stabilizing of nisoxetine in hNET. Interestingly, an H-bond between the protonated amine and conserved Phe317 (TMH6) lasted around 80 % of the simulation but was not shown in the IFD-pose. Also, in section 5.2.2, the hydrophobic pocket in subsite C was pointed out as important for NET-selectivity (192, 219, 232). The ortho-methoxy phenyl was placed in this hydrophobic region, which differed from that observed in hSERT and hDAT (figure 24). The MD simulations revealed that Val148 (hDAT: Val152; hSERT: Ile172), conserved Phe323, conserved Phe317, and Ala477 (hDAT: Ala480; hSERT: Thr497) contributed to stabilizing this moiety through hydrophobic interactions that lasted more than 30 % of the simulation (lilac bars in figure 38). Many of these interactions were, however, described section 4.3.1 based on the five frames from the MD simulation.

Moreover, a water molecule in subsite C also created a stabilizing water bridge with the methoxy oxygen that persevered for 34 % of the simulation, reinforcing the favorable placement of the ortho-methoxy phenyl in subsite C. Joseph et.al (232) proposed that the ability to interact in the vicinity of subsite C, and displace water molecules in this region, shift selectivity towards NET for a substance. The same article pointed out that the binding of nisoxetine in this region was similar to that seen for the catechol group of the NE, and in contrast to DA that placed the catechol in the vicinity of subsite B. Observed from the schematic diagram of nisoxetine-hNET (figure 38), it is possible to see that water molecules (light grey spheres) surrounded the methoxy- and ether group of nisoxetine, indicating that complex water-mediated networks contribute to stabilizing moieties in subsite C. The same water molecule also interacted with Asp75 (TMH1) through an H-bond.

Methylphenidate was further looked at in hDAT. However, as reported in table 4, methylphenidate had similar preference for both DAT and NET (DAT/NET ratio: 0.92). The

same tendencies were also observed for the other included DAT-selective ligands (e.g., MDPV and α-PVP): hence, it appeared that high DAT-selectivity was associated with high NET-selectivity compared to SERT – but not vice versa (see table 4). According to Andersen et.al (192), almost 80 % of the residues within 8 Å in the S1-site of hNET and hDAT are conserved. In the same article, it was drawn attention to that several NET-and DAT inhibitors have been developed (e.g., methylphenidate) and drugs with high selectivity for NET (e.g., atomoxetine), but not substances that exhibit an extensive preference for DAT over NET. The background for this type of preference is poorly understood, yet it is suggested that the non-conserved residues and binding mode in NET (i.e., subsite C) is an essential part of the preferences for NET over DAT. Residues in EL4 and the extracellular permeation pathway have also been suggested to play a role in the selectivity for NET over DAT, however, this was not examined in the present study (192).

Moving further, only the H-bond with Asp79 (TMH1) and π-π interaction with the conserved Phe326 (TMH6), as observed in the IFD-pose of methylphenidate in hDAT, were maintained over 30 % of the simulation (figure 26 and 39) – implying that these interactions are important for recognition and stabilization of methylphenidate in hDAT. On the other hand, the cation-π interaction with Phe76 (TMH1) persisted less than 30 % – in the description of the five frames (section 4.3.1) this specific interaction was only seen in frame 1. However, the bar chart in figure 39, showed that this residue in total was involved in hydrophobic interactions with methylphenidate in around 60 % of the simulation (including the cation-π interaction), which supports that Phe76 (hNET: Phe72; hSERT: Tyr95) may be a determinant for methylphenidate's preference in DAT (and NET). Fascinatingly, a π-π interaction with the conserved Tyr156 (TMH3) in subsite B was present in 77 % of the simulation time, which was not shown in the IFD-pose, indicating that the placement of the aromatic moiety between subsite B and C was favorable. Lastly, Val152 (TMH3) in subsite B was also engaged in hydrophobic interactions with methylphenidate (bar chart in figure 39) – this residue is conserved in hNET (Val148), while in hSERT the corresponding residue is Ile172. Hence, this underpins the role of Val in the selectivity for hNET and hDAT over hSERT.

Contrasting the binding mode of nisoxetine in hNET, methylphenidate did not "explore" subsite C in hDAT to the same extent (figure 24). However, water molecules also surrounded both the piperidine ring and aromatic moiety (and methyl group in the methyl ester) of methylphenidate in hDAT (see figure 39). Thus, implying that interacting water networks

also is important for binding to DAT. In fact, a water bridge was mediated with the protonated amine of methylphenidate and Phe320 (TMH6) in 39 % of the simulation time (figure 39). Two studies (42, 233) observed that interactions with water molecules in the S1-site of hDAT are important for stabilizing the biogenic DA in the binding pocket – before the transporter "transforms" to an inward-opening conformation, supporting the role of water in the binding to DAT. Interestingly, methylphenidate's occupation of the region between subsites B and C was similar to that observed for the catechol of DA by Joseph et.al (232). Consequently, the three-step cycle was suggested to accelerate faster when the S2 (vestibular)-site also was occupied, which was not examined in the present study.

When it comes to the MDMA-hSERT system, no water molecules were observed to interact with MDMA or the residues in the S1-site (figure 40). Several studies on the translocation process and binding of substrates to hSERT have been performed (51, 52, 145, 229), yet the role of water molecules in the S1-site is minimally stated. However, as pointed out by Hellsberg et.al (234), hydration of the orthosteric S1-site is an important stage in the three-step mechanism in hSERT. In the present study, it appeared that water bridges with MDMA not played a major role in the stabilization of this ligand in the S1-pocket. In this case, it would have been interesting to run MD simulations of MDMA in hNET too, to observe if any interactions with water molecules, lasting over 30 % of the simulation, occurred.

Furthermore, the same intermolecular interactions that were detected in the pose of MDMA in hSERT (figure 29) were maintained for more than 90 % of the entire simulation (figure 40). This was expected, due to that the "dynamic visualization", displayed in figure 37, showed little conformational changes in MDMA and the position in the S1-pocket (this was also observed in the RMSD plot of MDMA, see section 4.3.2.1). These results indicate that both an H-bond with Asp98 (TMH1) and Tyr95 (TMH1), and cation-π interaction with Tyr95 are important for both the recognition and stabilization of MDMA in the binding pocket. Additionally, the MD simulations revealed that the non-conserved Ile172 in TMH3 (hNET: Val148; hDAT: Val152) was engaged in hydrophobic interactions with MDMA in more than 38 % of the simulation, underpinning the role of this residue in the binding-preference for SERT.

Finally, several articles describe that vanoxerine is a selective atypical inhibitor of DAT (96, 97, 187, 204). Unfortunately, in the present study the studies on vanoxerine were done in

hSERT and not hDAT. In the future, it would therefore be interesting to do the same analysis in the outward-and inward facing hDAT.

Interestingly, several extra interactions were exposed to last more than 30 % of the simulation than observed in the IFD-pose of vanoxerine in the inward-facing hSERT (figure 41 and 32, respectively). Firstly, the findings underpin the importance of the creation of both an H-bond and salt bridge with Asp98 (TMH1) for the recognition and binding of vanoxerine. Secondly, as described in section 5.2.2, the movement of Phe335 (TMH6) closer to the "center" of the S1-pocket seemed to be a key for the stabilization of vanoxerine. Phe335 was involved in interactions in more than 120 % of the simulation, comprising both a π-π interaction with the 4-fluorophenyl (33 %), cation-π interaction with the protonated amine (60 %), and other non-specific hydrophobic interactions. Additionally, Phe341 (TMH6) took part in interactions with vanoxerine in around 90 % of the simulation, through both a π-π interaction (41 %) and other non-specific hydrophobic interactions (~50 %).

The MD simulations in the present study support the fact that the diphenylmethoxy moiety of vanoxerine is a structural key for binding an inward-facing conformation of the MATs (97, 187, 204). Through the trajectories, several residues in the pocket (Phe341, Phe335, Ile172, and Tyr176) of the diphenylmethoxy interacted with this moiety via hydrophobic interactions (over 30 % of the simulation, figure 41), thus, stabilizing the complex. The monosubstituted aromatic ring was, on the other hand, stabilized by Phe347 (TMH6) and Tyr95 (TMH1) for over 40 % of the 100 ns. These interactions were described in section 3.4.1 in more detail.

Few studies were available on vanoxerine's binding to the outward-facing conformation of the MATs. Ortore et.al (187) performed a docking in the outward-facing hSERT and found a similar binding mode as the present study. However, the article did not discuss the interactions in the docking pose. Previously, the salt bridge with Asp in TMHs, Asp98 in hSERT, was stated as crucial for recognition and binding to the MATs (41, 42, 51, 231). In this study, this interaction was only maintained in 43 % of the trajectories (figure 42) in the last system, which may explain that binding to the outward-facing hSERT is less favorable for vanoxerine – nor an H-bond with this residue was created, as observed for all the other systems. As described in section 4.3.3, it seemed that this ionic interaction was "replaced" with a cation-π interaction with Tyr95 (TMH1).

The 4-fluorophenyl rings were stabilized through π-π interactions in more than 30 % of the simulation, comprising Tyr175 (TMH3) in subsite B and Phe341 (TMH6) in subsite C. Additionally, Val501 and Phe334 in subsite C interacted with one of the fluorophenyl rings through hydrophobic interactions (over 30 % of the time), similarly, Ile172 and Ala174 (TMH3) contributed to stabilization in subsite B. In contrast, the monosubstituted aromatic ring did not engage in any specific intermolecular interactions throughout the simulation – as observed in the inward-facing hSERT. As touched on earlier, the conformation of vanoxerine differed from that observed in the inward-facing hSERT. As detected from figure 37, this conformation may not have been favorable, especially since it did not allow the formation of a salt bridge with Asp98 (TMH1). Lastly, Phe335 did not maintain hydrophobic interactions with vanoxerine that lasted over 30 % of the 100 ns in the outward-facing conformation (figure 42).

In an inward-open conformation of the MATs, the release of both ions and substrate to cytosol is promoted by hydration of the binding sites (96). However, from the MD simulations in the present study, water bridges were present in around 1 % in each system with vanoxerine (figure 41 and 42), indicating that water may play a minor role in the stabilization of vanoxerine. As a note, vanoxerine is a large molecule, hence, it is not transported to cytosol but rather is suggested to block the transporter in an inward-facing conformation (96). An interesting note is that the large occlusion of the S1-pocket by vanoxerine, in the inward-facing conformation, hinders water to enter the binding pocket – which is an important last step before translocation of the substrate to cytosol. Nonetheless, there were difficult to find studies regarding the role of water in the binding of atypical inhibitors.

Again, the mechanism and binding mode of atypical inhibitors are poorly understood. There are many studies supporting that vanoxerine binds the inward-facing MATs (specifically DAT), but if it binds this state directly or via the occluded state is not entirely investigated (96, 97, 187, 204).

5.4 Future prospects

As previously mentioned, a vital goal set by WHO (62), for the period 2022-2031, is the development of new and effective treatment for CNS disorders - to value the brain health. The pathophysiology behind disorders in CNS is complex and not fully understood; however, involved in several of these conditions and their comorbidities are the imbalance and disruption in monoaminergic neurotransmission. This comprises, amongst others, multiple sclerosis, ADHD, major clinical depression, anxiety, and Parkinson's disease (202, 235, 236).

In the treatment of ADHD, methylphenidate has been a mainstay by acting on both DAT and NET with high potency (table 4). However, the enhanced mesolimbic dopaminergic transmission is linked to potential for abuse and addiction (see section 1.7). Non-stimulants, such as the sNRI atomoxetine, are also effective in reducing core symptoms of ADHD without any abuse potential – demonstrating a huge advantage. Owing absence of randomized clinical studies lasting more than 12 weeks, it is difficult to state which is the most effective. Yet, methylphenidate is considered as the first-line therapy (237). Moreover, reuptake inhibitors of DAT are also proposed to be beneficial as an add-on therapy in the treatment of non-motor symptoms in patients with Parkinson's disease. This includes symptoms like depression, cognitive deficits, and fatigue (236). In multiple sclerosis, selective NET-and SERT-inhibitors are suggested to reduce inflammation in CNS caused by this neurodegenerative disorder (235). Additionally, as described in earlier chapters, SSRIs are an established part of the treatment of severe depressive disorders (202).

All in all, there is yet a need for effective treatment for CNS disorders that are deficient in adverse side effects - and a greater understanding of the role of MATs in their pathophysiology. The orthosteric site in MATs is highly structurally conserved, making it challenging to design drugs that exhibit great selectivity for a specific MAT. In this study, however, non-conserved residues in the S1-site and specific structural features in the included ligands appeared to be important for determining selectivity towards hNET, hDAT, and hSERT – which can be used as starting points for the development of novel drugs with high selectivity and potency for the MATs, and their role in the treatment of CNS disorders.

Additionally, the anti-addictive properties of atypical inhibitors, make these substances valuable for further investigation of treatment of stimulant addiction (97, 207, 218). Unfortunately, this study only examined the atypical inhibitors in the inward-facing hSERT.

In the future, it would have been interesting to run MD simulations for other substances than vanoxerine (such as JHW007) in both the inward-and outward facing conformation of all MATs. Besides, models of the inward-facing hNET and hDAT should be investigated to further identify determinants for selective binding to the MATs in an inward-facing conformation.

Finally, the result in the present study is based on a theoretic computational approach. As discussed in section 5.1 to 5.3, computational methods are based on approximations and simplifications. The ability to penetrate BBB, the complete three-step mechanism in binding to the MATs (thereby the suggested effect of EL4 for MAT-selectivity), and allosteric effects were also neglected in this study. Hence, to get a more comprehensive and accurate understanding of determinants for selective binding to the MATs, the methods and results should be combined- and tested experimentally (e.g., mutational studies).

6 Conclusion

The MATs (i.e., DAT, SERT, and NET) are vital therapeutic targets for several pathophysiological conditions in CNS, such as ADHD, clinical depression, and anxiety. Involvement of disrupted neurotransmission in several CNS disorders makes these transporters, likewise, potential targets for the development of new and effective drugs in treatment of these conditions. With an increasing focus on brain health, considering WHO's vision for 2022-2031, there is a need for novel modifying and preventive treatment (62). Regarding the expanding use of illicit psychostimulants, with potential for abuse and addiction, there is also a need for drugs that can treat withdrawal symptoms and have anti-additive properties: substances binding the inward-facing conformation of the MATs, such as the atypical DAT-inhibitor vanoxerine, have shown these kinds of properties – and further investigation is highly valuable. The latter also applies to therapeutic stimulants with the potential for addiction, e.g., methylphenidate.

In this study, outward-facing homology models of hDAT and hNET were constructed, besides models of the outward- and inward-facing hSERT. These models were of high quality. Based on the generated human MAT-models, conserved and divergent residues in the S1-site of hDAT, hNET, and hSERT were mapped. All in all, IFD and MD simulations were further used to investigate interactions between psychostimulants and other substances (i.e., antidepressants, a non-stimulant, atypical inhibitors, and research standards) with the MATs, as well as their binding mode – where the goal was to identify determinants for selective binding to, respectively, hDAT, hNET, and hSERT.

The results indicate that non-conserved, divergent, residues in the S1-site play a key role in MAT-selectivity. These residues shape the polarity and steric environment in the orthosteric (S1) pocket, thus the stabilization of both substrates and inhibitors, interactions and orientation of ligands in each MAT. Besides, structural features in the ligands also appeared to play a role in MAT-selectivity, concerning the binding mode and formation of intermolecular interactions.

In short: in the outward-facing MAT-models, ligands with high preference for DAT also exhibited this for NET – compared to SERT, but not vice versa. For typical inhibitors, an extended α-sidechain appeared to increase the selectivity for hDAT (and hNET) (e.g.,

methylphenidate and MDPV) over hSERT, while ortho-substitutions on aromatic moieties seemed to shift the selectivity from hDAT and hSERT to hNET (e.g., atomoxetine and nisoxetine). Here, subsite C in hNET indicated to play an important role, where ortho-substituents were buried and interacted with hydrophobic residues, which differed from hDAT and hSERT. In total, some involved key residues were the non-conserved: Ala145:Tyr151: Ser420 in hNET (hDAT: Ser149: Phe155: Ala423; hSERT: Ala169: Tyr175: Thr439), and Val148 (hDAT: Val152; hSERT: Ile172). On the other hand, ligands with para-substituted- or 3,4-substituted aromatic rings (e.g., MDMA, MMAI, and paroxetine) seemed to shift selectivity towards hSERT, especially compared to hDAT. These moieties were stabilized in subsite B, where two non-conserved residues seemed to be important: Tyr175 (hNET: Tyr151; hDAT: Phe155) and Thr439 (hNET: Ser420; hDAT: Ala423), creating both polar and non-polar interactions. Additionally, 4-fluorophenyl moieties also indicated to favor hSERT over hNET and hDAT, some involved key residues involved were: Thr497 (hNET: Ala477; hDAT: Ala480) and Tyr95 (hNET: Phe72; hDAT: Phe76).

The atypical inhibitors are a structurally heterogeneous group, making it difficult to determine specific structural features important for binding an inward-facing conformation of the MATs. However, the MD simulations of vanoxerine in hSERT revealed that the movement of Phe335:Phe341: Phe347 (TMH6) and Ala441 (TMH8) closer into the S1-site, compared to the position in outward-facing conformation, was important for the creation of a hydrophobic pocket, where the aromatic moieties of the atypical inhibitors could stabilize and interact.

The MD simulations indicated that water molecules also seemed to play a role in the stabilization and creation of water-bridges with ligands in hNET and hDAT, but not to the same extent in hSERT.

Finally, no correlation between IFD-score and selectivity for the MATs were observed, which may be explained by MATs ability to accommodate distinct ligands by induced fitting, but also that the IFD-process was constrained to only the S1-site.

In summary, the concept of different pharmacological effects regarding binding to DAT, NET, or SERT is a vital driving force for future design of drugs performing high selectivity and potency for specific MATs. The findings in this study are highly worthful to further investigate.

Reference list

1. Informedhealth.org. How does the nervous system work? . Cologne, Germany Institute for Quality and Efficiency in Health Care (IQWiG); 2009 [Updated 2016] [cited 2022 December 08]. Available from: https://www.ncbi.nlm.nih.gov/books/NBK279390/.
2. Ludwig P, Reddy V, Varacallo M. Neuroananatomy, Central Nevous System (CNS). 2022 [cited 2022 December 08]. In: StatPearls [Internet]. Treasure Island [cited 2022 December 08]. Available from: https://www.ncbi.nlm.nih.gov/books/NBK442010/.
3. Purves D, Augustine G, Fitzpatrick D, et al. The subdivisions of the Central Nervous System. 2001 [cited 2022 December 08]. In: Neuroscience 2nd edition [Internet]. Sunderland (MA): Sinauer Associates, [cited 2022 December 08]. Available from: https://www.ncbi.nlm.nih.gov/books/NBK10926/.
4. Kaiser J, Lugo-Pico J. Neuronanatomy, Spinal Nerves. Updated 2022 [cited 2022 December 08]. In: StatPearls [Internet]. Treasure Island (FL), [cited 2022 December 08]. Available from: https://www.ncbi.nlm.nih.gov/books/NBK542218/.
5. Noggle CA, Moreau AR. Peripheral Nervous System. In: Goldstein S, Naglieri JA, editors. Encyclopedia of Child Behavior and Development. Boston, MA: Springer US; 2011. p. 1079-80.
6. Akinrodye M, Lui F. Neuroanatomy, Somatic Nervous System. Updated 2021 [cited 2022 December 08]. In: StatPearls [Internet]. Treasure Island (FL), [cited 2022 December 08]. Available from: https://www.ncbi.nlm.nih.gov/books/NBK556027/.
7. Tindle J, Tadi P. Neuroanatomy, Parasympathetic Nervous System. Updated 2021 [cited 2022 December 08]. In: StatPearls [Internet]. Treasure Island (FL), [cited 2022 December 08]. Available from: https://www.ncbi.nlm.nih.gov/books/NBK553141/.
8. Rao M, Gershon MD. The bowel and beyond: the enteric nervous system in neurological disorders. Nat Rev Gastroenterol Hepatol. 2016;13(9):517-28.
9. National Institute of Health. SEER Training Modules: Introduction to the Nervous System: National Cancer Institute. ; [cited 2022 December 08]. Available from: https://training.seer.cancer.gov/anatomy/nervous/
10. Thau L, Reddy V, Singh P, . Anatomy, Central Nervous System. Updated 2022 [cited 2022 December 09]. In: StatPearls [Internet]. Treasure Island (FL), [cited 2022 December 09]. Available from: https://www.ncbi.nlm.nih.gov/books/NBK542179/.
11. Brodal P. 3Structure of the Neuron and Organization of Nervous Tissue. 2016 [cited 2022 December 10]. In: The Central Nervous System [Internet]. Oxford University Press, [cited 2022 December 10]. Available from: https://doi.org/10.1093/med/9780190228958.003.0001.
12. Dotiwala AK, McCausland C, Samra NS. Anatomy, Head and Neck, Blood Brain Barrier. Updated 2022 [cited 2022 December 08]. In: StatPearls [Internet]. Treasure Island (FL), [cited 2022 December 08]. Available from: https://www.ncbi.nlm.nih.gov/books/NBK519556/.
13. Alexander JJ. Blood-brain barrier (BBB) and the complement landscape. Molecular Immunology. 2018;102:26-31.
14. Wong A, Ye M, Levy A, Rothstein J, Bergles D, Searson P. The blood-brain barrier: an engineering perspective. Frontiers in Neuroengineering. 2013;6.
15. MedlinePlus. Myelin. US: National Library of Medicine. ; Updated 2021 [cited 2022 December 10]. Available from: https://medlineplus.gov/ency/article/002261.htm.
16. The principles of nerve cell communication. Alcohol Health Res World. 1997;21(2):107-8.
17. Maiese K. Neurotransmission USA: MDS Manual 2022 [cited 2022 December 10]. Available from: https://www.msdmanuals.com/professional/neurologic-disorders/neurotransmission/neurotransmission.
18. Chen G, Guo X. Chapter Four - Neurobiology of Chinese Herbal Medicine on Major Depressive Disorder. In: Zeng B-Y, Zhao K, editors. International Review of Neurobiology. 135: Academic Press; 2017. p. Chapter 4.1.

19. Brodal P. Synaptic Function. 2016 [cited 2022 December 11]. In: The Central Nervous System [Internet]. Oxford University Press, [cited 2022 December 11]. Available from: https://doi.org/10.1093/med/9780190228958.003.0004.
20. *Khan Academy*. Neuron action potentials: The creation of a brain signal 2022 [cited 2022 December 10]. Available from: https://www.khanacademy.org/test-prep/mcat/organ-systems/neuron-membrane-potentials/a/neuron-action-potentials-the-creation-of-a-brain-signal.
21. Madhurantakam S, Karnam JB, Brabazon D, Takai M, Ahad IU, Balaguru Rayappan JB, et al. "Nano": An Emerging Avenue in Electrochemical Detection of Neurotransmitters. ACS Chemical Neuroscience. 2020;11(24):4024-47.
22. Grider MH, Jessu R, Kabir R. Physiology, Action Potential. Updated 2022 [cited 2022 December 10]. In: StatPearls [Internet]. Treasure Island (FL), [cited 2022 December 10]. Available from: https://www.ncbi.nlm.nih.gov/books/NBK538143/.
23. Purves D, Augustine G, Fitzpatrick D, et al. Excitatory and Inhibitory Postsynaptic Potentials. 2001 [cited 2022 December 10]. In: Neuroscience [Internet]. Sunderland (MA): Sinauer Associates. 2nd edition. [cited 2022 December 10]. Available from: https://www.ncbi.nlm.nih.gov/books/NBK11117/
24. Azizi SA. Monoamines: Dopamine, Norepinephrine, and Serotonin, Beyond Modulation, "Switches" That Alter the State of Target Networks. The Neuroscientist. 2020;28(2):121-43.
25. Grouleff J, Ladefoged L, Koldsø H, Schiøtt B. Monoamine transporters: Insights from molecular dynamics simulations. Frontiers in pharmacology. 2015;6:235.
26. Juárez Olguín H, Calderón Guzmán D, Hernández García E, Barragán Mejía G. The Role of Dopamine and Its Dysfunction as a Consequence of Oxidative Stress. Oxid Med Cell Longev. 2016;2016:9730467.
27. Luo SX, Huang EJ. Dopaminergic Neurons and Brain Reward Pathways: From Neurogenesis to Circuit Assembly. Am J Pathol. 2016;186(3):478-88.
28. Berridge KC, Kringelbach ML. Pleasure systems in the brain. Neuron. 2015;86(3):646-64.
29. Habibi M. Dopamine Receptors. In: Kompoliti K, Metman LV, editors. Encyclopedia of Movement Disorders. Oxford: Academic Press; 2010. p. 326-9.
30. Mishra A, Singh S, Shukla S. Physiological and Functional Basis of Dopamine Receptors and Their Role in Neurogenesis: Possible Implication for Parkinson's disease. J Exp Neurosci. 2018;12:1179069518779829.
31. Berger M, Gray JA, Roth BL. The expanded biology of serotonin. Annu Rev Med. 2009;60:355-66.
32. Athar S. Serotonin and Tryptophan. In: Kompoliti K, Metman LV, editors. Encyclopedia of Movement Disorders. Oxford: Academic Press; 2010. p. 104-8.
33. Hussain LS, Reddy V, Maani CV. Physiology, Noradrenergic Synapse. Updated 2022 [cited 2022 December 16]. In: StatPearls [Internet]. Treasure Island (FL), [cited 2022 December 16]. Available from: https://www.ncbi.nlm.nih.gov/books/NBK540977/
34. Lin H, Vartanian O. A Neuroeconomic Framework for Creative Cognition. Perspectives on Psychological Science. 2018;13.
35. Triarhou LC. Dopamine and Parkinsons's Disease. 2000-2013 [cited 2022 December 15]. In: Madame Curie Bioscience Database [Internet]. Austin (TX): Landes Bioscience, [cited 2022 December 15]. Available from: https://www.ncbi.nlm.nih.gov/books/NBK6271/
36. Alex KD, Pehek EA. Pharmacologic mechanisms of serotonergic regulation of dopamine neurotransmission. Pharmacol Ther. 2007;113(2):296-320.
37. Howell LL, Kimmel HL. Monoamine transporters and psychostimulant addiction. Biochemical Pharmacology. 2008;75(1):196-217.
38. Seo D, Patrick CJ, Kennealy PJ. Role of Serotonin and Dopamine System Interactions in the Neurobiology of Impulsive Aggression and its Comorbidity with other Clinical Disorders. Aggress Violent Behav. 2008;13(5):383-95.
39. Szabo ST, Blier P. Functional and pharmacological characterization of the modulatory role of serotonin on the firing activity of locus coeruleus norepinephrine neurons. Brain Research. 2001;922(1):9-20.

40. Mongeau R, Blier P, de Montigny C. The serotonergic and noradrenergic systems of the hippocampus: their interactions and the effects of antidepressant treatments. Brain Research Reviews. 1997;23(3):145-95.
41. Aggarwal S, Mortensen OV. Overview of Monoamine Transporters. Curr Protoc Pharmacol. 2017;79:12.6.1-.6.7.
42. Grouleff J, Ladefoged LK, Koldsø H, Schiøtt B. Monoamine transporters: insights from molecular dynamics simulations. Frontiers in Pharmacology. 2015;6.
43. Colas C. Toward a Systematic Structural and Functional Annotation of Solute Carriers Transporters—Example of the SLC6 and SLC7 Families. Frontiers in Pharmacology. 2020;11.
44. Góral I, Łątka K, Bajda M. Structure Modeling of the Norepinephrine Transporter. Biomolecules. 2020;10(1).
45. Vaughan RA, Foster JD. Mechanisms of dopamine transporter regulation in normal and disease states. Trends in Pharmacological Sciences. 2013;34(9):489-96.
46. Reith ME, editor. Neurotransmitter transporters; structure, function, and regulation, 2d ed. Portland: Portland: Ringgold Inc; 2002.
47. Seeman P, Niznik HB. Dopamine receptors and transporters in Parkinson's disease and schizophrenia. The FASEB Journal. 1990;4(10):2737-44.
48. Mandic-Maravic V, Grujicic R, Milutinovic L, Munjiza-Jovanovic A, Pejovic-Milovancevic M. Dopamine in Autism Spectrum Disorders—Focus on D2/D3 Partial Agonists and Their Possible Use in Treatment. Frontiers in Psychiatry. 2022;12.
49. Cheng MH, Block E, Hu F, Cobanoglu MC, Sorkin A, Bahar I. Insights into the Modulation of Dopamine Transporter Function by Amphetamine, Orphenadrine, and Cocaine Binding. Frontiers in Neurology. 2015;6.
50. Wang KH, Penmatsa A, Gouaux E. X-ray structure of Drosophila dopamine transporter bound to psychostimulant methamphetamine Protein Data Bank; 2015 [Available from: https://www.rcsb.org/structure/4XP6 , 10.2210/pdb4XP6/pdb
51. Gabrielsen M, Kurczab R, Ravna AW, Kufareva I, Abagyan R, Chilmonczyk Z, et al. Molecular mechanism of serotonin transporter inhibition elucidated by a new flexible docking protocol. Eur J Med Chem. 2012;47(1):24-37.
52. Zeppelin T, Ladefoged LK, Sinning S, Schiøtt B. Substrate and inhibitor binding to the serotonin transporter: Insights from computational, crystallographic, and functional studies. Neuropharmacology. 2019;161:107548.
53. Zhu R, Sandtner W, Ahiable JEA, Newman AH, Freissmuth M, Sitte HH, et al. Allosterically Linked Binding Sites in Serotonin Transporter Revealed by Single Molecule Force Spectroscopy. Frontiers in Molecular Biosciences. 2020;7.
54. Plenge P, Abramyan AM, Sørensen G, Mørk A, Weikop P, Gether U, et al. The mechanism of a high-affinity allosteric inhibitor of the serotonin transporter. Nature Communications. 2020;11(1):1491.
55. Coleman JA, Green EM, Gouaux E. X-ray structure of the ts3 human serotonin transporter complexed with paroxetine at the central site: Protein Data Bank; 2016 [Available from: https://www.rcsb.org/structure/5I6X , 10.2210/pdb5I6X/pdb.
56. Browman KE, Fox GB. 6.05 - Attention Deficit Hyperactivity Disorder. In: Taylor JB, Triggle DJ, editors. Comprehensive Medicinal Chemistry II. Oxford: Elsevier; 2007. p. 117-38.
57. Jha P, Ragnarsson L, Lewis RJ. Structure-Function of the High Affinity Substrate Binding Site (S1) of Human Norepinephrine Transporter. Front Pharmacol. 2020;11:217.
58. Penmatsa A, Wang KH, Gouaux E. X-ray structure of Drosophila dopamine transporter in complex with nisoxetine: Protein Data Bank; 2015 [Available from: https://www.rcsb.org/structure/4XNU , 10.2210/pdb4XNU/pdb.
59. Kurian MA, Gissen P, Smith M, Heales SJR, Clayton PT. The monoamine neurotransmitter disorders: an expanding range of neurological syndromes. The Lancet Neurology. 2011;10(8):721-33.
60. Teleanu RI, Niculescu A-G, Roza E, Vladâcenco O, Grumezescu AM, Teleanu DM. Neurotransmitters—Key Factors in Neurological and Neurodegenerative Disorders of the Central Nervous System. International Journal of Molecular Sciences. 2022;23(11):5954.

61. Montana Goverment. Neurological Disorders: Montana Department of Public Health and Human Services [cited 2023 January 04]. Available from: https://dphhs.mt.gov/schoolhealth/chronichealth/neurologicaldisorders
62. World Health Organization. Follow-up to the political declaration of the third high-level meeting of the General Assembly on the prevention and control of non-communicable diseases (A75/10 Add.4). 2022 [Available from: https://apps.who.int/gb/ebwha/pdf_files/WHA75/A75_10Add4-en.pdf
63. Pagonabarraga J, Álamo C, Castellanos M, Díaz S, Manzano S. Depression in Major Neurodegenerative Diseases and Strokes: A Critical Review of Similarities and Differences among Neurological Disorders. Brain Sciences [Internet]. 2023; 13(2).
64. Anghelescu I, Heuser I. Psychostimulants. In: Offermanns S, Rosenthal W, editors. Encyclopedia of Molecular Pharmacology. Berlin, Heidelberg: Springer Berlin Heidelberg; 2008. p. 1038-44.
65. Sinita E, Coghill D. The use of stimulant medications for non-core aspects of ADHD and in other disorders. Neuropharmacology. 2014;87:161-72.
66. Nierenberg A. Unipolar major depression in adults: Augmentation of antidepressants with stimulants and stimulant-like drugs. Waltham, Ma: UpToDate. ; Updated 2021 [cited 2023 February 03]. Available from: https://www.uptodate.com/contents/unipolar-major-depression-in-adults-augmentation-of-antidepressants-with-stimulants-and-stimulant-like-drugs/print#H280698
67. Brande L. Effects of Stimulant Drugs: Short-Term, Long-Term, Side Effects, and Treatment: American Addiction Centers; 2022 [cited 2023 January 06]. Available from: https://drugabuse.com/stimulants/effects-use/.
68. EMCDDA. New psychoactive substances (NPS): European Monitoring Centre for Drugs and Drug Addiction [cited 2023 January 07]. Available from: https://www.emcdda.europa.eu/topics/nps_en
69. UNODC. Early Warning Advisory on New Psychoactive Substances: United Nations Office on Drugs and Crime; [cited 2023 January 07]. Available from: https://www.unodc.org/LSS/Page/NPS
70. Shafi A, Berry AJ, Sumnall H, Wood DM, Tracy DK. New psychoactive substances: a review and updates. Ther Adv Psychopharmacol. 2020;10:2045125320967197.
71. Docherty JR, Alsufyani HA. Pharmacology of Drugs Used as Stimulants. The Journal of Clinical Pharmacology. 2021;61(S2):S53-S69.
72. Sheffler ZM, Patel P, Abdijadid S. Antidepressants. Updated 2022 [cited 2023 January 07]. In: StatPearls [Internet]. Treasure Island (FL), [cited 2023 January 07]. Available from: https://www.ncbi.nlm.nih.gov/books/NBK538182/.
73. Chu A, Wadhwa R. Selective Serotonin Reuptake Inhibitors. Updated 2022 [cited 2023 January 08]. In: StatPearls [Internet]. Treasure Island (FL), [cited 2023 January 08]. Available from: https://www.ncbi.nlm.nih.gov/books/NBK554406/.
74. Moraczewski J, Aedma K. Tricyclic Antidepressants. Updated 2022 [cited 2023 January 08]. In: StatPearls [Internet]. Treasure Island (FL), [cited 2023 January 08]. Available from: https://www.ncbi.nlm.nih.gov/books/NBK557791/.
75. Boku S, Nakagawa S, Toda H, Hishimoto A. Neural basis of major depressive disorder: Beyond monoamine hypothesis. [Oxford, England] ; [Malden, Mass.] :2018. p. 3-12.
76. Konyushok M. Why Neurologists Should Remember About Antidepressants. European Journal of Medical and Health Sciences. 2020;2(4).
77. Loi B, Sahai MA, De Luca MA, Shiref H, Opacka-Juffry J. The Role of Dopamine in the Stimulant Characteristics of Novel Psychoactive Substances (NPS)-Neurobiological and Computational Assessment Using the Case of Desoxypipradrol (2-DPMP). Front Pharmacol. 2020;11:806.
78. Bahji A, Mesbah-Oskui L. Comparative efficacy and safety of stimulant-type medications for depression: A systematic review and network meta-analysis. Journal of Affective Disorders. 2021;292:416-23.

79. Parker G. Psychostimulants as antidepressants: Their nuanced role? Australian & New Zealand Journal of Psychiatry. 2022;56(10):1226-9.
80. Clinic. C. Attention-Deficit/Hyperactivity Disorder (ADHD): Nonstimulant Therapy (Strattera) & Other ADHD Drugs: Cleveland Clinic; 2021 [cited 2023 January 08]. Available from: https://my.clevelandclinic.org/health/drugs/12959-attention-deficit-hyperactivity-disorder-adhd-nonstimulant-therapy-strattera--other-adhd-drugs
81. Jarończyk M, Walory J. Novel Molecular Targets of Antidepressants. Molecules [Internet]. 2022; 27(2).
82. De Crescenzo F, Ziganshina LE, Yudina EV, Kaplan YC, Ciabattini M, Wei Y, et al. Noradrenaline reuptake inhibitors (NRIs) for attention deficit hyperactivity disorder (ADHD) in adults. Cochrane Database of Systematic Reviews. 2018(6).
83. Bhat S, Newman AH, Freissmuth M. How to rescue misfolded SERT, DAT and NET: targeting conformational intermediates with atypical inhibitors and partial releasers. Biochemical Society Transactions. 2019;47(3):861-74.
84. Farzam K, Faizy RM, Saadabadi A. Stimulants. Updated 2022 [cited 2023 January 09]. In: StatPearls [Internet]. Treasure Island (FL), [cited 2023 January 09]. Available from: https://www.ncbi.nlm.nih.gov/books/NBK539896/.
85. Zachary SM, Patel P, Abdijadid S. Antidepressants. Updated 2022 [cited 2023 January 09]. In: StatPearls [Internet]. [cited 2023 January 09]. Available from: https://www.ncbi.nlm.nih.gov/books/NBK538182/.
86. Clinic. C. Depression Medicines: Cleveland Clinic; 2019 [cited 2023 January 09]. Available from: https://my.clevelandclinic.org/health/treatments/9301-depression-medicines.
87. Henning A, Kurtom M, Espiridion ED. A Case Study of Acute Stimulant-induced Psychosis. Cureus. 2019;11(2):e4126.
88. Foong AL, Patel T, Kellar J, Grindrod KA. The scoop on serotonin syndrome. Can Pharm J (Ott). 2018;151(4):233-9.
89. Whiskey E, Taylor D. A review of the adverse effects and safety of noradrenergic antidepressants. Journal of Psychopharmacology. 2013;27(8):732-9.
90. Andrade C, Rao NS. How antidepressant drugs act: A primer on neuroplasticity as the eventual mediator of antidepressant efficacy. Indian J Psychiatry. 2010;52(4):378-86.
91. Nyberg F. Structural plasticity of the brain to psychostimulant use. Neuropharmacology. 2014;87:115-24.
92. Fernandez-Espejo E, Rogriguez-Espinosa N. Psychostimulant Drugs and Neuroplasticity. Pharmaceuticals (Basel). 2011;4(7):976-91.
93. Henssler J, Heinz A, Brandt L, Bschor T. Antidepressant Withdrawal and Rebound Phenomena. Dtsch Arztebl Int. 2019;116(20):355-61.
94. American Addiction Centers. Chemical Imbalance & Drug Abuse in the Brain: Dopamine, Serotonin & More Updated 2022 [cited 2023 10 January]. Available from: https://americanaddictioncenters.org/health-complications-addiction/chemical-imbalance
95. NIDA. Drugs and the Brain. 2022. Available from: https://nida.nih.gov/publications/drugs-brains-behavior-science-addiction/drugs-brain.
96. Schmitt KC, Rothman RB, Reith ME. Nonclassical pharmacology of the dopamine transporter: atypical inhibitors, allosteric modulators, and partial substrates. J Pharmacol Exp Ther. 2013;346(1):2-10.
97. Reith MEA, Blough BE, Hong WC, Jones KT, Schmitt KC, Baumann MH, et al. Behavioral, biological, and chemical perspectives on atypical agents targeting the dopamine transporter. Drug and Alcohol Dependence. 2015;147:1-19.
98. Shaikh SA, Li J, Enkavi G, Wen PC, Huang Z, Tajkhorshid E. Visualizing functional motions of membrane transporters with molecular dynamics simulations. Biochemistry. 2013;52(4):569-87.
99. Gu Y, Li M. Chapter 3 - Molecular Modeling. In: Ishida H, Agag T, editors. Handbook of Benzoxazine Resins. Amsterdam: Elsevier; 2011. p. 103-10.
100. Amarante AM, Oliveira GS, Ierich JCM, Cunha RA, Freitas LCG, Franca EF, et al. 7 - Molecular Modeling Applied to Nanobiosystems. In: Da Róz AL, Ferreira M, de Lima Leite F,

Oliveira ON, editors. Nanoscience and its Applications: William Andrew Publishing; 2017. p. 179-220.
101. Vyas VK, Ukawala RD, Ghate M, Chintha C. Homology modeling a fast tool for drug discovery: current perspectives. Indian J Pharm Sci. 2012;74(1):1-17.
102. Alberts B, Johnson A, Lewis J, Raff M, Roberts K, Walter P. Molecular Biology of the Cell: Protein Function. New York: Garland Science; 2002. Available from: https://www.ncbi.nlm.nih.gov/books/NBK26911/.
103. Choi I-G, Kim S-H. Evolution of protein structural classes and protein sequence families. Proceedings of the National Academy of Sciences. 2006;103(38):14056-61.
104. Gromiha MM, Saranya N, Selvaraj S, Jayaram B, Fukui K. Sequence and structural features of binding site residues in protein-protein complexes: comparison with protein-nucleic acid complexes. Proteome Sci. 2011;9 Suppl 1(Suppl 1):S13.
105. Muhammed MT, Aki-Yalcin E. Homology modeling in drug discovery: Overview, current applications, and future perspectives. [Oxford] :2019. p. 12-20.
106. Ravna AW, Sylte I. Homology Modeling of Transporter Proteins (Carriers and Ion Channels). In: Orry AJW, Abagyan R, editors. Homology Modeling: Methods and Protocols. Totowa, NJ: Humana Press; 2012. p. 281-99.
107. Cheng Y. Membrane protein structural biology in the era of single particle cryo-EM. Current Opinion in Structural Biology. 2018;52:58-63.
108. Martí-Renom MA, Stuart AC, Fiser A, Sánchez R, Melo F, Sali A. Comparative protein structure modeling of genes and genomes. Annu Rev Biophys Biomol Struct. 2000;29:291-325.
109. Wheeler D, Bhagwat M. Comparative Genomics: Humana Press; 2007. Available from: https://www.ncbi.nlm.nih.gov/books/NBK1734/.
110. Pearson WR. An introduction to sequence similarity ("homology") searching. Curr Protoc Bioinformatics. 2013;Chapter 3:Unit3.1.
111. LLC S. Prime 4.0 User Manual. New York.2015. p. 41-6.
112. Wiltgen M. Algorithms for Structure Comparison and Analysis: Homology Modelling of Proteins. In: Ranganathan S, Gribskov M, Nakai K, Schönbach C, editors. Encyclopedia of Bioinformatics and Computational Biology. Oxford: Academic Press; 2019. p. 38-61.
113. Gani OABSM. Signposts of Docking and Scoring in Drug Design. Chemical Biology & Drug Design. 2007;70(4):360-5.
114. Bruce A, Johnson A, Lewis J, Raff M, Roberts K, Walter P. Molecular Biology of the Cell: The Lipid Bilayer. New York: Garland Science; 2002. Available from: https://www.ncbi.nlm.nih.gov/books/NBK26871/.
115. Alberts B, Johnson A, Lewis J, Raff M, Roberts K, Walter P. Molecular Biology of the Cell: Membrane Proteins. New York: Garland Science; 2002. Available from: https://www.ncbi.nlm.nih.gov/books/NBK26878/.
116. LLC S. Induced Fit Docking Protocol 2015-2. New York.2015. p. 1-7.
117. Ramadurai S, Holt A, Krasnikov V, van den Bogaart G, Killian JA, Poolman B. Lateral diffusion of membrane proteins. J Am Chem Soc. 2009;131(35):12650-6.
118. Du X, Li Y, Xia YL, Ai SM, Liang J, Sang P, et al. Insights into Protein-Ligand Interactions: Mechanisms, Models, and Methods. Int J Mol Sci. 2016;17(2).
119. Kitchen DB, Decornez H, Furr JR, Bajorath J. Docking and scoring in virtual screening for drug discovery: methods and applications. Nature Reviews Drug Discovery. 2004;3(11):935-49.
120. Salahudeen MS, Nishtala PS. An overview of pharmacodynamic modelling, ligand-binding approach and its application in clinical practice. Saudi Pharm J. 2017;25(2):165-75.
121. Hollingsworth SA, Dror RO. Molecular Dynamics Simulation for All. Neuron. 2018;99(6):1129-43.
122. LLC S. Desmond 4.2 User Manual. New York. 2015. p. 9-25.
123. Jabeen A, Mohamedali A, Ranganathan S. Protocol for Protein Structure Modelling. In: Ranganathan S, Gribskov M, Nakai K, Schönbach C, editors. Encyclopedia of Bioinformatics and Computational Biology. Oxford: Academic Press; 2019. p. 252-72.

124. Roy K, Kar S, Das RN. Chapter 5 - Computational Chemistry. In: Roy K, Kar S, Das RN, editors. Understanding the Basics of QSAR for Applications in Pharmaceutical Sciences and Risk Assessment. Boston: Academic Press; 2015. p. 151-89.
125. Sasidharan S, Saudagar P. Chapter 23 - Prediction, validation, and analysis of protein structures: A beginner's guide. In: Tripathi T, Dubey VK, editors. Advances in Protein Molecular and Structural Biology Methods: Academic Press; 2022. p. 373-85.
126. Patrick GL. An introduction to medical chemistry. Oxford: Oxford University Press; 2013. p. 816
127. Loschwitz J, Olubiyi OO, Hub JS, Strodel B, Poojari CS. Chapter Seven - Computer simulations of protein–membrane systems. In: Strodel B, Barz B, editors. Progress in Molecular Biology and Translational Science. 170: Academic Press; 2020. p. 273-403.
128. Lewis-Atwell T, Townsend PA, Grayson MN. Comparisons of different force fields in conformational analysis and searching of organic molecules: A review. Tetrahedron. 2021;79:131865.
129. Hwang SB, Lee CJ, Lee S, Ma S, Kang Y-M, Cho KH, et al. PMFF: Development of a Physics-Based Molecular Force Field for Protein Simulation and Ligand Docking. The Journal of Physical Chemistry B. 2020;124(6):974-89.
130. Hernández-Rodríguez M, Rosales-Hernández M, Mendieta-Wejebe J, Martínez-Archundia M, Correa-Basurto J. Current Tools and Methods in Molecular Dynamics (MD) Simulations for Drug Design. Current medicinal chemistry. 2016;23.
131. EMCDDA. European Drug Report 2022: Trends and Developments Luxembourg: Publications Office on the European Union; 2022 [Available from: 10.2810/75644.
132. LLC S. Maestro 10.2 User Manual. New York. 2015. p. 1-10.
133. LLC S. Maestro [Internet] 2022 [cited 2022 September 28]. Available from: https://www.schrodinger.com/products/maestro.
134. Altschul SF, Gish W, Miller W, Myers EW, Lipman DJ. Basic local alignment search tool. Journal of Molecular Biology. 1990;215(3):403-10.
135. wwPDB consortium. Protein Data Bank: the single global archive for 3D macromolecular structure data. Nucleic Acids Res. 2019;47(D1):D520-d8.
136. Wang KH, Penmatsa A, Gouaux E. X-ray structure of Drosophila dopamine transporter bound to neurotransmitter dopamine: Protein Data Bank; 2015 [Available from: https://www.rcsb.org/structure/4XP1 , 10.2210/pdb4XP1/pdb
137. Wang KH, Penmatsa A, Gouaux E. X-ray structure of Drosophila dopamine transporter in complex with cocaine: Protein Data Bank; 2015 [Available from: https://www.rcsb.org/structure/4XP4 , 10.2210/pdb4XP4/pdb
138. Wang KH, Penmatsa A, Gouaux E. X-ray structure of Drosophila dopamine transporter bound to psychostimulant D-amphetamine: Protein Data Bank; 2015 [Available from: https://www.rcsb.org/structure/4xp9 , 10.2210/pdb4XP9/pdb.
139. Coleman JA, Green EM, Gouaux E. X-ray structure of the ts3 human serotonin transporter compleced with s-citalopram at the central and allosteric sites: Protein Data Bank; 2016 [Available from: https://www.rcsb.org/structure/5I73 , 10.2210/pdb5I73/pdb.
140. Yang D, Coleman JA, Gouaux E. Cryo-EM Structure of the wild-type human serotonin transporter in complex with ibogaine and 15B8 Fab in the inward conformation: Protein Data Bank; 2019 [Available from: https://www.rcsb.org/structure/6DZZ , 10.2210/pdb6DZZ/pdb.
141. The UniProt Consortium. UniProt: the universal protein knowledgebase in 2021. Nucleic Acids Research. 2020;49(D1):D480-D9.
142. Lomize MA, Lomize AL, Pogozheva ID, Mosberg HI. OPM: Orientations of Proteins in Membranes database. Bioinformatics. 2006;22(5):623-5.
143. Mosberg HI, Lomize MA, Pogozheva ID, Joo H, Lomize AL. Orientations of Proteins in Membranes (OPM) database. Updated: 2023 February 10.
144. Roth BL, Lopez E, Patel S, Kroeze WK. The Multiplicity of Serotonin Receptors: Uselessly Diverse Molecules or an Embarrassment of Riches? : The Neuroscientist, 6:252-262; 2000 [cited 2023 February 17]. Available from: https://pdsp.unc.edu/databases/kidb.php.

145. Coleman JA, Green EM, Gouaux E. X-ray structures and mechanism of the human serotonin transporter. Nature. 2016;532(7599):334-9.
146. Coleman JA, Yang D, Zhao Z, Wen P-C, Yoshioka C, Tajkhorshid E, et al. Serotonin transporter–ibogaine complexes illuminate mechanisms of inhibition and transport. Nature. 2019;569(7754):141-5.
147. Newell PD, Fricker AD, Roco CA, Chandrangsu P, Merkel SM. A Small-Group Activity Introducing the Use and Interpretation of BLAST. J Microbiol Biol Educ. 2013;14(2):238-43.
148. Wang KH, Penmatsa A, Gouaux E. Neurotransmitter and psychostimulant recognition by the dopamine transporter. Nature. 2015;521(7552):322-7.
149. LLC S. Protein Preparation Guide. New York.2012. p. 1-13.
150. Madhavi Sastry G, Adzhigirey M, Day T, Annabhimoju R, Sherman W. Protein and ligand preparation: parameters, protocols, and influence on virtual screening enrichments. Journal of Computer-Aided Molecular Design. 2013;27(3):221-34.
151. LLC S. Protein Preparation Wizard: Schrödinger, Inc.; [cited 2022 October 20]. Available from: https://www.schrodinger.com/science-articles/protein-preparation-wizard.
152. Schrödinger Inc. When adding N terminal residues to a protein, the coordinates are added to the end of the coordinate list. Is there a way of putting the coordinates in residues order? : KNOWLEDGE BASE; 2015 [updated 2015 May 11; cited 2022 October 20]. Available from: https://www.schrodinger.com/kb/477.
153. Schrödinger Inc. How do I align independent chains in two or more protein structures? : KNOWLEGDE BASE; 2016 [updated 2016 December 2; cited 2022 October 11]. Available from: https://www.schrodinger.com/kb/1426.
154. Wlodawer A. Stereochemistry and Validation of Macromolecular Structures. Methods Mol Biol. 2017;1607:595-610.
155. LLC S. Maestro 10.2 User Manual. New York. 2015. p. 270-3.
156. Laskowski RA, MacArthur MW, Moss DS, Thornton JM. PROCHECK: a program to check the stereochemical quality of protein structures. Journal of Applied Crystallography 1993;26(2):283-91.
157. LLC S. Maestro 10.2 User Manual New York. 2015. p. 254-7.
158. LLC S. Superposition Panel: Schrödinger, Inc. ; Updated 2014 [cited 2023 February 08]. Available from: http://gohom.win/ManualHom/Schrodinger/Schrodinger_2015-2_docs/maestro/help_Maestro/tools_menu/super_panel.html.
159. Kufareva I, Abagyan R. Methods of protein structure comparison. Methods Mol Biol. 2012;857:231-57.
160. Castro-Alvarez A, Costa AM, Vilarrasa J. The Performance of Several Docking Programs at Reproducing Protein-Macrolide-Like Crystal Structures. Molecules. 2017;22(1).
161. LLC S. LigPrep 3.4: User Manual New York. 2015. p. 1-5.
162. Schrödinger Inc. What is the structure of LigPrep? : KNOWLEDGE BASE; 2011 [updated 2011 June 3; cited 2022 October 29]. Available from: https://www.schrodinger.com/kb/1243.
163. Penmatsa A, Wang KH, Gouaux E. X-ray structure of Drosophila dopamine transporter with subsiteB mutations (D121G/S426M) bound to beta-CFT or Win35428: Protein Data Bank; 2015 [Available from: https://www.rcsb.org/structure/4XPG, 10.2210/pdb4XPG/pdb
164. Abramyan AM, Stolzenberg S, Li Z, Loland CJ, Noé F, Shi L. The Isomeric Preference of an Atypical Dopamine Transporter Inhibitor Contributes to Its Selection of the Transporter Conformation. ACS Chemical Neuroscience. 2017;8(8):1735-46.
165. LLC S. Desmond 4.2 User Manual 2015. New York. ; [9-17].
166. wwPDB consortium. Membrane protein (OPM): Protein Data Bank; Updated 2021 [cited 2023 February 11]. Available from: https://www.rcsb.org/docs/search-and-browse/browse-options/membrane-protein-opm
167. LLC S. Protein Structure Alignment Panel: Schrödinger, Inc. ; Updated 2014 [cited 2023 February 20]. Available from: http://gohom.win/ManualHom/Schrodinger/Schrodinger_2015-2_docs/maestro/help_Maestro/tools_menu/protein_structure_alignment.html

168. Kadaoluwa Pathirannahalage SP, Meftahi N, Elbourne A, Weiss ACG, McConville CF, Padua A, et al. Systematic Comparison of the Structural and Dynamic Properties of Commonly Used Water Models for Molecular Dynamics Simulations. Journal of Chemical Information and Modeling. 2021;61(9):4521-36.
169. Penmatsa A, Wang KH, Gouaux E. X-ray structures of Drosophila dopamine transporter in complex with nisoxetine and reboxetine. Nature Structural & Molecular Biology. 2015;22(6):506-8.
170. LLC S. What is considered a good GlideScore? : KNOWLEDGE BASE; 2010 [updated 4 December 2010; cited 2023 January 26]. Available from: https://www.schrodinger.com/kb/639.
171. LLC S. What is the difference between GlideScore and Emodel, and which should I use for ranking poses? : KNOWLEDGE BASE; 2016 [updated 19 May 2016; cited 2023 January 25]. Available from: https://www.schrodinger.com/kb/1027.
172. LLC S. What is the difference between the docking score and GlideScore from the results of a docking run? : KNOWLEDGE BASE; 2019 [updated 30 September 2019; cited 2023 January 25]. Available from: https://www.schrodinger.com/kb/348.
173. Burlingham BT, Widlanski TS. An Intuitive Look at the Relationship of Ki and IC50: A More General Use for the Dixon Plot. Journal of Chemical Education. 2003;80(2):214.
174. Aykul S, Martinez-Hackert E. Determination of half-maximal inhibitory concentration using biosensor-based protein interaction analysis. Analytical Biochemistry. 2016;508:97-103.
175. Rickli A, Hoener MC, Liechti ME. Monoamine transporter and receptor interaction profiles of novel psychoactive substances: Para-halogenated amphetamines and pyrovalerone cathinones. European Neuropsychopharmacology. 2015;25(3):365-76.
176. Simmler L, Buser T, Donzelli M, Schramm Y, Dieu L-H, Huwyler J, et al. Pharmacological characterization of designer cathinones in vitro. British Journal of Pharmacology. 2013;168(2):458-70.
177. Simmler LD, Rickli A, Hoener MC, Liechti ME. Monoamine transporter and receptor interaction profiles of a new series of designer cathinones. Neuropharmacology. 2014;79:152-60.
178. Luethi D, Kaeser PJ, Brandt SD, Krähenbühl S, Hoener MC, Liechti ME. Pharmacological profile of methylphenidate-based designer drugs. Neuropharmacology. 2018;134:133-40.
179. Luethi D, Kolaczynska KE, Docci L, Krähenbühl S, Hoener MC, Liechti ME. Pharmacological profile of mephedrone analogs and related new psychoactive substances. Neuropharmacology. 2018;134:4-12.
180. Tatsumi M, Groshan K, Blakely RD, Richelson E. Pharmacological profile of antidepressants and related compounds at human monoamine transporters. European Journal of Pharmacology. 1997;340(2):249-58.
181. Hysek CM, Simmler LD, Nicola VG, Vischer N, Donzelli M, Krähenbühl S, et al. Duloxetine Inhibits Effects of MDMA (“Ecstasy") In Vitro and in Humans in a Randomized Placebo-Controlled Laboratory Study. PLOS ONE. 2012;7(5):e36476.
182. Bhat S, Guthrie DA, Kasture A, El-Kasaby A, Cao J, Bonifazi A, et al. Tropane-Based Ibogaine Analog Rescues Folding-Deficient Serotonin and Dopamine Transporters. ACS Pharmacol Transl Sci. 2021;4(2):503-16.
183. Busti AJ. The Inhibitory Constant (Ki) and its Use in Understanding Drug Interactions: EBM Consult, LLC; 2015 [cited 2023 February 15]. Available from: https://www.ebmconsult.com/articles/inhibitory-constant-ki-drug-interactions.
184. Torres GE, Gainetdinov RR, Caron MG. Plasma membrane monoamine transporters: structure, regulation and function. Nature Reviews Neuroscience. 2003;4(1):13-25.
185. Rudin D, Liechti ME, Luethi D. Molecular and clinical aspects of potential neurotoxicity induced by new psychoactive stimulants and psychedelics. Experimental Neurology. 2021;343:113778.
186. Pantsar T, Poso A. Binding Affinity via Docking: Fact and Fiction. Molecules. 2018;23(8).
187. Ortore G, Orlandini E, Betti L, Giannaccini G, Mazzoni MR, Camodeca C, et al. Focus on Human Monoamine Transporter Selectivity. New Human DAT and NET Models, Experimental Validation, and SERT Affinity Exploration. ACS Chem Neurosci. 2020;11(20):3214-32.

188. Sitbon E, Pietrokovski S. Occurrence of protein structure elements in conserved sequence regions. BMC Struct Biol. 2007;7:3.
189. Cheng MH, Bahar I. Monoamine transporters: structure, intrinsic dynamics and allosteric regulation. Nat Struct Mol Biol. 2019;26(7):545-56.
190. Robinson SW, Afzal AM, Leader DP. Chapter 13 - Bioinformatics: Concepts, Methods, and Data. In: Padmanabhan S, editor. Handbook of Pharmacogenomics and Stratified Medicine. San Diego: Academic Press; 2014. p. 259-87.
191. Nepal B, Das S, Reith ME, Kortagere S. Overview of the structure and function of the dopamine transporter and its protein interactions. Front Physiol. 2023;14:1150355.
192. Andersen J, Ringsted KB, Bang-Andersen B, Strømgaard K, Kristensen AS. Binding site residues control inhibitor selectivity in the human norepinephrine transporter but not in the human dopamine transporter. Sci Rep. 2015;5:15650.
193. Luethi D, Liechti ME. Designer drugs: mechanism of action and adverse effects. Archives of Toxicology. 2020;94(4):1085-133.
194. Krippendorff B-F, Lienau P, Reichel A, Huisinga W. Optimizing Classification of Drug-Drug Interaction Potential for CYP450 Isoenzyme Inhibition Assays in Early Drug Discovery. Journal of Biomolecular Screening. 2007;12(1):92-9.
195. Clauss NJ, Daws LC. 1.08 - Neurotransmitter Transporters and Their Role in the Pharmacological Actions of Therapeutic and Abused Drugs. In: Kenakin T, editor. Comprehensive Pharmacology. Oxford: Elsevier; 2022. p. 165-204.
196. Derijks HJ, Heerdink ER, Janknegt R, De Koning FH, Loonen BOAJ, Egberts AC. Visualizing pharmacological activities of antidepressants: a novel approach. The open pharmacology journal. 2008;2(1).
197. Mustafa NS, Bakar NHA, Mohamad N, Adnan LHM, Fauzi N, Thoarlim A, et al. MDMA and the Brain: A Short Review on the Role of Neurotransmitters in Neurotoxicity. Basic Clin Neurosci. 2020;11(4):381-8.
198. Verrico CD, Miller GM, Madras BK. MDMA (Ecstasy) and human dopamine, norepinephrine, and serotonin transporters: implications for MDMA-induced neurotoxicity and treatment. Psychopharmacology. 2007;189(4):489-503.
199. Nichols DE. Entactogens: How the Name for a Novel Class of Psychoactive Agents Originated. Frontiers in Psychiatry. 2022;13.
200. Ding YS, Naganawa M, Gallezot JD, Nabulsi N, Lin SF, Ropchan J, et al. Clinical doses of atomoxetine significantly occupy both norepinephrine and serotonin transports: Implications on treatment of depression and ADHD. NeuroImage. 2014;86:164-71.
201. Mei X, Wang L, Yang B, Li X. Sex differences in noradrenergic modulation of attention and impulsivity in rats. Psychopharmacology. 2021;238(8):2167-77.
202. Pourhamzeh M, Moravej FG, Arabi M, Shahriari E, Mehrabi S, Ward R, et al. The Roles of Serotonin in Neuropsychiatric Disorders. Cellular and Molecular Neurobiology. 2022;42(6):1671-92.
203. Sharma H, Santra S, Dutta A. Triple reuptake inhibitors as potential next-generation antidepressants: a new hope? Future Med Chem. 2015;7(17):2385-406.
204. Schmitt KC, Zhen J, Kharkar P, Mishra M, Chen N, Dutta AK, et al. Interaction of cocaine-, benztropine-, and GBR12909-like compounds with wild-type and mutant human dopamine transporters: molecular features that differentially determine antagonist-binding properties. Journal of Neurochemistry. 2008;107(4):928-40.
205. Tunstall BJ, Ho CP, Cao J, Vendruscolo JCM, Schmeichel BE, Slack RD, et al. Atypical dopamine transporter inhibitors attenuate compulsive-like methamphetamine self-administration in rats. Neuropharmacology. 2018;131:96-103.
206. Avelar AJ, Cao J, Newman AH, Beckstead MJ. Atypical dopamine transporter inhibitors R-modafinil and JHW 007 differentially affect D2 autoreceptor neurotransmission and the firing rate of midbrain dopamine neurons. Neuropharmacology. 2017;123:410-9.
207. Jacobs MT, Zhang Y-W, Campbell SD, Rudnick G. Ibogaine, a Noncompetitive Inhibitor of Serotonin Transport, Acts by Stabilizing the Cytoplasm-facing State of the Transporter*. Journal of Biological Chemistry. 2007;282(40):29441-7.

208. Burtscher V, Hotka M, Li Y, Freissmuth M, Sandtner W. A label-free approach to detect ligand binding to cell surface proteins in real time. eLife. 2018;7:e34944.
209. Jinn-Moon Y, Hsu DF, editors. Consensus scoring criteria in structure-based virtual screening. Conference, Emerging Information Technology 2005; 2005 15-15 Aug. 2005.
210. Larsen MA, Plenge P, Andersen J, Eildal JN, Kristensen AS, Bøgesø KP, et al. Structure-activity relationship studies of citalopram derivatives: examining substituents conferring selectivity for the allosteric site in the 5-HT transporter. Br J Pharmacol. 2016;173(5):925-36.
211. Glennon RA, Dukat M. Structure-Activity Relationships of Synthetic Cathinones. In: Baumann MH, Glennon RA, Wiley JL, editors. Neuropharmacology of New Psychoactive Substances (NPS): The Science Behind the Headlines. Cham: Springer International Publishing; 2017. p. 19-47.
212. Zhou J. Norepinephrine transporter inhibitors and their therapeutic potential. Drugs Future. 2004;29(12):1235-44.
213. Sakloth F, Kolanos R, Mosier PD, Bonano JS, Banks ML, Partilla JS, et al. Steric parameters, molecular modeling and hydropathic interaction analysis of the pharmacology of para-substituted methcathinone analogues. British Journal of Pharmacology. 2015;172(9):2210-8.
214. Simmler LD, Liechti ME. Interactions of Cathinone NPS with Human Transporters and Receptors in Transfected Cells. Curr Top Behav Neurosci. 2017;32:49-72.
215. Kumar A, Kumar P. Construction of pioneering quantitative structure activity relationship screening models for abuse potential of designer drugs using index of ideality of correlation in monte carlo optimization. Archives of Toxicology. 2020;94(9):3069-86.
216. Yadav-Samudrala BJ, Eltit JM, Glennon RA. Synthetic Cathinone Analogues Structurally Related to the Central Stimulant Methylphenidate as Dopamine Reuptake Inhibitors. ACS Chemical Neuroscience. 2019;10(9):4043-50.
217. Liechti M. Novel psychoactive substances (designer drugs): overview and pharmacology of modulators of monoamine signaling. Swiss Med Wkly. 2015;145:w14043.
218. Bhat S, Newman AH, Freissmuth M. How to rescue misfolded SERT, DAT and NET: targeting conformational intermediates with atypical inhibitors and partial releasers. Biochem Soc Trans. 2019;47(3):861-74.
219. Sørensen L, Andersen J, Thomsen M, Hansen SM, Zhao X, Sandelin A, et al. Interaction of antidepressants with the serotonin and norepinephrine transporters: mutational studies of the S1 substrate binding pocket. J Biol Chem. 2012;287(52):43694-707.
220. Zheng G, Xue W, Wang P, Yang F, Li B, Li X, et al. Exploring the Inhibitory Mechanism of Approved Selective Norepinephrine Reuptake Inhibitors and Reboxetine Enantiomers by Molecular Dynamics Study. Scientific Reports. 2016;6(1):26883.
221. Zhao H, Tang S, Du L. Hydrogen bond docking site competition in methyl esters. Spectrochimica Acta Part A: Molecular and Biomolecular Spectroscopy. 2017;181:122-30.
222. Steele TWE, Spires Z, Jones CB, Glennon RA, Dukat M, Eltit JM. Non-conserved residues dictate dopamine transporter selectivity for the potent synthetic cathinone and psychostimulant MDPV. Neuropharmacology. 2021;200:108820.
223. Islas ÁA, Moreno LG, Scior T. Induced fit, ensemble binding space docking and Monte Carlo simulations of MDMA 'ecstasy' and 3D pharmacophore design of MDMA derivatives on the human serotonin transporter (hSERT). Heliyon. 2021;7(8):e07784.
224. Palusiak M, Grabowski SJ. Methoxy group as an acceptor of proton in hydrogen bonds. Journal of Molecular Structure. 2002;642(1):97-104.
225. Coleman JA, Gouaux E. Structural basis for recognition of diverse antidepressants by the human serotonin transporter. Nature Structural & Molecular Biology. 2018;25(2):170-5.
226. Beuming T, Kniazeff J, Bergmann ML, Shi L, Gracia L, Raniszewska K, et al. The binding sites for cocaine and dopamine in the dopamine transporter overlap. Nat Neurosci. 2008;11(7):780-9.
227. Verma V. Classic Studies on the Interaction of Cocaine and the Dopamine Transporter. Clin Psychopharmacol Neurosci. 2015;13(3):227-38.
228. Henry LK, Field JR, Adkins EM, Parnas ML, Vaughan RA, Zou M-F, et al. Tyr-95 and Ile-172 in Transmembrane Segments 1 and 3 of Human Serotonin Transporters Interact to Establish High Affinity Recognition of Antidepressants*. Journal of Biological Chemistry. 2006;281(4):2012-23.

229. Koldsø H, Autzen HE, Grouleff J, Schiøtt B. Ligand induced conformational changes of the human serotonin transporter revealed by molecular dynamics simulations. PLoS One. 2013;8(6):e63635.
230. Lu C, Wu C, Ghoreishi D, Chen W, Wang L, Damm W, et al. OPLS4: Improving Force Field Accuracy on Challenging Regimes of Chemical Space. Journal of Chemical Theory and Computation. 2021;17(7):4291-300.
231. Góral I, Łątka K, Bajda M. Structure Modeling of the Norepinephrine Transporter. Biomolecules [Internet]. 2020; 10(1).
232. Joseph D, Pidathala S, Mallela AK, Penmatsa A. Structure and Gating Dynamics of Na+/Cl–Coupled Neurotransmitter Transporters. Frontiers in Molecular Biosciences. 2019;6.
233. Shan J, Javitch JA, Shi L, Weinstein H. The Substrate-Driven Transition to an Inward-Facing Conformation in the Functional Mechanism of the Dopamine Transporter. PLOS ONE. 2011;6(1):e16350.
234. Hellsberg E, Ecker GF, Stary-Weinzinger A, Forrest LR. A structural model of the human serotonin transporter in an outward-occluded state. PLoS One. 2019;14(6):e0217377.
235. Carandini T, Cercignani M, Galimberti D, Scarpini E, Bozzali M. The distinct roles of monoamines in multiple sclerosis: A bridge between the immune and nervous systems? Brain, Behavior, and Immunity. 2021;94:381-91.
236. Müller T. Experimental Dopamine Reuptake Inhibitors in Parkinson's Disease: A Review of the Evidence. J Exp Pharmacol. 2021;13:397-408.
237. Bushe C, Day K, Reed V, Karlsdotter K, Berggren L, Pitcher A, et al. A network meta-analysis of atomoxetine and osmotic release oral system methylphenidate in the treatment of attention-deficit/hyperactivity disorder in adult patients. Journal of Psychopharmacology. 2016;30(5):444-58.

Supplementary materials

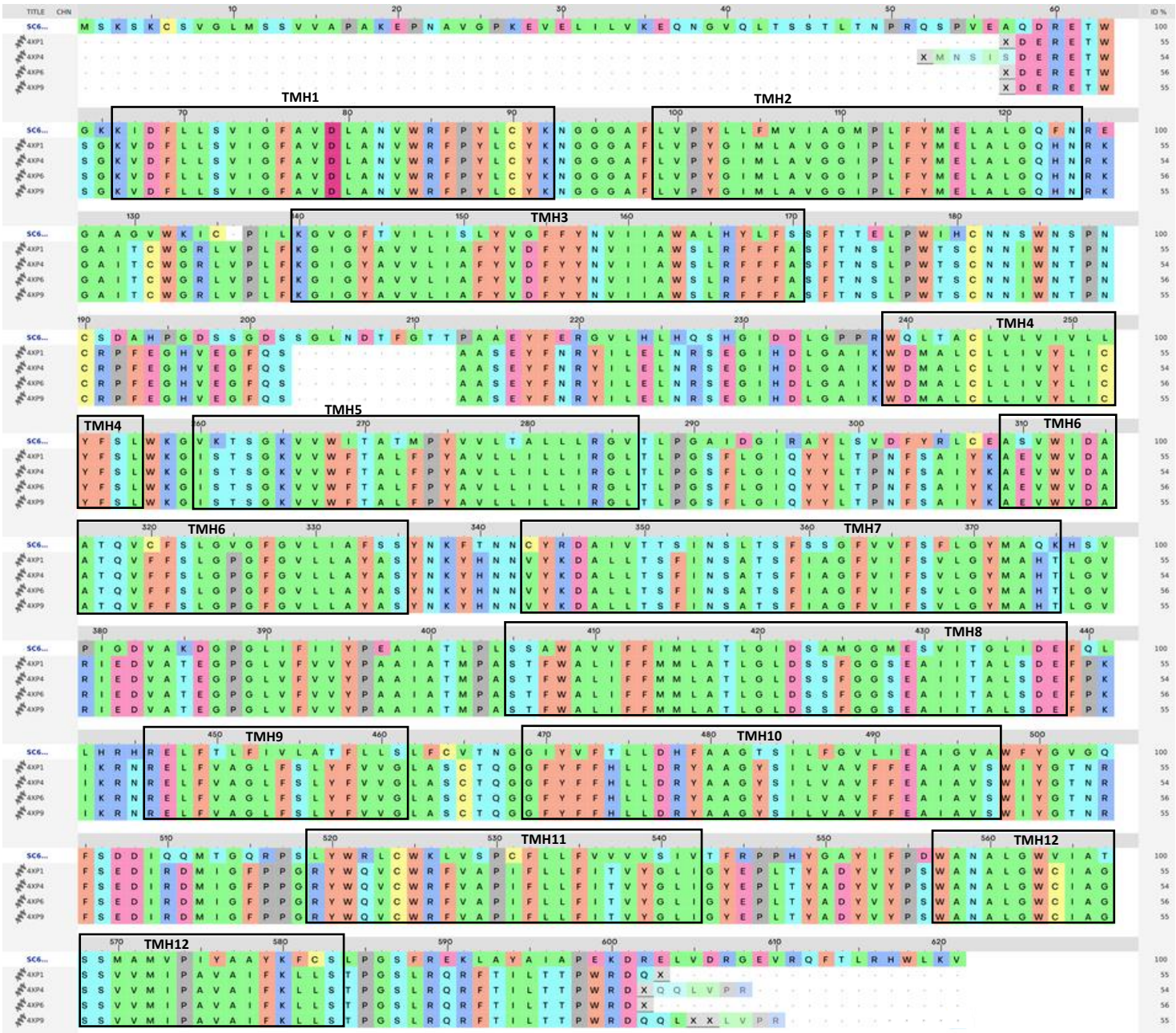

Figure S1: *Multiple sequence alignment of the sequences from all the dDATs (PDB-codes: 4XP1, 4XP4, 4XP6, 4XP9), after performing protein preparation, to the human sequence of DAT (UniProtKB-code: SC6A3). The proteins from PDB were used as templates to build the homology models of the outward-facing hDATs in MSV (Schrödinger, release 2022-3)- as described in section 3.3.4. Asp79 (Aps46 in dDAT) (TMH1) is highlighted with a hot pink color. The twelve TMHs (TMH1-TMH12) are labeled in bold letters.*

All the dDAT sequences are identical, however, there are some differences in the solved lengths (represented as "X" in the alignment). The alignment is adjusted by manually "removing" gaps from the secondary structures and the binding site.

The percentage of identity, with respect to the target sequence, is displayed in the right in the figure. Roundings compared to the Protein BLAST alignment are done by the MSV (Schrödinger, release 2022-3).

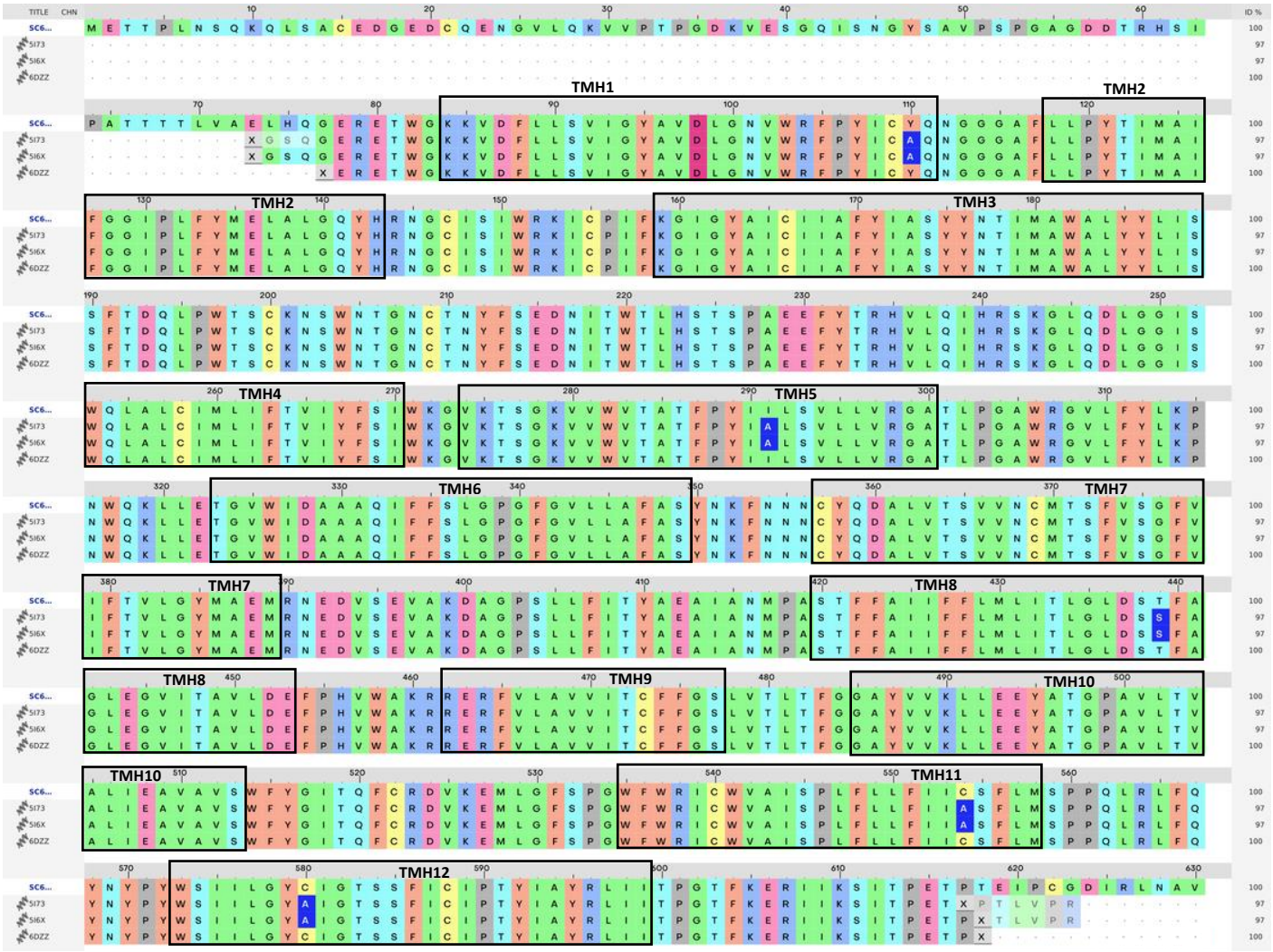

Figure S2: *Multiple sequence alignment of the "modified" human outward-facing SERT (PDB-code: 5I73 and 5I6X)-, and inward-facing SERT (PDB-code: 6DZZ) sequences, after performing protein preparation, to the human sequence of SERT (UniprotKB-code: SC6A4). The proteins from PDB were used as templates to build the models of the outward- and inward-facing hSERTs, respectively, in MSV (Schrödinger, release 2022-3) – as described in section 3.3.4. Asp98 (TMH1) is highlighted with a hot pink color. The twelve TMHs (TMH1-TMH12) are labeled in bold letters.*

The proteins in 5I73 and 5I6X are ts3-constructs, meaning that there are three thermostabilizing mutations in the sequences (i.e., Ile291Ala, Thr439Ser, and Tyr110Ala). These are highlighted in dark blue. Two other mutations are also found in the sequences (Cys554Ala, and Cys580Ala). The solved sequence length of all the templates also differs (represented as "X" in the alignment). For the 6DZZ-protein structure, the N-and C terminals are truncated.

There were no gaps in the secondary structures or the binding sites in this alignment.

The percentage of identity, with respect to the target sequence, is displayed in the right in the figure. Roundings compared to the Protein BLAST alignment are done by the MSV (Schrödinger, release 2022-3).

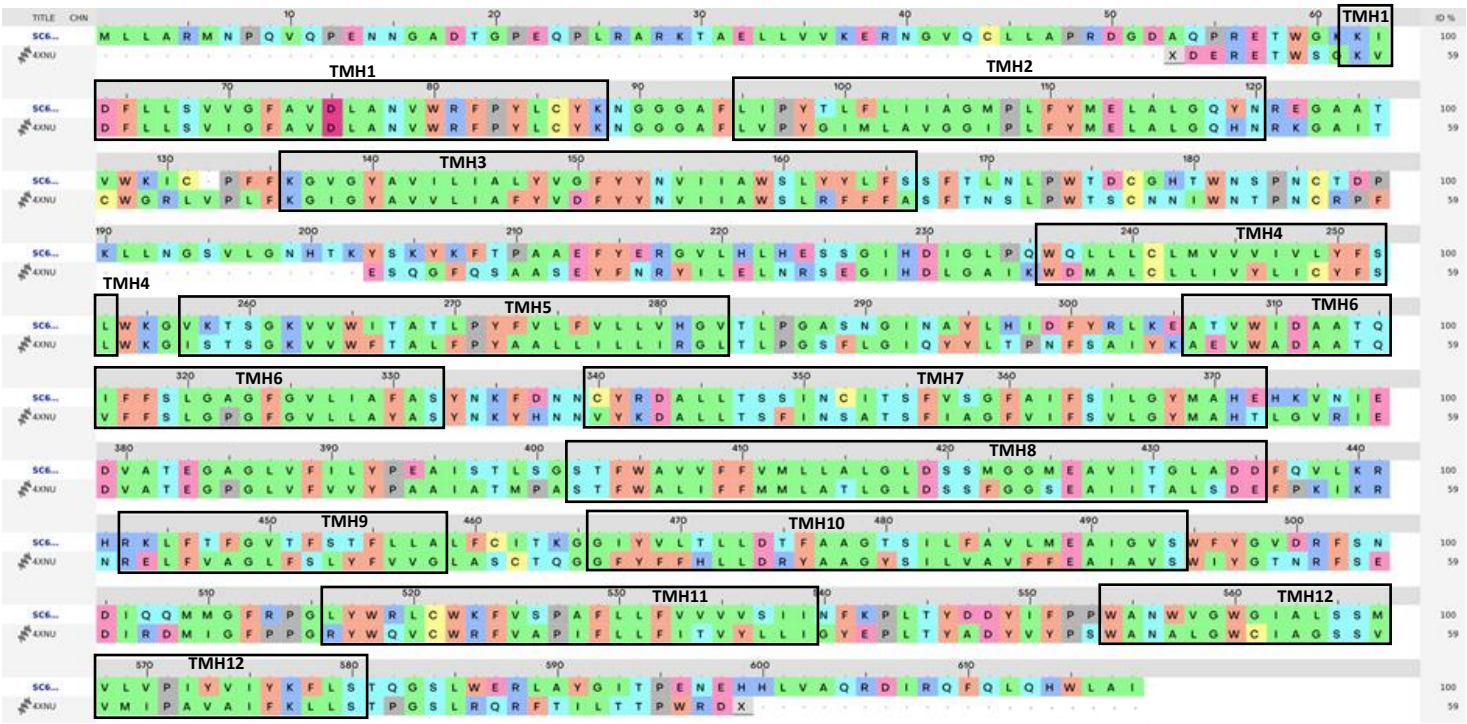

Figure S3: *Alignment of dDAT (PDB-code: 4XNU), after performing protein preparation, to the human sequence of NET (UniProtKB-code: SC6A2). These sequences were used to build the homology model of hNET in MSV (Schrödinger, release 2022-3), as described in section 3.3.4. Asp75 (Aps46 in dDAT) (TMH1) is highlighted with a hot pink color. The twelve TMHs (TMH1-TMH12) are labeled in bold letters.*

There are several differences between corresponding residues, but the overall identity is ~59 %, with respect to the target, as shown to the right in the figure. A rounding of the percentage identity compared to the Protein BLAST alignment is done by the MSV (Schrödinger, release 2022-3). The solved length of the template is shorter than the target sequence as well (represented as "X" in the alignment). The alignment is adjusted by manually "removing" gaps from the secondary structures and the binding site.

```
HETATM 8397  N   B40 A 601     -151.944-142.546 195.072  1.00 92.81           N1+
HETATM 8398  C89 B40 A 601     -153.352-142.727 194.473  1.00100.73           C
HETATM 8399  C   B40 A 601     -153.890-141.324 194.130  1.00106.01          C
HETATM 8400  CB  B40 A 601     -153.294-143.681 193.247  1.00101.53          C
HETATM 8401  CG  B40 A 601     -154.637-144.149 192.682  1.00106.24          C
HETATM 8402  CD1 B40 A 601     -154.677-144.631 191.370  1.00 95.80          C
HETATM 8403  CD2 B40 A 601     -155.805-144.164 193.456  1.00107.41          C
HETATM 8404  CE1 B40 A 601     -155.866-145.122 190.836  1.00 93.36          C
HETATM 8405  CE2 B40 A 601     -156.994-144.652 192.922  1.00101.10          C
HETATM 8406  CZ  B40 A 601     -157.021-145.124 191.614  1.00 95.72          C
HETATM 8407  CM  B40 A 601     -151.326-143.787 195.735  1.00 86.92          C
HETATM 8408 H__1 B40 A 601     -151.985-141.816 195.772  1.00 92.81          H
HETATM 8409 H__2 B40 A 601     -151.315-142.225 194.345  1.00 92.81          H
HETATM 8410  HA  B40 A 601     -153.908-143.157 195.307  1.00100.73          H
HETATM 8411 1HXT B40 A 601     -154.914-141.378 193.758  1.00106.01          H
HETATM 8412 2HXT B40 A 601     -153.903-140.672 195.005  1.00106.01          H
HETATM 8413 3HXT B40 A 601     -153.291-140.838 193.359  1.00106.01          H
HETATM 8414  HB1 B40 A 601     -152.756-144.597 193.493  1.00101.53          H
HETATM 8415  HB2 B40 A 601     -152.727-143.199 192.447  1.00101.53          H
HETATM 8416  HD1 B40 A 601     -153.785-144.638 190.763  1.00 95.80          H
HETATM 8417  HD2 B40 A 601     -155.805-143.820 194.478  1.00107.41          H
HETATM 8418  HE1 B40 A 601     -155.894-145.495 189.823  1.00 93.36          H
HETATM 8419  HE2 B40 A 601     -157.894-144.672 193.517  1.00101.10          H
HETATM 8420  HZ  B40 A 601     -157.948-145.493 191.198  1.00 95.72          H
HETATM 8421  HM1 B40 A 601     -150.399-143.446 196.193  1.00 86.92          H
HETATM 8422  HM2 B40 A 601     -152.029-144.162 196.481  1.00 86.92          H
HETATM 8423  HM3 B40 A 601     -151.117-144.512 194.951  1.00 86.92          H
HETATM 8424 NA    NA A 603     -147.157-142.372 196.848  1.00 76.63         Na1+
HETATM 8425 NA    NA A 604     -148.024-147.821 191.395  1.00 80.29         Na1+
HETATM 8426 CL    CL A 605     -144.127-139.055 199.669  1.00 83.05         Cl1-
HETATM 8427  O   HOH A 703     -149.547-140.713 195.422  1.00 80.94          O
HETATM 8428  H1  HOH A 703     -149.807-139.802 195.101  1.00 80.94          H
HETATM 8429  H2  HOH A 703     -149.043-141.190 194.693  1.00 80.94          H
HETATM 8430  O   HOH A 705     -144.676-149.158 191.706  1.00 70.79          O
HETATM 8431  H1  HOH A 705     -145.230-149.000 192.523  1.00 70.79          H
HETATM 8432  H2  HOH A 705     -145.141-149.828 191.121  1.00 70.79          H
```

Figure S4: *Clipping displaying the pdb-text file of all the het groups (named HETATM) included in the methamphetamine-dDAT complex (PDB- structure 4XP6). The ligand, methamphetamine, was manually named "C89" from "CA" (marked with a red box) to make it recognizable as a ligand and separated from the amino acid residues by MSV in Prime (Schrödinger, release 2022-3).*

```
HETATM 7549  C7  MPO C 704     -154.406-135.472 163.694  1.00107.15           C
HETATM 7550  C1  CLR C 705     -139.112-158.252 201.907  1.00 98.70           C
HETATM 7551  C2  CLR C 705     -140.088-159.325 202.381  1.00 96.07           C
HETATM 7552  C3  CLR C 705     -141.071-158.726 203.380  1.00 92.05           C
HETATM 7553  C4  CLR C 705     -141.905-157.688 202.637  1.00 92.74           C
HETATM 7554  C5  CLR C 705     -141.102-156.780 201.717  1.00 91.21           C
HETATM 7555  C6  CLR C 705     -141.620-155.577 201.438  1.00 87.01           C
HETATM 7556  C7  CLR C 705     -140.731-154.369 201.292  1.00 91.23           C
HETATM 7557  C8  CLR C 705     -139.549-154.729 200.413  1.00 90.53           C
HETATM 7558  C9  CLR C 705     -138.848-155.977 200.937  1.00 93.13           C
HETATM 7559  C10 CLR C 705     -139.791-157.180 201.064  1.00 94.57           C
HETATM 7560  C11 CLR C 705     -137.610-156.300 200.092  1.00 91.70           C
HETATM 7561  C12 CLR C 705     -136.653-155.109 199.908  1.00 92.81           C
HETATM 7562  C13 CLR C 705     -137.406-153.865 199.443  1.00 93.03           C
HETATM 7563  C14 CLR C 705     -138.528-153.609 200.424  1.00 88.46           C
HETATM 7564  C15 CLR C 705     -139.020-152.208 200.111  1.00 83.37           C
HETATM 7565  C16 CLR C 705     -137.748-151.471 199.684  1.00 85.08           C
HETATM 7566  C17 CLR C 705     -136.669-152.528 199.496  1.00 89.24           C
HETATM 7567  C18 CLR C 705     -137.965-154.107 198.042  1.00 85.23           C
HETATM 7568  C19 CLR C 705     -140.084-157.730 199.673  1.00 85.23           C
HETATM 7569  C20 CLR C 705     -135.791-152.164 198.307  1.00 89.68           C
HETATM 7570  C21 CLR C 705     -134.613-153.124 198.145  1.00 91.53           C
HETATM 7571  C22 CLR C 705     -135.278-150.732 198.490  1.00 86.27           C
HETATM 7572  C23 CLR C 705     -134.101-150.455 197.554  1.00 81.27           C
HETATM 7573  C24 CLR C 705     -133.382-149.173 197.942  1.00 78.97           C
HETATM 7574  C25 CLR C 705     -132.804-148.458 196.725  1.00 78.69           C
HETATM 7575  C26 CLR C 705     -131.929-147.277 197.141  1.00 75.52           C
HETATM 7576  C27 CLR C 705     -133.927-147.981 195.811  1.00 77.46           C
HETATM 7577  O1  CLR C 705     -141.931-159.739 203.952  1.00 83.04           O
HETATM 7578  N   1WE C 706     -150.706-142.384 196.513  1.00 77.31           N
HETATM 7579  C99 1WE C 706     -152.082-142.925 196.472  1.00 78.46           C
HETATM 7580  C   1WE C 706     -152.596-142.904 197.905  1.00 75.96           C
HETATM 7581  CB  1WE C 706     -152.939-142.058 195.544  1.00 79.55           C
HETATM 7582  CG  1WE C 706     -154.158-142.771 195.001  1.00 81.26           C
HETATM 7583  CD1 1WE C 706     -154.132-143.261 193.697  1.00 84.18           C
HETATM 7584  CD2 1WE C 706     -155.308-142.921 195.775  1.00 78.82           C
HETATM 7585  CE1 1WE C 706     -155.239-143.922 193.166  1.00 79.15           C
HETATM 7586  CE2 1WE C 706     -156.415-143.580 195.240  1.00 84.89           C
HETATM 7587  CZ  1WE C 706     -156.385-144.080 193.939  1.00 79.47           C
HETATM 7588  C8  P4G C 707     -180.009-146.245 199.777  1.00113.36           C
HETATM 7589  C7  P4G C 707     -179.702-144.990 199.019  1.00121.58           C
HETATM 7590  O4  P4G C 707     -180.888-144.183 198.853  1.00123.97           O
HETATM 7591  C6  P4G C 707     -180.643-142.787 198.536  1.00120.44           C
HETATM 7592  C5  P4G C 707     -179.601-142.614 197.431  1.00119.79           C
HETATM 7593  O3  P4G C 707     -179.579-141.209 197.072  1.00123.44           O
HETATM 7594  C4  P4G C 707     -179.376-140.959 195.674  1.00124.46           C
HETATM 7595  C3  P4G C 707     -180.209-139.707 195.231  1.00120.27           C
HETATM 7596  O2  P4G C 707     -179.685-138.516 195.899  1.00114.76           O
HETATM 7597  C2  P4G C 707     -180.573-137.381 195.860  1.00116.83           C
HETATM 7598  C1  P4G C 707     -181.715-137.561 196.839  1.00111.37           C
HETATM 7599  H81 P4G C 707     -179.197-146.762 199.888  1.00136.04           H
HETATM 7600  H82 P4G C 707     -180.664-146.769 199.285  1.00136.04           H
HETATM 7601  H83 P4G C 707     -180.373-146.010 200.663  1.00136.04           H
HETATM 7602  H71 P4G C 707     -179.350-145.217 198.155  1.00145.90           H
```

Figure S5: *Clipping displaying the pdb-text file of some of the het groups (named HETATM) included in the amphetamine-dDAT complex (PDB- structure 4XP9). The ligand, D-amphetamine, was manually named "C99" from "CA" (marked with a red box) to make it recognizable as a ligand and separated from the amino acid residues by MSV in Prime (Schrödinger, release 2022-3).*

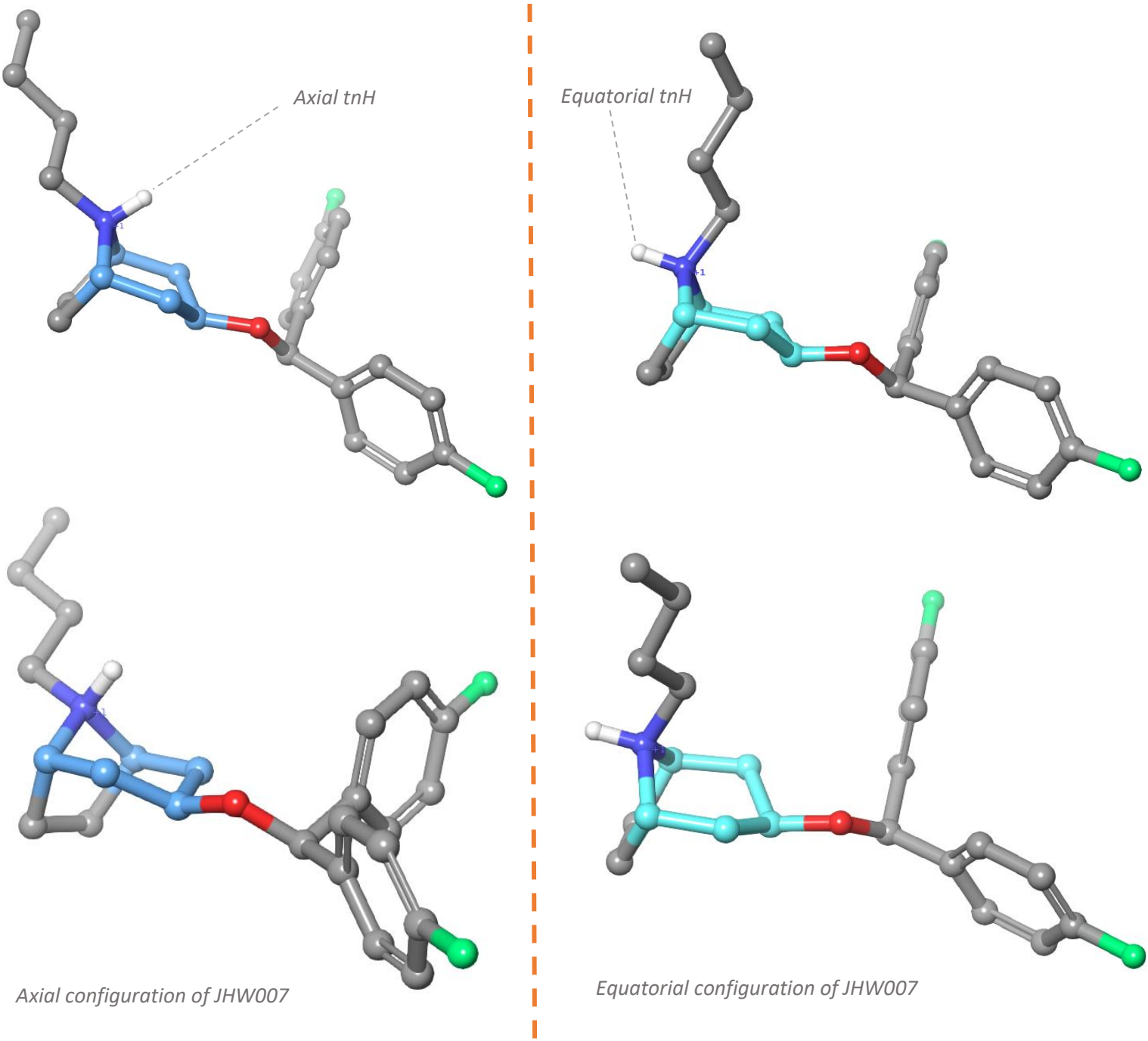

Figure S6: *3D representation of the axial-and equatorial configuration of JHW007, meaning the configuration of the hydrogen attached to the tertiary amine in the tropane ring (tNH). The six-carbon ring is colored blue (axial) and turquoise (equatorial) in each representation, respectively. The picture is from the side-view for both configurations to see the tropane ring and the attached amine hydrogen clearer.*

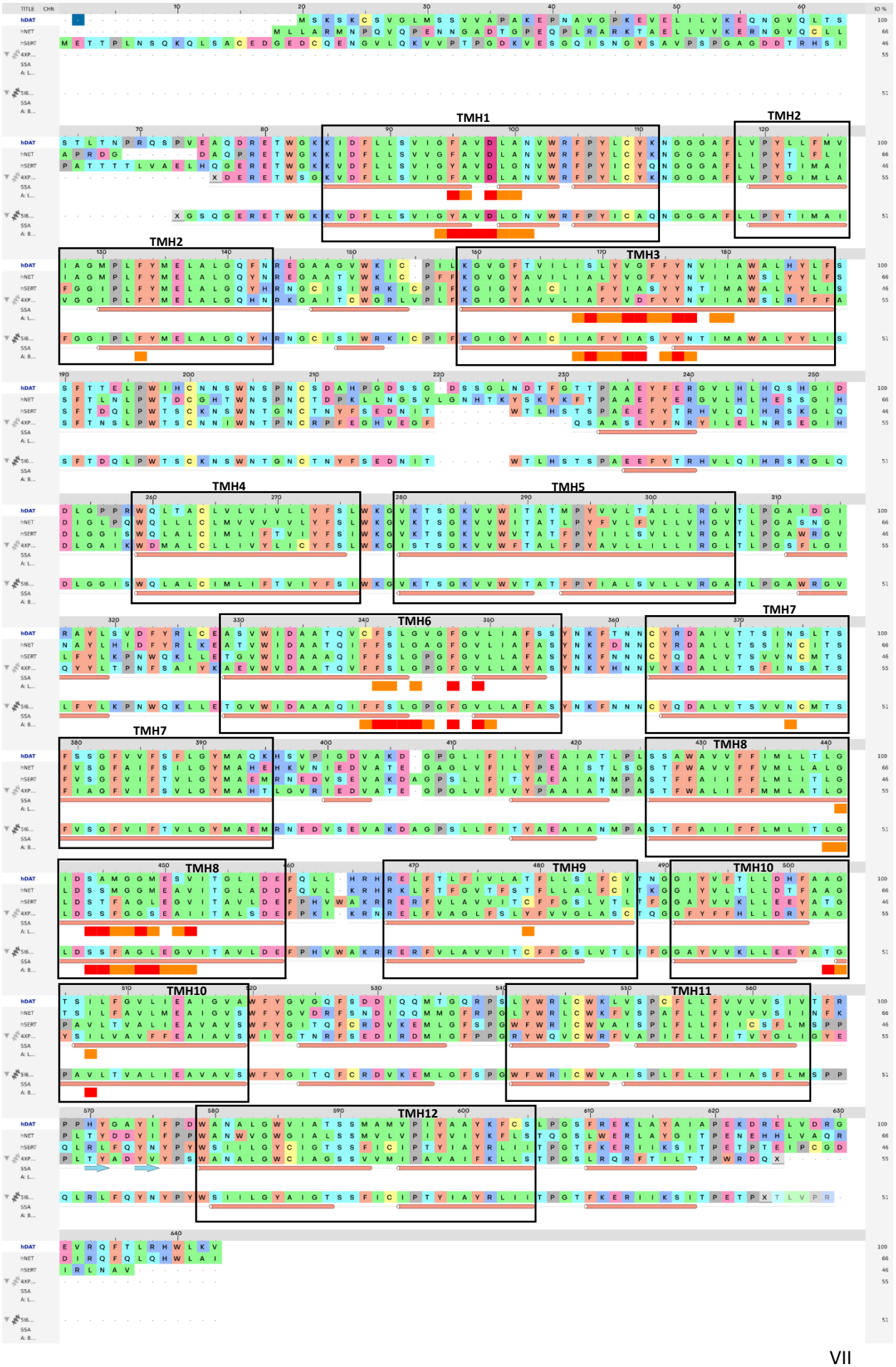
TMH1
TMH2
TMH2
TMH3
TMH4
TMH5
TMH6
TMH7
TMH7
TMH8
TMH8
TMH9
TMH10
TMH10
TMH11
TMH12

Figure S7: *Multiple sequence alignment of the hDAT-, hNET-, and hSERT-sequence from UniProtKB, and the template-sequences of the ts3-construct of hSERT (PDB-code: 5I6X) bound to paroxetine and dDAT (PDB-code: 4XP1) bound to DA, after performed protein preparation, generated in MSV (Schrödinger, release 2022-3). The twelve TMHs (TMH1-TMH2) are labeled in bold letters. Amino acid residues in contact with the ligands are highlighted under the secondary structures: the red colors represent residues within 4 Å from the ligand, while the orange color represents residues within 6 Å from the ligand.*

The alignment profile corresponding amino acid residues in the three MATs, where the crucial Asp in TMH1 is highlighted in a hot pink color (hDAT: Asp79; hNET: Asp75; hSERT: Asp98). Conserved- and divergent amino acids can be observed from the figure but are also provided in table 1 (supplementary material).